

**Investigation into the magnetic and the
structural properties of two low-dimensional
antiferromagnets
TiPO₄ and CrOCl**

Von der Fakultät Mathematik und Physik der Universität Stuttgart
zur Erlangung der Würde eines Doktors der Naturwissenschaften
(Dr. rer. nat.) genehmigte Abhandlung

vorgelegt von

Patrick Gerald Reuvekamp

aus St. Catharines (Kanada)

Hauptberichter: Prof. Dr. Bernhard Keimer

Mitberichter: Prof. Dr. Martin Dressel

Tag der mündlichen Prüfung: 12.11.2014

Max-Planck-Institut für Festkörperforschung

Universität Stuttgart

2014

This thesis is dedicated to my parents and late maternal grandparents who supported me unconditionally throughout my educational journey.

Erklärung über die Eigenständigkeit der Dissertation

Ich versichere, dass ich die vorliegende Arbeit mit dem Titel

"Investigation into the magnetic and the structural properties of two low-dimensional antiferromagnets TiPO_4 and CrOCl "

selbständig verfasst und keine anderen als die angegebenen Quellen und Hilfsmittel benutzt habe; aus fremden Quellen entnommene Passagen und Gedanken sind als solche kenntlich gemacht.

Declaration of Authorship

I hereby certify that the dissertation entitled

"Investigation into the magnetic and the structural properties of two low-dimensional antiferromagnets TiPO_4 and CrOCl "

is entirely my own work except where otherwise indicated. Passages and ideas from other sources have been clearly indicated.

Name/Name: Patrick Gerald Reuvekamp

Unterschrift/Signed: _____

Datum/Date: 15.11.2014

Abstract

Titanium (III) phosphate TiPO_4 ($3d^1$ electronic configuration with $S = \frac{1}{2}$) is a one-dimensional quantum antiferromagnet exhibiting non-conventional spin-Peierls behaviour at low temperatures. Chromium oxychloride CrOCl ($3d^3$ electronic configuration with $S = \frac{3}{2}$) is a two-dimensional antiferromagnet consisting of ferromagnetic spin chains interconnected by competing anti- and ferromagnetic spin exchanges interactions. The magnetic and the structural properties of these compounds are intimately related via magnetoelastic coupling. Incommensurate and commensurate phases are observed at low temperatures in both compounds. These systems are investigated using various experimental techniques, i.e. magnetic susceptibility, heat capacity, dielectric, Raman scattering and electron paramagnetic resonance measurements. The magnetoelastic coupling in these compounds is explored using a thermal expansion cell commissioned and tested in the course of this dissertation work.

TiPO_4 consists of quasi one-dimensional Ti^{3+} spin $S = \frac{1}{2}$ chains running along the \mathbf{c} -axis with strong antiferromagnetic intrachain coupling ($J_{\text{intra}} = -965$ K, $J_{\text{inter}} = -20$ K). A two-stage spin-Peierls transition occurs in TiPO_4 consisting of two successive phase transitions at $T_{c1} \approx 74$ K and $T_{c2} \approx 110$ K. The temperature dependence of the lattice parameters as well as the magnetic field and the pressure dependence of the two phase transitions are studied extensively. The results are analyzed and discussed in terms of the spin-Peierls theory and the crystallographic data.

CrOCl is characterized by an intricate two-dimensional intrachain and inter-chain spin exchange scenario. A low temperature monoclinic distortion occurs at the onset of the commensurate antiferromagnetic order at $T_N \approx 13.5$ K. The commensurate phase is preceded by an incommensurate antiferromagnetic phase starting below 27 K. Ferromagnetic spin exchange interactions are dominant in contrast to the low temperature antiferromagnetic ordering. In low temperature regime ($T < 30$ K), various measurement techniques are employed to construct extended (H, T) magnetic phase diagrams for $H \parallel \mathbf{c}$ and $H \perp \mathbf{c}$. The phase diagrams are very complex resulting from the magnetic frustration of

the competing spin exchange interactions. The spin exchange interactions are investigated by employing spin polarized density functional theory calculations and classical mean-field/Monte Carlo simulations. Using the density functional theory results, the extended (H, T) magnetic phase diagrams are discussed in terms of the ANNNI model.

Abstrakt

Titan(III)-phosphate TiPO_4 (elektronische Konfiguration $3d^1$, $S = \frac{1}{2}$) ist ein eindimensionaler Quantenantiferromagnet, bei dem tiefen Temperaturen unkonventionelle Spin-Peierls Verzerrungen auftreten. CrOCl (elektronische Konfiguration $3d^3$, $S = \frac{3}{2}$) ist ein zwei-dimensionaler Antiferromagnet, in dem ferromagnetische Spinketten über konkurrierende anti- und ferromagnetische Austauschkopplung miteinander wechselwirken. Die magnetischen und die strukturellen Eigenschaften dieser Verbindungen sind eng über magnetoelastische Wechselwirkungen miteinander verknüpft. Inkommensurable und kommensurable Strukturen werden bei tiefen Temperaturen für beide Verbindungen beobachtet. Beide Systeme werden mit diversen experimentellen Techniken untersucht, z. B. mittels Suszeptibilitätsmessungen, Bestimmung der spezifischen Wärmekapazität als Funktion des Magnetfeldes und der Temperatur, dielektrische Messungen, EPR Messungen und mittels Raman Spektroskopie. Die magnetoelastischen Eigenschaften werden mithilfe eines Tieftemperaturdilatometers bestimmt.

TiPO_4 besteht aus quasi ein-dimensionalen Ti^{3+} $S = \frac{1}{2}$ Spinketten mit sehr großer antiferromagnetischer Intrakettenkopplung ($J_{\text{intra}} = -965$ K, $J_{\text{inter}} = -20$ K). Für TiPO_4 wird ein zweistufiger Spin-Peierls Übergang bei $T_{c1} \approx 74$ K und bei $T_{c2} \approx 110$ K beobachtet. Sowohl die Temperaturabhängigkeit der Gitterkonstanten, als auch die Magnetfeld- und die Druckabhängigkeit von T_{c1} und T_{c2} werden ausgiebig studiert. Die Resultate werden anhand von gängigen Spin-Peierls Theorien sowie anhand der Kristallstruktur diskutiert.

CrOCl weist außerordentlich komplexe Austauschkopplungen innerhalb der Chrom Schichten auf. Obwohl ferromagnetische Austauschwechselwirkungen insgesamt dominieren, kommt es bei tiefen Temperaturen zu antiferromagnetischer Ordnung. Beim Einsetzen der antiferromagnetisch geordneten Phase bei $T_N \approx 13.5$ K beobachtet man eine monokline Verzerrung der Kristallstruktur. Zuvor wird eine inkommensurable antiferromagnetische Phase zwischen 27 K and 13.5 K ausgebildet. Eine Vielzahl experimenteller Techniken wird bei tiefen Temperaturen dazu benutzt, um die (H, T) Phasendiagramme

für $H \parallel \mathbf{c}$ und $H \perp \mathbf{c}$ aufzuklären. Die Phasendiagramme erweisen sich als außerordentlich komplex und spiegeln die magnetische Frustration infolge konkurrierender Austauschwechselwirkung wider. Die Austauschwechselwirkungen werden mithilfe spinpolarisierter Dichtefunktionalrechnungen und klassischer Mean-Field Monte-Carlo Simulationen untersucht und im Rahmen des ANNNI Modells diskutiert.

List of Publications

1. R. S. Gonnelli, D. Daghero, M. Tortello, G. A. Ummarino, Z. Bukowski, J. Karpinski, P. G. Reuvekamp, R. K. Kremer, G. Profeta, K. Suzuki and K. Kuroki, *Fermi-surface topological phase transitions and horizontal order-parameter nodes in CaFe_2As_2 under pressure*, submitted for publication.
2. P. G. Reuvekamp, R. K. Kremer, J. Köhler, and A. Bussmann-Holder, *Spin-lattice coupling induced crossover from negative to positive magnetostriction in EuTiO_3 from thermal expansion measurements*, Physical Review B **90**, 094420 (2014).
3. P. G. Reuvekamp, R. K. Kremer, J. Köhler, and A. Bussmann-Holder, *Evidence for the first-order nature of the structural instability in EuTiO_3 from thermal expansion measurements*, Physical Review B **90**, 104105 (2014).
4. M. Stingaciu, P. G. Reuvekamp, C. W. Tai, R. K. Kremer and M. Johnsson, *The magnetodielectric effect in BaTiO_3 - $\text{SrFe}_{12}\text{O}_{19}$ nanocomposites*, Journal of Materials Chemistry C **2**, 325–330 (2014).
5. M. Bykov, J. Zhang, A. Schönleber, A. Wölfel, S. I. Ali, S. van Smaalen, R. Glaum, H. J. Koo, M. H. Whangbo, P. G. Reuvekamp, J. M. Law, C. Hoch and R. K. Kremer, *Spin-Peierls distortions in TiPO_4* , Physical Review B **88**, 184420 (2013).
6. I. Zimmermann, R. K. Kremer, P. G. Reuvekamp and M. Johnsson, *Crystal structure and magnetic properties of $\text{Cr}_3\text{Te}_5\text{O}_{13}\text{Cl}_3$* , Dalton Transactions **42**, 8815–8819 (2013).
7. J. M. Law, P. G. Reuvekamp, R. Glaum, C. Lee, J. Kang M. H. Whangbo and R. K. Kremer, *Quasi-one-dimensional antiferromagnetism and multiferroicity in CuCrO_4* , Physical Review B **84**, 014426 (2011).
8. P. G. Reuvekamp, F. S. Razavi, C. Hoch, J. S. Kim, R. K. Kremer and A. Simon, *Spontaneous stoichiometry change in single crystals of superconducting $(\text{Ba}_{1-x}\text{K}_x)\text{Fe}_2\text{As}_2$ grown by a rapid-Heating Sn-flux method*, Journal of Superconductivity and Novel Magnetism **22**, 353-356 (2009).

Contents

1	Introduction	1
2	Theory	5
2.1	Thermal expansion	5
2.1.1	Origins of the thermal expansion of solids	6
2.1.2	Magnetostriction	14
2.1.3	Phase transitions	15
2.1.4	Analysis of thermal expansion measurements	16
2.2	Heat capacity	17
2.3	Magnetic susceptibility	19
3	Experimental methods	21
3.1	Magnetic susceptibility	21
3.2	Electron paramagnetic resonance spectroscopy	24
3.3	Heat capacity measurements	28
3.4	Dielectric measurements	32

3.5	Thermal expansion measurements using a capacitance dilatometer	35
3.5.1	Measurement considerations	41
3.5.2	The calibration procedure and reference curves for the miniature dilatometer	42
4	Titanium (III) Phosphate	47
4.1	Introduction	47
4.2	Spin chains systems	48
4.3	Electronic Peierls and spin-Peierls systems	54
4.3.1	The electronic Peierls transition	54
4.3.2	The spin-Peierls transition	57
4.3.3	Overview of known spin-Peierls compounds	60
4.3.4	The effect of magnetic fields on the spin-Peierls transition	64
4.3.5	The effect of pressure on the spin-Peierls transition . . .	65
4.4	The room temperature crystal structure and the magnetic properties of TiPO_4	67
4.5	The low temperature crystal structure	71
4.6	Sample preparation	78
4.6.1	Magnetization measurements	78
4.6.2	Thermal expansion measurements	80
4.7	Results	86
4.7.1	Magnetization measurements	86
4.7.2	Thermal expansion measurements	90
4.8	Discussion	102
4.9	Summary	109

5	Chromium Oxychloride	111
5.1	Introduction	111
5.2	The structural and the magnetic properties of CrOCl observed in previous studies	112
5.3	Sample preparation and experimental methods	120
5.3.1	Magnetic measurements	122
5.3.2	Heat capacity measurements	129
5.3.3	Thermal expansion measurements	133
5.3.4	Dielectric measurements	143
5.4	Results	150
5.4.1	Magnetic phase diagrams	150
5.4.2	Neutron diffraction measurements	153
5.4.3	High temperature anomalies	160
5.4.4	Density functional calculations of the spin exchange interactions	166
5.5	Discussion	174
5.6	Summary	183
6	Conclusions	185
7	Zusammenfassung	189
A	Software for the collection and the analysis of the thermal expansion data	197
A.1	Data collection	197
A.2	Data processing	198

A.3	Selected excerpts of the data processing code	205
A.3.1	Calculation of the gap and $\Delta L/L$	205
A.3.2	Spline smoothening algorithm	209
	Bibliography	211
	Curriculum Vitae	225
	Acknowledgements	226

List of Figures

2.1	The harmonic and the anharmonic potential energy $u(x)$ curves for a single atom in a crystal	9
2.2	The bond-stretching and the tension effect central force mechanisms	13
3.1	The Magnetic Properties Measurement System from Quantum Design	22
3.2	The electron paramagnetic resonance sample probe for a small crystal	26
3.3	The Bruker X-band EPR spectrometer	27
3.4	The construction of the Physical Property Measurement System calorimeter sample puck	29
3.5	Heat flow diagram for the thermal relaxation method	30
3.6	The mounting of a crystal for the dielectric measurements	33
3.7	Dielectric measurement probe with the socket mounting option	33
3.8	Schematic diagram of a sample with conducting electrodes	34
3.9	A three-dimensional image of the thermal expansion dilatometer cell	38

LIST OF FIGURES

3.10	A Schematic diagram showing the mounting of the sample within the thermal expansion dilatometer cell	39
3.11	The top and the bottom of the thermal expansion dilatometer cell with a copper reference sample and a silver spacer	40
3.12	The top view of the thermal expansion dilatometer cell in the Physical Property Measurement System Fork	40
3.13	The three reference samples for calibrating the thermal expansion dilatometer cell: borosilicate glass (BSi), copper (Cu) and lead (Pb)	43
3.14	The length change and the relative error for the National Bureau of Standards Borosilicate glass (BSi) reference sample	44
3.15	The length change and the relative error for the National Bureau of Standards copper (Cu) reference sample	45
3.16	The length change and the relative error for the TU Wien Lead (Pb) reference sample	46
4.1	The effect of the raising/lowering operators on the spin arrangement of a one-dimensional $S = \frac{1}{2}$ Heisenberg system	49
4.2	The spinon continuum observed for KCuF_3 from inelastic neutron scattering measurements	50
4.3	The temperature dependent magnetic susceptibility of a spin $S = \frac{1}{2}$ nearest neighbour antiferromagnetic Heisenberg chain . .	52
4.4	The temperature dependent magnetic heat capacity of a spin $S = \frac{1}{2}$ nearest neighbour antiferromagnetic Heisenberg chain . .	53
4.5	The Peierls distortion for an artificial one-dimensional chain of atoms	55

LIST OF FIGURES

4.6	The temperature dependence of the DC conductivity for TTF-TCNQ	56
4.7	The dependence of the low-lying spin excitation energies on the \mathbf{k} vector for uniform antiferromagnetic and dimerized one-dimensional Heisenberg chains	58
4.8	The temperature dependent magnetic susceptibility of a one-dimensional Heisenberg antiferromagnetic chain and a one-dimensional spin-Peierls system.	59
4.9	The molar magnetic susceptibility for a single crystal of CuGeO_3	62
4.10	The molar magnetic susceptibility, the thermal expansion and the heat capacity measurements of TiOBr and TiOCl	63
4.11	The crystal structure of TiPO_4 at room temperature	68
4.12	The magnetic susceptibility and the heat capacity of TiPO_4	69
4.13	The low temperature crystal structures of TiPO_4 in the $Pmnm$, the $Pbnm$ and the $P2_1nm$ space groups	72
4.14	The temperature dependence of the molar magnetic susceptibility χ_{mol} , the intensities of the (2 4 3 -1) satellite Bragg reflection and the \mathbf{q} -scan along the \mathbf{a}^* axis for TiPO_4	75
4.15	The temperature dependence of the three lattice parameters and the cell volume of TiPO_4	77
4.16	The component and the assembly of the high pressure copper-beryllium clamp cell	79
4.17	The neutron Laue-backscattering image of the TiPO_4 single crystal SC1	81
4.18	The orientation of the unpolished TiPO_4 single crystal SC1	82
4.19	The orientation of the polished TiPO_4 single crystal SC1	83
4.20	Images of TiPO_4 crystals RC and RC1	84

LIST OF FIGURES

4.21	The placement of the TiPO ₄ single crystal SC1 in the thermal expansion dilatometer cell	85
4.22	The temperature dependent molar magnetic susceptibility of the three TiPO ₄ samples (PS1, PS2 and RC1)	87
4.23	The temperature dependent magnetic susceptibility of the TiPO ₄ fine crystalline powders PS1 and PS2 under pressure	88
4.24	The pressure dependence of the two phase transitions (T_{c1} and T_{c2}) of TiPO ₄	89
4.25	The temperature dependent length change along the c -axis relative to 300 K of the TiPO ₄ single crystal SC1 with $H = 0$ Tesla	90
4.26	The zero magnetic field temperature dependent length change relative to 300 K along the a , b and c axes of the TiPO ₄ single crystal SC1	92
4.27	The zero magnetic field temperature dependent volume change relative to 300 K of the TiPO ₄ single crystal SC1	93
4.28	The zero magnetic field temperature dependent average linear coefficient of thermal expansion $\alpha_m(T)$ along the a , b and c axes of the TiPO ₄ single crystal SC1	94
4.29	The thermal expansion along the c -axis of the TiPO ₄ single crystal SC1 at 0 Tesla and 9 Tesla ($H \perp \mathbf{c}$)	96
4.30	The 0 Tesla and 9 Tesla average linear coefficient of thermal expansion $\alpha_m(T)$ curves of the TiPO ₄ single crystal SC1 ($H \perp \mathbf{c}$) near the T_{c1} and the T_{c2} transitions	98
4.31	The temperature dependent length change relative to 300 K and the average linear coefficient of thermal expansion $\alpha_m(T)$ of the TiPO ₄ crystals RC and RC1 with $H = 0$ Tesla	100

LIST OF FIGURES

4.32	The magnetostriction along the <i>c</i> -axis vs. temperature and its derivative with respect to temperature of the TiPO ₄ single crystal SC1	101
4.33	The quadratic magnetic field dependence of the lock-in transition T_{c1} for three TiPO ₄ crystals (SC1, RC and RC1)	104
4.34	The zero magnetic field temperature dependent length change along the <i>c</i> -axis relative to 300 K of the TiPO ₄ single crystal SC1	107
5.1	The crystal structure of CrOCl at room temperature	113
5.2	The temperature dependent inverse molar magnetic susceptibility of CrOCl	114
5.3	The low temperature magnetic structure of CrOCl projected along <i>a</i> -axis	115
5.4	The temperature dependent molar magnetic susceptibility and inverse molar magnetic susceptibility of CrOCl measured parallel and perpendicular to the <i>c</i> -axis	116
5.5	The low temperature heat capacity C_p and the magnetic susceptibilities (χ_{\parallel} and χ_{\perp}) of CrOCl	117
5.6	The preliminary (H, T) magnetic phase diagram of CrOCl for $H \parallel c$	118
5.7	The temperature dependence of $(0 \bar{2} 5)$ and $(2 \bar{1.5} 1)$ reflections of CrOCl near the Néel transition $T_N \approx 13.5$ K	119
5.8	Multiple CrOCl crystals with a greenish appearance	121
5.9	The temperature dependent inverse molar magnetic susceptibility of CrOCl up to 800 K	124

LIST OF FIGURES

5.10	The magnetization loops of a CrOCl crystal with $H \perp \mathbf{c}$ for temperatures between 2 K and 18 K	125
5.11	The magnetization of a CrOCl crystal with $H \perp \mathbf{c}$ and $H \parallel \mathbf{c}$ at 4.2 K, 10.1 K, 15 K and 20 K as measured in a pulsed magnetic field	126
5.12	The magnetization per Cr atom of a CrOCl crystal and the derivative of the magnetization with respect to the magnetic field at 4.2 K with $H \perp \mathbf{c}$ and $H \parallel \mathbf{c}$	127
5.13	The derivative with respect to magnetic field of the magnetization of a CrOCl crystal with $H \perp \mathbf{c}$ and $H \parallel \mathbf{c}$ at 4.2 K, 10.1 K, 15 K and 20 K.	128
5.14	The zero magnetic field temperature dependent heat capacity of a CrOCl crystal	129
5.15	The temperature dependent heat capacity of a CrOCl crystal at various magnetic field with $H \perp \mathbf{c}$	131
5.16	The magnetic field dependent heat capacity of a CrOCl crystal at constant temperatures of 3.5 K and 11.0 K with $H \perp \mathbf{c}$ and $H \parallel \mathbf{c}$	132
5.17	The two CrOCl samples (the pressed pellet and the crystal stack) used for the thermal expansion measurements	133
5.18	The temperature dependent length change relative to 5 K of two CrOCl samples (the pressed pellet and the crystal stack) for the heating and the cooling cycles at $H = 0$ Tesla	134
5.19	The low temperature thermal expansion measurements of two CrOCl samples (the pressed pellet and the crystal stack) for the heating and the cooling cycles at $H = 0$ Tesla	135

LIST OF FIGURES

5.20	The temperature dependent length change of the CrOCl crystal stack at various magnetic fields ($H \parallel \mathbf{c}$ and $H \perp \mathbf{c}$)	138
5.21	The temperature dependent average linear coefficient of thermal expansion $\alpha_m(T)$ of the CrOCl crystal stack at various magnetic fields ($H \parallel \mathbf{c}$ and $H \perp \mathbf{c}$)	139
5.22	The magnetostriction at constant temperatures of the CrOCl crystal stack for $H \perp \mathbf{c}$	141
5.23	The magnetostriction at constant temperatures of the CrOCl crystal stack for $H \parallel \mathbf{c}$	142
5.24	Mounting of a CrOCl crystal for the dielectric measurements . .	143
5.25	The temperature dependence of the relative dielectric constant ϵ_r of a CrOCl crystal in a zero magnetic field for the heating cycle	144
5.26	The temperature dependence of the relative dielectric constant ϵ_r of a CrOCl crystal at various magnetic fields ($H \perp \mathbf{c}$)	146
5.27	The temperature dependence of the relative dielectric constant ϵ_r of a CrOCl crystal at various magnetic fields ($H \parallel \mathbf{c}$)	147
5.28	The magnetocapacitance of a CrOCl crystal at constant temperatures with $H \perp \mathbf{c}$ showing the results for 2.0 K, 7.5 K, 10.0 K, 12.0 K and 16.0 K	148
5.29	The magnetocapacitance of a CrOCl crystal at constant temperatures with $H \parallel \mathbf{c}$ showing the results for 2.0 K, 7.5 K, 10.0 K, 12.0 K and 16.0 K	149
5.30	The extended (H, T) magnetic phase diagrams of CrOCl for $H \parallel \mathbf{c}$ and $H \perp \mathbf{c}$	152
5.31	The temperature dependence of the propagation vector component σ_2 below 27 K for CrOCl	155

LIST OF FIGURES

5.32	The temperature dependent intensities of three magnetic Bragg reflections for CrOCl	156
5.33	The low temperature magnetic structure of CrOCl in the commensurate and the incommensurate phases	158
5.34	The magnetic spin density waves of CrOCl along the \mathbf{b} -axis for the commensurate and the incommensurate phases	159
5.35	The temperature dependence of the relative dielectric constant ϵ_r and the relative length change between 210 K and 285 K for CrOCl	160
5.36	The electron paramagnetic resonance spectrum of a tiny CrOCl crystal with $H \parallel \mathbf{c}$ measured at 245 K	161
5.37	The temperature dependence of the intensity, the resonance field and the g-factor ($H \parallel \mathbf{c}$) for a CrOCl crystal	162
5.38	A microscope image of a tiny CrOCl crystal ($\sim 40 \mu\text{m} \times \sim 130 \mu\text{m}$) showing the position at which the Raman spectra were measured	163
5.39	The Raman spectra of a tiny CrOCl crystal at 5 K, 50 K and 275 K	164
5.40	The temperature dependence of the two A_g modes (f_1 and f_2) in CrOCl for $50 \text{ K} < T < 290 \text{ K}$	165
5.41	The relevant spin exchange pathways in the low temperature monoclinic structure of CrOCl	167
5.42	The spin configurations for the GGA+ U calculations – Part 1 of 2	168
5.43	The spin configurations for the GGA+ U calculations – Part 2 of 2	169

LIST OF FIGURES

5.44 The spin exchange coupling constants as a function of the on-site repulsion U 171

5.45 The slabs of the quadratic Cr single layers in CrOCl 174

5.46 The temperature dependence of $\chi_M \times T$ for CrOCl in a magnetic field of 1 Tesla 176

5.47 The low temperature magnetic structures calculated in the *mcp*has simulations 178

5.48 The three-dimensional axial next-nearest neighbour Ising model 180

A.1 The Physical Property Measuring System MultiVi user input macro window for the thermal expansion macro 198

A.2 The graphical user interface (GUI) for the thermal expansion data processing program 199

A.3 The graphical user interface (GUI) and the information available for temperature scans in the Data Graphing tab of the thermal expansion data processing program 199

A.4 The schematic diagram of the miniaturized thermal expansion dilatometer cell indicating the essential distance parameters summarized in Table A.1 202

List of Tables

4.1	The spin-Peierls transition temperatures of various organic spin-Peierls compounds	60
4.2	The zero magnetic field transition temperatures of T_{c1} and T_{c2} of three TiPO_4 crystals (SC1, RC and RC1)	95
4.3	The downshift of the T_{c1} lock-in transition temperature in three TiPO_4 crystals (SC1, RC and RC1)	99
4.4	The total shift of the spin-Peierls transition temperature(s) under pressure for various spin-Peierls compounds	102
4.5	The coefficient η of the quadratic magnetic field dependence for TTF-CuBDT, MEM(TCNQ) ₂ , TTF-AuBDT, CuGeO_3 and α' - NaV_2O_5 obtained from various measurement techniques.	105
5.1	The lattice parameters of the isostructural MOCl ($M = \text{Ti, V}$ and Cr) compounds	112
5.2	The lattice parameters and the structural details from the neutron powder diffraction measurements on CrOCl	154
5.3	The relative energies (in meV) of the eight ordered spin configurations with on-site repulsion $U = 0$ eV and 2 eV	170

LIST OF TABLES

5.4	The spin exchange coupling constants from the DFT calculations for on-site repulsion $U = 0, 1, 2, 3$ and 4 eV	170
5.5	The Curie-Weiss temperatures θ_{MF} (1 and 2) of the two unique atomic sites and the average value as a function of the on-site repulsion $U = 0, 1, 2, 3$ and 4 eV	172
5.6	The mean-field Néel transition temperature T_{N}^{MF} as a function of the on-site repulsion $0 \leq U \leq 2$ eV	181
A.1	The description of all parameters in the titled plate capacitance formula	201

Low-dimensional quantum spin systems and their unique properties have reattracted significant attention due to their essential role for superconductivity in high- T_c cuprates. Low-dimensional spin systems feature magnetic chains/planes with strong intrachain or intraplane spin exchange coupling being prevalent. Interchain or interplane couplings are significantly weaker and their effects become relevant only at very low temperatures. Ideal one- and two-dimensional systems exhibit intriguing magnetic phenomena. This had already been realized in 1925 by Ernst Ising in a theoretical treatment of a chain with magnetic moments allowed to point either up or down. These moments were coupled by nearest neighbour interaction.[1] To his own surprise, Ising found that such an ‘Ising-chain’, as it was later named, exhibits long-range magnetic order only at $T = 0$ K. The field of low-dimensional magnetism was further explored through Onsager’s treatment of a two-dimensional Ising system in 1944.[2] In an exact analytical treatment, Onsager demonstrated that a square planar Ising magnet exhibits long-range magnetic order with a logarithmic singularity in the heat capacity at finite temperatures T .

Low-dimensional magnets with Heisenberg type spin exchange coupling ($\propto \vec{S}_i \cdot \vec{S}_j$) started to draw attention in the early 1960s when the first diagonalization of the energy matrix for small systems became possible. Bonner and Fisher calculated the magnetic susceptibility and the heat capacity of $S = \frac{1}{2}$ finite chains (up to eleven sites) or rings of ferro/antiferromagnetic systems with nearest neighbour Heisenberg type exchange coupling.[3] These results were then extrapolated to infinite systems and have been frequently used to analyze experimental results.

In the meantime, the magnetic susceptibility and the heat capacity of $S = \frac{1}{2}$ chains with nearest neighbour Heisenberg spin exchange coupling has been calculated with more modern techniques (quantum Monte Carlo and Density Matrix Renormalization Group calculations).[4–6] High precision Padé approximations of these results have been established enabling more elaborate comparisons with experimental data. Recently, a similar treatment for spins $S > \frac{1}{2}$ has been published by Law *et al.* [7].

For antiferromagnetic chains/planes, both the magnetic susceptibility and the heat capacity are characterized by broad maxima at temperatures comparable to the spin exchange coupling constant.[8] These maxima are due to short-range antiferromagnetic ordering. Similar to Ising chains, long-range ordering is not observed at finite temperatures. These findings were put into a more general theoretical perspective by Mermin and Wagner.[9, 10] They showed that isotropic Heisenberg type spin exchange coupled chains/planar systems do not exhibit long-range ordering for $T > 0$ K. Of particular interest are the excitations observed in low dimensional systems. For example, the excitations in ideal Heisenberg chains (‘spinons’) are gapless fermions with a spin of $\frac{1}{2}$. [11]

These theoretical results triggered the early efforts to experimentally identify and characterize low-dimensional magnets. A compilation of the results from this early period can be found in two review articles by de Jongh and Miedema [12] and Steiner *et al.* [13]. A more recent account of two-dimensional systems has been compiled by de Jongh [14]. The model systems in this early period were essentially inorganic materials such as the famous TMMC ($[(\text{CH}_3)_4\text{N}] \cdot [\text{MnCl}_3]$) compound[15]. In TMMC, the magnetic Mn-Cl framework is constructed by connecting $[\text{MnCl}_6]^{4-}$ octahedral chains via opposite triangular faces. The resulting octahedral chains are separated by $[\text{N}(\text{CH}_3)_4]^{4+}$ spacers effectively reducing the interchain spin exchange interaction. TMMC forms almost an ideal ($J_{\text{inter}}/J_{\text{intra}} \leq 0.01\%$) antiferromagnetic Heisenberg chain. The rather large spins of the Mn^{2+} ($S = \frac{5}{2}$) cations allowed a treatment within terms of a classical spin ($S \rightarrow \infty$) scenario.[16]

Early on the quantum limit ($S \rightarrow \frac{1}{2}$) was investigated e.g. on Cu^{2+} , V^{4+} and Ti^{3+} salts. In 1975, Bray *et al.* found that organic donor-acceptor insulator materials, e.g. TTF-CuBDT and TTF-AuBDT, also constitute good $S = \frac{1}{2}$ quasi low-dimensional quantum antiferromagnets.[17] Bray *et al.* discovered that such organic chain magnets can undergo a transition at low temperature into a non-magnetic ground state involving a minute structural distortion (‘dimerization’) of the chains. Analogous to the electronic-Peierls case [18], this transition was called a ‘spin-Peierls’ transition. The spin-Peierls transition can be understood as a consequence of the magnetoelastic coupling of the spin degrees of freedom to the lattice vibrations. The first inorganic spin-Peierls systems, CeGeO_3 , was found by Hase *et al.* in 1993, however inorganic spin-Peierls systems remained rare.[19, 20] In the early 2000s, it was shown that some Ti^{3+} ($3d^1$ electronic configuration with $S = \frac{1}{2}$) systems also exhibit spin-Peierls transitions. In contrast to the known spin-Peierls systems, these compounds (e.g. TiOCl and TiOBr) reach the spin-Peierls ground state by two sequential phase transitions.[21, 22] Law *et al.*, in the Chemieservice group (Max Planck Institute for Solid State Research), discovered similar behaviour in TiPO_4 in 2011.[23, 24] As compared to TiOX ($X = \text{Cl}, \text{Br}$), TiPO_4 exhibits a much simpler crystal structure with predominant ($J_{\text{inter}}/J_{\text{intra}} < 2\%$, $J_{\text{intra}} \approx 960$ K) intrachain spin exchange coupling. Similar to TiOX , two sequential phase transitions were detected with an interesting structurally intermediate incommensurate regime.[23, 24]

The rather complex structure of TiOX (see the discussion in Chapter 5) made it difficult to identify the relevant spin exchange pathways. The distant neighbour exchange coupling and the competing interactions lead to an exchange scenario in which magnetic frustration cannot be excluded. In order to explore these issues more deeply, the isostructural system CrOCl was considered as an example. CrOCl ($3d^3$ electronic configuration with $S = \frac{3}{2}$) has been shown to be long-range antiferromagnetically ordered at 4.2 K by Christensen *et al.* [25] in 1975. A subsequent study of the isotypic antiferromagnetic compound VOCl (V^{3+} electronic configuration with $S = 1$) detected a structural modification associated with the low temperature antiferromagnetic ordering.[26] Orientational studies on CrOCl in the Chemieservice group indicated a complex magnetic ordering behaviour and established an intricate preliminary (H, T) magnetic phase diagram. A transition to a monoclinic crystal structure at low temperatures, similarly to VOCl , was also detected for

CrOCl. Antiferromagnetic ordering contrasts with the positive Curie-Weiss constant extracted from the magnetic susceptibility data indicating predominant ferromagnetic spin exchange interactions. These findings implied that magnetoelastic coupling combined with competing spin exchange interactions are an essential feature of CrOCl.

In this thesis, I investigate the magnetic and the structural properties of TiPO_4 and CrOCl by various experimental techniques. A thermal expansion dilatometer cell allowing measurements in magnetic fields down to low temperature was commissioned in the course this Thesis. It is used extensively to study the magnetoelastic properties of both compounds. The structural and the magnetic field dependence associated with the spin-Peierls phase transitions in TiPO_4 are explored in depth. For CrOCl, detailed magnetic phase diagrams are constructed from thermal expansion, heat capacity, magnetization and magnetodielectric measurements. Additionally, the results of the density functional theory (DFT) calculations of the spin exchange constants are used to study the extended (H, T) magnetic phase diagrams using Monte Carlo simulations. The results are discussed in terms of the axial next-nearest neighbour Ising (ANNNI) model.

In this Chapter, I will review the thermal expansion of solids starting from the earliest theories and experiments in the eighteenth and nineteenth centuries. I will also discuss the effect of magnetostriction and phase transitions on the thermal expansion of solids. Additionally, the heat capacity and the magnetic susceptibility in terms of thermodynamics are examined.

2.1 Thermal expansion

Thermal expansion is defined as a change in the length or the volume of a solid as the temperature is increased by one degree Celsius.[27–29] Typically, a positive change in the length or the volume occurs with increasing temperature. But the opposite case (a negative change with increasing temperature) has also been observed (e.g. Invar(FeNi36)) and attracts a lot of attention¹. The basic mechanisms behind both cases will be discussed later in this Chapter.

After C. Huygens invented the pendulum clock in 1656, it was discovered that the variation in the pendulum length affected the period of the pendulum oscillation². The thermal expansion of a solid was first demonstrated by Gravesande in 1719 using a brass ring and a brass sphere. The sphere passed through the ring easily at room temperature. But the sphere could no longer pass through ring when the sphere was heated.[31]

¹In 1920, Guillaume (Charles Édouard) won the Nobel Prize in Physics for his discovery of Invar's unique thermal expansion properties. For more information, please consult Ref. [30] for more details.

²The period of a pendulum τ is defined as $\tau = 2\pi\sqrt{L/g}$ where L is the length of the pendulum and g is the gravitational constant ($9.81 \frac{m}{s^2}$).[27]

The primary area of early thermal expansion research focused on the materials (e.g. brass or iron) used to produce the clock pendulum. The accuracy of the clock varied depending on the thermal expansion of the clock pendulum. The development of instruments to measure thermal expansion was motivated by the reduced precision of clocks associated with the variation in the pendulum length. In the 1730s, P. Van Musschenbroek and G. Graham developed the first instruments to qualitatively measure the thermal expansion of solids called ‘dilatometers’. In the later part of eighteenth century, quantitative instruments were invented using existing optical and mechanic methods to precisely determine thermal expansion of solids³. [31]

2.1.1 Origins of the thermal expansion of solids

The first macroscopic theories for explaining the thermal expansion of solids were proposed in late nineteenth and early twentieth centuries. Between 1893 and 1906, K.F. Slotte [32–34] and G. Mie [35] published the first theoretical attempts trying to explain the thermal expansion of materials. Both Mie’s and Slotte’s theoretical work focused on the "kinetic theory of monatomic bodies". Slotte studied the relationship between the physical properties and the compressibility producing results which are comparable to the later work of Mie. [35] In 1903, Mie utilized classical mechanics and known specific heat laws to find the two following ratios for metals [36]:

$$\text{Ratio 1 : } \frac{3\alpha V}{\kappa_T} \quad \text{and} \quad \text{Ratio 2 : } \frac{3\alpha V}{\kappa_T C_v} \quad (2.1)$$

where $3\alpha = \beta$ assuming a cubic/isotropic environment, β is the volumetric coefficient of thermal expansion, α is the linear coefficient of thermal expansion, κ_T is the isothermal compressibility, C_v is the heat capacity at constant volume and V is the atomic volume. When empirical values at room temperature for various metals are substituted in Equation 2.1, it was observed that the Ratio 1 ranged from $2.2 \cdot 10^{-8}$ to $6.8 \cdot 10^{-8}$ and Ratio 2 ranged 0.9 to 2.6 for metals ranging sodium to bismuth. The variation of ratios in Equation 2.1 can be attributed to the nonrealistic approximation of the repulsion potential in the metals. [36–38]

³Information about the quantitative methods for measuring thermal expansion can be found in Chapter 3 of Ref. [31].

The first theory to successfully capture the essential relationship connecting thermal expansion to other thermodynamic quantities was reported by E. Grüneisen. In 1908, Grüneisen published a paper stating that the ratio of the volumetric coefficient of thermal expansion β and the heat capacity at constant pressure C_p was roughly constant over a large temperature range for various metals with the exception of the ferromagnetic transition in iron.[27, 37] Following this initial paper, Grüneisen proposed a theory to further the overall understanding of the thermal expansion in 1912. Grüneisen's theory used the quantum Einstein model to describe the lattice vibration in a crystal with all the lattice vibration vibrating at the same frequency ν . Furthermore, the frequency ν was volume dependent due to anharmonic contributions to the pair potential between the two atoms. The anharmonicity of the pair potential was then described by the Grüneisen function [27]:

$$\gamma = \frac{d \ln \nu}{d \ln V} \quad (2.2)$$

where ν is the frequency of the crystal vibration and V is the volume. The Grüneisen function can also be written in the terms of the thermodynamic quantities: the heat capacity, the thermal expansion and the elasticity. These aforementioned thermodynamic quantities of a material can be qualitatively correlated. If a material can not be easily compressed, then the thermal expansion would be small. If a material has a large heat capacity, the thermal expansion will be larger due to the absorption of more energy in the material. The elasticity of a material can be defined in terms of the adiabatic κ_S and the isothermal κ_T compressibilities [39]:

$$\kappa_T = - \left(\frac{\partial \ln V}{\partial P} \right)_T \quad \text{and} \quad \kappa_S = - \left(\frac{\partial \ln V}{\partial P} \right)_S \quad (2.3)$$

where P is defined as the pressure. The heat capacity of the material under constant volume (C_v) and pressure (C_p) can be defined [39]:

$$C_v = \left(\frac{\partial \ln U}{\partial T} \right)_V \quad \text{and} \quad C_p = \left(\frac{\partial \ln(U + PV)}{\partial T} \right)_P \quad (2.4)$$

where U is the internal energy and V is the volume.

The volumetric coefficient of thermal expansion β is defined as [39]:

$$\beta = \left(\frac{\partial \ln V}{\partial T} \right)_P \quad (2.5)$$

The Grüneisen function can be defined using the heat capacity, the thermal expansion and the elasticity as follows⁴ [39]:

$$\gamma = \frac{\beta V}{\kappa_T C_v} = \frac{\beta V}{\kappa_S C_p} \quad (2.6)$$

The Grüneisen function γ from Equation 2.6 only considers the dependence of the volume and the vibrational contributions⁵. Furthermore, γ is unitless and weakly dependent on temperature with a magnitude on the order of one for all temperatures. The sign of β is determined by the sign of γ since the remaining thermodynamic quantities are all positive.[27]

Thermal expansion can be further examined by analyzing the lattice vibration of a crystal. As the temperature of the crystal is increased, the amplitude of the vibrations increases producing a large number of overtones which intermingle with the harmonic vibrations. The presence of the overtones results in the anharmonic vibrations. The effect of anharmonic vibrations for an ideal crystal with a single atom can be seen in Figure 2.1. If the potential energy $u(x)$ for the atom can be described by an ideal harmonic oscillator, the potential energy curve will be a parabola with a vertex V. The average interatomic distance would equate to the lattice constant a for an ideal harmonic oscillator since the largest displacement of the atom on both sides of the vertex V would be equal in a symmetric parabolic potential. If the average interatomic distance does not change with energy and/or temperature, it can be concluded that a thermal expansion would not be observed. In the case of anharmonic vibrations, the potential energy curve of atom would be described by the parabolic blue curve with the additional asymmetric red tail in Figure 2.1. For this potential energy curve, a deviation in the parabolic shaped curve is present as x increases resulting in a shift of the average interatomic distance from a to \bar{x} .[40] The maximum displacement of the vibrating atom at energy u_0 would be different at points **L** and **R** resulting in a thermal expansion of $\bar{x} - a$.[40]

⁴For further details about this derivation, please consult pp. 13 -14 and p. 30 in Ref. [39].

⁵Using the Grüneisen function, other useful thermodynamic relations can also be derived and these relations are discussed on p. 30 of Ref. [39].

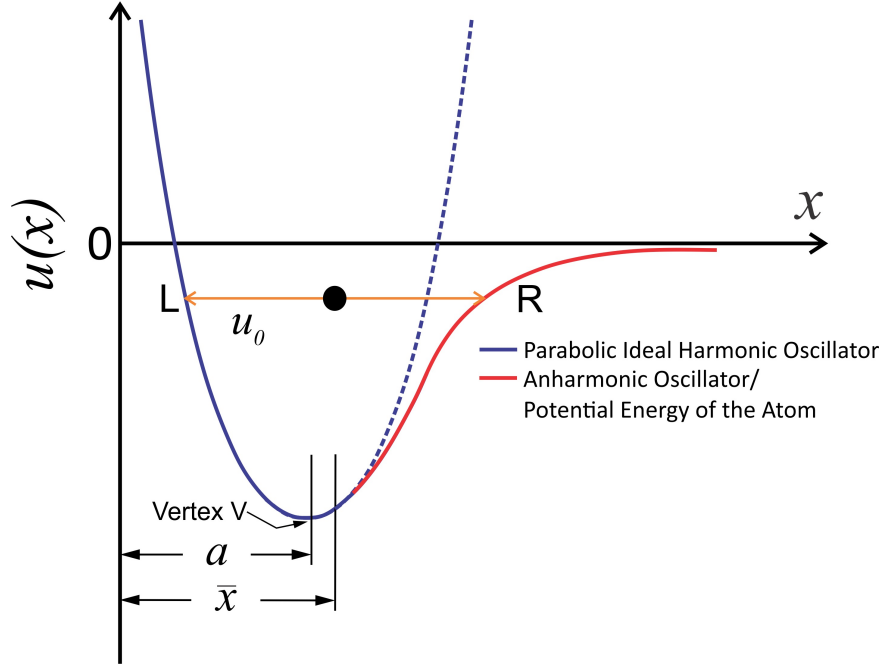


Figure 2.1: The harmonic and the anharmonic potential energy $u(x)$ curves for a single atom in a crystal. This Figure was reproduced from Ref. [40].

The effect of the anharmonic terms in the potential energy can be demonstrated by the following example [40]:

Considering two neighbouring atoms with an equilibrium displacement x at $T = 0$ K, the potential energy of the two neighbouring atoms in a one-dimensional chain can be described by $u(x)$:

$$u(x) = fx^2 - gx^3 - hx^4 \text{ for } f > 0, g > 0 \text{ and } h > 0 \quad (2.7)$$

where f is the coefficient of the harmonic oscillator term, g is the coefficient of the mutual repulsion term and h is the coefficient of the attenuation term for large amplitudes. The potential energy $u(x)$ has both harmonic (fx^2) and anharmonic (gx^3 and hx^4) terms. The anharmonic terms in $u(x)$ are only comparable to the harmonic term when the amplitudes of the vibrations are large resulting in anharmonic vibrations. The average displacement \bar{x} can be calculated using the Boltzmann distribution and the final result is:

$$\bar{x} = \frac{\int_{-\infty}^{\infty} x e^{\frac{-u(x)}{k_B T}} dx}{\int_{-\infty}^{\infty} e^{\frac{-u(x)}{k_B T}} dx} = \dots = \frac{3}{4} \frac{g}{f^2} k_B T \quad (2.8)$$

Additionally, the linear coefficient of thermal expansion $\alpha(T)$ can be calculated as follows:

$$\alpha(T) = \frac{d\bar{x}}{dT} = \frac{3}{4} \frac{g}{f^2} k_B \quad (2.9)$$

In Equation 2.9, $\alpha(T)$ is only nonzero if $g \neq 0$. Hence, anharmonic contributions to the potential energy are required to observe thermal expansion. However, the prediction that $\alpha(T)$ is constant for all temperatures is misleading. Using quantum statistics instead, $\alpha(T)$ can be calculated with quantum mechanical anharmonic oscillators. The energy of the classical oscillator ($k_B T$) is replaced with the average energy of the quantum mechanic oscillator $\left(\bar{E} = \frac{1}{2} \hbar \omega + \frac{\hbar \omega}{e^{\frac{\hbar \omega}{k_B T}} - 1} \right)$. After replacing the $k_B T$ term in Equation 2.8, the average displacement of the atoms \bar{x} can be rewritten as:

$$\bar{x} = \frac{3}{4} \frac{g}{f^2} \left(\frac{1}{2} \hbar \omega + \frac{\hbar \omega}{e^{\frac{\hbar \omega}{k_B T}} - 1} \right) \quad (2.10)$$

The linear coefficient of thermal expansion $\alpha(T)$ using Bose-Einstein statistics can be calculated as:

$$\alpha(T) = \frac{d\bar{x}}{dT} = \frac{3}{4} \frac{g}{f^2} k_B \left(\frac{\hbar \omega}{k_B T} \right)^2 \frac{e^{\frac{\hbar \omega}{k_B T}}}{\left(e^{\frac{\hbar \omega}{k_B T}} - 1 \right)^2} \quad (2.11)$$

In Equation 2.11, the low temperature regime as $T \rightarrow 0$ and $k_B T \ll \hbar \omega$ can be simplified as:

$$\alpha(T) = \frac{3}{4} \frac{g}{f^2} k_B \left(\frac{\hbar \omega}{k_B T} \right)^2 e^{\frac{-\hbar \omega}{k_B T}} \quad (2.12)$$

From Equation 2.12, the linear coefficient of thermal expansion $\alpha(T)$ approaches zero as the temperature approaches zero.[40] In Equation 2.9–2.12, $\alpha(T)$ is always positive since the coefficients f and g are positive. Hence, the anharmonic contribution to potential energy always results in a positive value of $\alpha(T)$ thus this mechanism can be used to explain positive thermal expansion. But some semiconductors (e.g. Si, Ge, ZnS and CdTe) and anisotropic solids (e.g. CeCu₆ and CeAl₃) exhibit negative thermal expansion (contraction) with increasing temperature.[27, 29] Other mechanisms must be considered to account for negative thermal expansion.

The existence of negative thermal expansion requires a more detailed study of the individual vibrations contributing to the Grüneisen function⁶. The influence of the individual lattice vibrations can be modeled using the quasiharmonic approximation. In the quasiharmonic approximation, the effect of the anharmonic contributions to the potential energy are considered as a first order perturbation at low temperature. The anharmonic contributions results in the different normal mode vibrations interacting with each other. The individual normal mode frequencies also depend on the volume and the strain. The interaction between normal modes vibrations creates thermal resistance whereas the volume/strain dependence on the normal mode frequencies results in the thermal expansion via thermal pressure. Each normal mode vibration of the lattice can be distinguished by a characteristic Grüneisen mode parameter γ_i [39]:

$$\gamma_j = \frac{d \ln \nu_j}{d \ln V} \quad (2.13)$$

where ν_j is the frequency of each normal mode vibration.

The effect of the lattice vibrations can be interpreted by the two following central force mechanisms⁷ [27, 39]:

Bond-stretching: repulsive

Bond-stretching or bond anharmonicity is the most dominant vibrational contribution to the thermal expansion. The mechanism originates from the anharmonic contributions to the potential energy resulting in an average nonzero displacement x . Bond-stretching increases the mean distance between atoms through a mean repulsive force (see Figure 2.2a) producing positive γ_j contributions. But this mechanism only explains the longitudinal motion of the vibration along the line joining the two atoms.[27, 39]

⁶Thermal expansion can also be influenced by magnetic and electric fields. More information about these interactions can found in Ref. [27], Ref. [29] and Ref. [39].

⁷A third central force mechanism called bond rotations also exists. But the effect of bond rotations are negligible and cancel each other out in most cases. For more information about the bond rotations mechanism, please consult p. 9 in Ref. [27] and p. 68 in Ref. [39] for more details about this mechanism.

Tension effect: attractive

Tension effect or the tension mechanism arises from the transverse or perpendicular vibrations of atoms. If the mean atomic positions of the atoms **A** and **B** are fixed (see Figure 2.2b), the transverse motion of atom **B** (the dotted line) results in the mean distance between the atoms increasing. A tension pulls the atoms toward each other to restore the original mean distance between the atoms producing negative γ_j contributions.[27, 39]

When considering the vibrations present in a crystal, it is important to consider both the bond-stretching and the tension effect mechanisms since vibrations will occur in both the longitudinal and the transverse directions. The vibrational Grüneisen mode parameters γ_j can be summed up to find the vibrational Grüneisen function in an isotropic environment. The Grüneisen function γ_{vib} is the average of Grüneisen mode parameters (γ_j) "weighted by the heat capacity (c_j) of each mode" [39]:

$$\gamma_{vib} = \frac{\sum_j c_j \gamma_j}{\sum_j c_j} \quad (2.14)$$

The volumetric coefficient of thermal expansion from vibrations can be calculated as follows [39]:

$$\beta_{vib} = \frac{\kappa_T}{V} \sum_j c_j \gamma_j \quad (2.15)$$

In Equation 2.15, the vibrational Grüneisen mode parameters γ_j contributions are multiplied by the corresponding heat capacity value. The sign of the β_{vib} is determined by the dominant mechanism in the crystal.[39] Additional interactions with the magnetic fields and electric fields as well as the electrons themselves may also contribute to the volumetric coefficient of thermal expansion. These additional contributions⁸ are material specific and particularly dependent on the crystal structure of the solid.[27]

⁸A full treatment of the interaction between electric and/or magnetic fields with a material can only be achieved by analyzing the strain and the stress tensors in the particular material. Please consult Refs. [27], [41], [42] and [43] for more details about the treatment of magnetic and electric fields.

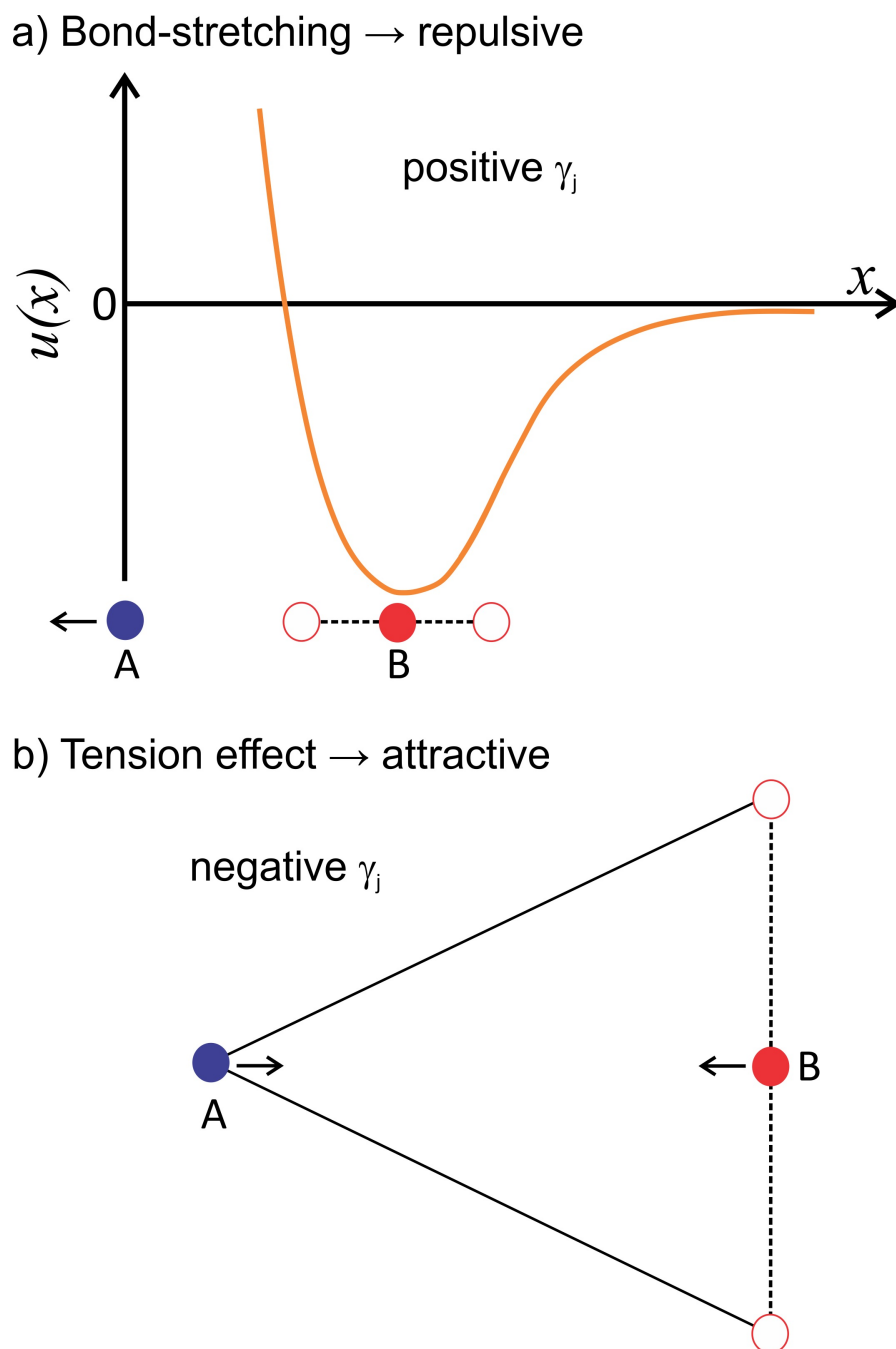


Figure 2.2: The bond-stretching central force mechanism (a) and the tension effect central force mechanism (b) which result in repulsive and attractive forces respectively. The dotted line denotes the oscillation amplitude of atom **B** with respect to atom **A**. This Figure was reproduced from a figure in Ref. [39].

2.1.2 Magnetostriction

An example of the interaction between magnetic fields and the thermal expansion of a solid can be demonstrated through the magnetostriction. Magnetostriction occurs when the dimensions of a sample change after the sample becomes magnetized by a magnetic field or magnetic ordering. When the sample is magnetized, the spins and the electron orbitals of the atoms are aligned in the crystal lattice due to spin-orbit coupling. The spins and the electron orbitals are rotated to a new orientation determined by the crystal anisotropy.[41, 44]

In 1842, magnetostriction was discovered by J. P. Joule while studying the affect of weak magnetic fields on an iron rod. He observed that the length of the iron rod increased when magnetized along the length of the rod. This type of magnetostriction is called the Joule effect with two subtypes: longitudinal and volume magnetostriction. The longitudinal magnetostriction is anisotropic and defined as a magnetically induced strain λ [44] :

$$\lambda = \frac{\Delta l}{l} \quad (2.16)$$

When a magnetic field is applied to magnetize the sample, Equation 2.16 only describes the change in the length of the sample parallel to the applied magnetic field. In comparison, the volume magnetostriction is defined as [44]:

$$\omega = \frac{\Delta V}{V} \quad (2.17)$$

The volume magnetostriction is isotropic with all dimensions changing equally with the application of a magnetic field. The volume magnetostriction is smaller than the longitudinal magnetostriction such that $\lambda \gg \omega$. [44]

The sign of λ can be negative or positive resulting in contraction or expansion in the direction parallel to the applied magnetic field respectively. In general, λ can vary in magnitude from 10^{-1} to 10^{-9} . The varying magnitude of λ is illustrated in the following list of the various materials [41, 42, 45, 46]:

- $\lambda \approx 10^{-1} - 10^{-2}$ for "giant" magnetostriction compounds such as PrAl_2 and TbFe_2 .
- $\lambda \approx 10^{-5} - 10^{-6}$ for ferromagnetic materials such as Fe and Co.
- $\lambda \approx 10^{-5} - 10^{-6}$ for ferrimagnetic materials such as Fe_3O_4 and MnFe_2O_4 .
- $\lambda \approx 10^{-5} - 10^{-7}$ for antiferromagnetic materials such as Cr and Fe_2O_3 .
- $\lambda \approx 10^{-8} - 10^{-9}$ for paramagnetic materials such as Ta, Ti and Zr.
- $\lambda \approx 10^{-6} - 10^{-9}$ for diamagnetic material such as Bi.

2.1.3 Phase transitions

The thermal expansion will exhibit anomalies which can be attributed to phase transitions similar to heat capacity. The volumetric coefficient of thermal expansion $\beta(T)$ is indirectly dependent on the Gibbs free energy G through entropy S . This relationship can be explored by rewriting $\beta(T)$ as follows:

$$\beta(T) = \left(\frac{\partial \ln V}{\partial T} \right)_P = \frac{1}{V} \left(\frac{\partial V}{\partial T} \right)_P \quad (2.18)$$

Using one of the four Maxwell relations [$(\frac{\partial V}{\partial T})_P = -(\frac{\partial S}{\partial P})_T$], Equation 2.18 can be rewritten as [47]:

$$\beta(T) = -\frac{1}{V} \left(\frac{\partial S}{\partial P} \right)_T \quad (2.19)$$

Since $S = -\left(\frac{\partial G}{\partial T}\right)_P$, this results in [47]:

$$\beta(T) = -\frac{1}{V} \left[\frac{\partial}{\partial P} \left(-\frac{\partial G}{\partial T} \right)_P \right]_T = \frac{1}{V} \frac{\partial^2 G}{\partial P \partial T} \quad (2.20)$$

Heat capacity at constant pressure has a similar thermodynamic definition [47]:

$$C_p = -T \left(\frac{\partial^2 G}{\partial T^2} \right)_p \quad (2.21)$$

The Gibbs free energy G is always continuous across a phase transition but the derivatives of G may not be continuous. For a first order phase transition, the

first derivatives of G are not continuous due to a kink in G at the phase transition. For second order phase transitions, the first derivative of G is continuous with kink at the phase transition. But in both cases, $\beta(T)$ (the second derivative of G) would exhibit discontinuities at the phase transition.[39] Specifically for thermal expansion, discontinuities in the volume and the strain result from first order transitions whereas second order transitions exhibit discontinuities in the coefficients of thermal expansion.[31]

2.1.4 Analysis of thermal expansion measurements

Thermal expansion data are typically expressed by various quantities depending on the measurement method. The volumetric coefficient of thermal expansion is denoted by $\beta(T)$ while the linear coefficient of thermal expansion is denoted by $\alpha(T)$. For practical purposes, the temperature derivative of $\beta(T)$ is approximated by a quotient of the differences resulting in the mean volumetric coefficient of thermal expansion which is defined as:

$$\beta(T) \approx \beta_m(T) = \frac{1}{V_{RT}} \frac{\Delta V}{\Delta T} = \frac{1}{V_{RT}} \frac{V(T + \Delta T) - V(T)}{\Delta T} \quad (2.22)$$

where V_{RT} is the room temperature volume of the sample and $\Delta T \ll T$.

The linear coefficient of thermal expansion $\alpha(T)$ and the mean/average linear coefficient of thermal expansion $\alpha_m(T)$ can be written as [27]:

$$\alpha(T) = \left(\frac{\partial \ln L}{\partial T} \right)_p \approx \frac{1}{L_{RT}} \left(\frac{\partial L}{\partial T} \right)_p \quad (2.23)$$

$$\alpha(T) \approx \alpha_m(T) = \frac{1}{L_{RT}} \frac{L(T + \Delta T) - L(T)}{\Delta T} \quad (2.24)$$

where L_{RT} is the room temperature length of the sample and $\Delta T \ll T$. When calculating $\alpha_m(T)$ using Equation 2.24, it is important to consider the deviations from $\alpha(T)$ due to the finite size of the temperature intervals. But these deviations can be ignored when the length of the sample is approximately equal over the complete range.[27, 31, 39]

The percentage linear thermal expansion is often used in literature and defined as the following [27]:

$$L_{\%} = 100 \cdot \frac{\Delta L}{L_{RT}} \quad (2.25)$$

In this thesis, the relative length change is used instead of the percentage linear thermal expansion. The length change relative to temperature T_1 or magnetic field H_1 is defined as⁹:

$$\frac{\Delta L}{L}(H_1 \text{ or } T_1) = \frac{\Delta L(H, T)}{L_{RT}} - \frac{\Delta L(H_1 \text{ or } T_1)}{L_{RT}} \quad (2.26)$$

The common zero point can be a temperature T_1 for temperature scans or a magnetic field H_1 for magnetic field scans. When working with multiple relative length change curves, all curves must be shifted to the common zero point in order to the normalize set of the curves.

2.2 Heat capacity

The heat capacity¹⁰ of a material can be defined as the amount of heat required to raise the temperature of the material by one degree unit of temperature under constant conditions. In its most general form, the heat capacity can be expressed as [48]:

$$C_{x,y} = \lim_{dT \rightarrow 0} \left(\frac{dQ}{dT} \right)_{x,y} \quad (2.27)$$

where the parameters x and y describe the constant conditions under which the heat input dQ raises the temperature by dT .

⁹More information about the data processing of the thermal expansion data is provided in Appendix A.

¹⁰Heat capacity and the term specific heat are sometime interchanged. Specific heat is the heat capacity for one gram of material.[48]

Specifically, the heat capacity can be defined under a constant pressure or volume as follows [39, 48]:

$$C_p = \left(\frac{dQ}{dT} \right)_P = \left(\frac{\partial H}{\partial T} \right)_P = T \left(\frac{\partial S}{\partial T} \right)_P = -T \left(\frac{\partial^2 G}{\partial T^2} \right)_P \quad (2.28)$$

$$C_v = \left(\frac{dQ}{dT} \right)_V = \left(\frac{\partial U}{\partial T} \right)_V = T \left(\frac{\partial S}{\partial T} \right)_V = -T \left(\frac{\partial^2 F}{\partial T^2} \right)_V \quad (2.29)$$

where U is the internal energy, H is the enthalpy $U + PV$, F is the Helmholtz free energy and G is the Gibbs free energy.

C_p can be estimated through measurements over finite intervals whereas C_v is usually calculated from C_p using the following relation [39, 48]:

$$C_v = C_p - \frac{\beta^2 VT}{\kappa_T} \quad (2.30)$$

where β is the volumetric coefficient of thermal expansion, V is the volume, T is the temperature and κ_T is the isothermal compressible. But C_v and C_p are approximately equal for solid or liquid systems and the second term in Equation 2.30 can be safely ignored. The difference between C_v and C_p should only be considered for gaseous¹¹ systems.[48] At high temperature, the heat capacity at constant volume can be described using classical statistical mechanics through the Dulong-Petit law. This law states that the heat capacity can be calculated in the following way [48]:

$$C_v = 3rR \quad (2.31)$$

where r is the number of atoms in one molecule and R is the universal gas constant or the Reynolds number.[48]

But the quantum theory must be used instead in the low temperature regime. The heat capacity can have contributions from the lattice vibrations (viz. phonons), the electrons (i.e. in a metal) and the magnetic excitations at low temperatures. The lattice vibrations have a T^3 dependence whereas the electrons contribution exhibit a linear dependence of T . In a magnetic material, an additional contribution from the magnetic excitations proportional to $T^{\frac{d}{n}}$ may also be observed where d is the dimensionality of the lattice and n is the

¹¹Please consult Ref. [48] for more information about the difference between C_v and C_p in gaseous systems.

exponent of the magnetic dispersion relation ($\omega \propto k^n$). In ferromagnetic and antiferromagnetic compounds, the exponent n is 2 (parabolic magnetic dispersion) and 1 (linear magnetic dispersion) respectively. In a three-dimensional system, the heat capacity at low temperatures for a ferromagnetic transition would be proportional to $T^{\frac{3}{2}}$ whereas an antiferromagnetic transition would be proportional to T^3 instead.[48–54] More information about these contributions can be found in Refs. [39], [48] and [54].

2.3 Magnetic susceptibility

A magnetic solid is composed of many atomic magnetic dipole moments. The average/mean magnetic moment of the bulk per unit volume is then defined as the magnetization.[55] For example, consider a magnetic system with all the magnetic moments pointing along the z-axis having a constant moment of μ_B . The magnetization of this system can be calculated as follows [56]:

$$M = \mu_B \sum_{i=1}^N \vec{S}_i. \quad (2.32)$$

In a real magnetic system, the applied magnetic field H induces a magnetic induction B and this response is a characteristic property of the system. The magnetic induction B is defined as (in the cgs system) [57]:

$$B = H + 4\pi M \quad (2.33)$$

The magnetization can be defined as:

$$M = \frac{m}{V} \quad (2.34)$$

where m is the magnetic moment and V is the volume of system. The type of and interaction between the dipole moments from the ions, the atoms and the molecules in the system affects the magnetization.[57]

From thermodynamics, the isothermal magnetization of the system is defined as [56]:

$$M = - \left(\frac{\partial F}{\partial H} \right)_T = - \left(\frac{\partial^2 F}{\partial H^2} \right)_T \quad (2.35)$$

where F is the Helmholtz free energy. The isothermal magnetic susceptibility of the system is defined as [56]:

$$\chi = \left(\frac{\partial M}{\partial H} \right)_T \quad (2.36)$$

If the magnetic field dependence of $M(H)$ is linear then χ can be approximated by the following relation [58]:

$$\chi \approx \left(\frac{M}{H} \right)_T \quad (2.37)$$

When the temperature dependence of the magnetic moment is measured, the magnetic susceptibility at each temperature can be calculated through scaling the moment by the applied magnetic field. This technique can be used for all magnetic systems which are not ferromagnetic or ferrimagnetic. More over, antiferromagnetic systems can be also be treated using Equation 2.37 if $g\mu_B \ll k_B T$.

Experimental methods

In this thesis, a variety of experimental techniques are used to study the materials presented. Magnetic susceptibility, heat capacity, dielectric, electron paramagnetic resonance and thermal expansion measurements are employed to characterize CrOCl and TiPO₄. In following sections, I will provide an overview of each experimental method which will be utilized in the following chapters.

3.1 Magnetic susceptibility

Magnetization measurements were performed using a Magnetic Property Measurement System (Quantum Design, MPMS-XL7). The system uses a radio frequency superconducting quantum interference device (SQUID)¹ and radio frequency detection circuit² to measure the magnetic moment of the sample. The magnetometer can measure magnetic moments on the order of 1×10^{-7} emu. During the measurement, the sample is scanned over a set distance (usually ~ 4.0 cm) through the superconducting detection pickup coil set and the voltage of the SQUID is recorded for a discrete number of positions (typically 24 to 32 points). The SQUID response voltage vs. sample position curve is then analyzed using the iterative regression algorithm³.

¹A SQUID device utilizes a Josephson junction consisting of two superconducting electrodes separated by a weak link. For more information about Josephson junctions and other SQUID devices please consult Refs. [59] and [60].

²The SQUID is coupled via a flux transformer to a radio frequency detection circuit. The flux transformer itself is connected to the superconducting pickup coil. For detailed information about the detection circuit please consult Chapter 12 of Ref. [60].

³For more information about the iterative regression algorithm please consult Ref. [61].

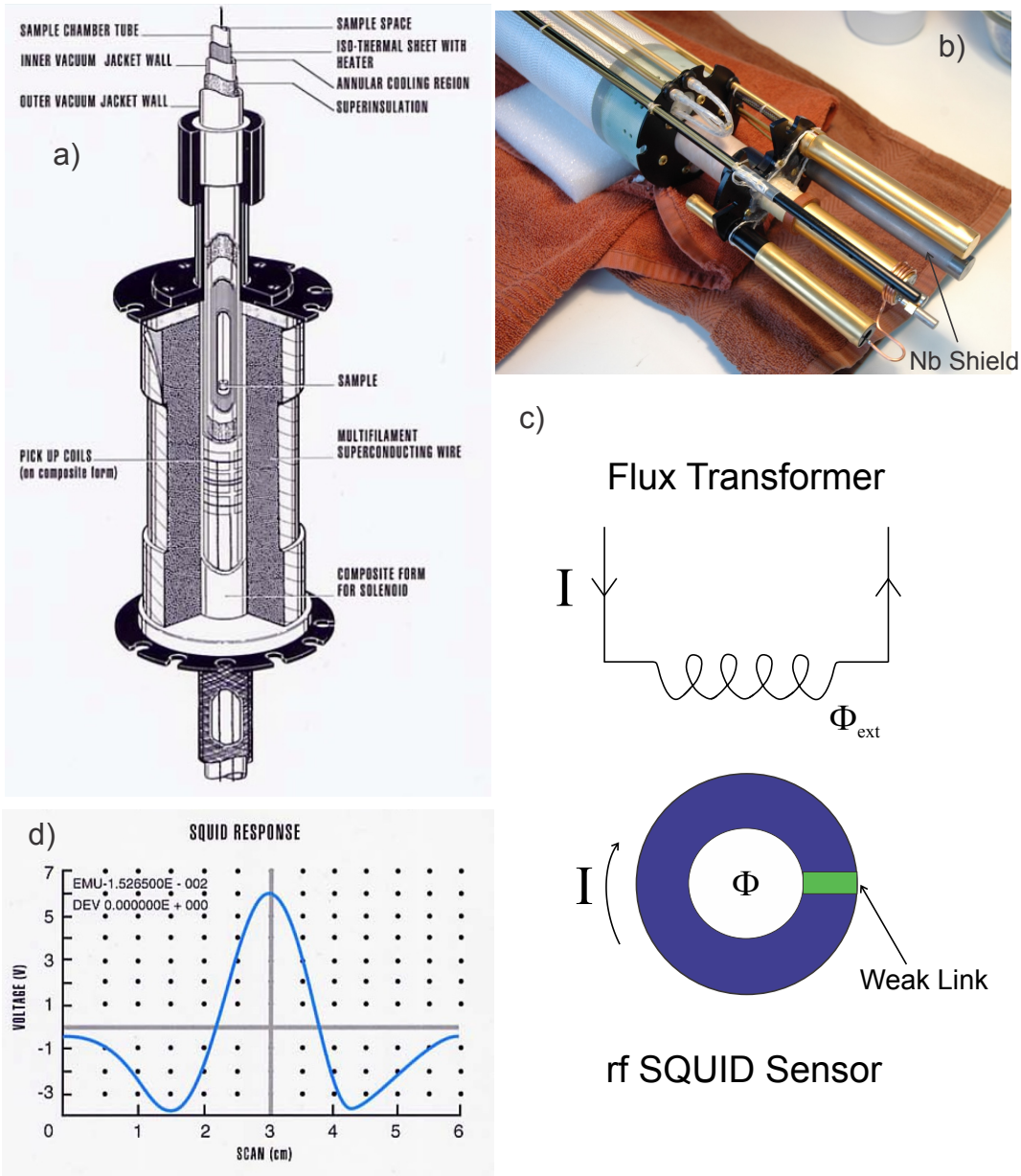


Figure 3.1: The Magnetic Properties Measurement System from Quantum Design: (a) The construction of the magnet, the sample space and the pickup/detection coil reprinted from Ref. [58] with permission. © 2014 Quantum Design, Inc. (b) The bottom of the magnetometer showing the niobium (Nb) shield which houses the SQUID and the flux transformer. (c) A schematic diagram showing the coupling of the flux transformer and the SQUID sensor reproduced from a figure in Ref. [62]. The external flux Φ_{ext} from the flux transformer induces an internal flux Φ in the SQUID sensor. (d) The typical voltage response of the SQUID for a full scan of 6 cm reprinted from Ref. [58] with permission. © 2014 Quantum Design, Inc.

The magnetic moment of the sample M_s is obtained from the aforementioned algorithm. The mass magnetization of the sample $M(T, H)$ is calculated from the magnetic moment of the sample⁴ using the following equation [58]:

$$M(T, H) \left[\frac{\text{cm}^3}{\text{g}} \right] = \frac{M_s[\text{cm}^3]}{m_s[\text{g}]} \quad (3.1)$$

where m_s is mass of the sample. For temperature scan measurements at a constant magnetic field, the molar magnetic susceptibility of a sample is calculated using the following relation [58]:

$$\chi_{\text{mol}} \left[\frac{\text{cm}^3}{\text{mol}} \right] = \frac{M_s[\text{cm}^3] \times M_{\text{molar}}[\text{g/mol}]}{m_s[\text{g}] \times H[\text{Oe}]} \quad (3.2)$$

where M_{molar} is the molar mass of the sample and H is the applied magnetic field. Alternatively for the magnetic field scans at a constant temperature, the magnetic moment can be calculated in terms of Bohr magnetons μ_B as follows:

$$M_B[\mu_B] = \frac{M(H)[\text{cm}^3/\text{g}]M_{\text{molar}}[\text{g/mol}]}{N_A[\text{mol}^{-1}]\mu_B[\text{erg/G}]} = \frac{M(H)[\text{cm}^3/\text{g}]M_{\text{molar}}[\text{g/mol}]}{5584.94[\text{cm}^3/\text{mol}]} \quad (3.3)$$

where $M(H)$ is the mass magnetization of the sample at a magnetic field of H , N_A is Avogadro's number and μ_B is one Bohr magneton in units of erg/G with a value of $9.2740678 \times 10^{-21}$.

⁴The magnetic moment is measured in terms of the 'emu'. The 'electromagnetic units' or 'emu' has dimensions of cm^3 but it is not a unit. More information about the 'emu' and other magnetic units can be found in Refs. [58], [63] and [64].

3.2 Electron paramagnetic resonance spectroscopy

Electron paramagnetic resonance (EPR) is a spectroscopy method utilizing the absorption of electromagnetic radiation (typically several GHz) by a paramagnetic sample exposed to an external magnetic field. The external magnetic field H splits the energy levels of the unpaired spins in a sample by the Zeeman energy. The microwave resonance is observed at H_{res} , if the energy difference ΔE between the magnetic levels matches the microwave quanta $h\nu$ such that [65]:

$$\Delta E = h\nu = g \cdot \mu_B \cdot H_{Res} \text{ and } \Delta M_s = \pm 1 \quad (3.4)$$

where ΔM_s is the difference of the magnetic quantum numbers of the energy levels and g defines the g-factor of the resonating spin system. Deviations of the g-factor from the free electron value of 2.0023 can be related to internal fields, e.g. spin exchange interaction to neighbouring spin moments. In addition, electric fields from neighbouring charges acting on the electron orbits (via spin-orbit coupling in case of a finite orbital angular momentum) can lead to crystal electric field splitting. Additionally, hyperfine coupling with the nucleus can also influence the g-factor.[65]

Typically, in a lab-based EPR microwave frequencies range between 1 and 100 GHz resulting in resonance magnetic fields between 0.035 to 3.5 Tesla.[66] Modern EPR developments utilizing pulsed magnetic fields allows the operating microwave frequency to be increased to several hundred GHz or even the THz regime.[67, 68] Standard lab-based EPR spectrometers operate at a constant microwave frequency in continuous-wave (cw) mode. The microwave resonance is then probed by sweeping the external magnetic field. Additionally, in order to detect the resonance accurately, a small high-frequency field (typically 100 kHz) is superimposed on the slowly ramped external magnetic field. This additional field improves the signal-to-noise ratio in the resulting signal. The resulting signal from the microwave detection diode is filtered and amplified using a phase sensitive amplifier (lock-in amplifier). This so-called effect modulation of the slowly varying external magnetic field combined with the phase sensitive detection technique implies that the first derivative of the microwave absorption P_{abs} is being detected.[69, 70]

The measured EPR spectra can often be well described in terms of Lorentzian line shapes as:

$$\frac{dP_{\text{abs}}}{dH} \propto \frac{d}{dH} \left(\frac{\Delta H + \zeta(H - H_{\text{res}})}{(H - H_{\text{res}})^2 + \Delta H^2} + \frac{\Delta H + \zeta(H + H_{\text{res}})}{(H + H_{\text{res}})^2 + \Delta H^2} \right) \quad (3.5)$$

where P_{abs} is the absorbed microwave power (viz. the measured spectrum), ΔH is the half-width at half-maximum (HWHM), H_{res} is the resonance field, and ζ measures the degree of mixture between the dispersion and the absorption signals. The second contribution in Equation 3.5 refers to the so-called ω -resonance resulting from the opposite precession of the spin. EPR spectra exhibiting broadening ($|H_{\text{res}}| \approx \Delta H$) can be fitted more accurately when the ω -resonance is utilized. Relaxation effects and internal fields can result in the broadening of the spectra⁵. For a narrow EPR spectra ($|H_{\text{res}}| \gg \Delta H$), only the left part of Equation 3.5 is required to fit the EPR spectra. Additionally, the fitting of the spectra can be improved further when an offset and a linear variation of the background signal with the field are also considered.[23]

The EPR spectrometer (see Figure 3.3) used in this thesis operates at ~ 9.5 GHz (X-band). The magnetic fields are produced by a Bruker iron core BE25 magnet which is controlled by a Bruker BH15 power supply. EPR spectra can be measured for temperatures between 2.5 K and 300 K using an Oxford continuous flow cryostat. The sample is mounted on the teflon platform of the probe. The probe is inserted into the cryostat at point **b** in Figure 3.3.

⁵For more information about broadening in EPR spectra please consult Refs. [65], [69] and [71].

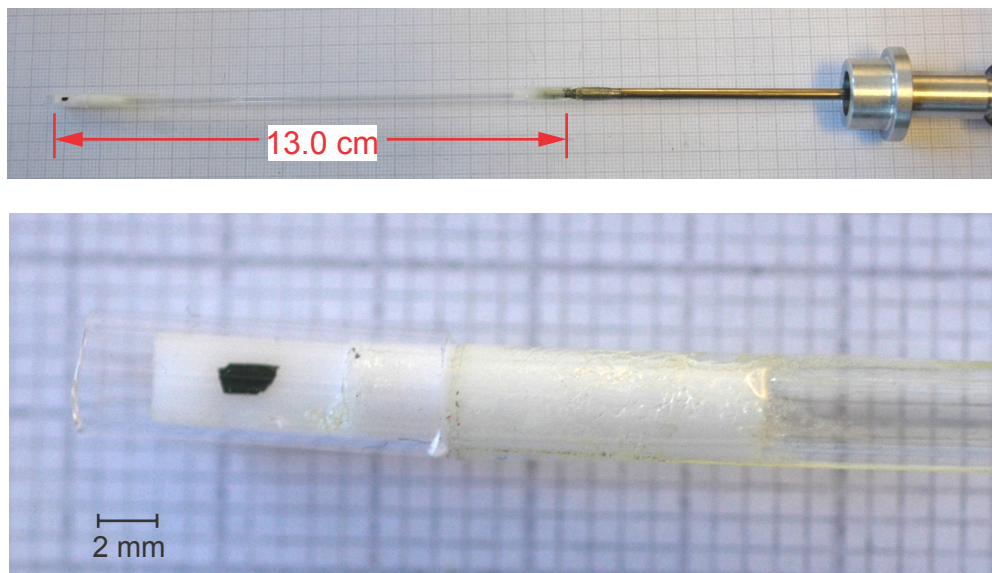


Figure 3.2: Electron paramagnetic resonance sample probe showing a small crystal mounted onto the teflon platform.

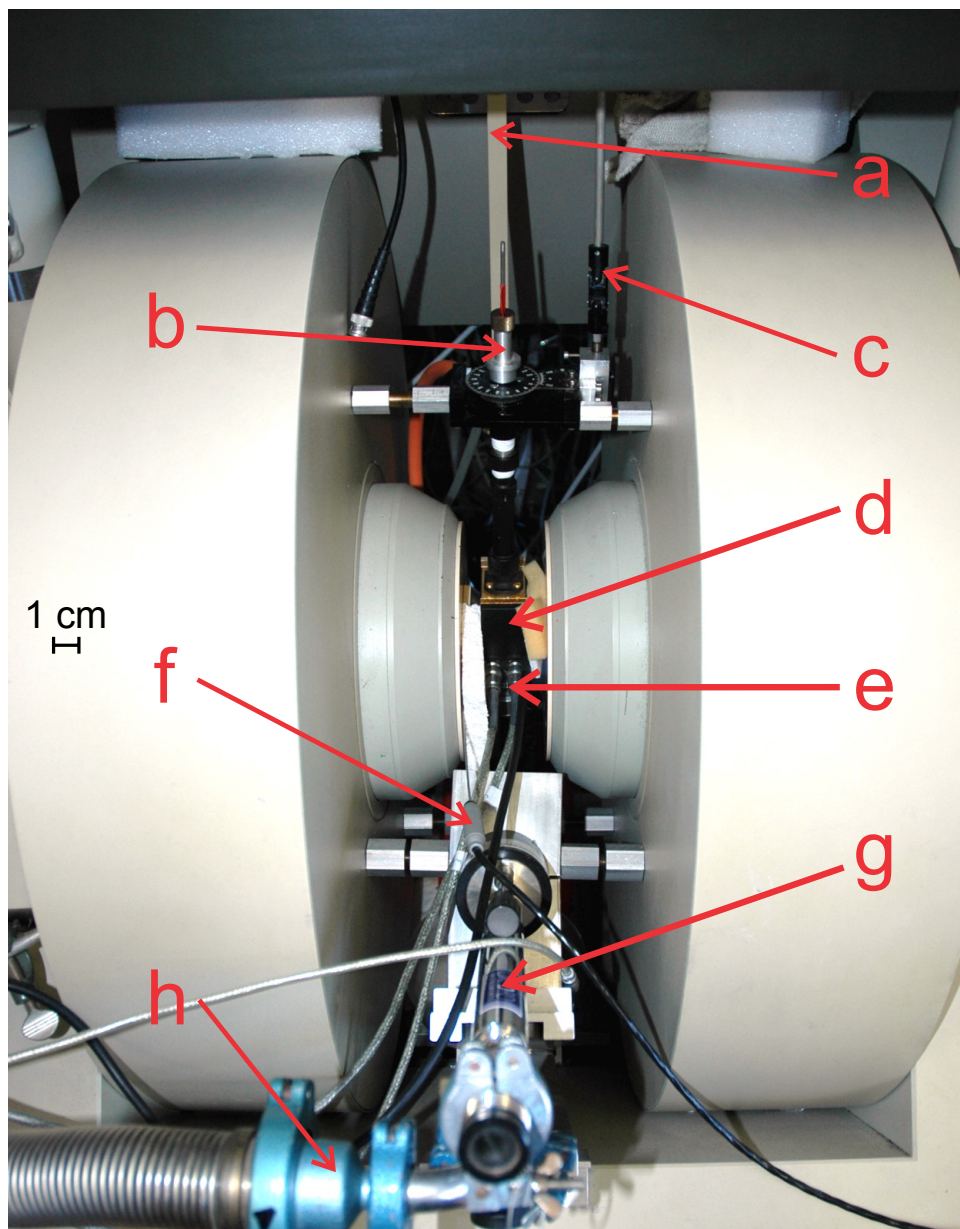


Figure 3.3: The Bruker X-band EPR spectrometer showing: **a** - the wave guide for the incoming microwave radiation, **b** - the sample mounting probe, **c** - the automatic sample rotator, **d** - the microwave cavity in which the sample is placed, **e** - the co-axial cables for 100 kHz effect modulator **f** - the hall probe for measuring the magnetic field, **g** - the top of the continuous flow cryostat and **h** - the high vacuum line for the cryostat.

3.3 Heat capacity measurements

Heat capacity measurements were performed under high vacuum for temperatures ranging from 1.8 K to 300 K in magnetic fields up to 9 Tesla. The thermal relaxation method was utilized for the measurements. This method is particularly useful for small samples since the results can be obtained faster than traditional methods such as the quasi-adiabatic Nernst method⁶.

In the thermal relaxation method, the sample is placed on a platform (see Figure 3.4) which is thermally linked to the environment by eight wires. The wires are used to connect the platform to the environment and thereby provide a well defined heat conductance path. The sample itself is thermally anchored to the platform using a minute amount of vacuum grease (i.e. Apiezon N). The platform consists of a $3 \times 3 \text{ mm}^2$ sapphire chip with a heater and a calibrated thermometer attached to the bottom of the chip. The calorimeter is fixed to a gold plated copper frame ('sample puck') which is installed into a Physical Property Measurement System (Quantum Design, PPMS). The sample puck connects the calorimeter thermally and electrically to the PPMS. A thermal radiation shield is placed on top of the puck protecting the sample and the platform from thermal radiation as well as guarantees thermal equilibrium conditions.[73] After sufficient temperature stabilization (typically $10^{-6} \text{ K} \cdot \text{s}^{-1}$), the temperature of the sample and the platform are raised by firing a short heat pulse. Starting at the beginning of the heat pulse and after switching off the heater, the temperature evolution vs. time is dynamically determined. The individual temperatures of the sample and the platform vs. time are fitted to the solution of two coupled linear differential equations⁷ by varying two relaxation times (internal: from the platform to the sample; external: from platform and sample to the environment), the heat capacity of the sample and the starting temperature. All measurements are performed in a high vacuum environment in order to minimize the heat transfer from residual gases.

⁶The history and the principles of the quasi-adiabatic Nernst method are discussed in detail in Ref. [72].

⁷The two coupled linear differential equations are presented on p. 371 in Ref. [74] as Equation 2.

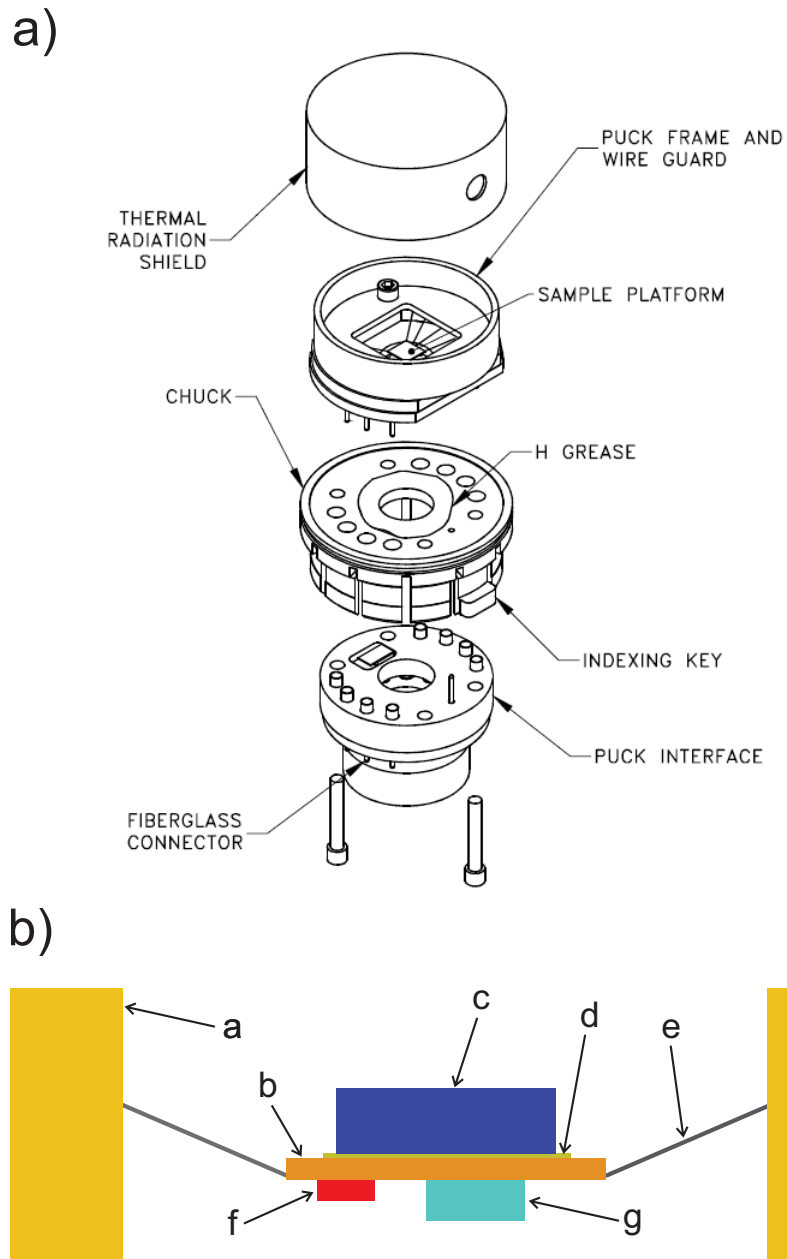


Figure 3.4: The construction of the PPMS calorimeter sample puck showing: a) The individual components of the PPMS puck reprinted from Ref. [73] with permission. © 2014 Quantum Design, Inc. b) A schematic diagram showing the construction of the sample platform. The sample platform consists of the following components: **a** - the wire guard/gold plated puck frame, **b** - the sapphire platform, **c** - the sample, **d** - the Apiezon N grease, **e** - the wires for thermal conduction, **f** - the heater and **g** - the bare chip Cernox thermometer. The lower part of this Figure was reproduced from Ref. [73].

The heat flow of the calorimeter is presented in Figure 3.5. This calorimetric method is particularly useful for fast measurements of small samples (typical masses 10 - 20 mg).

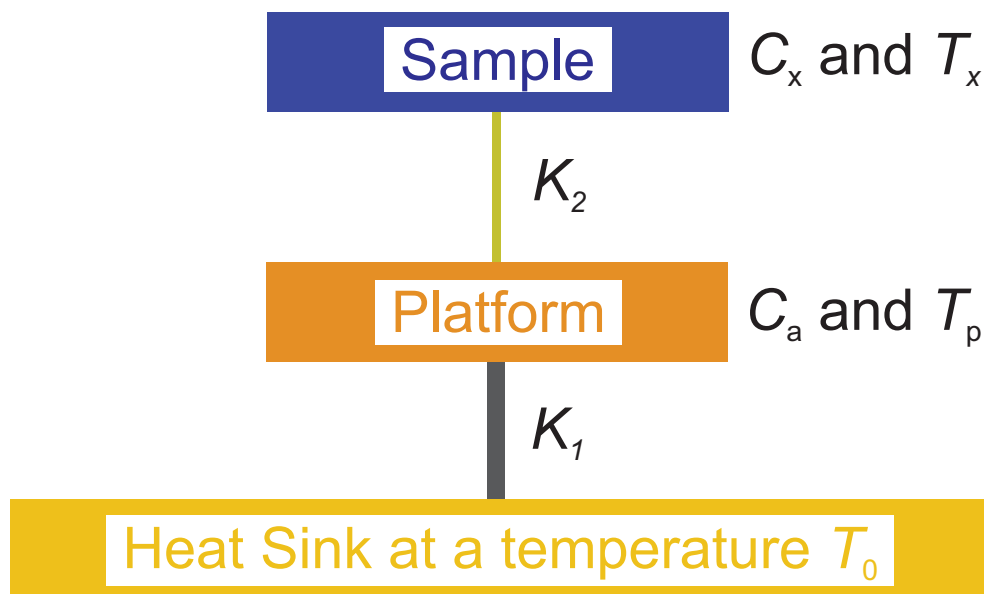


Figure 3.5: Heat flow diagram for the thermal relaxation method showing the relevant parameter for the sample, the platform and the heat sink. The temperatures of the sample, the platform and the heat sink are denoted as T_x , T_a and T_0 respectively. The addenda and the sample heat capacity are defined as C_a and C_x respectively. The thermal conductance between the platform and the environment is denoted as K_1 . The thermal conductance between the sample and the platform is indicated by K_2 . This Figure was reproduced from Ref. [75].

When a strong thermal connection exists between the platform and sample (viz. the sample and the platform are always in thermal equilibrium such that $K_2 \gg K_1$ and $T_x = T_a$), the temperature evolution vs. time can be modeled by the following equation [74]:

$$T_p(t) = T_0 + \Delta T \exp(-t/\tau) \quad (3.6)$$

where τ defines the external relaxation time, T_0 is the constant temperature of the heat sink and $T_p(t)$ is the temperature of the sample at a time t .

The total heat capacity C_{tot} can then be determined from the time constant of the decay τ such that [74]:

$$\tau = C_{tot}/K_1 \text{ if } K_2 \gg K_1 \text{ where } K_1 = \frac{P}{\Delta T} \quad (3.7)$$

where P is the power applied by the heater and ΔT is the change in the temperature of the platform/sample upon heating. C_{tot} comprises the heat capacity of the sapphire platform itself including all addenda (e.g. the Apiezon grease, the suspension/electrical wiring, the heater and the thermometer) and the heat capacity of the sample to be determined. Accordingly, the addenda heat capacity of calorimeter without the sample C_a must be carefully determined before the sample can be measured. The heat capacity of the sample C_x is then calculated by subtracting the predetermined addenda heat capacity C_a from the total heat capacity.[74]

The thermal relaxation method is implemented for the heat capacity option in the Physical Property Measurement System (Quantum Design, PPMS). The PPMS software uses a specific curve fitting algorithm developed by Hwang *et al.* [75]. However, the curve fitting algorithm uses a more complex technique than the one described above to calculate the heat capacity of the sample. The technique requires that an addenda measurement must be performed before measuring the sample. Using the addenda measurement and analytical methods, the heat capacity of sample $C_x(T)$ and the thermally conduction K_2 can be calculated. The normalized heat capacities of the sample are calculated from the following relation [73]:

$$C_p(T) \left[\frac{\text{J}}{\text{mol} \cdot \text{K}} \right] = C_x(T) \left[\frac{\text{J}}{\text{K}} \right] \cdot \frac{M_{molar}[\text{g/mol}]}{m_s[\text{g}]} \times 10^{-6} \quad (3.8)$$

where m_s is the sample mass and M_{molar} is the molar mass of the sample.

3.4 Dielectric measurements

Dielectric measurements were utilized for the characterization of the dielectric properties of the samples. The sample (e.g. a pressed pellet or a crystal) is used as a dielectric in a capacitor. The capacitor is fabricated by applying conducting contacts (electrodes) to opposite faces of the sample (see Figure 3.6 and 3.8).

In most cases, the sample is placed on a holder and the electrodes are connected using thin gold wires to the connection posts. The holder is then inserted into a socket on the measurement probe (see Figure 3.7) which has shielded coaxial cables connecting the capacitor to the measuring instrument. In order to measure the capacitance of the capacitor, different commercial LCR (Agilent Technologies E4980A Precision LCR Meter) or ultra-precision capacitance bridges (Andeen-Hagerling AH2500A, and AH2700) were utilized. All three instruments apply an oscillating voltage viz. electric field to the capacitor and analyze the response in terms of an electric circuit model (see Figure 3.8). In the electric circuit model, the parasitic conductance across the sample is interpreted as a resistor parallel to the capacitor under test. Typically, frequencies of up to several hundred kHz and oscillator voltages up to 20 V can be applied. Additionally, biasing by an internal or external DC voltage is also possible.

When dielectric measurements are performed directly on the sample using conducting electrodes, the measured capacitance of the sample must be normalized to the thickness of the sample and the area of the electrode pads via [76]:

$$C(T, H, \nu) = \frac{\epsilon_r \epsilon_0 A}{d} \quad (3.9)$$

where $C(T, H, \nu)$ is the measured capacitance at a fixed temperature, magnetic field and frequency, the product $\epsilon_r \epsilon_0$ is the permittivity, ϵ_r is the relative permittivity or the relative dielectric constant, ϵ_0 is the permittivity of free space, A is the area of the electrode pads and d is the thickness of the capacitor/sample.

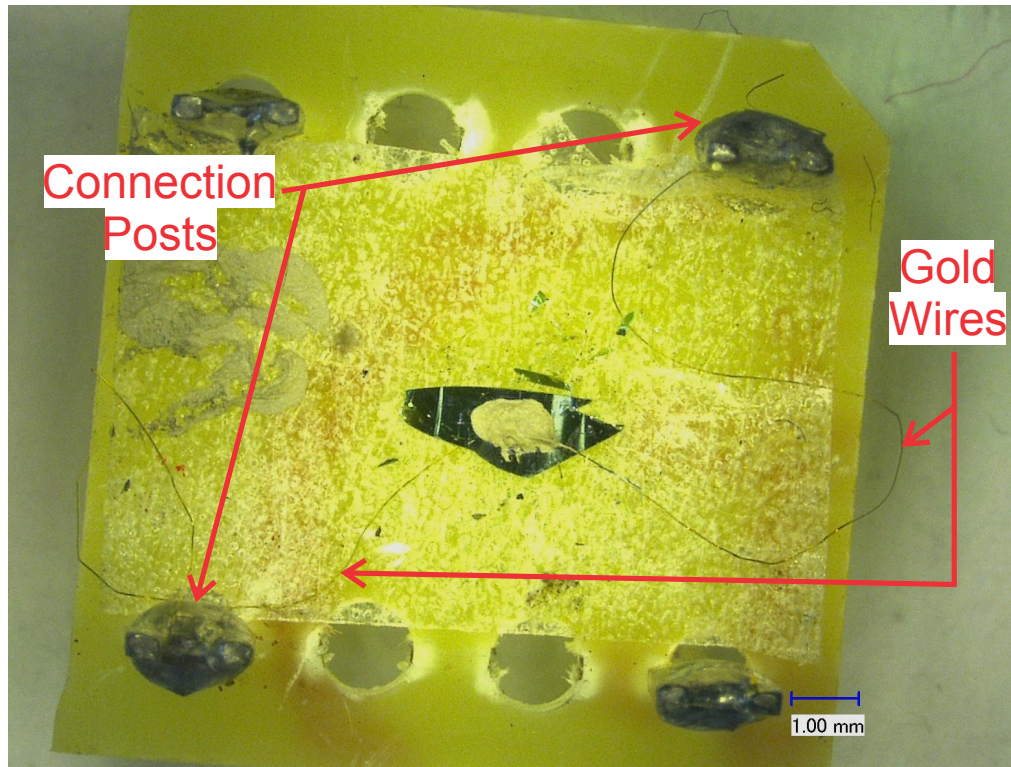


Figure 3.6: The mounting of a crystal for the dielectric measurements showing the sample holder, the crystal, the gold wires and the connection posts.

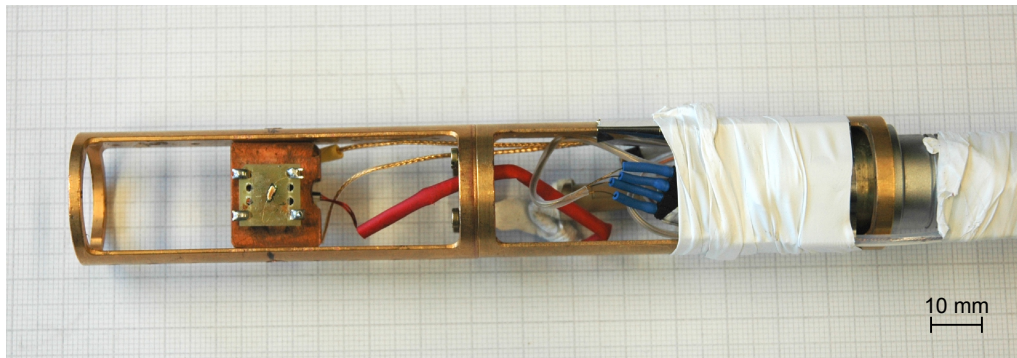


Figure 3.7: Dielectric measurement probe with the socket mounting option. The sample temperature was measured using a Lake Shore Cernox[®] CX-1050-AA temperature sensor placed in the copper plate underneath the sample. Two gold coloured coaxial cables running behind the copper plate connect to the top and the bottom of the sample through the sample holder. The coaxial cables run to the top of the probe where they can be connected to a measuring instrument.

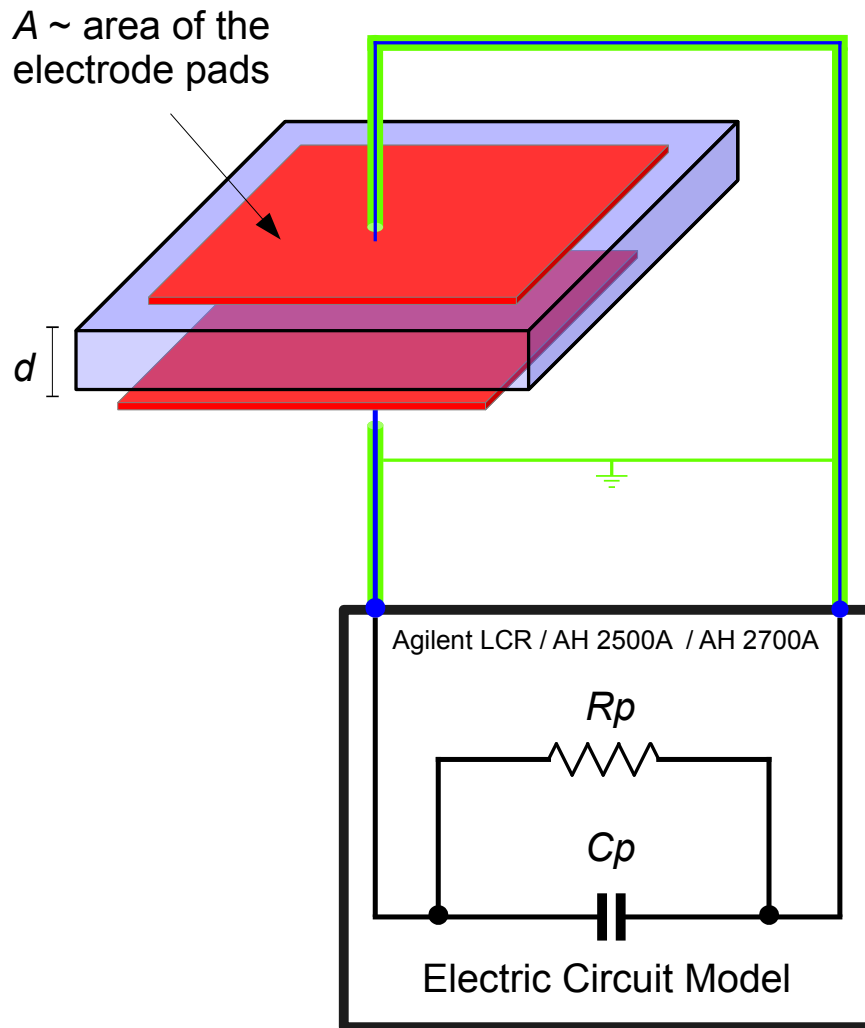


Figure 3.8: Schematic diagram of a sample with conducting electrodes and the electric circuit model showing conducting electrodes (the red squares) on both sides on the sample separated by the thickness of the sample d . The cables connecting the electrode pads to the measuring instrument are shielded (the green outline of the blue lines) and grounded together to reduce noise. In the electric circuit model, the capacitance and the resistance of the sample is denoted as C_p and R_p respectively.

The measured capacitance of the sample is normalized by rewriting Equation 3.9 in the following form:

$$\epsilon_r = f \cdot C(T, H, \nu) \quad \text{where} \quad f = \frac{d}{A\epsilon_0} \quad (3.10)$$

The factor f for the sample is calculated using the thickness and the electrode area of the sample. Using the factor f , the measured capacitance⁸ can be transformed into the relative permittivity of the sample ϵ_r . The temperature and/or magnetic field dependence of ϵ_r were measured for temperatures between 1.3 K and 300 K with magnetic fields up to 12 Tesla.

3.5 Thermal expansion measurements using a capacitance dilatometer

A capacitance dilatometer consists of a sample placed in between two electrodes separated by a gap width d . Prytherc, Haughton and Adcock developed the first capacitance dilatometer in the early 1930s.[31] The change in the sample length with temperature or magnetic field alters the gap between the two electrodes. The change in the gap distance Δd can directly be observed through the corresponding change in the capacitance of the electrodes ΔC via:

$$\Delta C \approx \epsilon_0 \frac{\Delta d}{d^2} \quad \text{from Equation 3.9 with } \epsilon_r = 1 \quad (3.11)$$

where d_0 is the initial gap distance. Before the 1960s, this effect was indirectly detected using the resonant oscillator approach⁹ since the small change in the capacitance of the dilatometer could not be accurately measured. In 1958, the measurement of small capacitance values became possible due to the development of the Lampard-Thomson theorem and the three-terminal AC method by Thomson.[77] Principally, White pioneered the use of three-terminal capacitance bridges for thermal expansion measurements in the 1960s.[31] The three-terminal capacitance bridges from the 1960s have evolved into the mod-

⁸The relative permittivity of the sample is proportional to the polarization of the dielectric. For more about this relationship please consult Refs. [40] and [76] for more information.

⁹The dilatometer forms a part of a tuned circuit located near the dilatometer. The change in the sample length is detected by a tuned circuit. The thermal expansion of the sample results in a change in the oscillation frequency of the tuned circuit. For more information about this measuring method please consult Ref. [31].

ern ultra-precision capacitance bridges of today¹⁰. The high accuracy of these bridges (i.e. 10^{-7} pF [78]) is achieved using an internal reference capacitor and ideal transformers. The small changes in the capacitance of the dilatometer can be resolved with a resolution of 10^{-12} m.[31]

The miniature capacitance dilatometer cell used to perform the measurements described in this thesis utilized a large area/small volume capacitor to perform high-sensitive thermal expansion measurements. Our dilatometer has been designed by Rotter *et al.*[79] and fits into the sample chamber of a Physical Property Measurement System (Quantum Design, PPMS). Using the PPMS, thermal expansion measurements can be performed down to 1.8 K (the base temperature of the PPMS system) in external magnetic fields up to 9 Tesla. The dilatometer is housed in a specially designed PPMS fork which allows the dilatometer to rotate by 90° (with respect to the external field). Thereby, the thermal expansion can be measured with the magnetic field oriented parallel or perpendicular to the direction of the thermal expansion. This special type of dilatometer was specifically designed to measure small samples. A suitable sample should have a thicknesses between 0.1 to 3 mm for a high resolution measurement. The lateral extension of the samples can be less than 0.5 mm. The hardness and the mechanical stability of the sample are extremely critical. The dilatometer uses a copper-beryllium spring to stabilize the upper part of the dilatometer. The spring exerts a small force ($\approx 50 - 500$ mN) onto the sample. The sample must sustain the force of the spring without cracking or changing its position.[79]

The dielectric capacitance of the two electrodes (typically separated by ~ 0.2 mm) of the dilatometer was measured with ultra-precision capacitance bridges manufactured by Andeen-Hagerling (AH 2700A - multi frequency or AH 2500A - single frequency 1 kHz)¹¹. A custom calibrated Lake Shore Cernox© CX-1050-SD temperature sensor was attached to the bottom half of the dilatometer using General Electric (GE) Varnish. Within the work of this thesis, an additional calibration of the temperature in external magnetic fields has been performed in order to compensate for the magnetoresistance effects

¹⁰For a more detailed description of the three-terminal capacitance bridge and how it functions, please consult Refs. [28], [31] and [39] for more information.

¹¹For more information about both capacitance bridges, please visit the manufacturer's webpage at <http://www.andeen-hagerling.com/>.

of Cernox thin film sensors¹². Depending on the temperature and the magnetic field, typically magnetoresistive effects do not exceed 2 to 3% of the resistance which translates into 4 to 5% of the temperature. In magnetic fields up to 9 Tesla and above ~ 25 K, the magnetoresistive effects are negligible. In the course of determining the precise shift of a spin-Peierls transition temperature with magnetic field, it turned out that the magnetoresistive effect is less than $\sim +15$ mK at 75 K and 9 Tesla which is consistent with existing literature.[81] These effects are quite small but they were still taken into consideration.

The body of the miniature capacitance dilatometer cell consists of an upper and a lower part manufactured from high purity silver. Insulation of the electrodes from the silver body is achieved using sapphire components (washers and discs). The construction of the dilatometer cell is outlined in detail in Figure 3.9. The typical way of mounting a sample within the dilatometer cell is illustrated in Figures 3.10 and 3.11. The sample in the desired measurement direction with respect to the crystal axes is placed on the sapphire disk in the middle of the bottom electrode with the appropriate silver spacer on top of the sample. The silver spacer is adjusted by subtracting the sample thickness by ~ 4.85 mm in order to obtain an optimal capacitance value between 6 pF and 9 pF. To finish the mounting of the sample within the dilatometer cell, the upper part of the cell must be carefully placed on top of the sample and the spacer. When the spacer is in the correct position (see Figure 3.12), the copper-beryllium spring can be placed on the brass screw and the nut can be tightened to stress the sample (50 - 500 mN of force). The complete mounting of the dilatometer cell is represented in Figure 3.12.[79]

¹²The effect of magnetoresistance on temperature sensors is tabulated in the Lake Shore temperature sensor catalog (see Ref. [80]) for Cernox sensors and many other sensors.

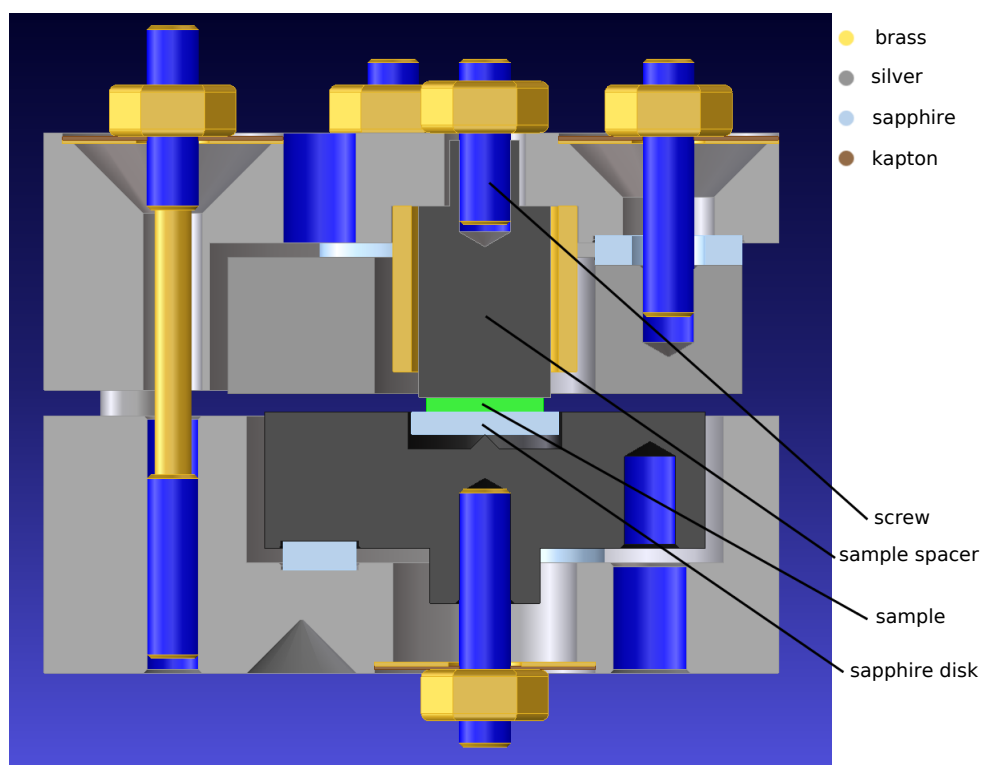


Figure 3.9: A three-dimensional image of the thermal expansion dilatometer cell with a sample (the green rectangle) showing the materials used for each component of the dilatometer. This Figure was reprinted from Ref. [82] with permission.

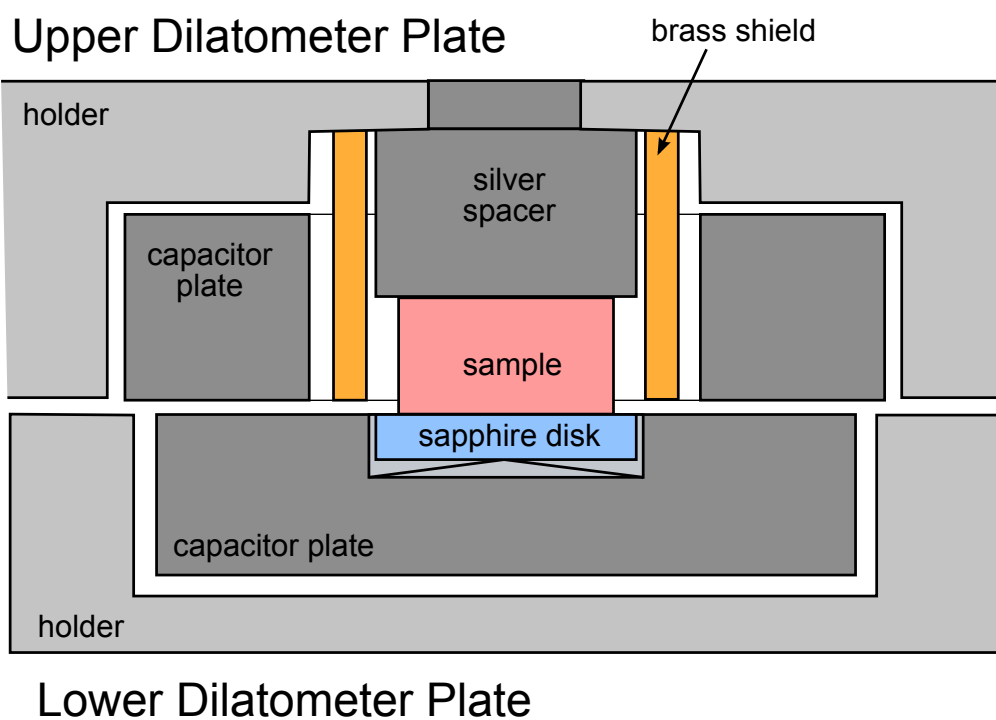


Figure 3.10: A schematic diagram showing the mounting of the sample within the thermal expansion dilatometer cell. This Figure was reprinted from Ref. [82] with permission.

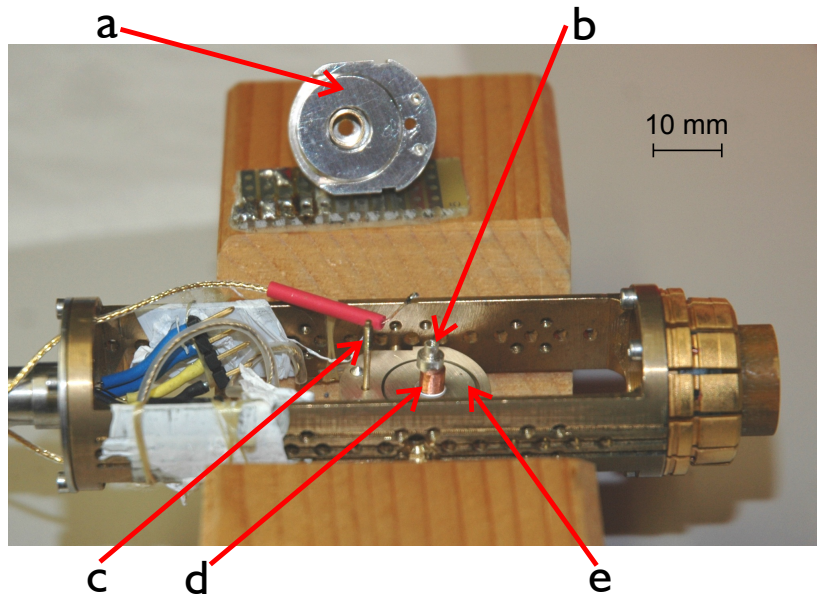


Figure 3.11: The PPMS fork with the thermal expansion dilatometer cell where **a** is the top of the dilatometer cell, **b** is the silver spacer, **c** is the threaded brass cylinder, **d** is the copper reference sample and **e** is the bottom of the dilatometer cell.

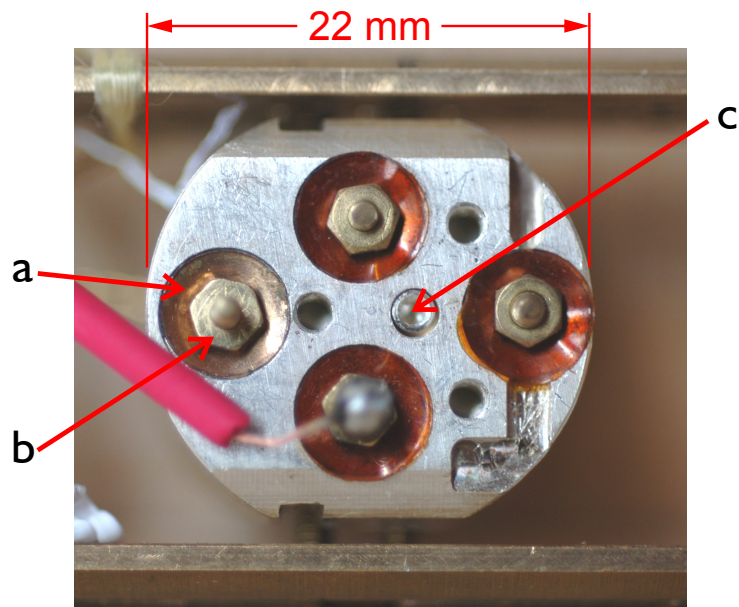


Figure 3.12: The top view of the thermal expansion dilatometer cell in the PPMS Fork where **a** is the copper-beryllium spring, **b** is the brass nut used to fix and tighten the dilatometer and **c** is the top of the silver spacer seen in Figure 3.11.

3.5.1 Measurement considerations

The dilatometer cell uses a tilted plate geometry such that the upper part of the cell is slightly inclined ($< 3^\circ$) relative to the bottom plate. The slightly tilted position of the upper part of the cell is supported at an exact pivot point using two silver conical/needle bearings and the sample itself acting as the third support. Additionally, sapphire washers are placed throughout the cell to provide electrical insulation and self-compensation in order to minimize background effects from the cell. The cell has a resolution on the order of 10^{-12} m or 0.001 Å. This resolution can be easily achieved using an Andeen-Hagerling ultra-precision capacitance bridge (AH2700A) by applying an oscillating voltage of 10 V at a frequency of 1 kHz with an sample time of 2.5 seconds per point or ~ 500 internal measurements per point. The capacitance of the electrodes can be measured as a function of temperature at a constant magnetic field or as a function of magnetic field at a constant temperature. After the measurements are performed¹³, the length change of the sample is determined by applying corrections for the length change of the body of the dilatometer and the spacer.[79] In the course of this thesis, I wrote a program ‘Thermal Expansion Dilatometer Data Processor’ to automatically perform these corrections. The program uses two calibration files to perform the necessary corrections: the literature values for the thermal expansion of silver and the background thermal expansion of the dilatometer. A detailed description of the program and its many options are provided in Appendix A.

The following points must also be considered when measuring the thermal expansion using a capacitance dilatometer:

1. All wiring connecting to the top/bottom electrodes of the dilatometer must be shielded using low temperature coaxial cables to reduce signal crosstalk.
2. When operating the dilatometer at low temperatures, ^4He exchange gas (typically 100 mbar at room temperature) is filled into the sample chamber for rapid thermalization. However, spurious contamination from oxygen¹⁴, nitrogen or moisture must be carefully avoided. Extra dielectric responses

¹³For more details about the sample mounting and other technical details please consult the dilatometer manual (Ref. [82]).

¹⁴For example, the condensation of oxygen results in a large dielectric effect including a significant thermal hysteresis near 50 K.[83]

are observed when the aforementioned contaminants condense to or evaporate from the capacitor plates. In order to avoid contamination, the sample chamber was evacuated to 10^{-5} mbar at room temperature and several purge cycles with ^4He exchange gas were performed. Additionally, the exchange pressure was monitored throughout the measurements in order to correlate any anomalies with contamination effects. A Leybold CERAVAC capacitance manometer was used to monitor the ^4He exchange gas pressure.[84]

3. The most important step in the mounting of a sample in the dilatometer is the handling of the copper-beryllium spring. Before using a copper-beryllium spring, it is important to minimize the jolt felt upon securing and tightening the brass nut (see Figure 3.12). The jolt of the spring can cause the sample to change its position during the tightening. The jolt can be eliminated by flattening the copper-beryllium spring using a curved glass dish to restore the shape of the spring before use. In some cases, careful re-tightening of the brass nut after the first thermal cycle can become necessary.

3.5.2 The calibration procedure and reference curves for the miniature dilatometer

The miniature dilatometer cell measures the relative length change of the sample hence calibration measurements are required.[79] The calibration of the dilatometer cell requires the adjustment of the three parameters (the diameter, the gap and the pivot) which are used in the tilted plate capacitance formula see Equation A.1 – A.7 in Appendix A. The three parameters can be estimated by measuring three distances within the cell (see Appendix A for more details). The three parameters must be adjusted due to the slight misalignment of the capacitor plates caused by the manufacturing tolerances.[82] The calibration of the dilatometer cell is achieved using three reference samples: National Bureau of Standards (NBS) borosilicate glass (BSi), NBS copper (Cu) and lead (Pb) from TU Wien. The reference samples have a cylindrical/prism shape with varying heights between 3.0 mm to 4.4 mm (see Figure 3.13).

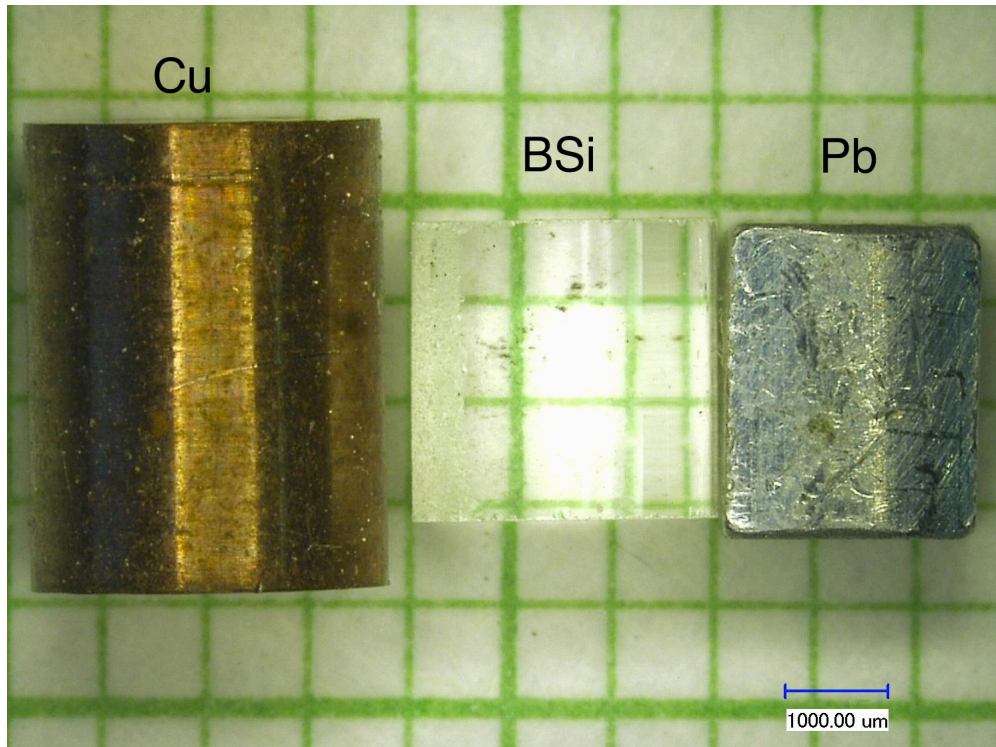


Figure 3.13: The three reference samples for calibrating the thermal expansion dilatometer cell: copper (Cu), borosilicate glass (BSi) and lead (Pb).

After the calibration measurements were performed, the results were compared to the relevant reference curves from the literature quoted in this thesis. The deviation of a measured curve from a literature curve for each reference sample is minimized by adjusting the three parameters. The calibrated values of the parameters for the dilatometer were found to be: diameter = 12.10 ± 0.05 mm, gap = 4.60 ± 0.05 mm and pivot = 9.8 ± 0.1 mm. The comparison between the reference and the measured/empirical curves for the three reference samples are shown in Figure 3.14 to 3.16 for the calibrated values of the diameter, the gap and the pivot.[82]

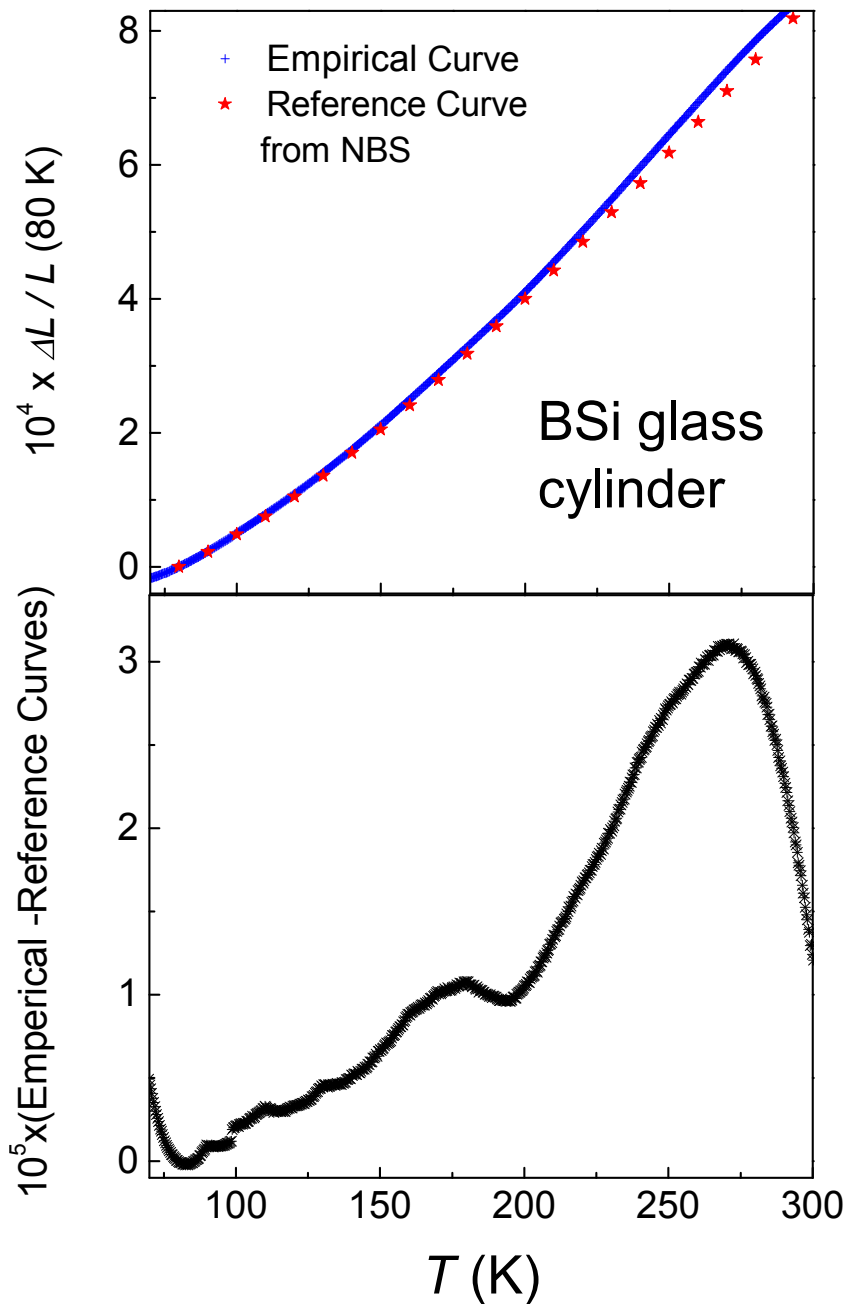


Figure 3.14: In the top graph, the length change is relative to 80 K for the National Bureau of Standards Borosilicate glass (BSi) reference sample showing the empirical curve in blue crosses and the reference curve in red stars can be seen. The reference curve was only measured to 80 K. The reference curve was obtained from the National Bureau of Standards. In the bottom graph, the relative error (empirical - reference curves) can be seen. The maximum deviation of the measured curve from the reference curve was less than 4%.

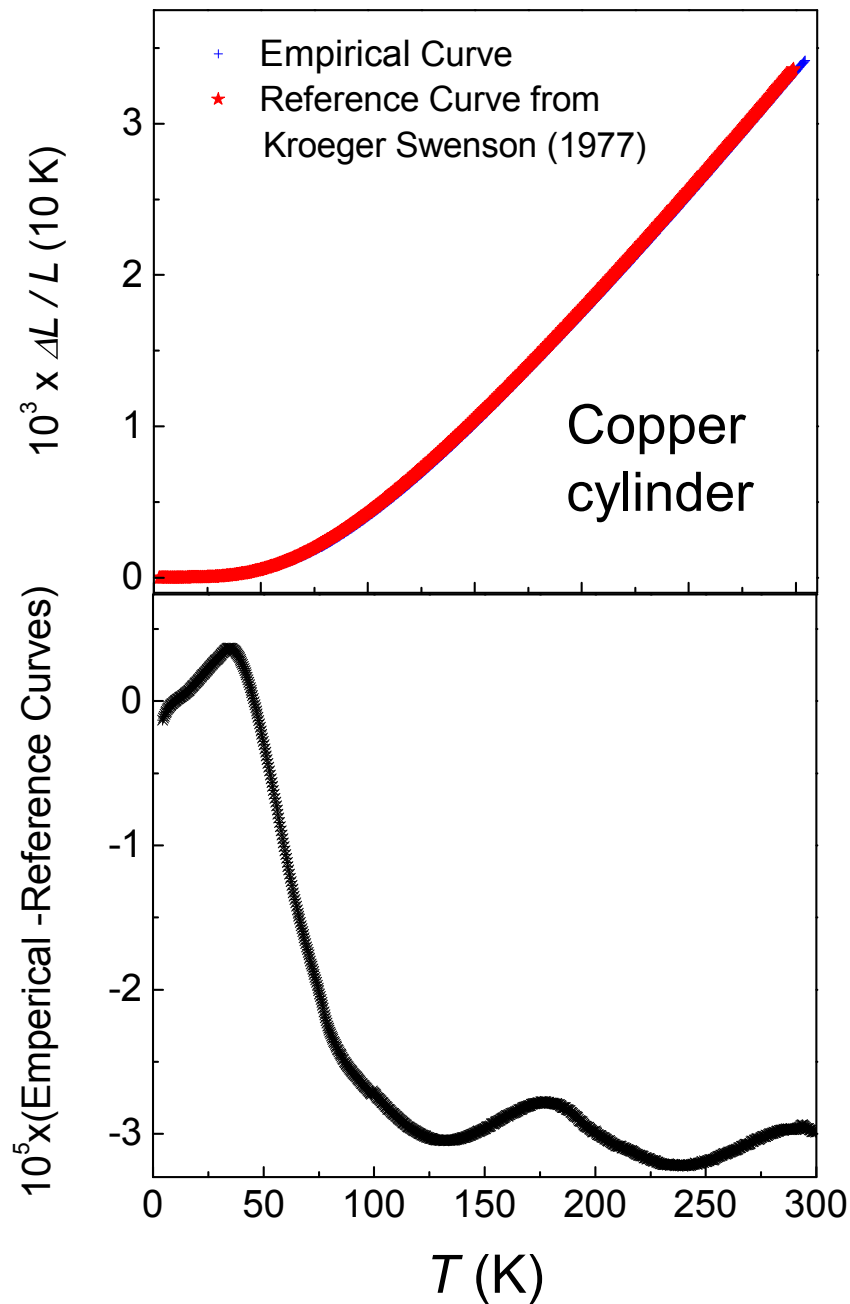


Figure 3.15: In the top graph, the length change is relative to 10 K for the National Bureau of Standards copper (Cu) reference sample showing the empirical curve in blue crosses and the reference curve in red stars can be seen. The reference curve was obtained from Ref. [85]. In the bottom graph, the relative error (empirical - reference curves) can be seen. The maximum deviation of the measured curve from the reference curve was less than 1.4%.

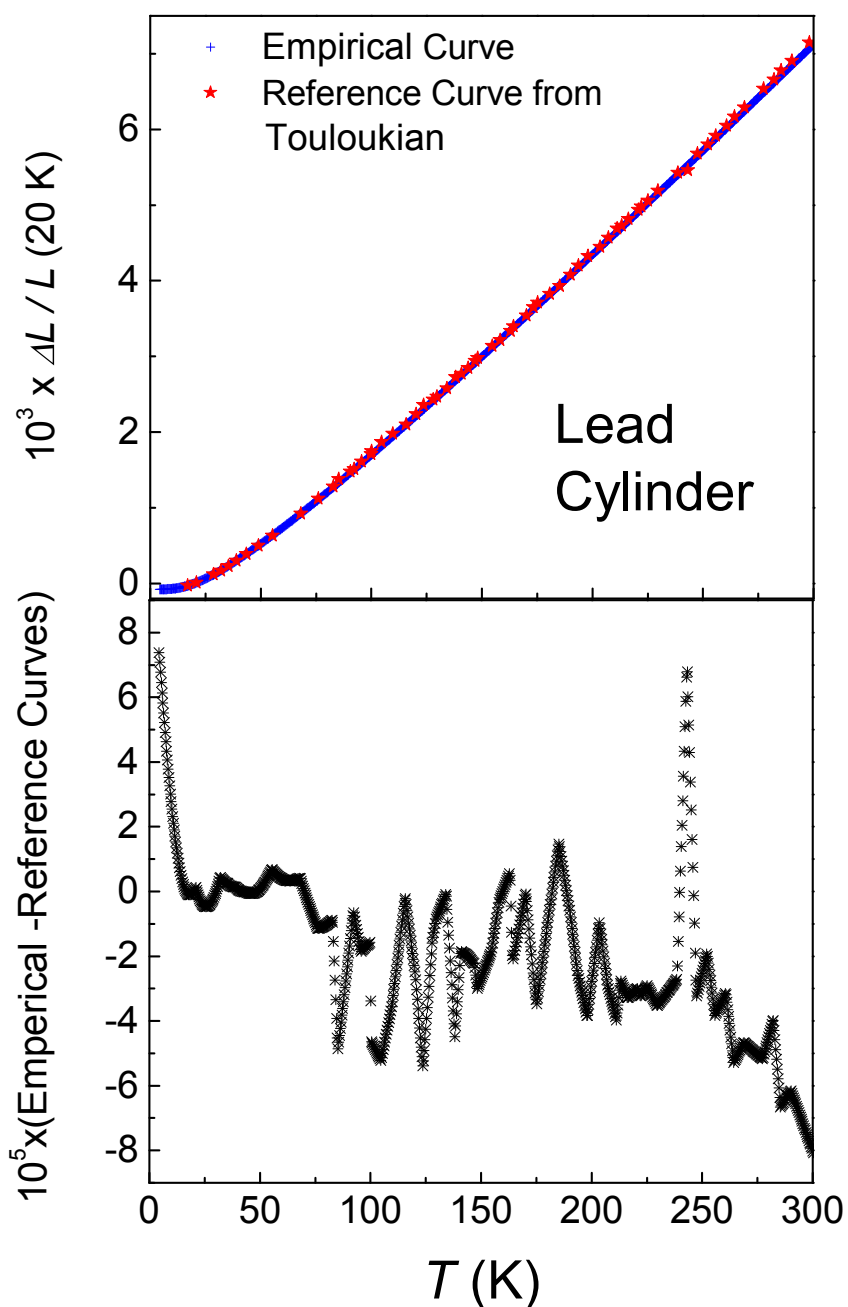


Figure 3.16: In the top graph, the length change is relative to 20 K for the TU Wien Lead (Pb) reference sample showing the empirical curve in blue crosses and the reference curve in red stars can be seen. The reference curve was obtained from Ref. [27]. In the bottom graph, the relative error (empirical - reference curves) for the TU Wien Lead (Pb) reference sample can be seen. The maximum deviation of the measured curve from the reference curve was less than 1.7%.

Titanium (III) Phosphate

4.1 Introduction

In this Chapter, I will discuss the magnetic and the structural properties of the low-dimensional $S = \frac{1}{2}$ Heisenberg antiferromagnet TiPO_4 . The special magnetic properties of TiPO_4 were discovered in the Chemieservice group (Max Planck Institute for Solid State Research) by Law *et al.* [23, 24]. TiPO_4 was proposed to be a non-conventional spin-Peierls compound with two successive phase transitions similar to the TiOX ($X = \text{Cl}, \text{Br}$) systems. After initial investigations by Kinomura *et al.* [86] and Glaum *et al.* [87–89], the magnetic and the thermal properties have been more recently characterized by Law *et al.* [23, 24]. Their investigation established the presence of two sequential magnetoelastic phase transitions. But a more detailed characterization of the nature of the phase transitions and especially of the low temperature crystal structures still needed to be done. Using thermal expansion measurements, I performed a detailed investigation of the length change along the crystallographic axes associated with the phase transitions. In collaboration with the crystallography group of Prof. van Smaalen (University of Bayreuth), the crystal structures at low temperatures were determined by single crystal x-ray diffraction measurements using synchrotron radiation. These investigations¹ conclusively demonstrated that TiPO_4 exhibits structural dimerization below ≈ 74 K explaining the observed singlet non-magnetic ground state. Between ≈ 74 K and ≈ 110 K, an intermediate phase occurs which is structurally incommensurate. Using magnetic susceptibility measurements, the pressure dependence

¹Part of the results described in this Chapter have been published in Ref. [90].

of the two phase transitions was also investigated.

4.2 Spin chains systems

One-dimensional arrangements of magnetic moments or spins ('spin chains') have attracted particular attention in solid state physics and especially in solid state magnetism. E. Ising performed the first theoretical treatment of a spin chain in 1925. The spin chain consisted of linearly arranged elementary magnets pointing either up or down and coupled by dipolar interaction. He found the surprising result that the spin chain model does not exhibit long-range ferromagnetic ordering².^[1] The absence of long-range ordering in low-dimensional systems realized by Ising for the first time has evolved into a more general foundation through the Mermin-Wagner theorem. This theorem can be summarized such that "long-range ordering at any finite temperature for dimensions less than three and effective exchange interactions" between "the spins are isotropic in spin space and of finite range" are absent.^[9, 91]

Today experimentally, Ising's model system is known as an Ising 'spin chain'. These spin chains can be approximately realized in crystals with strongly exchange coupled spin chains (intrachain spin exchange interaction) which are reasonably isolated from themselves in order to reduce interchain spin exchange interaction. The simplicity of spin chain systems allows theoretical computations of their properties to be obtained which are in good agreement with the experimental systems. However, the experimental realizations of spin chains are impeded by the presence of weak interchain spin exchange interactions which cannot generally be avoided. These weak interchain interactions are sufficient to drive the spin system into long-range magnetic ordering at low temperatures. Nevertheless, short-range correlations due to the low-dimensional fluctuations often dominate the properties of this systems in the temperature regime above the critical temperature. These correlations can be successfully investigated and compared with theoretical results for ideal systems. The short-range ordering may extend to very high temperatures comparable to the magnitude of the intrachain spin exchange interaction and lead to characteristic features in the magnetic susceptibility or the thermal properties.^[55]

²Ising originally stated that "daß ein solches Modell noch keine ferromagnetischen Eigenschaften besitzt".^[1]

A spin chain with isotropic antiferromagnetic intrachain spin exchange interaction (viz. Heisenberg exchange coupling) and vanishing interchain spin exchange can be described by the following Hamiltonian [92]:

$$\mathcal{H} = J \sum_{\langle ij \rangle} \vec{S}_i \vec{S}_j = J \sum_{\langle ij \rangle} S_i^z S_j^z + \frac{1}{2} (S_i^+ S_j^- + S_i^- S_j^+). \quad (4.1)$$

In addition to the Ising part ($S_i^z \cdot S_{i+1}^z$), the Hamiltonian (Equation 4.1) contains the products of the raising and lowering operators $S_i^+ S_j^-$ which act to flip neighbouring spins along the chain. The additional terms prevent long-range ordering from occurring and the Néel state is no longer an eigenstate. The raising/lowering operators create pairs of domain walls as the operators are applied along the chain.

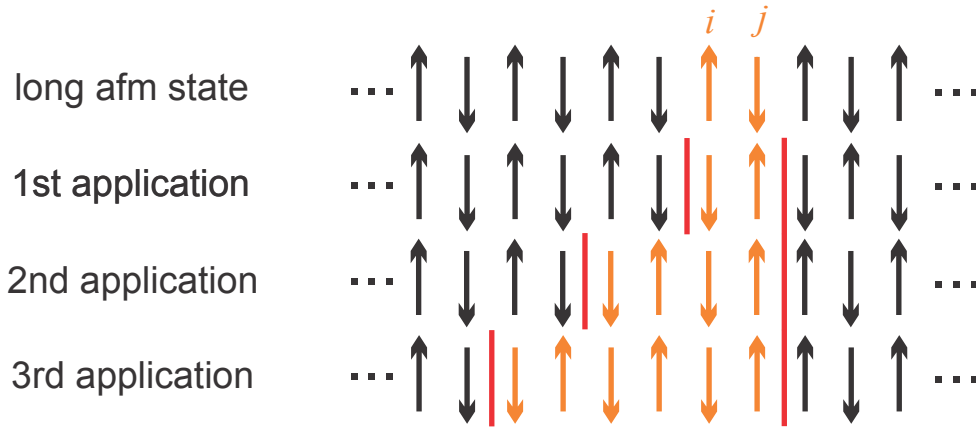


Figure 4.1: A schematic diagram of the spin arrangements for a one-dimensional $S = \frac{1}{2}$ Heisenberg system showing the effect of the raising/lowering operators $S_i^+ S_j^-$ after every application of the operators. The domain walls are denoted by the thick red lines. This Figure has been reproduced from Ref. [92].

The creation of these domain walls (‘solitons’) results in excitations which can progress through the chain freely. In Heisenberg spin chain systems, the continuum of excitations are known as ‘spinons’ which carry a spin $S = \frac{1}{2}$ and consequently are fermions.[92] The spinon spectrum of an antiferromagnetic chain has been calculated by des Cloizeaux and Pearson.[11]

The quantum nature of the excitation continuum in magnetic chain systems are particularly interesting. Experimentally, the excitation continuum has been observed through inelastic neutron scattering³ for KCuF_3 (see Figure 4.2) [94–98] and CuGeO_3 [99, 100].

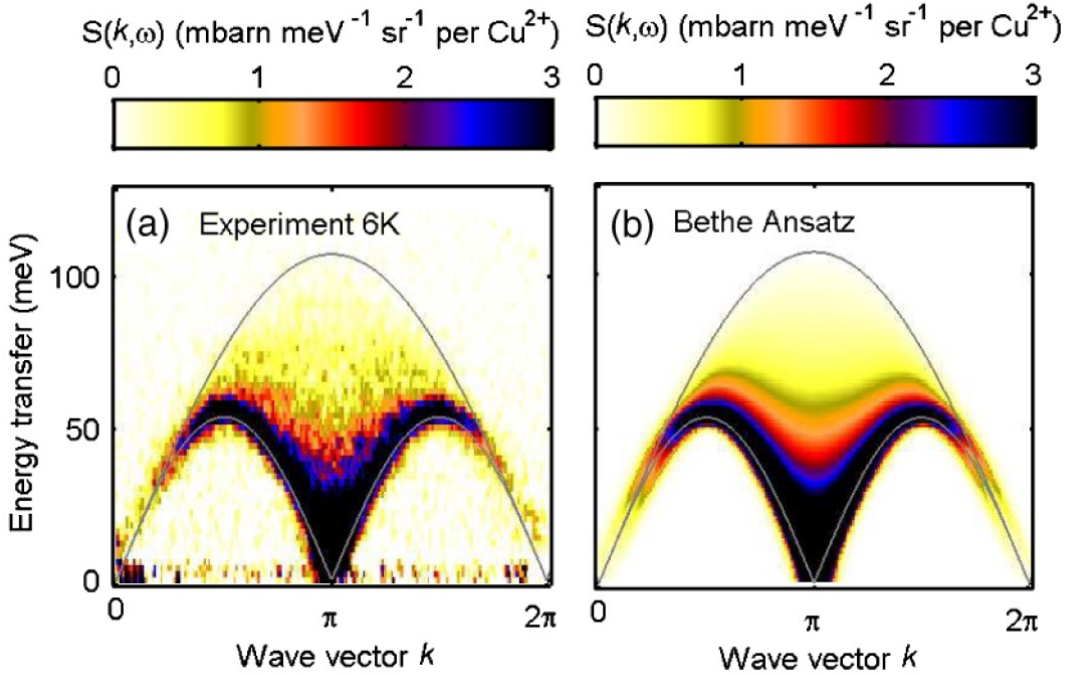


Figure 4.2: The inelastic neutron scattering results on KCuF_3 obtained by Lake *et al.*[96] showing the comparison with theory. (a) The multi-spinon continuum observed predominantly between the upper ($\omega_u(k)$) and lower ($\omega_l(k)$) boundaries for 2-spinon excitations (gray solid lines). (b) The dynamical structure factor $S(k, \omega)$ obtained from the algebraic Bethe Ansatz calculations. Reprinted figure with permission from B. Lake *et al.*, Physical Review Letters, **111**, 137205, 2013 (see Ref. [96]). Copyright (2014) by the American Physical Society. <http://journals.aps.org/prl/abstract/10.1103/PhysRevLett.111.137205>

³These experimental results can also be compared the theoretical results from the ‘Bethe Ansatz’ approach. The Bethe Ansatz approach was developed by H. Bethe in 1931.[93]

The effects of spin exchange couplings on the magnetic properties of Heisenberg chains have been investigated extensively. Bonner and Fisher used exact diagonalization of finite chain fragments ($N \leq 11$) to calculate the magnetic susceptibility, the heat capacity, the internal energy and the entropy of antiferromagnetic Heisenberg chains in 1964⁴. [3] They found that the magnetic susceptibility and the magnetic contribution to the heat capacity are characterized by broad maxima at temperatures which are linearly proportional to the intrachain spin exchange coupling. In 1994, the exact solution for $\chi(T)$ of the Heisenberg $S = \frac{1}{2}$ spin chain was obtained by Eggert, Affleck and Takahashi using the Bethe ansatz and a comparison with conformal field theory. [101] The conformal field theory results showed a logarithmic temperature dependence as $T \rightarrow 0$ K with an infinite slope in the magnetic susceptibility at $T \sim 0$ K. At temperatures much smaller than the intrachain exchange constant, the Eggert-Affleck-Takahashi numerical results are up to 10% larger than the Bonner-Fisher extrapolated results. Subsequently, Klümper *et al.* [102, 103] obtained even more precise results for the magnetic susceptibility and the heat capacity for Heisenberg $S = \frac{1}{2}$ chains with uniform nearest neighbour spin exchange interaction. Johnston *et al.* made the theoretical results easily accessible by providing detailed Padé approximation of Klümper *et al.* results. [8] The magnetic susceptibility and the heat capacity of the Heisenberg $S = \frac{1}{2}$ spin chain with uniform nearest neighbour interaction is presented in Figures 4.3 and 4.4 respectively. Recently, the magnetic susceptibility of Heisenberg spin chains with $S > \frac{1}{2}$ have been calculated by Law *et al.* [7] and evaluated in a Padé approximation using a similar procedure as Johnston *et al.* [8].

⁴Bonner and Fisher also performed similar calculation for ferromagnetic Heisenberg chains as well.

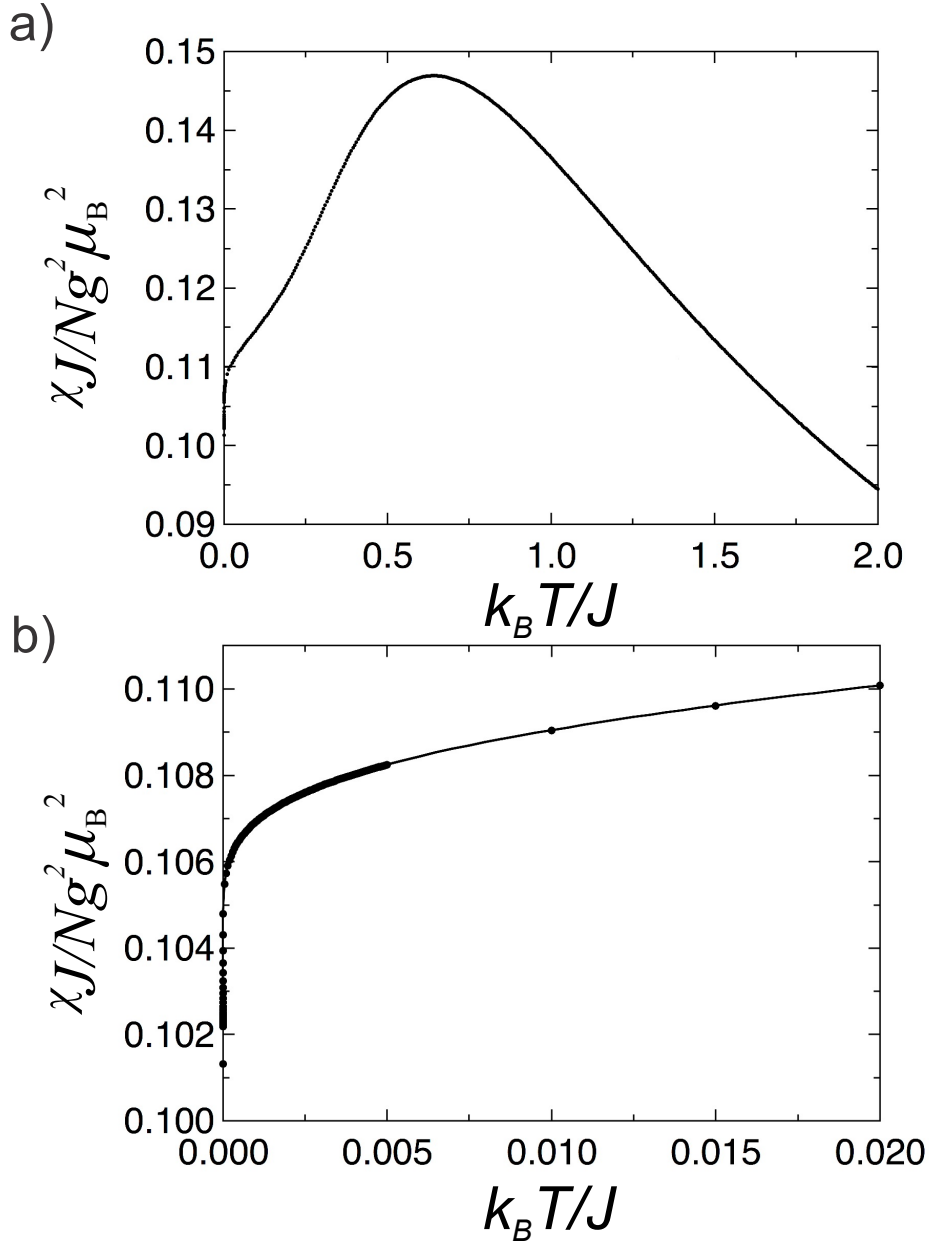


Figure 4.3: a) The magnetic susceptibility $\chi(T)$ of the spin $S = \frac{1}{2}$ nearest neighbour antiferromagnetic Heisenberg chain. b) Enlarged representation of the data in (a). The solid curve represents a calculation obtained from a Padé approximation by Johnston *et al.* [8] to data obtained by Klümper *et al.* [102, 103]. This Figure was produced from data in Ref. [8].

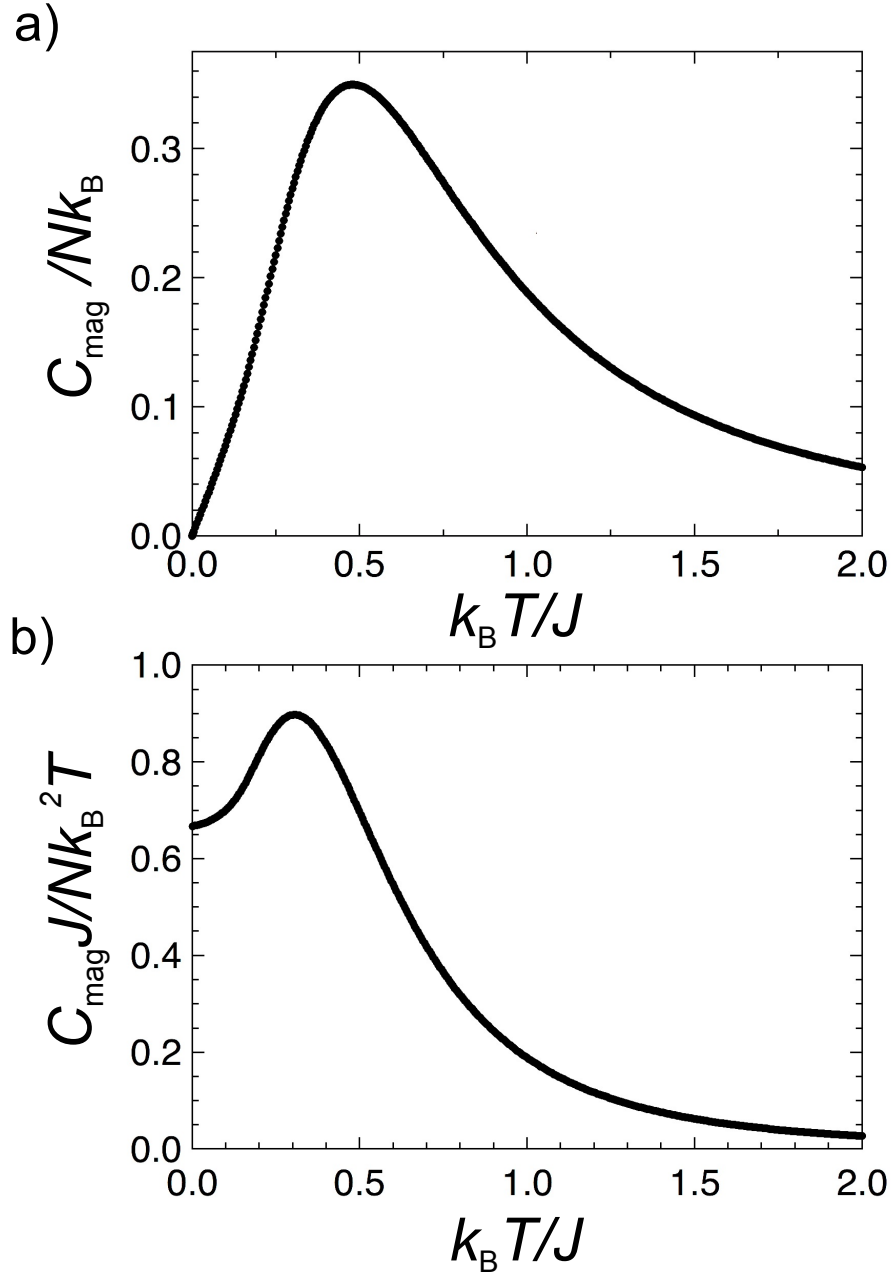


Figure 4.4: The magnetic heat capacity $C_{\text{mag}}(T)$, a) $C_{\text{mag}}(T)$, b) $C_{\text{mag}}(T)/T$ of the spin $S = \frac{1}{2}$ nearest neighbour antiferromagnetic Heisenberg chain. This Figure was produced from data in Ref. [8].

4.3 Electronic Peierls and spin-Peierls systems

In low-dimensional systems, the electronic Peierls in one-dimensional metals or the spin-Peierls transitions in one-dimensional magnets can be observed at low temperatures. Both Peierls transitions involve a lattice distortion which results in either an insulating or non-magnetic ground state.

4.3.1 The electronic Peierls transition

The possibility of the electronic Peierls transition was first conjectured in 1955 by R. Peierls. The Peierls transition occurs when the one-dimension lattice distorts and reduces symmetry by doubling the lattice spacing in order to minimize the total energy of the system.[104] The following instructive example given by Peierls illustrates the essential physics involved in a Peierls transition: Consider a one-dimensional linear chain of atoms with a lattice spacing of a and a half-filled valance band with one electron per atom. Every second atom is shifted by a small amount of δ , the distance between the atoms alternates between $a + \delta$ and $a - \delta$. The small shift of δ reduces the translational symmetry of the chain resulting in the formation of atom pairs ('dimerization') and, thereby, doubling the lattice spacing or periodicity to $2a$. The distorted chain is now described by a wave vector of $2K_f$ and an energy gap (2Δ) is formed at $\pm K_f$. The energy of the electrons in the distorted chain can be described using the perturbation theory with a weak periodic potential where the potential describes the distortion in the chain. A discontinuity forms in the energy of the electrons near $\pi/2a$ resulting in the opening of an energy gap at $\pi/2a$. [104] An example of the energy discontinuity applicable to an artificial monoatomic chain of equidistance atoms can be seen in Figure 4.5. The total energy of the electrons in the system will decrease since in the distorted chain only states below the energy gap are occupied. [104, 105]

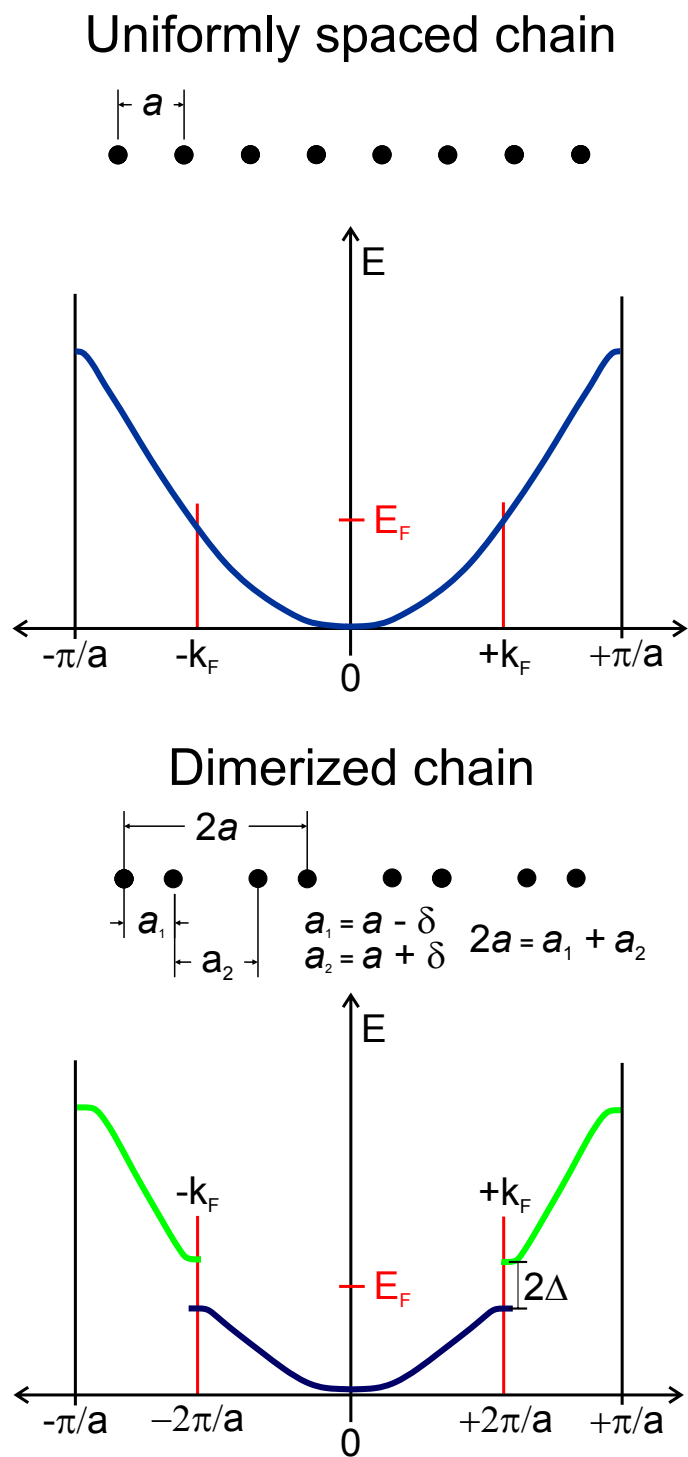


Figure 4.5: The Peierls distortion illustrated for an artificial one-dimensional chain of atoms. The electronic band structure and the position of the atoms in the chain are displayed before and after the Peierls distortion. This Figure was produced from figures in Refs. [106] and [107].

The opening of the energy gap has been observed experimentally via a metal-to-insulator transition. The electron Peierls transition was first observed in the early 1970s in one-dimensional metals⁵. One of the first identified electronic Peierls systems is the donor-acceptor salt tetrathiofulvalinium tetracyanoquinodimethane TTF-TCNQ. Figure 4.6 shows the DC electrical conductivity of TTF-TCNQ. Starting from room temperature, the conductivity $\sigma(T)/\sigma_{\text{RT}}$ increases with decreasing temperature proportional to $1/T^2$.

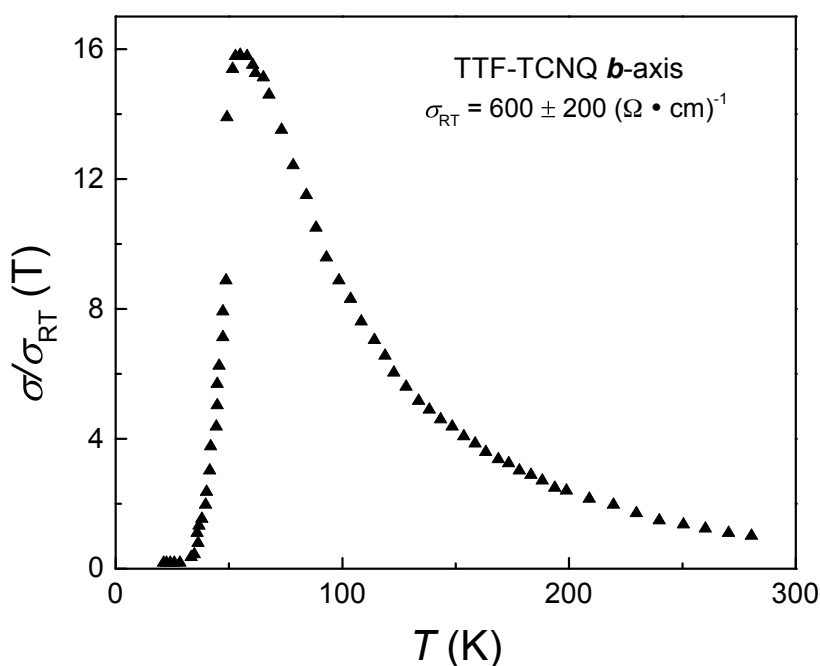


Figure 4.6: The temperature dependence of the DC conductivity for b -axis of TTF-TCNQ. This data was obtained from Tiedje’s Master thesis [110] written at the University of British Columbia (Vancouver, Canada).

A peak in the conductivity ratio occurs near 58 K with a conductivity value fifteen times the room temperature value. Thereafter, the conductivity quickly drops to zero near 52 K indicating the electronic Peierls transition into the insulating state.[108, 109] The electronic Peierls transition has also been identified from the metal-to-insulator transition in various other low-dimensional metal, such as $\text{K}_2[\text{Pt}(\text{CN})_4] \text{Br}_{0.30} \cdot 3\text{H}_2\text{O}$ (KCP) [18] or TaS_3 [111].[108, 111, 112]

⁵For more details, please consult the review articles by Toombs (Ref. [108]) or Berlinsky (Ref. [109]).

4.3.2 The spin-Peierls transition

The spin-Peierls transition is the magnetic equivalent of the electronic Peierls transition. The spin-Peierls transition has been observed in insulating materials with $S = \frac{1}{2}$ antiferromagnetic Heisenberg chains. The doubling of the lattice periodicity (lattice distortion with wave vector $q = 2K_f$) reduces the magnetic free energy and leads to a dimerization of the spin chain resulting in a singlet non-magnetic ground state. The decrease in the magnetic free energy supersedes the increase in the lattice free energy. The spin-Peierls transition opens an energy gap in the spin excitation spectrum separating the ground and the excited states. The zero-point oscillations can no longer occupy the excited states resulting in the loss of the degeneracy in the excitation spectrum and the lowering of the net magnetic free energy (see Figure 4.7).[113]

A spin-Peierls transition can be theoretically described using a Heisenberg Hamiltonian (see Equation 4.2) with antiferromagnetic spin exchange interaction J [112, 113]. The spin exchange interaction is modulated by the lattice vibrations due to a magnetoelastic coupling to the three-dimensional phonons bath. The lattice vibrations affect the spin Hamiltonian of the chains through the dependence of the spin exchange coupling J on the distances between the magnetic sites according to [112]:

$$\mathcal{H} = \sum_n \sum_{j=1}^N J_n(l, l+1) \mathbf{S}_j \cdot \mathbf{S}_{j+1} \quad (4.2)$$

wherein the first summation is carried out over the three-dimensional phonons surrounding the chains. The distance dependence of the antiferromagnetic spin exchange interactions J_n is obtained using a Taylor series expansion. From the Taylor series expansion, the so-called ‘linear J’ approximation is obtained as follows [112]:

$$J_n(l, l+1) = J + [\mathbf{u}_n(l) - \mathbf{u}_n(l+1)] \nabla_l J(l, l+1) \quad (4.3)$$

where \mathbf{u} are the three-dimensional lattice displacement operators.[112] In order to diagonalize this Hamiltonian, the spin operators are rewritten as pseudo-fermion operators using the Jordan-Wigner transformation. The final Hamiltonian can be solved using various methods such as the Hartree-Fock approxi-

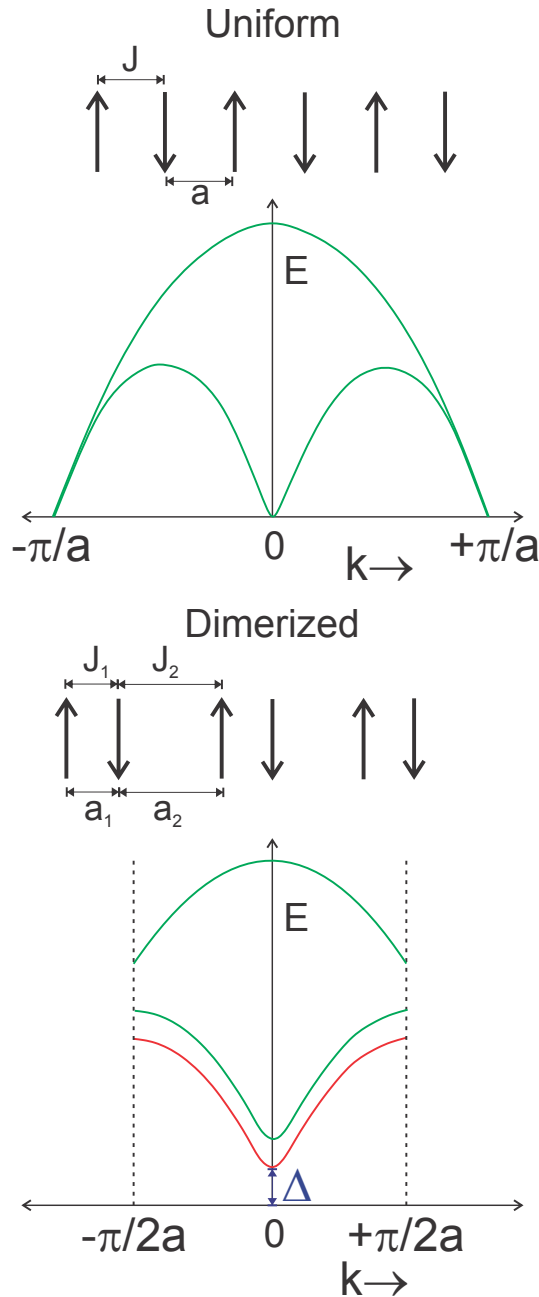


Figure 4.7: Schematic diagrams showing the dependence of the low-lying spin excitation energies \vec{k} vector for uniform and dimerized one-dimensional Heisenberg chains. The lower and the upper bounds of the magnetic excitations ('spinons') continuum are denoted by the green lines. In a uniform chain, the green lines are formed by a pair of free solitons in the antiferromagnetic spin arrangement. In the dimerized chain, the green lines are formed by the triplets states and the red line is the lowest triplet state. The spin gap between the singlet and the lowest triplet state is illustrated by the blue Δ . This Figure was produced from figures in Refs. [92] and [114].

mation, the Luttinger model technique or random phase approximation⁶. The theoretical results obtained by these methods compare well with data collected on real spin-Peierls systems with notable agreement.[113]

To illustrate the characteristic magnetic properties of a spin-Peierls system, the magnetic susceptibility for an idealized spin-Peierls system and an antiferromagnetic alternating Heisenberg chain can be compared (see Figure 4.8).

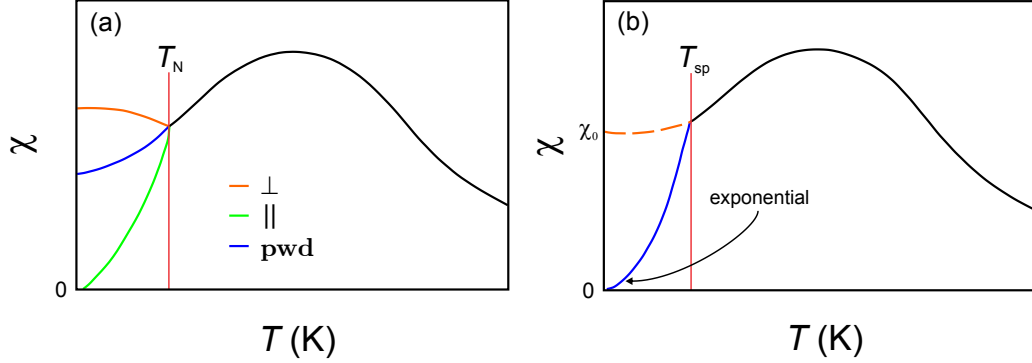


Figure 4.8: a) The temperature dependent magnetic susceptibility of a one-dimensional Heisenberg antiferromagnetic chain for a powder and a single crystal sample. The Néel temperature is denoted as T_N . b) The temperature dependent magnetic susceptibility of a one-dimensional spin-Peierls system for a powder and a single crystal sample. The spin-Peierls transition temperature is denoted as T_{sp} . The orange dashed line indicates the low temperature magnetic susceptibility in the absence of the spin-Peierls transition. This Figure was reproduced from a figure in Ref. [113].

For a spin-Peierls system, the opening of the gap in the spin excitation spectrum leads to a characteristic exponential isotropic decrease of the magnetic susceptibility below T_{sp} , which approaches zero for $T \rightarrow 0$ as displayed in Figure 4.8b. Below the spin-Peierls transition temperature T_{sp} , the system has a non-magnetic singlet ground state. In contrast to the spin-Peierls system, the antiferromagnetic alternating Heisenberg chain exhibits an anisotropic susceptibility below the Néel temperature and remains finite in some cases (e.g. for a polycrystalline sample – the **pwd** curve in Figure 4.8a). Long-range magnetic ordering occurs at T_N for the antiferromagnetic system resulting in a Néel ground state.[57, 113]

⁶For more details about each of these methods, please consult Ref. [113] for more information.

4.3.3 Overview of known spin-Peierls compounds

Spin-Peierls transitions have been observed in both organic and inorganic compounds. The first organic spin-Peierls compound to be discovered was the donor-acceptor compound TTF-CuBDT by Bray *et al.* [17] in 1975 with a transition temperature T_{sp} of 12 K. TTF-CuBDT is a donor-acceptor organic insulator consisting of tetrathiafulvalinium (TTF) and metal bisdithiolene (BDT) complexes similar to TTF-TCNQ. Following the discovery of TTF-CuBDT, many other organic spin-Peierls compounds were found with varying T_{sp} transition temperatures (see Table 4.1 as of 2001).

Compound	T_{sp} (K)
(TTF)CuBDT	12
(TTF)AuBDT	2
(TTF)CuBDSe	6
MEM(TCNQ) ₂	18
(TMTTF) ₂ PF ₆	20
(TMTTF) ₂ PF ₆	20
(BCPTTF) ₂ PF ₆	36
(BCPTTF) ₂ AsF ₆	32.5
α' -(ET) ₂ Ag(CN) ₂	5.8
β' -(ET) ₂ SF ₅ CF ₂ SO ₃	45
ζ -(ET)PF ₆	40

Table 4.1: The spin-Peierls transition temperatures of various organic spin-Peierls compounds. The data contained in this table was obtained from Ref. [115].

From Table 4.1, it becomes obvious that a large number of the organic spin-Peierls compounds share common organic building block molecules such as TTF and TCNQ.[115] The intrachain spin exchange coupling J for the compounds in Table 4.1 is of the order of 100 K.[19] There are only a small number of organic spin-Peierls compounds since a majority of organic solids exhibit Néel states or density wave ground states instead of rare spin-Peierls ground state.[115] Since 2001, more organic spin-Peierls compounds have been discovered including (DMe-DCNQI)₂M (M=Li and Ag) [116] and (*o*-DMTTF)₂X (X=Cl, Br and I) [117].

In 1993, the first inorganic spin-Peierls compound CeGeO₃ was discovered by Hase *et al.* [19] with a transition temperature T_{sp} of 14 K. The magnetic susceptibility (see Figure 4.9) of CuGeO₃ was measured with H parallel to the principle axes of the orthorhombic single crystal. Below 14 K, an exponential decrease to non-zero constant was observed in the magnetic susceptibilities for all three crystal orientations. Above 14 K, the magnetic susceptibilities were isotropic with a broad maximum near 56 K. The temperature dependence of the magnetic susceptibilities were modeled by a one-dimensional Heisenberg antiferromagnetic spin system with an antiferromagnetic spin exchange interaction J of 88 K. Hase *et al.* concluded that CuGeO₃ was a spin-Peierls compound based on the aforementioned magnetic susceptibility results and the magnetic field dependence of the spin-Peierls transition temperature which will be discussed in the next section. In 1996, Isobe and Ueda [118] discovered the second inorganic spin-Peierls compound α' -NaV₂O₅ with a T_{sp} of 35 K and $J = 441$ K. This compound is more complicated since charge ordering also plays a role in the observed transition to the non-magnetic ground state.[115, 119]

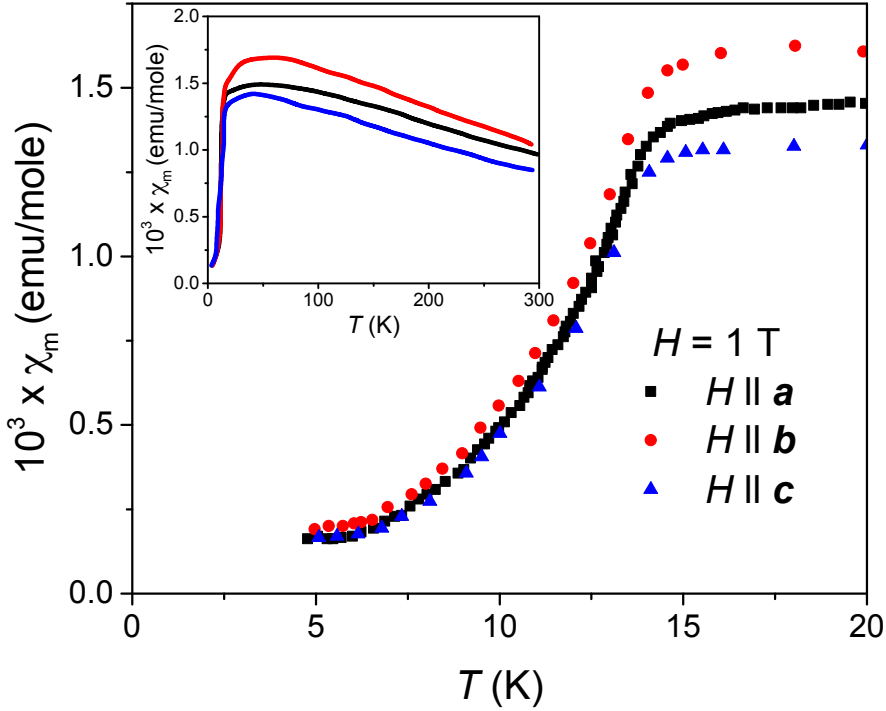


Figure 4.9: The molar magnetic susceptibility for a single crystal of CuGeO_3 with $H = 1$ Tesla. Main: The low temperature magnetic susceptibility below 20 K measured along the three crystallographic axes. Bulaevskii fitted the data using the Hamiltonian in Ref. [120] resulting in an alternation parameter γ equal to 0.71 and a spin exchange coupling J of 88 K. Inset: The magnetic susceptibility for temperatures between 4.5 K and 300 K measured along the three crystallographic axes. This Figure was produced from data in Ref. [121].

For almost a decade, CuGeO_3 and $\alpha\text{-NaV}_2\text{O}_5$ remained the only inorganic spin-Peierls compounds until the discovery of non-conventional inorganic spin-Peierls compounds. In 2003, the first non-conventional inorganic spin-Peierls compound TiOCl was discovered by Seidel *et al.* [21]. In TiOCl , the spin-Peierls state is characterized by a two-stage phase transition. The two-stage phase transition involving an intermediate phase (see Figure 4.10) consists of one continuous second order transition T_{c2} at 91 K and a first order transition T_{c1} at 67 K.[122, 123] The two-stage transition occurs due to the presence of an intermediate incommensurate phase between the room temperature phase and the spin-Peierls ground state.[90] In 2005, Palatinus *et al.* [22] substituted bromine for chlorine producing an additional spin-Peierls compound TiOBr with T_{c2} and T_{c1} equal to 48 K and 28 K (see Figure 4.10) respectively.

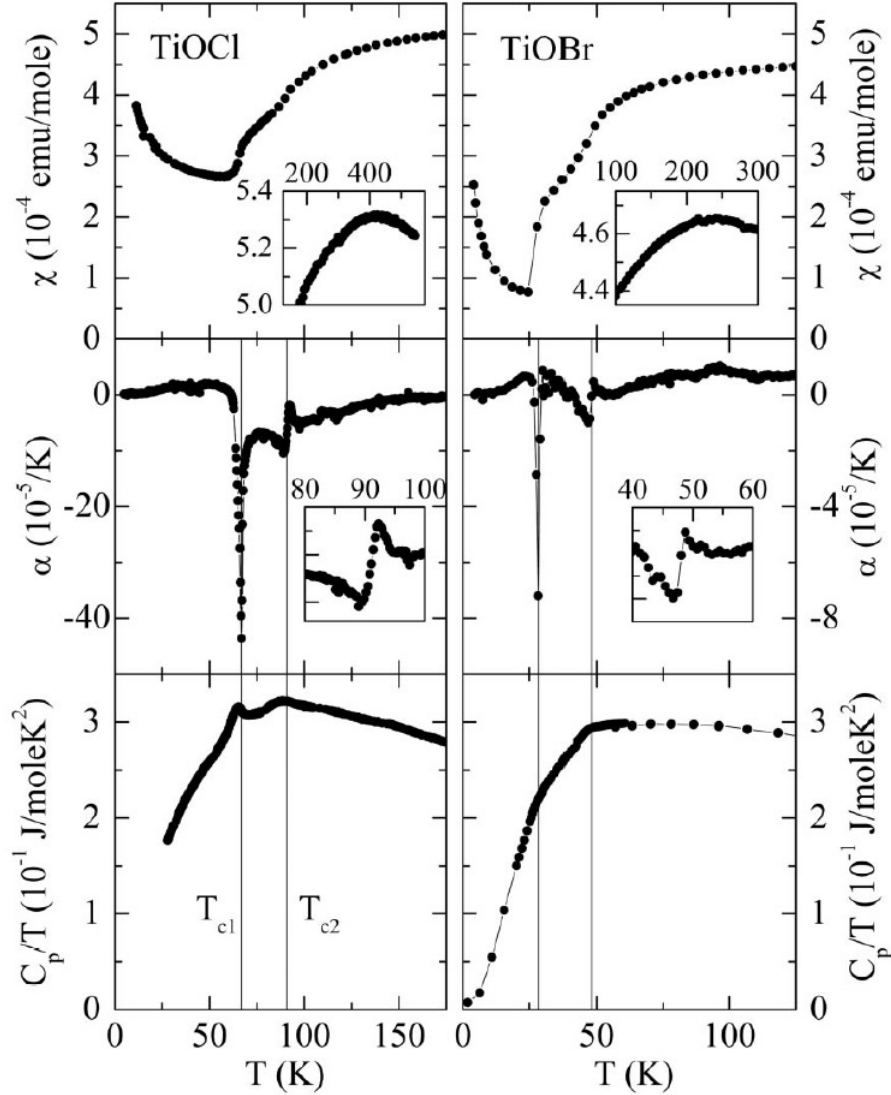


Figure 4.10: The molar magnetic susceptibility $\chi(T)$, the thermal expansion $\alpha(T)$ and the heat capacity $C_p(T)$ measurements of TiOBr and TiOCl. Reprinted figure with permission from R. Rückamp *et al.*, Physical Review Letters, **95**, 097203, 2005 (see Ref. [122]). Copyright (2014) by the American Physical Society. <http://journals.aps.org/prl/abstract/10.1103/PhysRevLett.95.097203>

The most recent spin-Peierls compound discovered, in 2011 by Law *et al.* [23, 24], is TiPO_4 . TiPO_4 also exhibits a two-stage spin-Peierls transition with T_{c2} and T_{c1} equal to ~ 110 K and ~ 74 K respectively.[24] Currently, TiPO_4 has the highest transition temperatures as well as the largest spin exchange coupling of any spin-Peierls compound known thus far with intrachain spin exchange coupling of almost 1000 K equivalent to 100 meV.[24]

4.3.4 The effect of magnetic fields on the spin-Peierls transition

An external magnetic field tends to align the spin moments and acts to break the spin dimers in the spin-Peierls system. An applied magnetic field thus diminishes the spin-Peierls transition temperature and above a critical field transforms from a commensurate to an incommensurate spin-Peierls state. For magnetic fields and Zeeman energy which are small compared to the spin-Peierls transition temperature T_{sp} , the spin-Peierls state continues to exist but the spin gap and T_{sp} decrease with increasing magnetic field.[113, 124, 125] The applied magnetic field splits the excited triplet states thereby decreasing the energy of the first excited and thus reducing the magnitude of the spin gap. Accordingly, the chemical potential of the system is lowered by the applied magnetic field. And the Fermi level continuously decreases as the magnetic field is raised⁷. Even though the chemical potential is shifted, the lattice distortion remains commensurate for small magnetic fields. Above a critical magnetic field H_c , the reduction of the Fermi level can result in alterations of the lattice distortion and induce incommensurate phases.[112, 113, 126] The incommensurate phases above H_c in spin-Peierls compounds have been studied by Kiryukhin, Keimer, Rønnow and others through x-ray/neutron scattering measurements.[127–130] For example, an incommensurate phase has been observed in CuGeO_3 above 12.5 Tesla [127, 129, 130] and above 11.5 Tesla in TTF-CuBDT [128].

The magnetic field dependence of the spin-Peierls transition was first investigated in detail using theoretical approaches in 1978 and experimental techniques for TTF-CuBDT in 1979. The effect of an applied magnetic field on an ideal spin-Peierls system was calculated by Bulaevskii *et al.* [131] and Bray [126] using mean-field theory and Cross [132] employing the boson algebraic approach⁸. A common feature of all three calculations is the quadratic downshift of the spin-Peierls transition ΔT_{sp} with the applied magnetic field H . The quadratic relationship between ΔT_{sp} and H can be expressed by the

⁷The mean-field treatment for the effect of an applied magnetic field on a spin-Peierls system can be seen in Section 2.4 of Ref. [113].

⁸A summary of the results for each calculation can be seen Ref. [113] in Section 2.4 and 2.5.

following relation [113]:

$$\frac{T_{\text{sp}}(H)}{T_{\text{sp}}(0)} = 1 - \eta_{\text{Th}} \left(\frac{\mu_{\text{B}}H}{k_{\text{B}}T_{\text{sp}}(0)} \right)^2 \text{ when } \mu_{\text{B}}H \ll k_{\text{B}}T_{\text{sp}}(0) \quad (4.4)$$

For an ideal spin-Peierls system, the coefficient of η_{Th} was observed to be 0.44 by Bray and Bulaevskii *et al.* while Cross arrived at a value of 0.36 for η_{Th} . [126, 131, 132]

Experimentally, the dependence of the spin-Peierls transition on an applied magnetic field was first investigated by Bray *et al.* on TTF-CuBDT. [133] They observed a quadratic dependence of the temperature shift ΔT_{sp} for applied magnetic fields up to 6.5 Tesla. As the applied magnetic field was further increased, the T_{sp} decreases faster than expected from Equation 4.4 due to a change in the commensurate distortion of the lattice for $H < 11.5$ Tesla. [133] With the discovery of CeGeO₃ by Hase *et al.* [20], the quadratic magnetic field dependence of the spin-Peierls transition became a key characteristic of the newly discovered spin-Peierls compound. Hase *et al.* rewrote Equation 4.4 as follows [20]:

$$1 - \frac{T_{\text{sp}}(H)}{T_{\text{sp}}(0)} = \eta \left(\frac{g\mu_{\text{B}}H}{2k_{\text{B}}T_{\text{sp}}(0)} \right)^2 \text{ when } 2\mu_{\text{B}}H \ll k_{\text{B}}T_{\text{sp}}(0) \quad (4.5)$$

The coefficient η is obtained by fitting the experimental data to Equation 4.5. η is a dimensionless number with a characteristic value for each spin-Peierls compound⁹.

4.3.5 The effect of pressure on the spin-Peierls transition

Spin-Peierls compounds are ideal suited for high pressure investigations due to the magnetoelastic nature of the spin-Peierls transition. The pressure affects both the phonons and the spin exchange interactions in the compound. The effect of pressure on the spin-Peierls transition temperature can vary significantly both in magnitude and sign. For example, the spin-Peierls transition in TTF-CuBDT is suppressed by 1.1 K or $\sim 10\%$ with an applied pressure of 0.6 GPa whereas the transition in MEM-(TCNQ)₂ is enhanced by 5.2 K or $\sim 30\%$ with an applied pressure of 0.3 GPa. [113, 134]

⁹A table of η values for various spin-Peierls compounds is presented on p. 105.

Spin-Peierls theory predicts that the application of pressure increases the dimerization of the chain such that the spin exchange coupling constant J increases linearly with increasing pressure. As J is increased, the spin-Peierls transition temperature also responds linearly with increasing pressure¹⁰ but the response can result in either a suppression or an enhancement of the spin-Peierls transition¹¹. [135, 136] All spin-Peierls compounds have, so far, exhibited a linear response of the transition temperatures over the measured pressure range (usually less than 10 kbar or 1 GPa) consistent with theory. [113, 134, 137–139]

The suppression of the spin-Peierls transition has been investigated by Bray in 1980. He observed that the spin-Peierls transition temperature will decrease with increasing pressure if the coupling between dimerized lattice mode and the applied pressure is harmonic. [135] But the increase in the spin-Peierls transition temperature with pressure involves more complex mechanisms. In 1986, Lépine studied the origins of the enhancement of the spin-Peierls transition temperature using similar methods as Bray. The theoretical model indicated that the spin-Peierls transition temperature increases with pressure when the coupling between dimerized lattice mode and the applied pressure is anharmonic and/or the spin-lattice coupling constant depends on the strain of the lattice. [136] The detailed mechanisms involved in this effect varies for each spin-Peierls compound.

The spin-Peierls transition temperature will only increase with pressure until a critical pressure P_c is reached. Above pressure P_c , the spin-Peierls state can disappear resulting in the formation of a metallic, a ferromagnetic or an electronic Peierls state. For example, CuGeO_3 has a ferromagnetic transition at 4.5 GPa and an insulator-to-metal transition occurs in MEM-(TCNQ)_2 occurs around ~ 0.34 GPa. [134, 137] Recently, Blanco-Canosa *et al.* suggested that TiOX ($X = \text{Cl}$ and Br) has a transition from a spin-Peierls to an electronic Peierls transition between 10 - 15 GPa. [138] Hence, the high pressure behaviour of spin-Peierls compounds are unique to each compound.

¹⁰The details of the mean-field approach are provided in Refs. [135] and [136].

¹¹The shift of the spin-Peierls transition(s) under pressure for various compounds are tabulated in Table 4.4 on p. 102.

4.4 The room temperature crystal structure and the magnetic properties of TiPO_4

The crystal structure of titanium(III) phosphate TiPO_4 is isostructural to the orthorhombic CrVO_4 structure-type (space group no. 63 $Cmcm$). The Ti^{+3} cations ($3d^1$ electronic configuration with $S = \frac{1}{2}$) are coordinated by slightly axially compressed O_6 octahedra while the P^{+5} cations are enclosed in O_4 tetrahedra (see Figure 4.11a). The TiPO_4 octahedra are connected via trans-edges to form TiO_2 corrugated ribbon chains running along the c -axis (see Figure 4.11b). The ribbon chains are linked together by sharing corners with the PO_4 tetrahedra. The room temperature lattice parameters of TiPO_4 are $a = 5.303 \text{ \AA}$, $b = 7.902 \text{ \AA}$ and $c = 6.349 \text{ \AA}$. [88]

Recent studies of TiPO_4 's magnetic properties have renewed interest in this low-dimensional system. The magnetic properties were first studied by Kinomura *et al.* [86] in 1982 and subsequently by Glaum *et al.* [88] in 1992. Both investigations indicated that temperature independent magnetism occurs above $\approx 150 \text{ K}$ and a dip below $\approx 150 \text{ K}$ followed a hyperbolic increase at low temperatures. Lately, Law *et al.* [23, 24] studied TiPO_4 using high resolution magnetic susceptibility measurements up to 800 K, heat capacity and nuclear magnetic resonance experiments. It was found that the high temperature region of the magnetic susceptibility can be very well modeled by an antiferromagnetic $S = \frac{1}{2}$ Heisenberg chain with uniform nearest neighbour exchange interaction of $J_{\text{nn}} = 965(10) \text{ K}$ (see the red line in Figure 4.12a). The fit of the magnetic susceptibility and EPR measurements coherently resulted in a g-factor of 1.94(3) indicating that small spin-orbit coupling effects were present. [23, 24] At low temperature, two anomalies were noted in the magnetic susceptibility and the heat capacity data, one at 74(0.5) K and a second one at 111(1) K (see Figure 4.12 b and c). Below 74 K, the susceptibility becomes temperature independent exhibiting a vanishing spin susceptibility indicative of a non-magnetic singlet ground state.

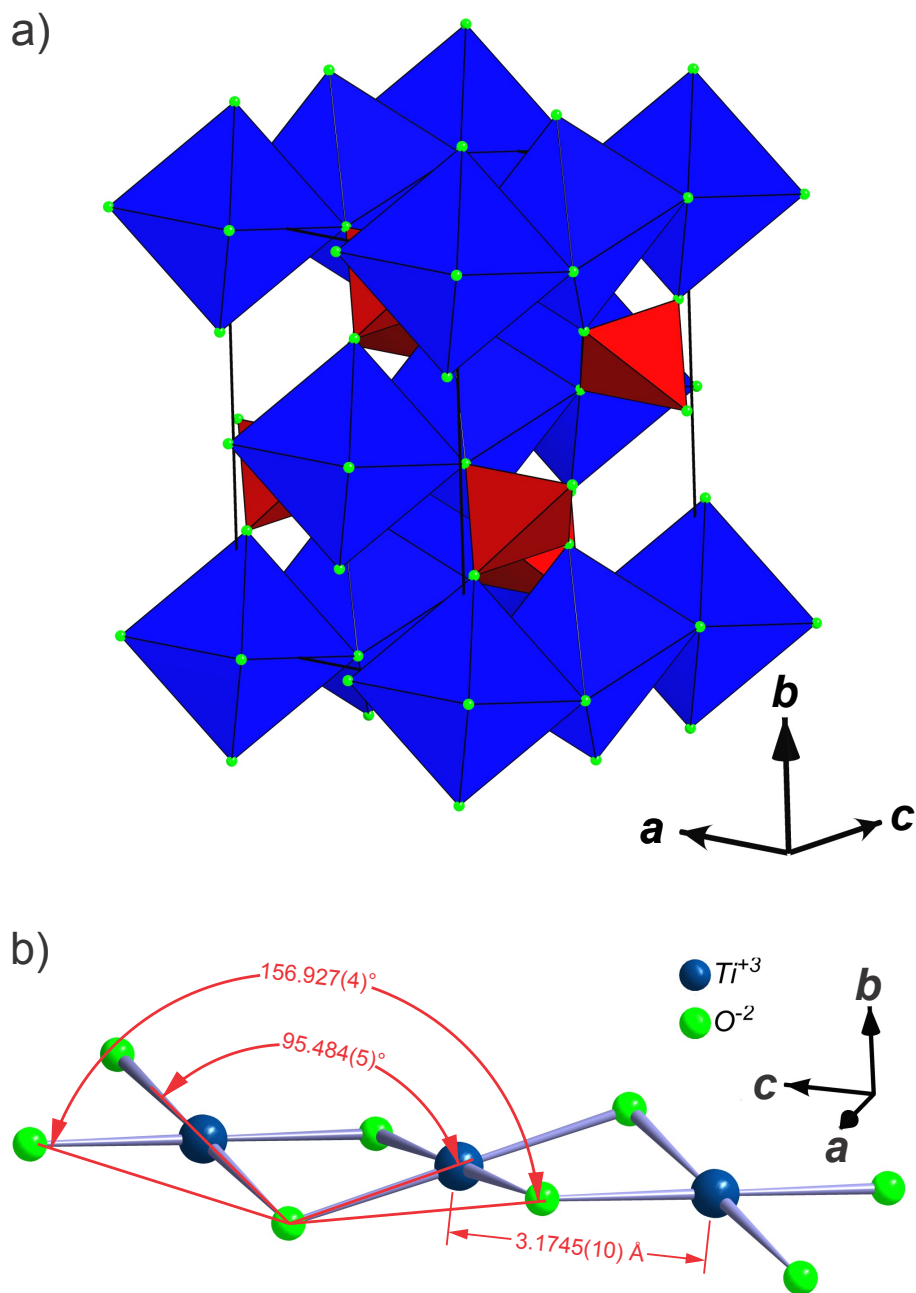


Figure 4.11: The crystal structure of TiPO_4 : a) The TiO_6 octahedra in blue, PO_4 in red and oxygen atoms in green are shown. b) The TiO_2 ribbons chains running along the c -axis are shown with distance of $3.1745(10) \text{ \AA}$ between the titanium cations and an angle of 95.5° between $\text{Ti}^{+3} - \text{O}^{-2} - \text{Ti}^{+3}$ at room temperature. At room temperature, the ribbons chains are buckled with an angle of 156.93° in the ac plane.[23, 88]

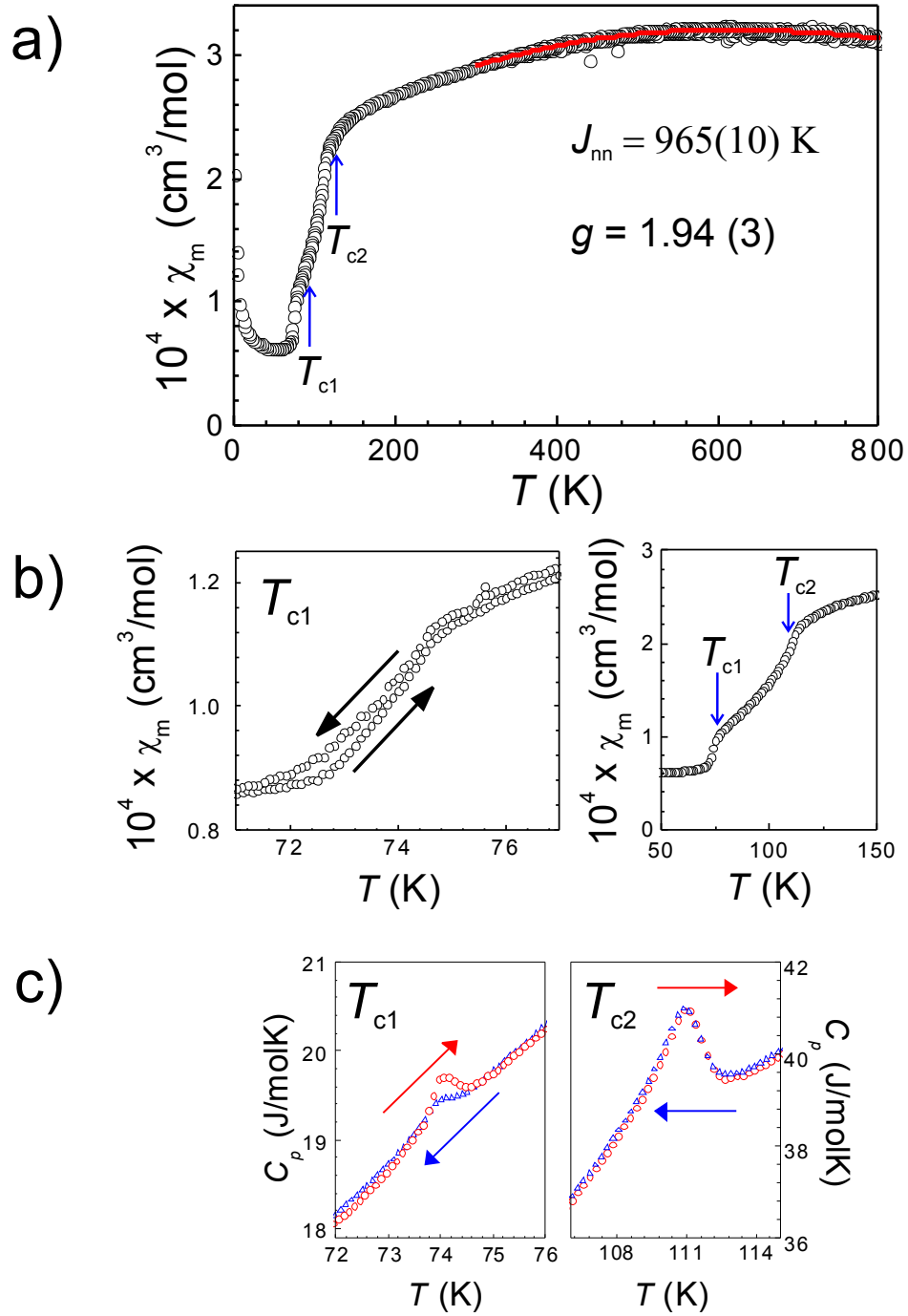


Figure 4.12: The magnetic susceptibility and the heat capacity of TiPO_4 : a) The high temperature magnetic susceptibility of TiPO_4 showing the antiferromagnetic $S = \frac{1}{2}$ Heisenberg chain fit as the solid red line. b) The magnetic susceptibility of TiPO_4 around the 74 K and 110 K. c) The heat capacity of TiPO_4 around 74 K and 110 K. This Figure was produced from figures presented in Ref. [23].

^{31}P nuclear magnetic resonance (NMR) measurements by Law *et al.* [23, 24] reveal that the ^{31}P NMR line becomes asymmetric and broad between 112 K and 74 K implying that an incommensurate phase may be present. Below 74 K, the broad continuum contracts into two narrow lines. The splitting of the lines suggested that two phosphorous sites exist at low temperature. Assuming that a spin-Peierls type dimerization develops below 74 K, the observation of two different P sites can be a consequence of the dimerization. However without a detailed low temperature structure determination, it remained unclear how the deformation of the PO_4 tetrahedra and the dimerization of the Ti chains are related.[23, 24]

Similar consecutive phase transitions (TiOCl: 67 K and 91 K; TiOBr: 28 K and 48 K) into a non-magnetic ground state were observed in the TiOX (X = Cl, Br).[21, 22] The high temperature magnetic susceptibility of TiOCl can also be well described using a $S = \frac{1}{2}$ Heisenberg chain with antiferromagnetic nearest neighbour spin exchange J_{nn} of ~ 660 K.[21, 122] Furthermore, analogous NMR results were obtained for the TiOX spin-Peierls compounds. Despite these similarities, there are notable differences between the TiOX and TiPO_4 . At room temperature, TiOX crystallizes in the orthorhombic FeOCl structure (space group no. 59 $Pm\bar{m}n$). The crystal structure of the TiOX is characterized by two-dimensional Ti^{+3} and O bilayers parallel to the **ab** plane with the X atoms located in between the bilayers.[122] Using low temperature x-ray diffraction measurements, it was observed that dimerization of the Ti ions in the bilayers occurs during the consecutive phase transitions. The high temperature transitions at T_{c2} occur continuously as the temperature decreases resulting in the formation of an incommensurate phase. As the temperature is further decreased, the incommensurate phase transforms into a commensurate spin-Peierls phase at a first order lock-in transition temperature T_{c1} . The dimerization of the Ti ions is attributed to the presence of the direct exchange interactions between neighbouring Ti ion spins.[122, 123, 140, 141]

However, the origin of the two-stage spin-Peierls transition in TiOCl and TiOBr cannot be uniquely resolved due to the intricate crystal structure of these compounds which allows for vastly more spin exchange pathways than TiPO_4 . The crystal structure of TiPO_4 is much simpler allowing for the spin exchange pathways to be clearly identified. Law *et al.* [23, 24] utilized density function (DFT) calculations employing the Vienna *ab initio* package to model the spin exchange couplings in TiPO_4 . The spin exchange interactions were represented

by the three following parameters: the intrachain coupling terms J_1 – nearest neighbour and J_2 – next-nearest neighbour and the interchain coupling term J_3 . Using the generalized gradient approximation with an on-site repulsion of 2 eV, the spin exchange couplings were all found to be antiferromagnetic: $J_1 = -988$ K, $J_2 = -1.4$ K and $J_3 = -20$ K. The nearest neighbour intrachain coupling term J_1 from both the high temperature magnetic susceptibility data and DFT calculation were quantitatively similar. Additionally, the J_1 term was remarkably large for a spin-Peierls compound. The TiPO_4 spin exchange interaction J_1 is fifty percent larger than the TiOCl spin exchange interaction. The intrachain spin exchange coupling J_1 is the predominate spin exchange coupling in the chain with the interchain J_3 equal to $\sim 2\%$ of the intrachain J_1 coupling.[23, 24]

4.5 The low temperature crystal structure

After the initial characterization of the magnetic properties of TiPO_4 , a full characterization of the low temperature crystal structure and the character of the two-stage phase transition was still pending. In a collaboration with the crystallography group of Prof. van Smaalen at University of Bayreuth, low temperature single crystal x-ray diffraction measurements were used to determine the crystal structure of TiPO_4 in the incommensurate phase and the commensurate phase.[90] Initially, the crystal structures of the commensurate and the incommensurate phase were solved using measurement datasets collected at 10 K and 82 K respectively. The crystal structure at 10 K (space group $Pbnm$) is characterized as a commensurate lock-in phase exhibiting a distance alternation (‘dimerization’) of the Ti chains. The Ti - Ti bond lengths alternated between 3.2304(25) Å and 3.1336(25) Å with an increase in the corrugation of the TiO_2 ribbons chains. The dimerization of the Ti chains amounts to approximately 3.1%. The TiO_2 ribbon chains buckling angle at 10 K amounts to 158.944(22)° as compared to the room temperature of 156.927(4)°.[90]

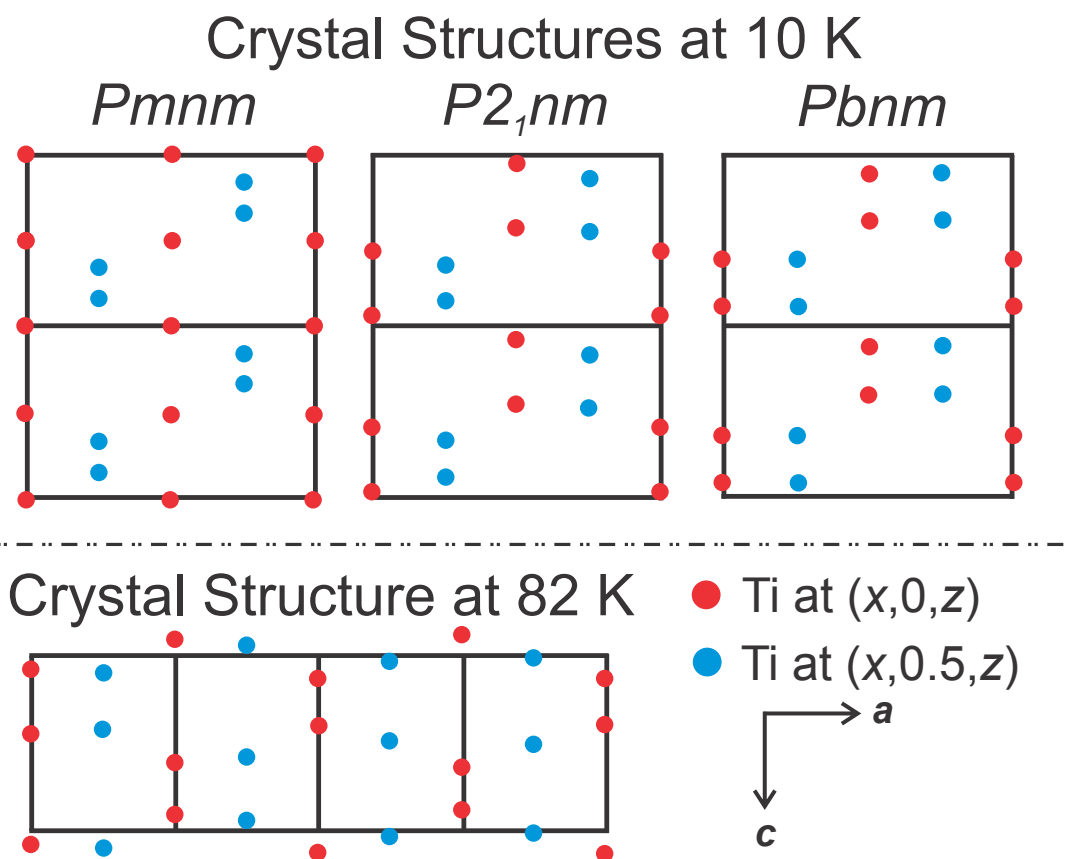


Figure 4.13: The low temperature crystal structures of TiPO_4 in the $Pmnm$, the $Pbnm$ and the $P2_1nm$ space groups are shown. In the commensurate phase, the projection along $[010]$ at 10 K for crystal structures in the $Pmnm$, the $P2_1nm$ and the $Pbnm$ symmetries with the $2a \times b \times c$ super cells are displayed. The projection along $[010]$ at 82 K in the incommensurate phase with a $4a \times b \times c$ super cell is outlined. The atomic displacements are multiplied by thirty for clarity. This Figure was produced from a figure in Ref. [90].

The crystal structure at 10 K was solved using the superspace approach¹². From the main reflections, the crystal structure at 10 K could be described within the room temperature space group $Cmcm$. The significantly weaker satellite reflections indicated three alternative space group solutions: two centrosymmetric space groups - $Pmnm$ and $Pbnm$ or the non-centrosymmetric space group $P2_1nm$. The three space group solutions generates three different low temperature crystal structures. Dimerization and bond length alternation along c -axis occurred for all space group solutions. The structure described by the space group $Pmnm$ exhibits dimerization in every second layer of chains along b -axis leaving a magnetic ground state at 10 K contrary to the magnetic susceptibility results. The structure described by the space group $Pbnm$ is characterized by an increased distortion of the TiO_6 octahedra when compared to the crystal structure at room temperature. The lattice parameters at 10 K in space group $Pbnm$ were calculated to be $a = 10.689(3)$ Å, $b = 7.9861$ Å, and $c = 6.364(5)$ Å. In the structure described by the $P2_1nm$ space group, the variations in the dimerization of the Ti chains results in four different P atoms positions. However, the positions of two pairs of P atoms were negligibly different and still consistent with the previously published NMR results by Law *et al.* [24] Additional DFT electronic structure calculations of the total energies were utilized to identify the most likely crystal structure at 10 K. These calculations indicated that the structure described by the $Pbnm$ space group has the lowest energy. However, the energies of the $P2_1nm$ and $Pmnm$ structures turned out to be very close (~ 0.5 meV) to the energy of the $Pbnm$ structure.[90]

Following the observation of the three possible low temperature structures, the variation of the crystal structure with temperature in the incommensurate phase was studied. Using \mathbf{q} -scans, the presence of superstructure reflections at $(h + \frac{1}{2}, k, l)$ were already noted at 10 K. These superstructure reflections could be indexed with the propagation vector $\mathbf{q} = (\sigma_1, 0, 0)$ where $\sigma_1 = \frac{1}{2}$. In order to follow the temperature evolution of σ_1 , the temperature dependence of the \mathbf{q} -vector for a strong superstructure reflection (2, 4, 3, -1) was measured between 70 K and 115 K (see Figure 4.14c). A discontinuity in the σ_1 value occurs near 75 K with a jump from 0.50 to 0.527 with σ_1 increasing continuously as the temperature increases. At 110 K, σ_1 reaches a maximum value of

¹²In the superspace approach, the crystal structure is described using separate parameters for the main reflections and the satellite reflections. The main reflections produce an average structure whereas a modulated structure is generated from the satellite reflections. For more details about the superspace approach, please consult Ref. [142].

0.565 before the superlattice satellite reflections disappear near 112 K. From these results, it was concluded that the doubling of the \mathbf{a} -axis occurs below T_{c1} (=75 K) leading to the commensurate lock-in phase. Between 74 K and 112 K, an incommensurately modulated intermediate phase occurs in agreement with the NMR results. A critical power law fit of the intensities was utilized near 110 K resulting in a critical temperature of 111.6(3) K. Above the critical temperature, the normalized intensity of the (2, 4, 3, -1) satellite Bragg reflection drops to zero. In Figure 4.14b, \mathbf{q} -scans were performed by tracking the integrated intensities of multiple superlattice reflections as a function of temperature. For each temperature, the superlattice reflections were indexed and the σ_1 component of the propagation vector was calculated. The discontinuous jump observed in σ_1 near T_{c1} implies that this transition is a first order phase transition. The continuous decrease of the normalized intensities of the satellite Bragg reflection near T_{c2} indicates that this transition is a continuous second order phase transition.[90]

The fact that the three possible low temperature commensurate structures are very close in their energies suggested an explanation of the occurrence of the intermediate incommensurate phase as a consequence of thermal fluctuations between the three low temperature structural possibilities. The fluctuations between the three energetically very close structures can explain the broad distribution of the ^{31}P NMR resonance positions observed in the intermediate phase. The PO_4 tetrahedra can be concluded to be largely rigid structural units due to the weak temperature dependence of the P - O distance and O - P - O angle in the intermediate phase. Additionally, the positions of the oxygen atoms in the TiO_6 octahedra are altered by the dimerization of the Ti chain. The dimerization causes further movement of the positions of the oxygen atoms in the TiO_6 octahedra in the neighbouring chains which are connected through the PO_4 tetrahedra. These findings suggested that the incommensurate intermediate phase results from structural fluctuations by way of the "competition and frustration of the spin-Peierls distortion in neighbouring Ti chains mediated by the elastic coupling" through the PO_4 tetrahedra.[90]

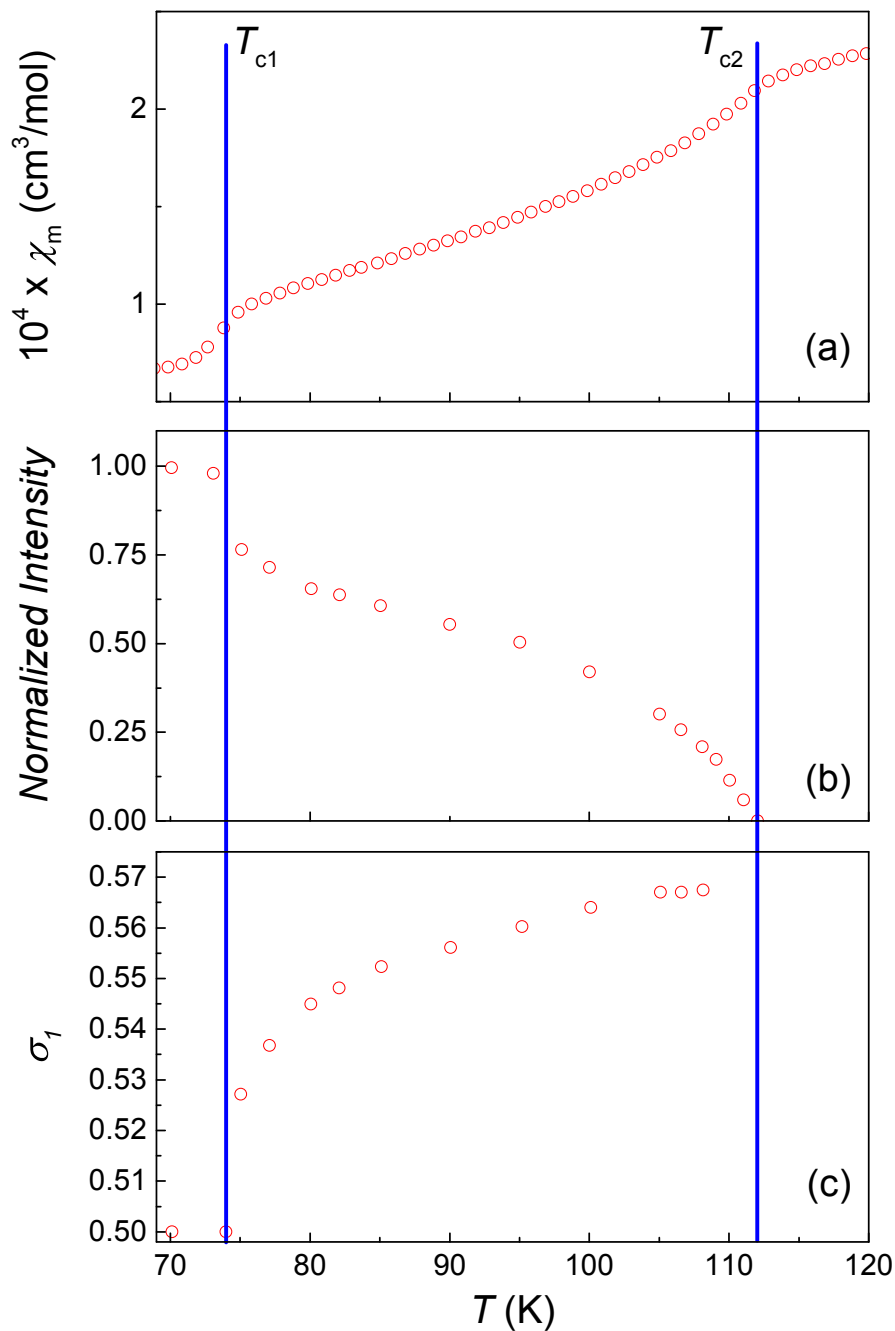


Figure 4.14: a) The temperature dependence of the molar magnetic susceptibility χ_m from Law *et al.* [23, 24] b) The temperature dependence of the normalized intensities for the (2, 4, 3, -1) satellite Bragg reflection of TiPO_4 . c) The temperature dependence of the \mathbf{q} -scan along the \mathbf{a}^* axis for TiPO_4 with \mathbf{q} -vector of $(\sigma_1, 0, 0)$. The error bars are not visible since the symbols are larger than the error bars. This Figure was produced from data in Refs. [23] and [90].

The temperature dependence of the lattice parameters of TiPO_4 have been studied by single crystal x-ray diffraction down to ~ 100 K by Law.[23] This study revealed a pronounced anisotropy of the thermal expansion in both the direction and the magnitude. Whereas the c contracts with decreasing temperature a and b expand i.e. they exhibit a negative thermal expansion. Furthermore, the volume of the unit cell contracts by ~ 0.5 % down to 100 K but the contraction occurs only below 175 K. Above 175 K, the volume appears to be unchanged from its room temperature value which is unreasonable. Due to the limited number of data points (six in total between 300 K and 100 K), the connection between the lattice anomalies and the phase transitions remains unclear. But these measurements give a clear indication that the lattice parameters and the structural phase transitions are intimately related. In this Chapter, the detailed temperature dependence of the lattice constants and the character of the transitions are studied using magnetic susceptibility and thermal expansion measurements.

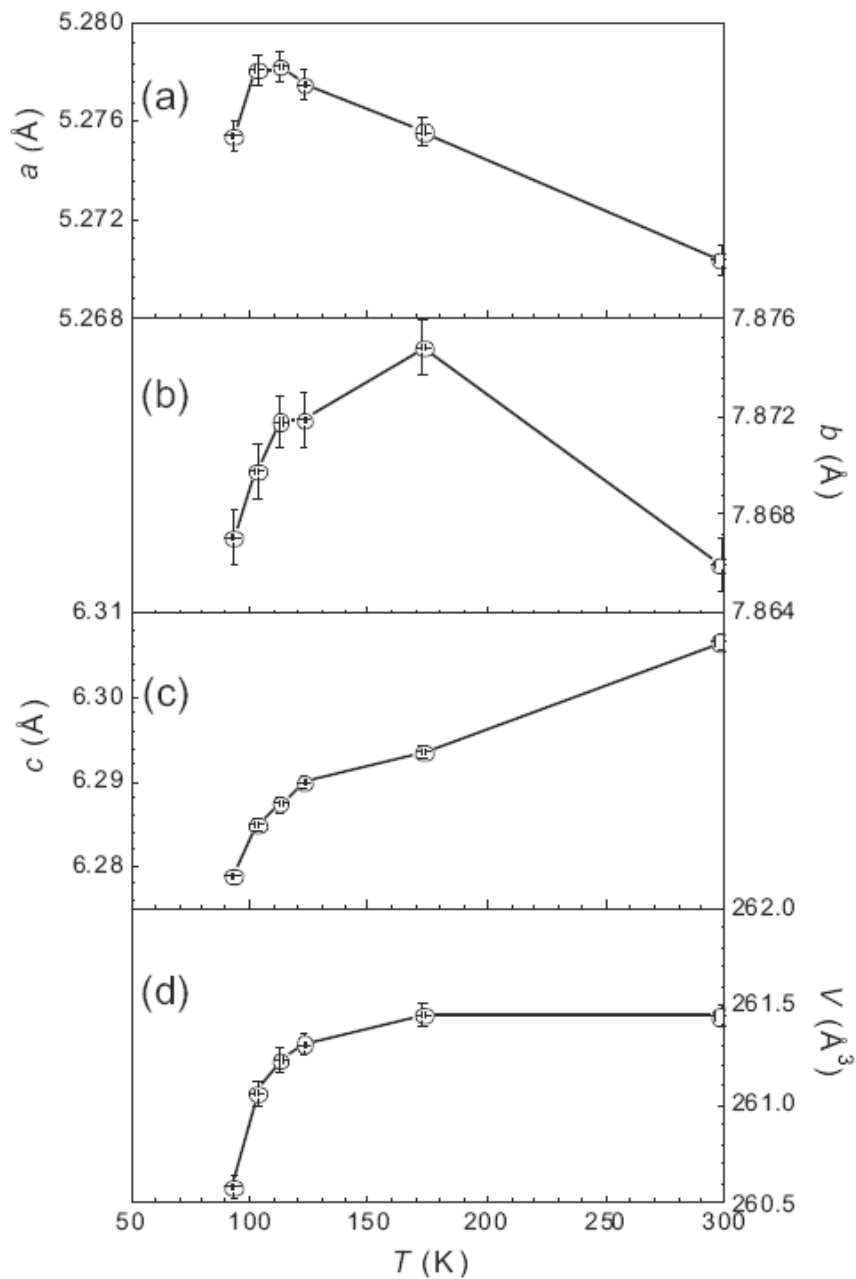
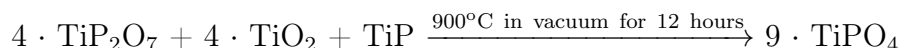


Figure 4.15: The temperature dependence of the three lattice parameters and the cell volume of TiPO_4 reprinted from Ref. [23] with permission.

4.6 Sample preparation

Large single crystals of TiPO_4 were grown¹³ from a polycrystalline powder using chemical vapour transport with a minute amount of iodine I_2 as the transport agent. The polycrystalline powder of TiPO_4 was produced using the following chemical reaction:



The details of the single crystal preparation can be found in Refs. [87] and [88].

4.6.1 Magnetization measurements

Magnetization measurements were performed on three samples (PS1, PS2 and RC1) with a Magnetic Property Measurement System (Quantum Design, MPMS-XL7) magnetometer (see Section 3.1). The two fine crystalline powders PS1 and PS2 had masses around ~ 100 mg. The crystal RC1 had a mass of ~ 0.9 mg. The fine crystalline powder samples and the crystal were filled into a standard gelatin capsule. The gelatin capsule has a diamagnetic background signal on the order of 10^{-6} emu which was subtracted. High pressure measurements were performed on the two fine crystalline powders (typical size of crystals ~ 0.1 mm x ~ 0.1 mm x ~ 0.1 mm) each with a mass of less than 15 mg. The home-build high pressure clamp cell has a high diamagnetic background on the order to 10^{-4} emu. The temperature dependence of the pressure cell's background signal varies from measurement to measurement and the empty pressure cell measurement can not be easily subtracted.

The high pressure clamp cell was constructed of a copper-beryllium Cu:Be (98%:2%) alloy with a maximum sample volume of ~ 0.02 cm³ and a maximum applied pressure of ~ 0.95 GPa. The components and the construction of the pressure cell is presented in Figure 4.16. The powder sample was filled into a small teflon container (see Figure 4.16b) with a small chip of high purity lead Pb. The high purity Pb chip was placed near the sample in the container and used as a manometer to measure the pressure applied to the sample. The pressure dependence of the superconducting transition temperature of Pb is well documented by Eiling and Schilling in Ref. [143]. A clear electronic liquid,

¹³I would like to thank Prof. Dr. R. Glaum and his collaborators at the University of Bonn for preparing the TiPO_4 samples.

3M Fluorinert¹⁴ FC-77 (Perfluorocycloether CAS # 52623-00-4), was chosen as the pressure transmitting medium and filled into the sample container in order to immerse the samples. FC-77 applies homogeneous pressure to the sample viz. hydrostatic conditions for pressures up to 0.95 GPa.[146]

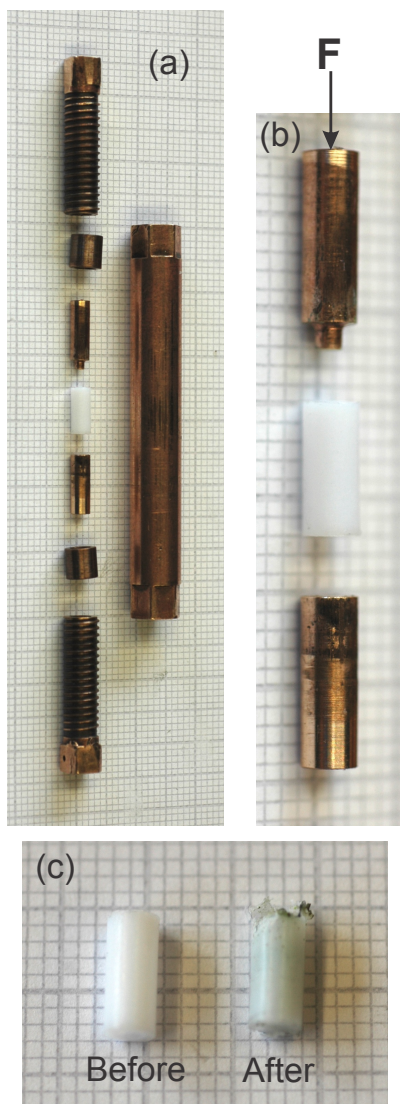


Figure 4.16: The component and the assembly of the high pressure copper-beryllium clamp cell on mm paper: a) The body and the internal components of the pressure cell b) The close-up view of the sample environment c) The condition of the teflon sample container before and after applying pressure.

¹⁴For more information about 3M Fluorinert please consult Refs. [144] and [145].

4.6.2 Thermal expansion measurements

The three crystals chosen for the thermal expansion measurements were grown in the same batch. The crystals of TiPO_4 are dichroic/pleochoric¹⁵ with a grayish-green and brownish-red appearance.[89] Neutron back-scattering Laue images using the Laue diffractometer OrientExpress at the Institute Laue-Langevin (Grenoble) were used to orient the largest crystal¹⁶. Orientation of the smaller crystals was done locally using either an image-plate single crystal x-ray diffractometer¹⁷ or a x-ray Laue camera with a backscattering geometry. In Figure 4.17, a neutron Laue-backscattering image of the as-grown (unpolished) crystal SC1 (the largest crystal used) is presented. Neutron backscattering allows the investigation of the bulk crystal to be probed as a whole. The crystal SC1 was found to be un-twinned as indicated by the sharp Laue spots. Figure 4.18 shows the faces of the crystal SC1 as determined by x-ray diffraction before polishing. After the orientation of the crystal was performed, SC1 was carefully polished in order to create flat faces for the \mathbf{a} , \mathbf{b} and \mathbf{c} axes. The final polished SC1 is displayed in Figure 4.19. The crystal had a volume of 0.6 mm^3 ($\sim 2 \text{ mg}$).

¹⁵Pleochrism occurs in a material when the hue, the purity and the intensity of material's colour varies as the material is rotated in a plane of polarized light. Dichroism occurs when two extreme colours are observed if the material is rotated in a plane of polarized light. For more information about Pleochrism, please consult Ref. [147] for more details.[147]

¹⁶I would like to thank Dr. B. Ouladdiaf from the Institute Laue-Langevin for his guidance and instructions on how to use the OrientExpress instrument.

¹⁷I would like to thank Dr. J. Nuss at the Max Planck Institute for Solid State Physics for performing the x-ray orientation on the image-plate diffractometer.

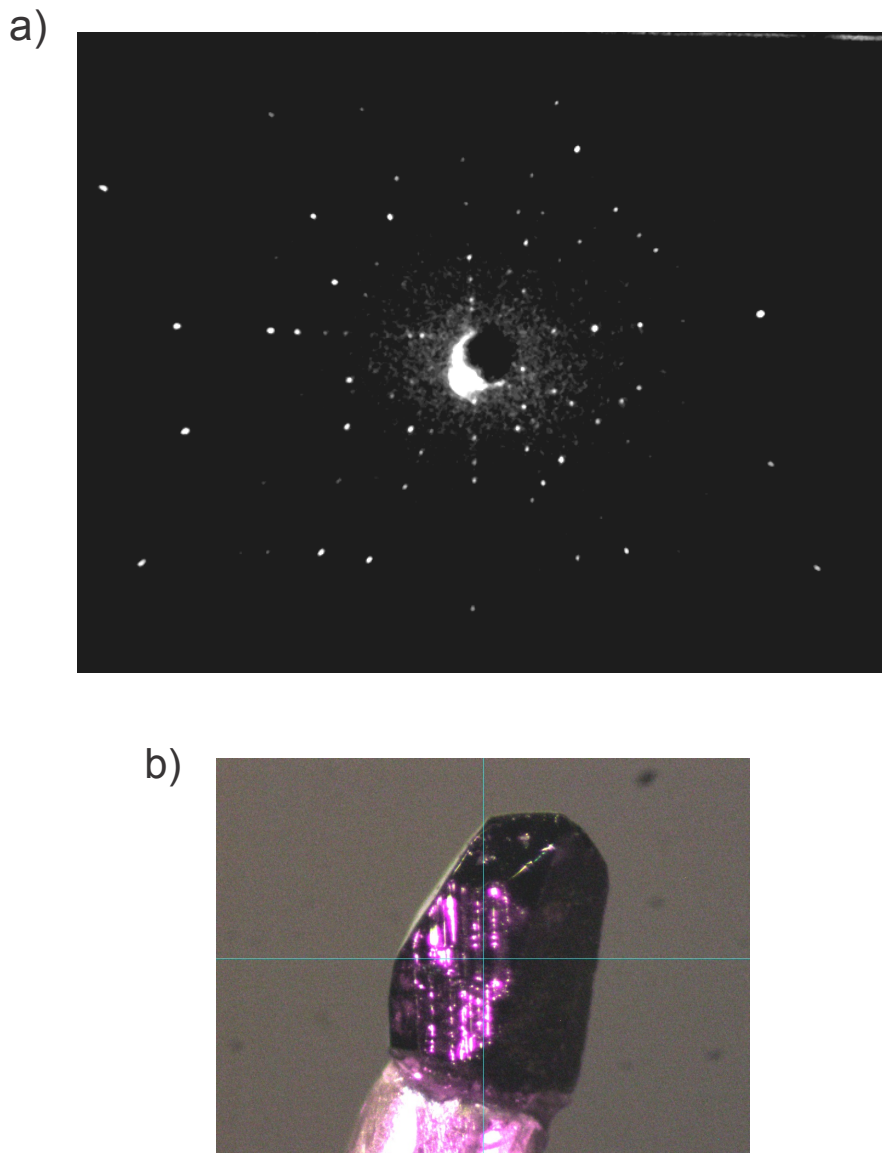


Figure 4.17: The orientation of the TiPO_4 single crystal SC1 using the neutron Laue backscattering instrument OrientExpress [148] which employs two cameras with a total recording area of 18 cm x 26 cm. The wavelength of the incident neutron beam varies between 0.4 Å and 5.1 Å. The cameras were placed at a distance of 51 mm from the sample: a) The neutron Laue backscattering image of the single crystal SC1. (b) The alignment of the single crystal SC1 in the neutron beam.

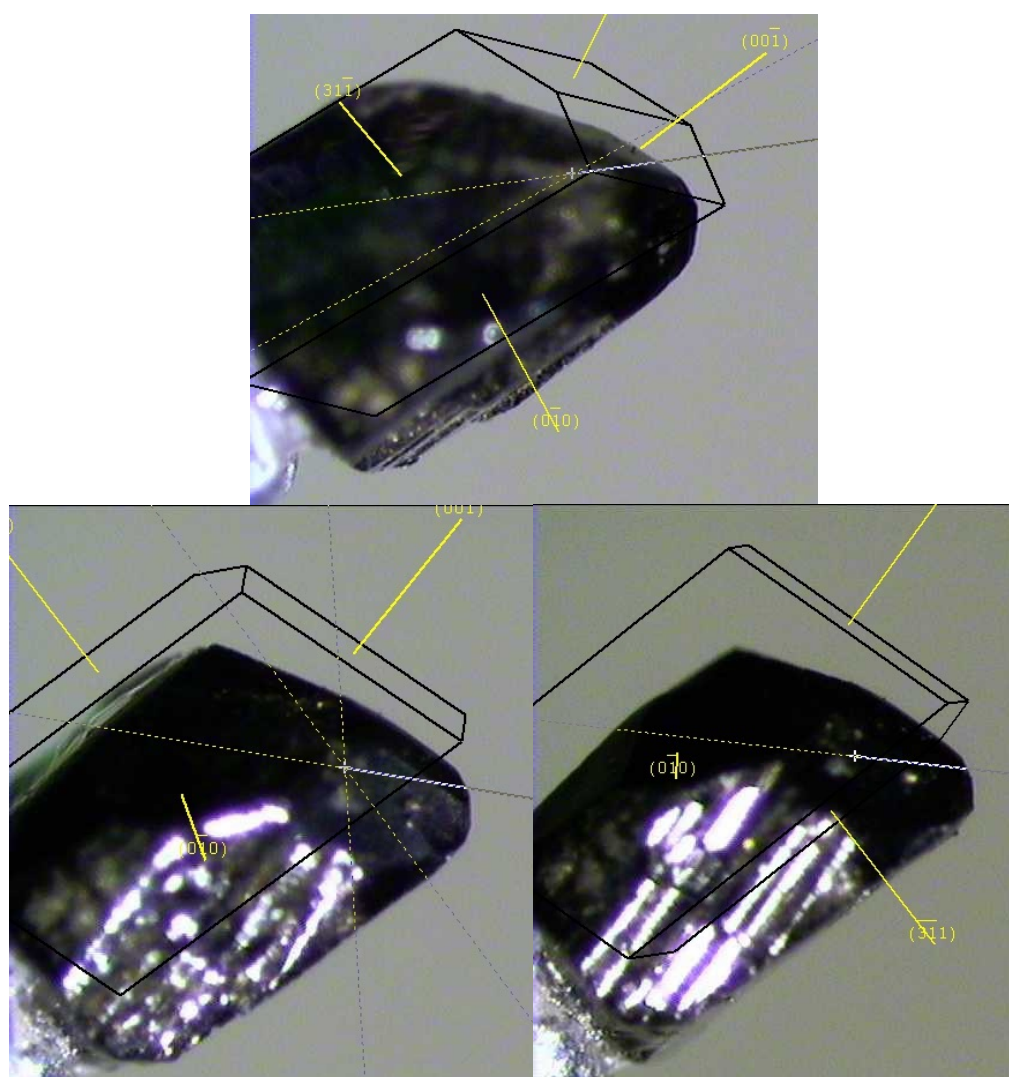


Figure 4.18: The orientation of the unpolished TiPO₄ single crystal SC1 with yellow lines indicating the lattice planes of the faces. I would like to thank Dr. J. Nuss for performing these x-ray measurements.

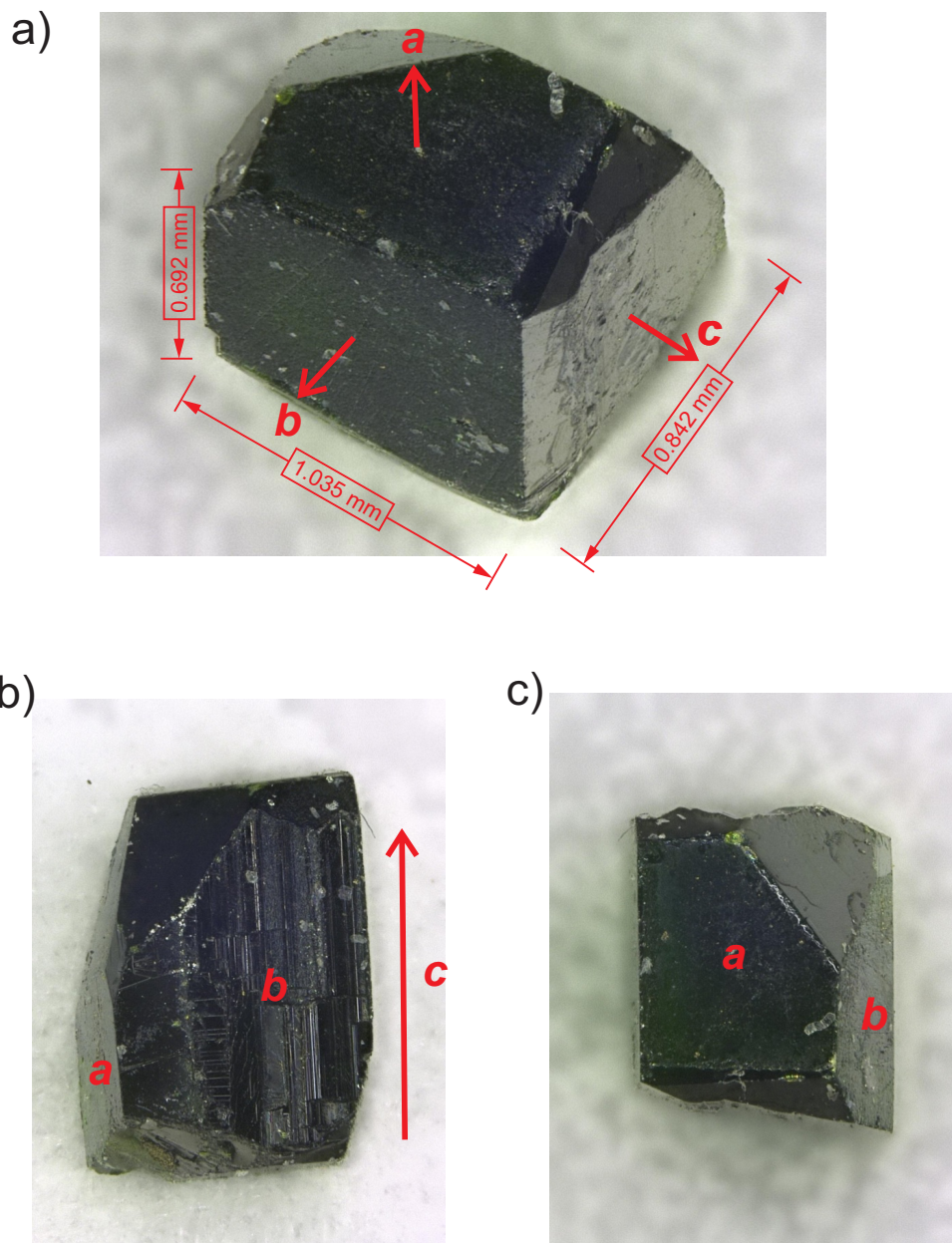


Figure 4.19: The orientation of the polished TiPO₄ single crystal SC1 a) The crystal had dimensions of 1.035 mm x 0.842 mm x 0.692 mm and a volume of 0.603 mm³. b) The growth of the crystal as **bc** planes along **a**-axis c) The unpolished **a**-axis of the crystal.

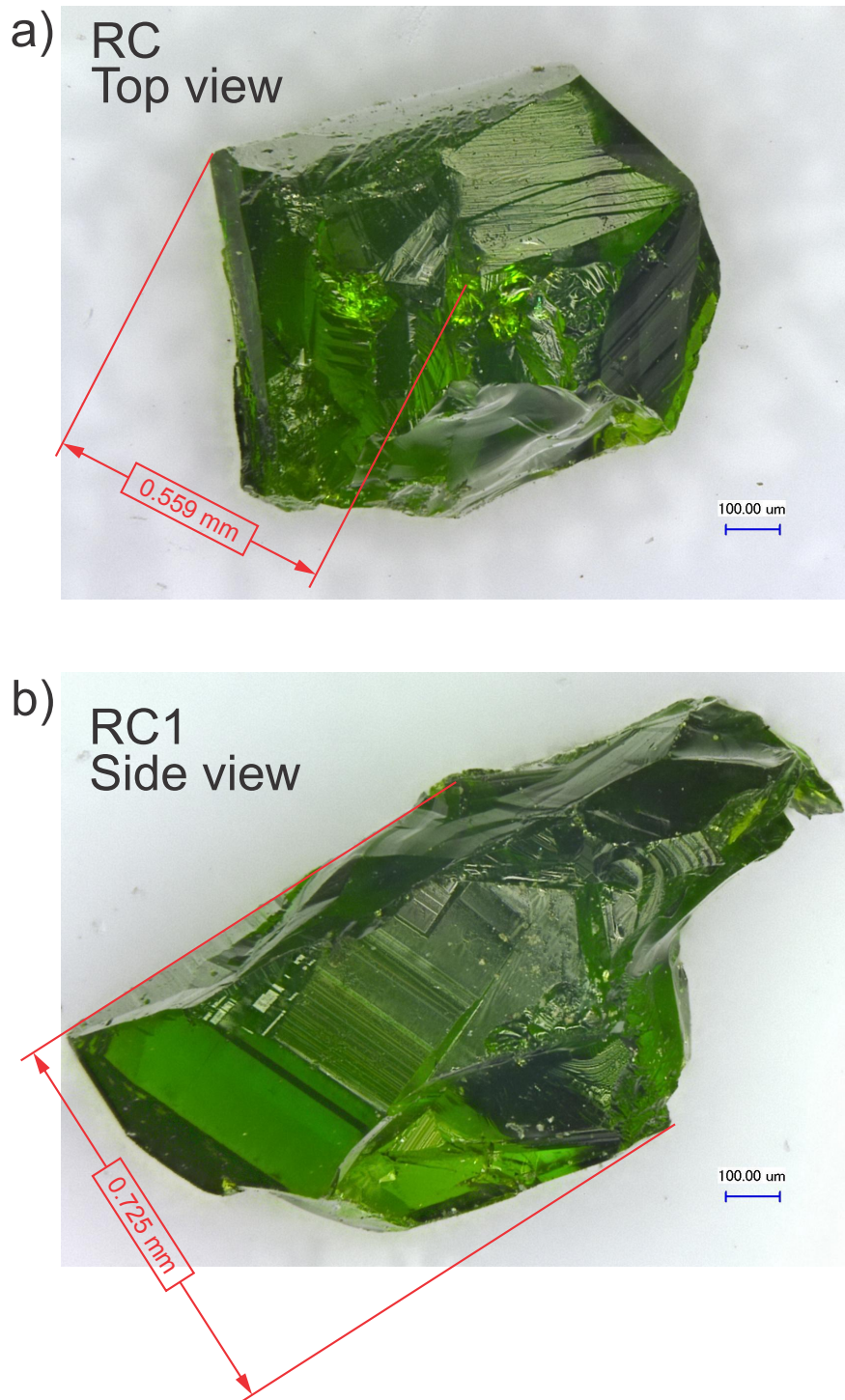


Figure 4.20: Images of TiPO_4 crystals RC and RC1 showing the thickness of crystals as determined by micrometer measurements. The red lines indicate the orientation, both perpendicular to the c -axis of the crystals, used for the thermal expansion measurements.

Two additional crystals of adequate size (see Figure 4.20) denoted as RC and RC1 from the same batch as SC1 were also selected and checked. These crystals turned out to be twinned only allowing thermal expansion measurements perpendicular to the c -axis. The placement of the TiPO_4 single crystal SC1 for determining the thermal expansion along the a -axis is depicted in Figure 4.21.

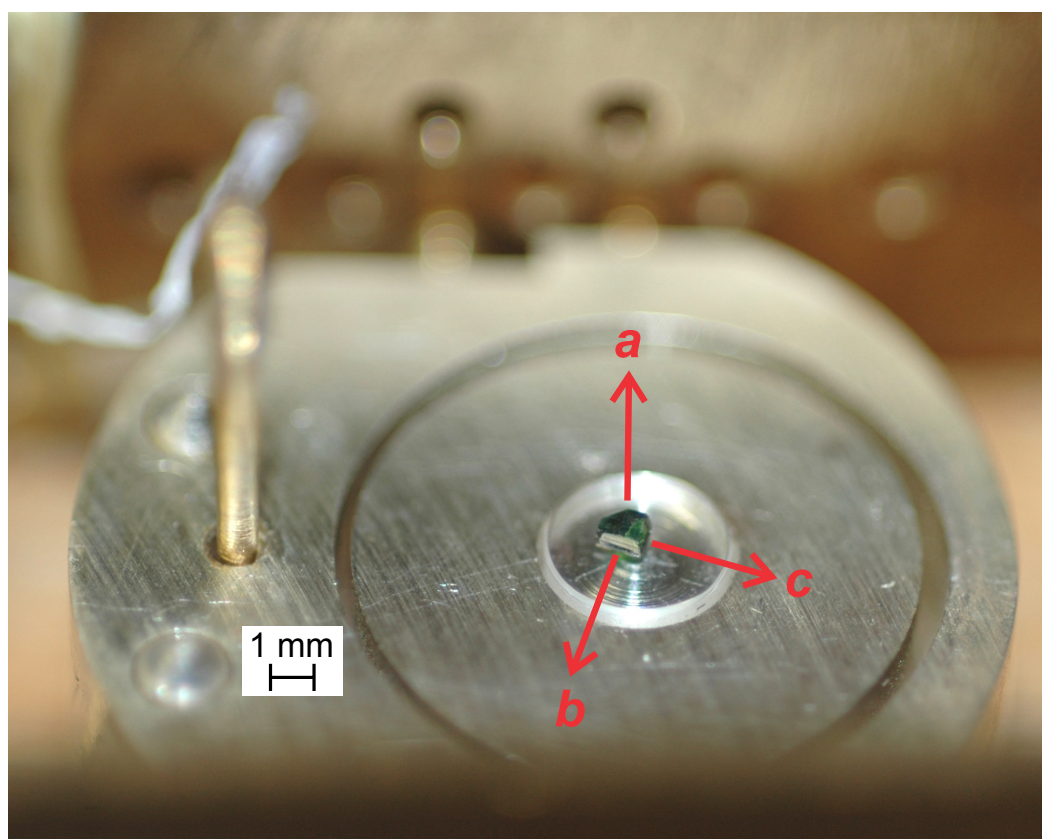


Figure 4.21: The placement of the TiPO_4 single crystal SC1 in the thermal expansion dilatometer cell for the measurement of the thermal expansion along the a -axis. The crystal is placed on a sapphire platform with a diameter of ~ 3 mm.

4.7 Results

4.7.1 Magnetization measurements

The magnetization measurements were conducted on three different TiPO_4 samples (PS1, PS2 and RC1). The temperature dependent magnetic susceptibility of the fine crystalline powders PS1 and PS2 were measured in a constant magnetic field of 0.3 Tesla whereas a magnetic field of 1 Tesla was used for the small crystal RC1. The raw magnetic susceptibility curves are presented in Figure 4.22(a). For PS1, a broad maximum occurs below $T_{c1} \approx 75$ K which was attributed to an unknown magnetic impurity of TiPO_4 . For PS2, the corrections for the diamagnetism of the closed shell electrons and the gelatin capsule as well as the paramagnetic impurities were performed. The results are displayed in Figure 4.22b. The diamagnetism of the closed shell electrons was calculated to be $-58 \times 10^{-6} \text{ cm}^3/\text{mol}$ from Selwood's Tables and this contribution must be subtracted.[149] The gelatin capsule's diamagnetic background is subtracted using a known reference curve. The 'Curie Tail' which is seen in all of the curves results from paramagnetic impurities. The Curie tail can be removed by first fitting the Curie-Weiss law to the low temperature susceptibility below T_{c1} as follows:

$$\chi_{imp}(T) = \frac{C_{imp}}{T - \theta_{imp}} + \chi_0 \quad (4.6)$$

where C_{imp} is the Curie constant, θ_{imp} is the Curie-Weiss temperature, χ_0 is a constant term. After subtracting the Curie tail, the resulting curve (see the red curve in Figure 4.22b) is nearly flat below T_{c1} consistent with a non-magnetic ground state.

High pressure magnetization measurements were performed on powders PS1 and PS2 at a constant magnetic field of 0.3 Tesla. The magnetization curves for temperatures between 50 K and 150 K are shown in Figure 4.23. The temperature dependent magnetic susceptibility curves exhibit a behaviour similar to the zero pressure (the gelatin capsule) measurements. The strong background of the pressure cell results in the smearing and the broadening of the transitions. However, the two transitions can clearly be discerned from the results.

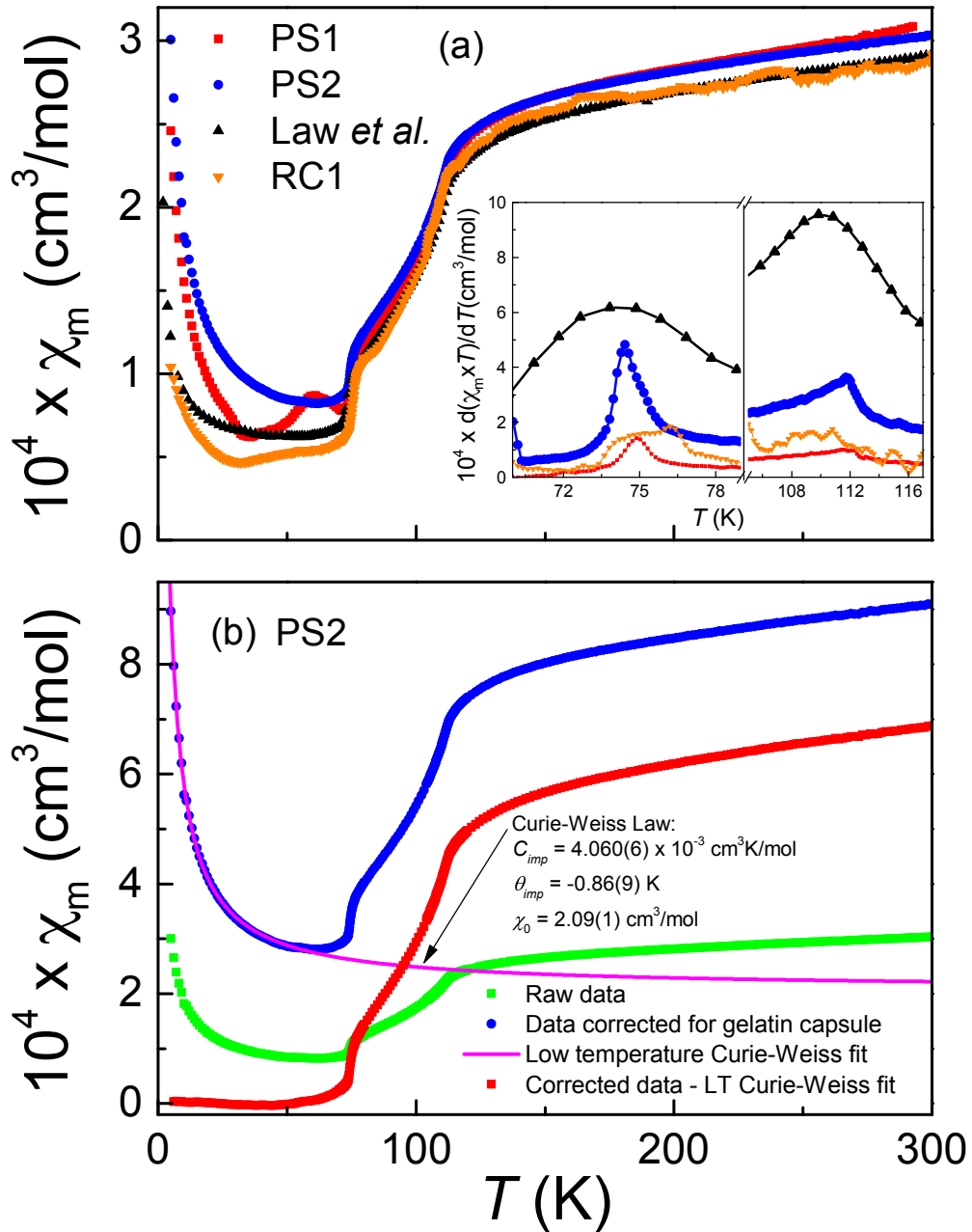


Figure 4.22: The temperature dependent molar magnetic susceptibility of the three TiPO₄ samples (PS1, PS2 and RC1) a) The uncorrected molar magnetic susceptibility curves of the three samples as well as the literature curve from Law *et al.* [24]. The inset highlights the derivatives of the magnetic susceptibilities near the phase transitions for the three different samples. b) The corrected molar magnetic susceptibility curve of PS2 showing the final curve in red.

Both transitions show a large positive shift exhibiting non-linear behaviour under pressure. The difference between the two transitions temperatures $T_{c2} - T_{c1} = 37(3)$ K remains roughly equal for all pressures consistent with the thermal expansion results (see Table 4.2 on p. 95).

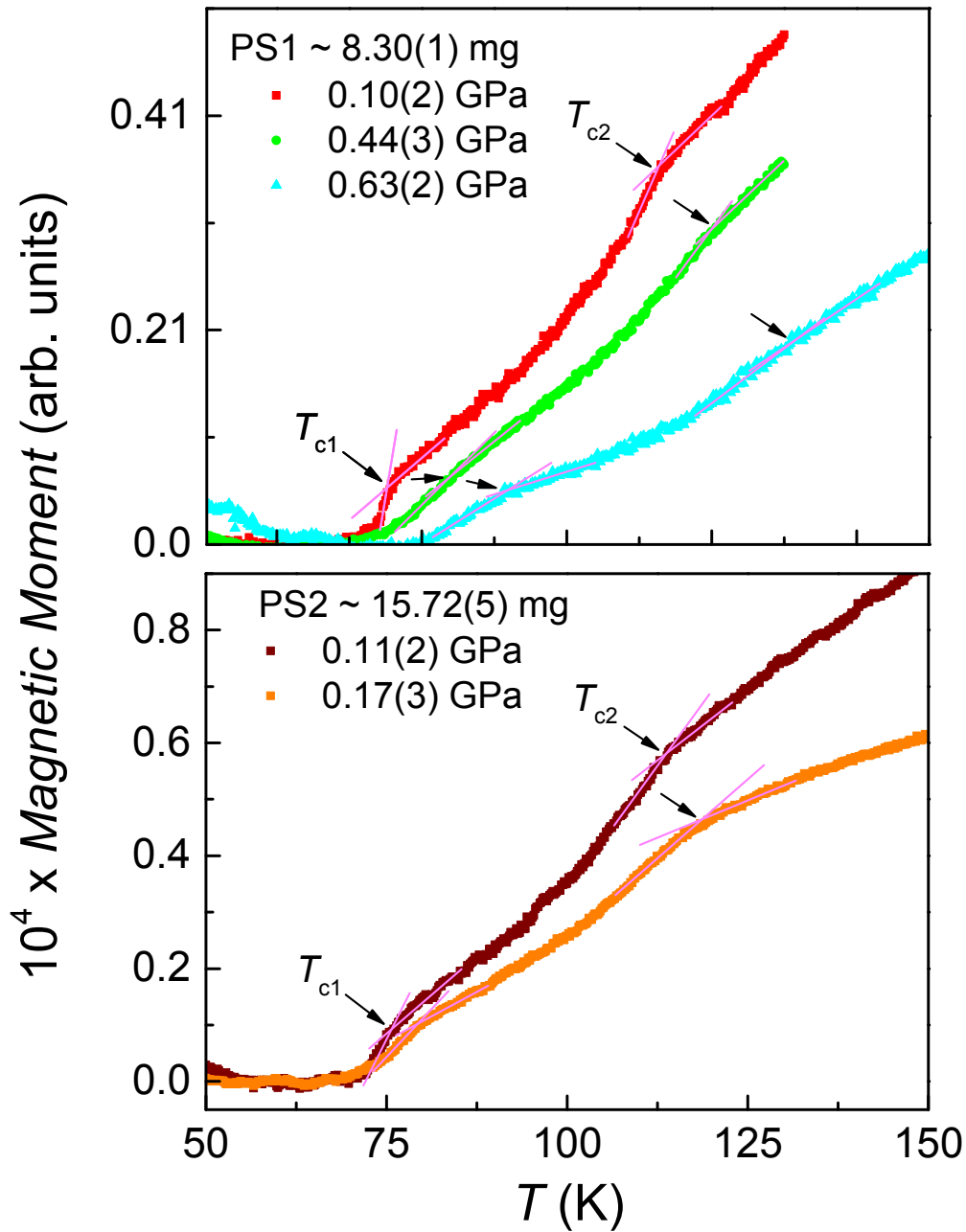


Figure 4.23: The temperature dependent magnetic susceptibility of the TiPO_4 fine crystalline powders PS1 and PS2 under pressure.

The pressure dependence of the transitions is presented in Figure 4.24. The slope of the data sharply increases after the pressure $P_1 \approx 0.6$ GPa by a factor of two to three for both transitions. T_{c1} and T_{c2} have a total shift of $+39(3)$ K / $+52(4)\%$ and $+42(5)$ K / $+37(5)\%$ respectively at 0.9 GPa. The pressure dependence of the transitions is similar for both samples (PS1 and PS2).

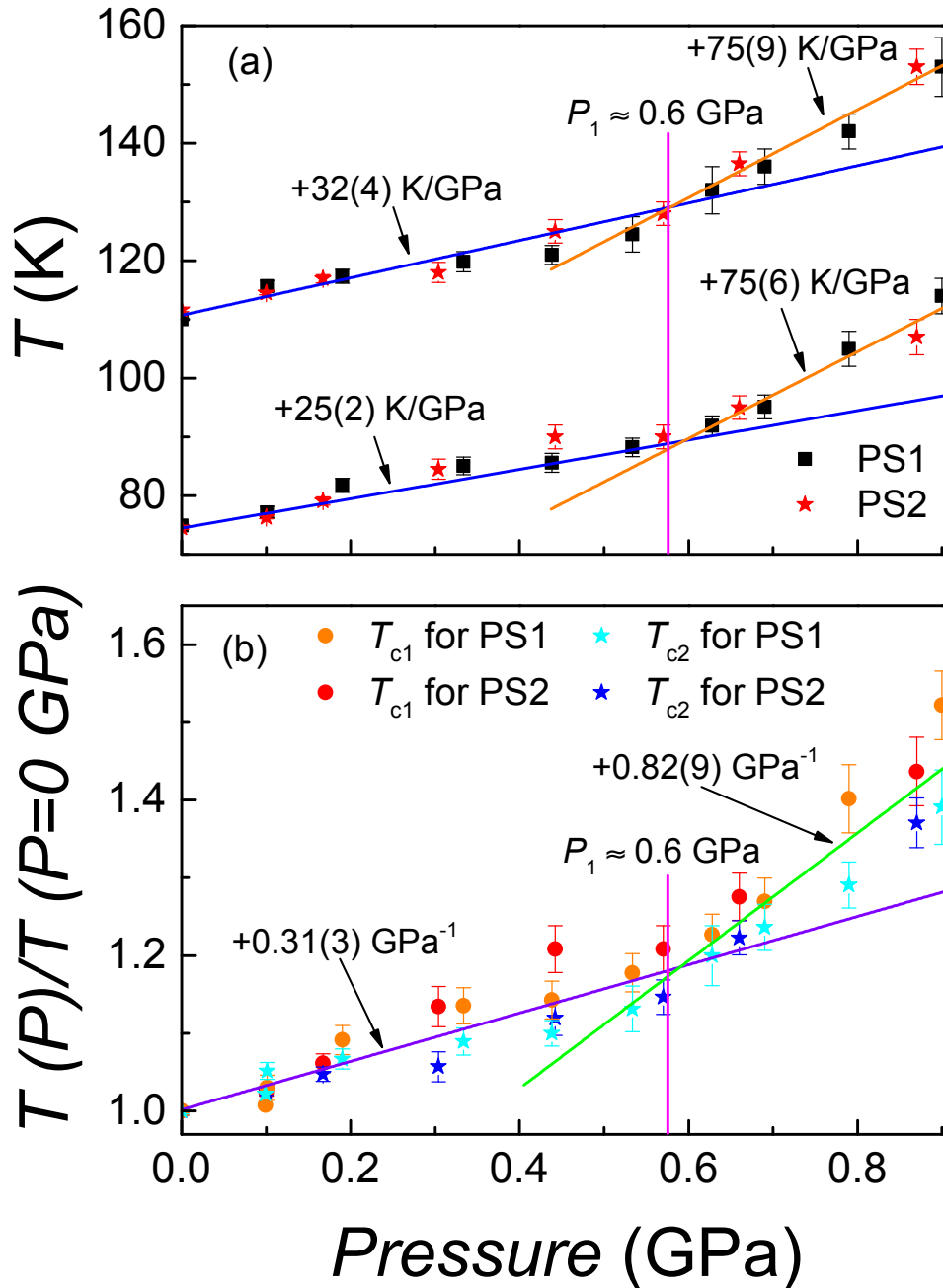


Figure 4.24: The pressure dependence of the two phase transitions (T_{c1} and T_{c2}) of TiPO_4 a) The raw results b) The normalized results.

4.7.2 Thermal expansion measurements

Initially, the thermal expansion along the c -axis of the TiPO_4 single crystal SC1 was studied. The measurements were performed by starting at 300 K and sweeping the temperature with a rate of 0.45 K/min down to 5 K (the cooling cycle). The temperature was subsequently swept at the same rate from 5 K to 300 K (the heating cycle). Figure 4.25 shows the two branches (cooling and heating) of the thermal expansion along the c -axis vs. temperature. The two transitions (T_{c1} and T_{c2}) are clearly visible near ~ 75 K and ~ 110 K which are in good agreement with the bulk magnetic and heat capacity data.[23, 24]

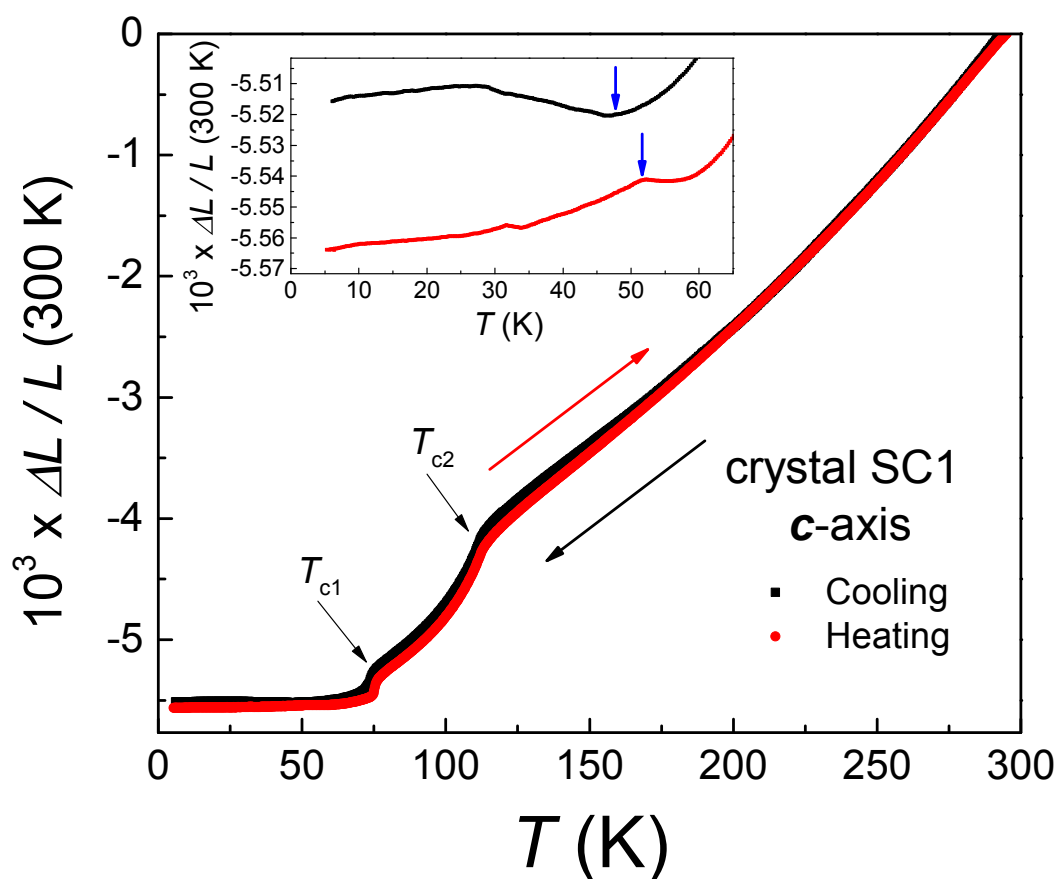


Figure 4.25: The temperature dependent length change along the c -axis relative to 300 K of the TiPO_4 single crystal SC1 with $H = 0$ Tesla. The data was measured by cooling from room temperature to 5 K followed subsequent heating to 5 K followed subsequent heating to room temperature. A sweeping rate of 0.45 K/min was utilized. The arrows in the inset point to the kinks in the curves observed near ~ 50 K.

At the two phase transitions, the length changes show pronounced anomalies. The lock-in transition at $T_{c1} \approx 75$ K from the dimerized low temperature spin-Peierls state to the incommensurately modulated intermediated phase exhibits a marked thermal hysteresis which characterizes it as a first order phase transition. At T_{c1} , the average linear coefficient of thermal expansion $\alpha_m(T)$ displays sharp spikes with different heights depending on the direction of the temperature change (see Figure 4.29 on p. 96). The sharp transitions allow the thermal hysteresis of the transition to be quantified precisely to 1.7(1) K. Measurements carried out at slower sweeping rates produced a somewhat smaller thermal hysteresis (≈ 1 K). $\alpha_m(T)$ at the second phase transition ($T_{c2} \approx 112$ K) has a notably different shape reminiscent of a λ -type anomaly which is characteristic of a second order phase transition. The small thermal hysteresis of 0.6(5) K observed for this phase transition results from the inherent noise of the data.

The c -axis exhibits a negative length change (contraction) with decreasing temperature over the complete temperature range down to ~ 50 K (see Figure 4.25). Below ~ 50 K, a very small ($\sim 0.2\%$) increase of the length change is seen in the cooling branch with a broad maximum. Following the broad maximum, the length decreases continuously resulting in a $\sim 0.1\%$ decrease in the length to 5 K. In contrast, the heating branch exhibits an increase in the length resulting in a kink at ~ 50 K. Following the kink, a shallow dip and subsequent monotonic increase occurs in the length thereafter. Whereas there is a contraction of the c -axis as the temperature decreases one observes an expansion perpendicular to the c -axis for the a and b axes. The magnitude of the expansion of the a and b axes is about five times smaller than the contraction along the c -axis leading to the overall contraction of the cell volume with decreasing temperature (see Figure 4.26). The temperature dependent volume change relative to 300 K is displayed in Figure 4.27. Below ~ 50 K, the contraction of the c -axis cannot compensate for the expansion of a and b axes resulting in a pronounced maximum in the volume change centred at ~ 29 K. At 29 K, the volume increases by 0.9% when compared to the volume at 60 K. The relative volume changes associated with the two phase transitions amounts to $\sim 7\%$ and $\sim 2.5\%$ for T_{c2} and T_{c1} respectively.

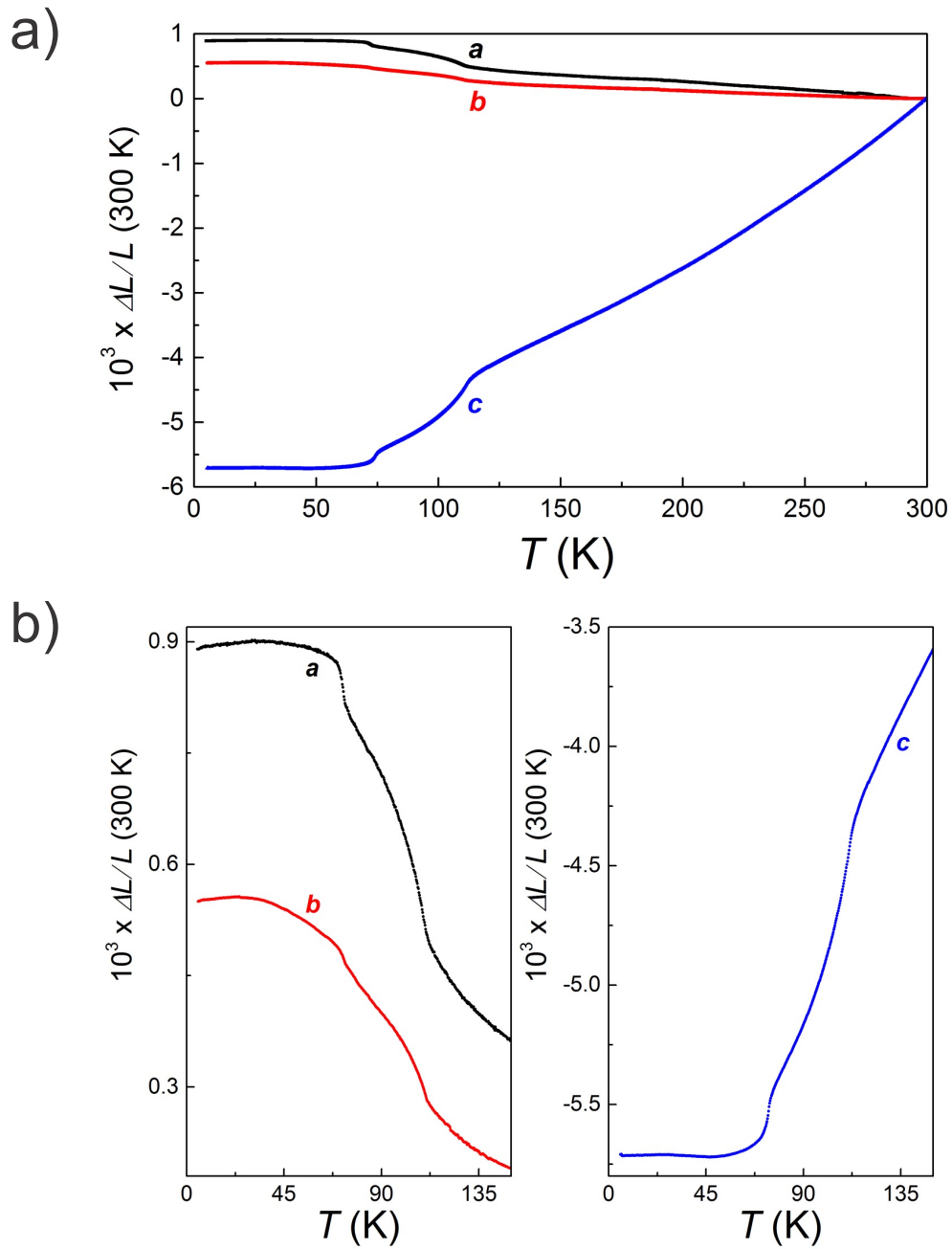


Figure 4.26: The zero magnetic field temperature dependent length change relative to 300 K along the *a*, *b* and *c* axes of the TiPO₄ single crystal SC1. (a) The temperature dependent length change relative to 300 K for the *a*, *b* and *c* axes (b) The enlarged view of the low temperature length change relative to 300 K for the *a*, *b* and *c* axes.

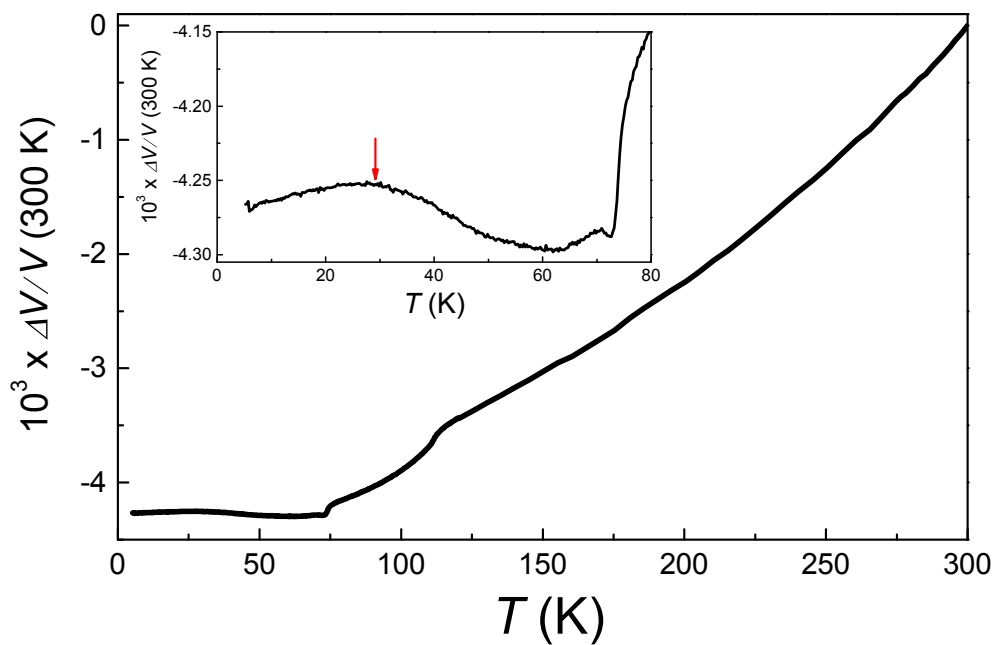


Figure 4.27: The zero magnetic field temperature dependent volume change relative to 300 K of the TiPO₄ single crystal SC1. The broad maximum in the volume change near ~ 29 K is indicated by the red arrow.

The average linear coefficient of thermal expansion $\alpha_m(T)$ curves for the three crystallographic axes (see Figure 4.28) are calculated using the data presented in Figure 4.26. The two phase transitions can clearly be distinguished for all of the $\alpha_m(T)$ curves. It is immediately noticeable that the transition temperatures depend on the orientation of the crystal within the dilatometer cell.

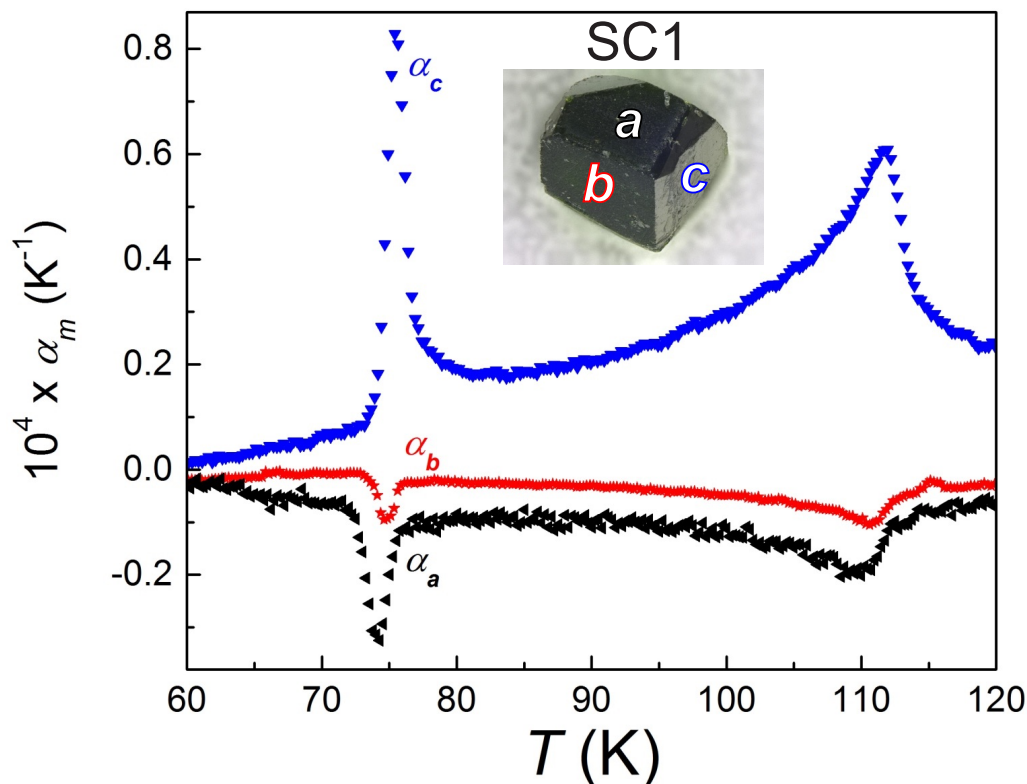


Figure 4.28: The zero magnetic field temperature dependent average linear coefficient of the thermal expansion $\alpha_m(T)$ along the **a**, **b** and **c** axes of the TiPO_4 single crystal SC1 showing the measured crystal. The thermal expansion was measured along the faces labeled in the inset picture.

The transition temperatures of T_{c1} and T_{c2} are presented in Table 4.2. Although the transition temperatures vary, the difference between the transition temperatures are constant within an experimental error of ± 0.5 K taken from the Gaussian fits. The slight variation of the transition temperatures is attributed to the pressure exerted on the crystal by the dilatometer cell.

Most importantly, the two transition (T_{c1} and T_{c2}) can clearly be distinguished for all of the $\alpha_m(T)$ curves. The T_{c1} transitions are sharp and well-defined while the T_{c2} transitions are significantly broader. The transition temperatures of T_{c1} and T_{c2} are obtained for three crystals by fitting the $\alpha_m(T)$ curves as discussed previously (see Table 4.2).

Orientation	T_{c1} (K)	T_{c2} (K)	T_{c2} (K) - T_{c1} (K)	Area
SC1				
<i>a</i>	74.01 ± 0.02	110.3 ± 0.6	36.3 ± 0.6	0.8715 mm^2
<i>b</i>	74.72 ± 0.02	111.4 ± 0.2	36.7 ± 0.2	0.7162 mm^2
<i>c</i>	75.49 ± 0.03	112.3 ± 0.2	36.8 ± 0.2	0.5827 mm^2
RC				
$\perp \mathbf{c}$	74.47 ± 0.02	111.9 ± 0.6	37.4 ± 0.6	—
RC1				
$\perp \mathbf{c}$	74.19 ± 0.01	111.7 ± 0.6	37.5 ± 0.6	—

Table 4.2: The zero magnetic field transition temperatures of T_{c1} and T_{c2} of three TiPO_4 crystals (SC1, RC and RC1) from heating cycle measurements. The transition temperature are determined by fitting the region containing the transition with a Gaussian. The force on the single crystal SC1 from the copper-beryllium spring of the dilatometer cell was applied across the area indicated. The calculated areas have an error bar of 0.0008 mm^2 . The area of crystals RC/RC1 is not available due to the irregular shape of the crystals.

Near the two phase transitions, the magnetic field dependence of the \mathbf{c} -axis thermal expansion was measured with a magnetic field of 9 Tesla applied perpendicular to the \mathbf{c} -axis for further comparison (see Figure 4.29). The measurements with an applied magnetic field of 9 Tesla are largely similar except a small field-induced downshift by $\sim 0.1 \text{ K}$ of the lock-in transition T_{c1} which will be analyzed in the next paragraph.

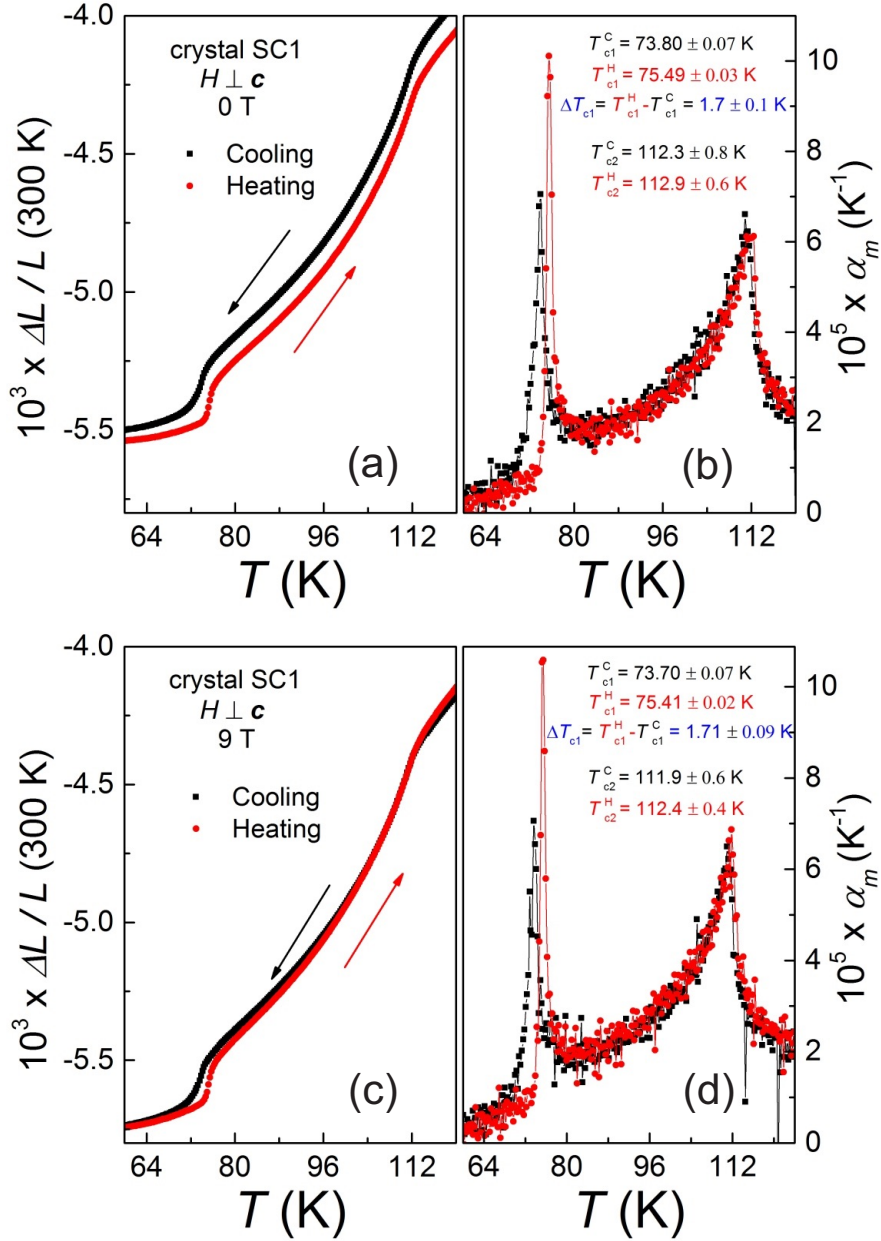


Figure 4.29: The thermal expansion measurements along c -axis of the TiPO₄ single crystal SC1 for the heating and the cooling cycles at 0 Tesla and 9 Tesla with $H \perp c$: (a) and (c) The length change relative to 300 K at 0 Tesla and 9 Tesla respectively and (b) and (d) The average linear coefficient of thermal expansion $\alpha_m(T)$ for the cooling and the heating cycles represented by the black and the red lines respectively. $\alpha_m(T)$ is obtained by taking the numerical derivatives of the curves on the left with temperature intervals of ~ 0.2 K. The precise transition temperatures are obtained by fitting a Gaussian to the anomalies in the $\alpha_m(T)$ curves. The lines used for the $\alpha_m(T)$ curves are a guide to the eyes.

In order to quantify the magnetic field dependence of the two phase transition temperatures, temperature scans were performed at various fixed magnetic fields up to 9 Tesla. The same temperature protocol was used for all the temperature scans. Due to the small magnitude of the transition temperature shifts, special care had to be taken for the magnetic field corrections of the Cernox temperature sensors calibration tables. In total, the magnetic field dependence of the two transitions were probed for three crystals. The results of the temperature scans near the two transitions at 0 Tesla and 9 Tesla is presented in Figure 4.30. The shift of the two transitions were quantified by fitting Gaussian functions to the data region containing the transitions. It can clearly be seen that only T_{c1} downshifts ($\Delta T_{c1} \approx 0.08$ K) at 9 Tesla whereas a magnetic field of 9 Tesla had a negligible effect on T_{c2} . The narrow anomalies in the average linear coefficient of thermal expansion $\alpha_m(T)$ for the lock-in transition at T_{c1} allowed its field dependence to be followed in detail. The field-induced downshift of T_{c1} was quantified using aforementioned fitting method. The field corrected results for all Gaussian fits are tabulated in Table 4.3. The results were then used to calculate the left and the right side of Equation 4.5 (see p. 65). The right side of the equation was calculated with the Landé g-factor¹⁸ of 1.94(1). Using the rules of the error propagation[150], the error bars for the left side (LS) and the right side (RS) of Equation 4.5 were calculated using the following equations:

$$\sigma(LS) = \frac{T_{c1}(H) + C}{T_{c1}(0)} \left(\frac{\sigma(T_{c1}(H)) + \sigma(C)}{|T_{c1}(H) + C|} + \frac{\sigma(T_{c1}(0))}{|T_{c1}(0)|} \right) \quad (4.7)$$

$$\sigma(RS) = \left(\frac{g\mu_B H}{2k_B T_{c1}(0)} \right)^2 |2| \left(\frac{\sigma(T_{c1}(0))}{|T_{c1}(0)|} + \frac{\sigma(g)}{|g|} \right) \quad (4.8)$$

where $C = -2.1 \times 10^{-7}$ K · Oe⁻¹ and $\sigma(C) = 0.1 \times 10^{-8}$ K · Oe⁻¹ correspond to the field correction coefficient (i.e. $T(H) = C \cdot T(0)$) and the error of the field correction coefficient respectively. The parameter η was obtained (see Figure 4.33 on p. 104) by fitting each data set to a straight line forcing the y-intercept to zero.

¹⁸The Landé g-factor in Equation 4.5 was calculated from the electronic paramagnetic resonance spectroscopy results obtained by Law *et al.* [23].

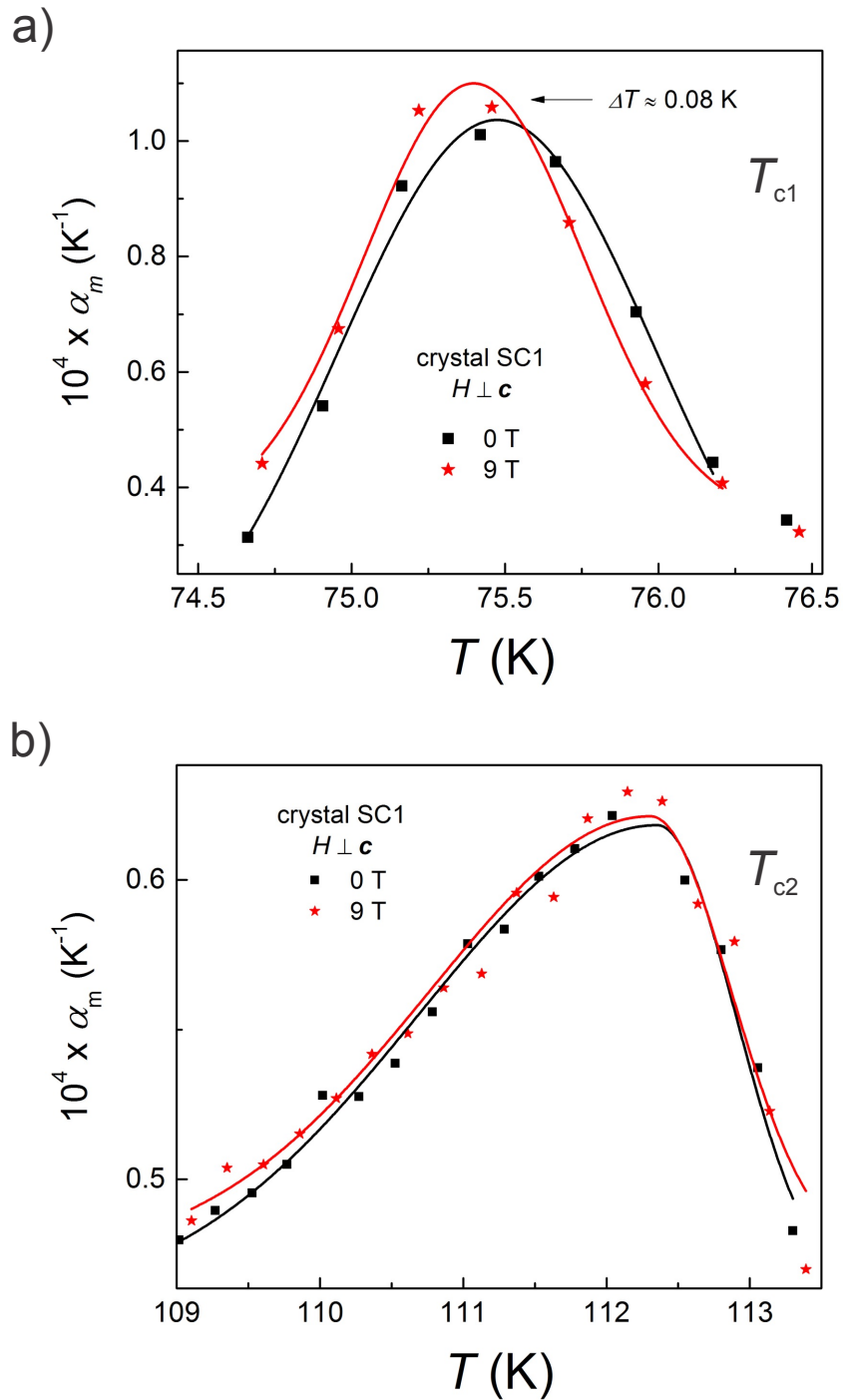


Figure 4.30: The 0 Tesla and 9 Tesla average linear coefficient of thermal expansion $\alpha_m(T)$ curves of the TiPO_4 single crystal SC1 ($H \perp c$) near the T_{c1} and the T_{c2} transitions. Gaussians (the solid lines) are fitted to the curves in order to obtain the transition temperatures. A single Gaussian function is fitted to T_{c1} whereas T_{c2} is fitted using a Bigaussian function instead.

Table 4.3 compiles the results for the downshifts of the lock-in transition observed in three TiPO_4 crystals.

Crystal	Orientation	$T_{c1}(0 \text{ Tesla})$	$T_{c1}(9 \text{ Tesla})$	ΔT_{c1}
SC1	$H \perp \mathbf{c}$	$75.49 \pm 0.03 \text{ K}$	$75.40 \pm 0.03 \text{ K}$	$90 \pm 60 \text{ mK}$
SC1	$H \perp \mathbf{c}$	$73.85 \pm 0.08 \text{ K}$	$73.75 \pm 0.06 \text{ K}$	$100 \pm 100 \text{ mK}$
RC	$H \parallel \mathbf{c}$	$74.47 \pm 0.01 \text{ K}$	$74.38 \pm 0.01 \text{ K}$	$90 \pm 40 \text{ mK}$
RC1	$H \parallel \mathbf{c}$	$74.19 \pm 0.01 \text{ K}$	$74.10 \pm 0.01 \text{ K}$	$90 \pm 20 \text{ mK}$

Table 4.3: The downshift of the T_{c1} lock-in transition temperature in three TiPO_4 crystals (SC1, RC and RC1)

Figure 4.31 displays the thermal expansion results of two crystals (denoted RC and RC1). Crystals RC and RC1 were measured to confirm the results obtained on the single crystal SC1 which cracked after several temperature cycles. The crystals RC1 and RC2 were significantly smaller than the single crystal SC1 and twinned such that only the length changes perpendicular to the \mathbf{c} -axis were accessible.

The effect of the magnetic fields can also be seen as a field-induced magnetostriction. Applying magnetic fields ($H \perp \mathbf{c}$) induces a noticeable magnetostriction in the temperature regime between $\sim 75 \text{ K}$ and $\sim 150 \text{ K}$ which is displayed in Figure 4.32 for 4.5 Tesla and 9 Tesla. The magnetostriction vs. temperature is non-monotonic with the dominant contribution ($\sim 60\% - 70\%$) occurring below the second phase transition at T_{c2} when the incommensurate phase is entered. At low temperatures, the magnetostriction is $\sim 10\%$ larger at 4.5 Tesla as compared to the 9 Tesla data. At both magnetic field, the derivatives of the magnetostriction with respect to temperature exhibit broad anomalies in the same temperature region as T_{c1} and T_{c2} (see Figure 4.32). The anomalies exhibit maxima centred near $\sim 85 \text{ K}$ to $\sim 90 \text{ K}$. These results imply that the magnetic fields have a pronounced effect on the incommensurate magnetic phase.

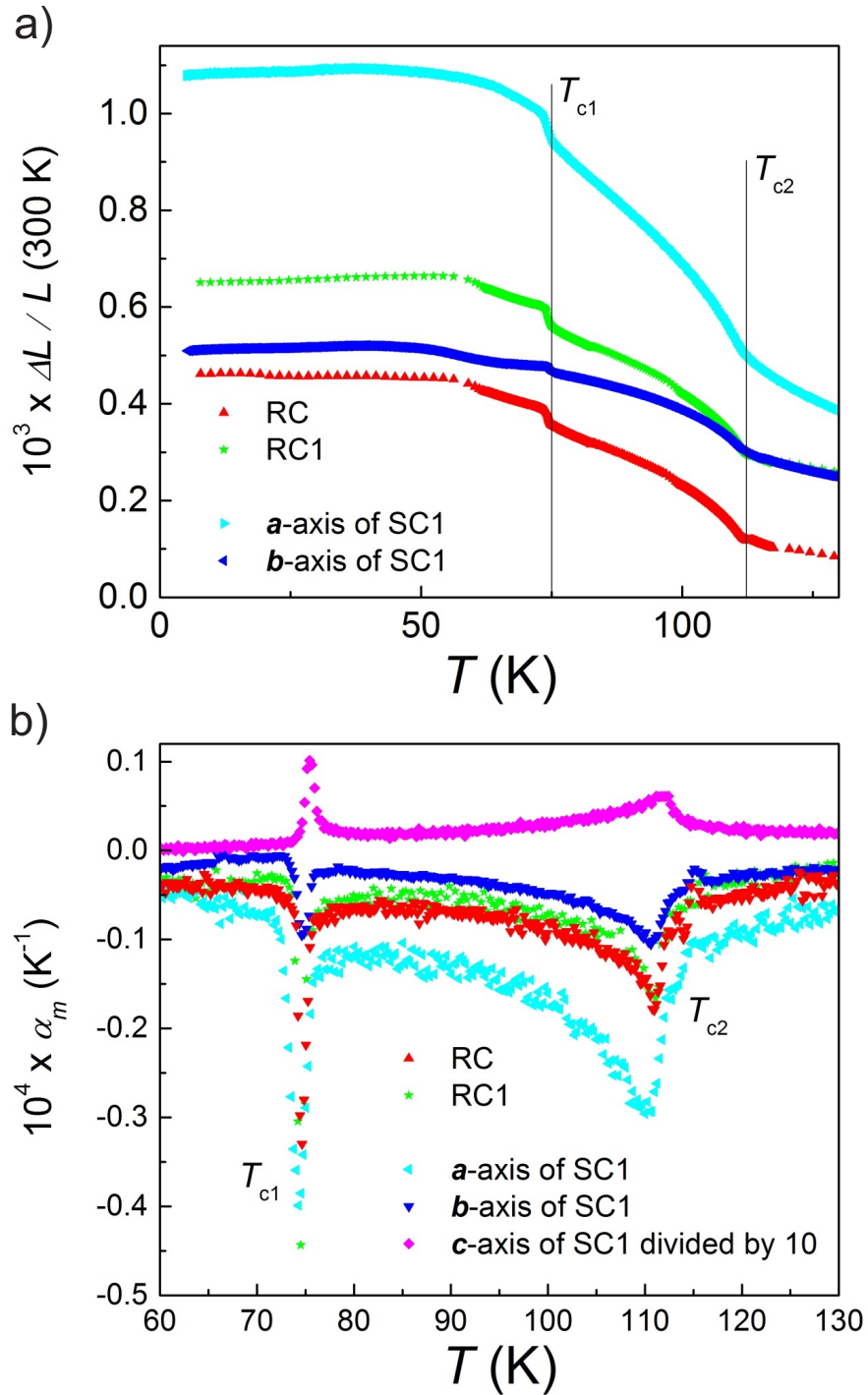


Figure 4.31: The temperature dependent length change relative to 300 K and the average linear coefficient of thermal expansion $\alpha_m(T)$ of the TiPO₄ crystals RC and RC1 with $H = 0$ Tesla. The results for crystals RC and RC1 are compared to the thermal expansion data of the single crystal SC1.

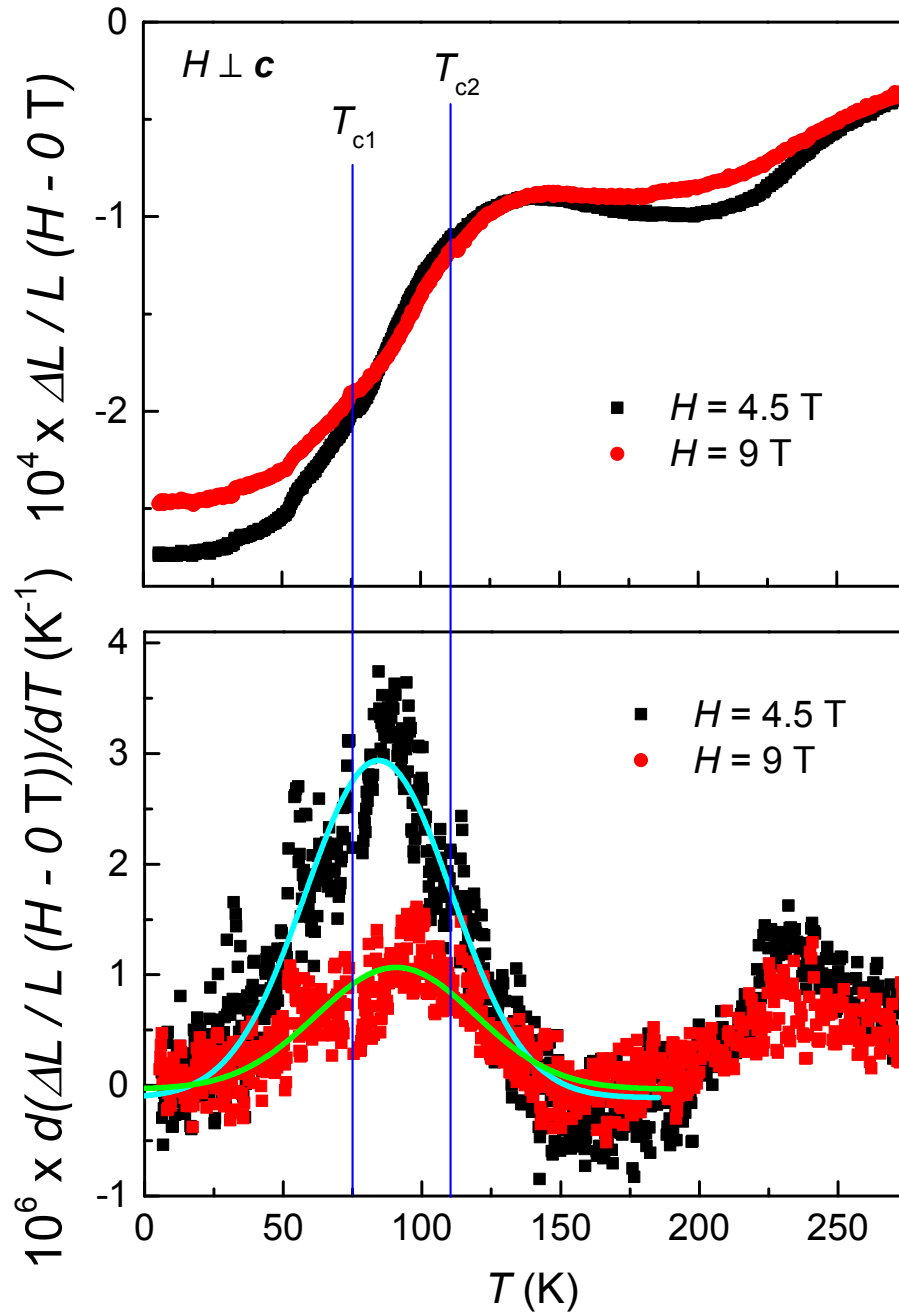


Figure 4.32: The magnetostriction vs. temperature and its derivative with respect to temperature of the TiPO_4 single crystal SC1 showing the magnetostriction observed at 4.5 Tesla and 9 Tesla with $H \perp c$. N.B. $\frac{\Delta L}{L}(H - 0 \text{ T}) = \frac{\Delta L}{L}(300 \text{ K})_H - \frac{\Delta L}{L}(300 \text{ K})_{0 \text{ T}}$. The solid lines are Gaussians used as a guide to the eyes.

4.8 Discussion

The temperature dependent magnetic susceptibility curves of the TiPO_4 samples are very similar to the results obtained by Law *et. al.* [24]. However, the derivative of the susceptibility with respect to the temperature indicate significantly sharper anomalies at T_{c1} and T_{c2} than observed by Law *et. al.* Under pressure, the transition temperatures of T_{c1} and T_{c2} increased exhibiting behaviour similar to other spin-Peierls compounds (see Table 4.4).

Compound	$T_{sp}(0 \text{ GPa})$	$\Delta T_{sp}/\Delta P$ (K/GPa)	Ref.
TTF-CuBDT	12 K	$P \leq 0.6 \text{ GPa}$: -1.8	[113]
MEM-(TCNQ) ₂	18 K	$P \leq 0.34 \text{ GPa}$: +20.0	[134]
CuGeO ₃	14 K	$P \leq 1.2 \text{ GPa}$: +4.8	[137]
TiOCl	$T_{c1} \simeq 66 \text{ K}$	$P \leq 1.0 \text{ GPa}$: +19.2	[138]
	$T_{c2} \simeq 91 \text{ K}$	$P \leq 1.0 \text{ GPa}$: +33.3	
TiOBr	$T_{c1} \simeq 28 \text{ K}$	$P \leq 0.6 \text{ GPa}$: +36.8	[139]
TiPO_4	$T_{c1} \simeq 75 \text{ K}$	$P \leq 0.6 \text{ GPa}$: +25(2) $0.6 < P \leq 0.9 \text{ GPa}$: +75(6) Total Shift at 0.9 GPa: +43(3)	this work
	$T_{c2} \simeq 110 \text{ K}$	$P \leq 0.6 \text{ GPa}$: +32(4) $0.6 < P \leq \text{GPa}$: +75(9) Total Shift at 0.9 GPa: +47(6)	

Table 4.4: The total shift of the spin-Peierls transition temperature(s) under pressure for various spin-Peierls compounds

In contrast to theory as well as other spin-Peierls compounds, the increase in the transition temperatures with pressure in TiPO_4 appears to be nonlinear over the measured pressure range up to $\approx 1 \text{ GPa}$. The pressure dependence of the transitions is linear below 0.6 GPa with a slope of approximately +27 K/GPa. Above 0.6 GPa, the pressure dependence remains linear but the slope doubles or triples with a value of +75 K/GPa. This is the steepest pressure dependence observed so far in a spin-Peierls compound. This behaviour indicates that a high pressure anomaly occurs around 0.6 GPa. Additional pressure cycling measurements were performed and the results indicated that the high pres-

sure phase is fully reversible. The total shift of the transition temperatures is approximately 30 to 40% larger than that observed in TiOX (X = Cl and Br).[138, 139] Overall, the sizable pressure effect on the transition temperatures can be ascribed to a strong positive pressure dependence of the spin exchange couplings. The high pressure anomaly may result from structural distortions in the chains which could significantly increase the intrachain spin exchange interaction. Additional high pressure measurements must be performed in order to clarify the high pressure crystal structure of TiPO₄.

Above 100 K, the thermal expansion measurements are consistent in terms of magnitude and anisotropy with the temperature dependent lattice parameters obtained by Law [23]. In contrast to Law's data, the measurements indicate a significant change of the cell volume which has not been previously observed. The measurements distinctively reveal the lattice changes associated with the two phase transitions at T_{c2} from the one-dimensional antiferromagnetically correlated state to the structurally incommensurate state and at T_{c1} to the lock-in dimerized spin-Peierls ground state. The shape of the average linear coefficient of thermal expansion $\alpha_m(T)$ near the phase transitions and their thermal hysteresis behaviour allows an unambiguous identification of the transitions (T_{c1} and T_{c2}) as first and second order phase transitions respectively.

Standard spin-Peierls theories make qualitative predictions (see Section 4.3.4 on p. 64) concerning the magnetic field dependence of the transition temperature. A downshift in the spin-Peierls transition proportional to the square of the applied magnetic field is expected for small fields such that the Zeeman energy is small compared to the spin gap Δ . Upon first inspection, the lock-in transition temperature shows a notable shift with magnetic field. However, the shifts are found to be considerably smaller than the expected magnitude according to the standard theory. For the transition T_{c2} from the paramagnetic to the incommensurate state, the downshift appears to be smaller or even negligible. The effect of the applied magnetic field on the two phase transitions is shown in Figure 4.30 on p. 98. The detailed magnetic field dependence of the lock-in transition temperature is tabulated in Table 4.3 on p. 99 and illustrated in Figure 4.33. Figure 4.33 displays the relative downshifts $\Delta T_{c1}/T_{c1}$ of the lock-in transition temperature vs. the square of the applied magnetic field.

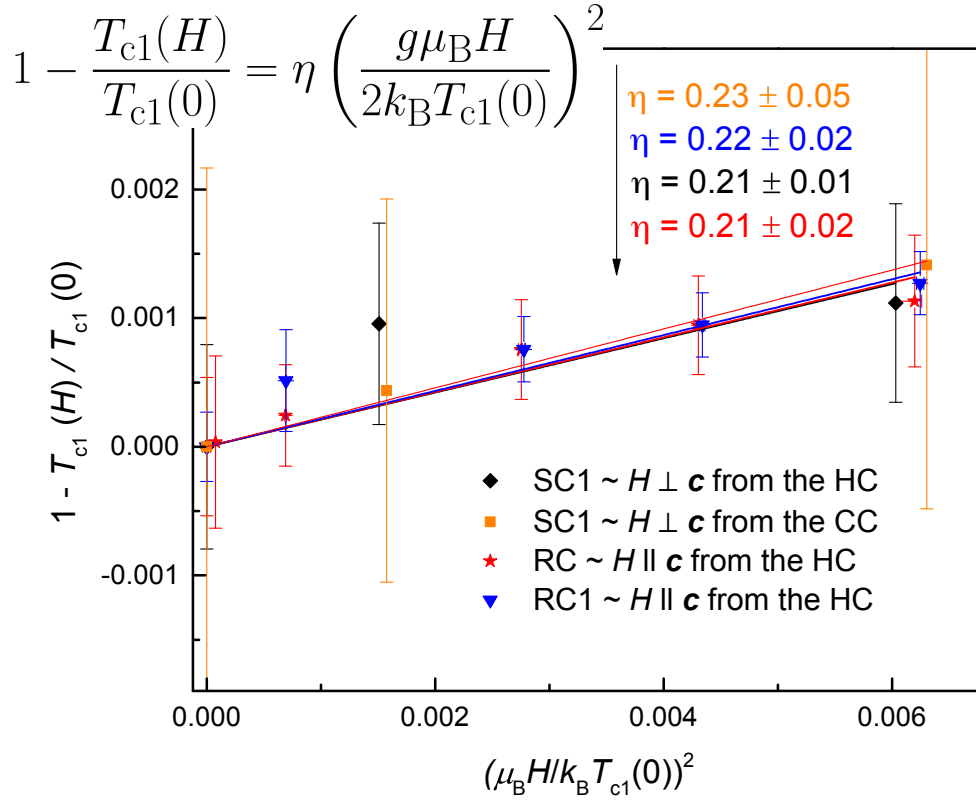


Figure 4.33: The quadratic magnetic field dependence of the lock-in transition T_{c1} for three TiPO_4 crystals using Equation 4.5 on p. 65 with a Landé g -factor of 1.94(1) and a maximum applied magnetic field of 9 Tesla. HC and CC denotes the heating and the cooling cycles respectively. The error bars along the horizontal axis are of the order of 10^{-6} and smaller than the symbols used.

The downshift of T_{c1} induced by a magnetic field of 9 Tesla amounts to ~ 90 mK. Within experimental errors, the downshifts are $\propto H^2$ with a significantly smaller coefficient η than predicted by standard spin-Peierls theory. The coefficient η does not depend on magnetic field orientation. Its values range between 0.21(2) to 0.23(5). From the measurements on three different crystals, the average η coefficient denoted as $\bar{\eta}$ was calculated to be 0.22(1). Table 4.5 contains a comparison of the coefficient η for several spin-Peierls compounds. From Table 4.5, the coefficient $\bar{\eta}$ for TiPO_4 is a factor of two smaller than the coefficient predicted by standard spin-Peierls theory ($\eta_{\text{Th}} = 0.36 - 0.44$) [126, 131, 132]. It comes close to the values observed for more exotic spin-Peierls compounds, such as $\text{MEM}(\text{TCNQ})_2$ or α' - NaV_2O_5 for which charge ordering occurs concurrently with the spin-Peierls transition.[119] TiPO_4 is only the second compound found which exhibits two sequential phase transitions after TiOX ($X = \text{Cl}, \text{Br}$). An explanation for the reduced coefficient η may also result from the non-standard character of the two-stage spin-Peierls transition in TiPO_4 .

Compound	$T_{sp}(0)$	η	References
α' - NaV_2O_5	35.0 K	0.072(8) – 0.093	[151], [152] and [153]
$\text{MEM}(\text{TCNQ})_2$	17.55 K	0.137(1)	[154]
TTF-CuBDT	12.0 K	0.38	[133]
CuGeO_3	14.0 K	0.46 – 0.50	[20], [125] and [155]
TTF-AuBDT	2.0 K	0.92(3)	[156]
TiPO_4	~ 75.0 K	0.22(1)	this work

Table 4.5: The coefficient η of the quadratic magnetic field dependence for TTF-CuBDT, $\text{MEM}(\text{TCNQ})_2$, TTF-AuBDT, CuGeO_3 and α' - NaV_2O_5 obtained from various measurement techniques.

The anisotropy of the relative lengths changes is sizeable and can be used to provide more insight into the microscopic structural processes involved in the two sequential phase transitions in TiPO_4 . The most pronounced and dominant feature of anisotropy is the contraction along the Ti chains (c -axis) upon cooling. The contraction results from the dimerization of the Ti atoms which below the lock-in transition leads to a commensurate superstructure. The length changes perpendicular to the Ti chains are negative i.e. the crystal expands along the a and the b axes upon cooling. The magnitude of the expansion perpendicular to the chains is approximately five times smaller than contraction along the chains. It is also apparent that the contraction associated with the two phase transitions exhibits varying behaviour. The majority of the length contraction results from the onset of dimerization at T_{c2} and amounts to $\sim 80\%$ of the total contraction (see Figure 4.34). This finding strongly supports the crystallographic structure data which concluded that the intermediate incommensurate phase has three energetically almost degenerate structures. All three structures comprise partially dimerized Ti chains. The intermediate phase results from a fluctuation between the energetically similar structures.

The magnetostriction measurements exhibit intriguing anomalies in the temperature range enclosed by T_{c1} and T_{c2} . A peaked anomaly occurs in the derivative of the magnetostriction with respect to temperature with the anomaly in the 4.5 Tesla data being larger than that of the 9 Tesla data. These anomalies are centred at 85 ± 7 K in the incommensurate phase with a broad width of ~ 55 K. As the DFT calculations have demonstrated, the region where the anomalies are observed can be characterized by three fluctuating slightly different low temperature crystal structures. The three crystal structures have energies differing by less than 1 meV. The Zeeman energy induced by the external magnetic fields is comparable to this energy differences. The observed response of the lattice to the magnetic fields indicates a sensitive magnetoelastic scenario. Tentatively, the observed magnetostriction can be assigned to the magnetic field affecting the fluctuation between the three possible intermediate phases. Additional directionally dependent magnetostriction experiments are planned to confirm this conjecture and to discern whether metastable states can be frozen in the incommensurate regime.

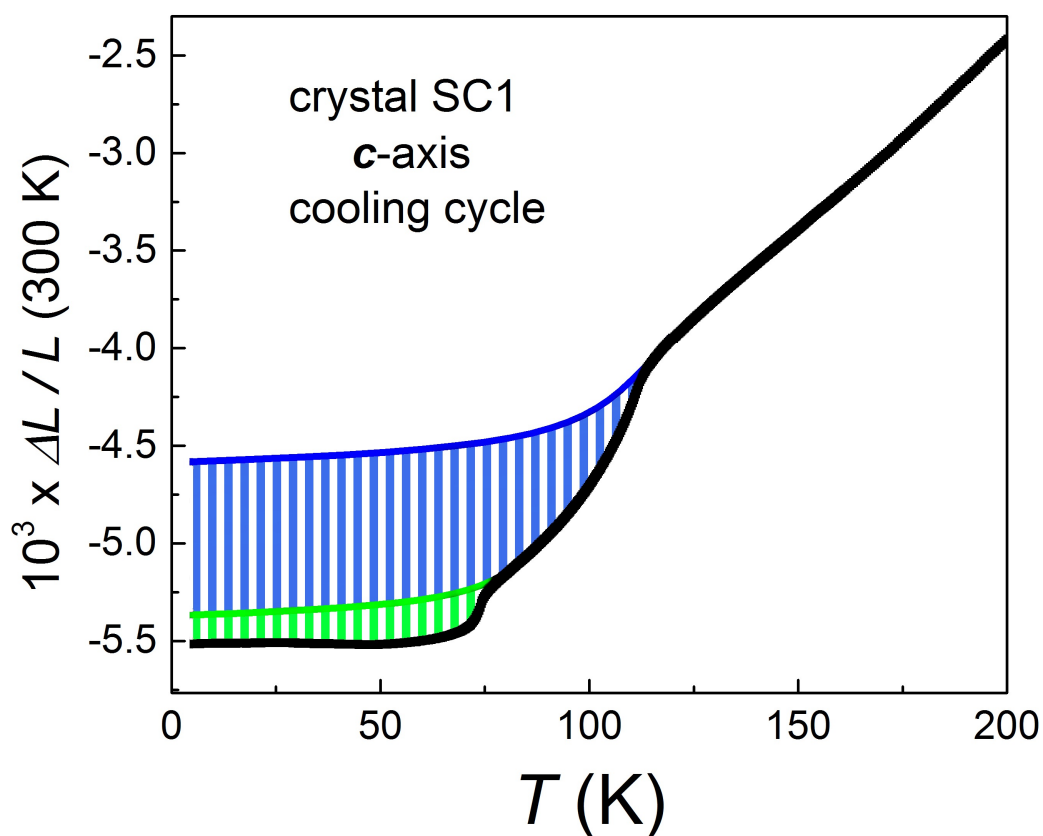


Figure 4.34: The zero magnetic field temperature dependent length change along the c -axis relative to 300 K of the TiPO_4 single crystal SC1 showing the two contraction regions in green and blue stripes associated with the phase transitions T_{c1} and T_{c2} respectively.

The low temperature transition into the commensurate lock-in phase involves the regular arrangement of fully dimerized chains along the directions perpendicular to the Ti chains. The connectivity between such dimerized chains is mediated by the fairly rigid PO_4 tetrahedra whose oxygen atoms comprise the environment of the Ti atoms. Steric hindrance effects from the relatively rigid PO_4 tetrahedra can be concluded from an examination of the O - P - O bonding angles and the P - O distances which remain rather unaffected by the phase transitions¹⁹. Consequently, the interchain response to the Ti - Ti dimerization are moderated by the O - P - O connections involving the rather rigid PO_4 tetrahedra. This scenario can explain the much smaller lattice response perpendicular to the Ti chains. A re-adjustment in the orientation of the PO_4 groups may also be the cause of the slight volume increase observed below ~ 60 K with decreasing temperature. The expansion along the \mathbf{a} -axis provides the dominant contribution to the total volume increase. Small secondary steric effects from the rigid PO_4 units may also explain the minute expansion along the Ti chains.

The high pressure magnetization results clearly indicated that the two phase transitions increased with hydrostatic pressure. This behaviour was also observed in the thermal expansion results for small uniaxial pressures. The \mathbf{a} -axis measurement had the lowest transition temperatures and the largest contact area (see Table 4.2) hence the lowest possible pressure. In contrast, the \mathbf{c} -axis measurement had the highest transition temperatures and the lowest contact area (see Table 4.2) hence the highest possible pressure. The \mathbf{b} -axis measurement had transition temperatures and a contact area in between that of the \mathbf{a} and \mathbf{c} axes measurements. The shifts in the transition temperatures T_{c1} and T_{c2} under the varying uniaxial pressure for the axes are 1.48(5) K and 2.0(8) K respectively. The maximum uniaxial pressure applied to the crystal, assuming a maximum applied force of ~ 500 mN²⁰, ranged from 6 to 9 bar depending on which axis is measured. The variation in the transition temperatures with uniaxial pressure is considerably larger than in the hydrostatic pressure results. Nevertheless, the uniaxial pressure dependence of transitions is reasonable considering the pressure sensitivity of this compound.

¹⁹More information about the crystallographic data is provide in a supplemental article (see Ref. [157]).

²⁰The copper-beryllium spring applies a force to the sample. For more information about the construction of the dilatometer cell please consult Section 3.5 on p. 35.

4.9 Summary

In Chapter Four, I have investigated the temperature dependence of the lattice and the magnetic properties of titanium (III) phosphate TiPO_4 . TiPO_4 is a non-conventional spin-Peierls compound characterized by a two-stage spin-Peierls transition which comprises two phase transitions: $T_{c1} \approx 74$ K and $T_{c2} \approx 110$ K. Magnetic susceptibility and thermal expansion measurements were used in this investigation. From the magnetic susceptibility measurements, the transitions T_{c1} and T_{c2} exhibited a sizable non-linear pressure dependence with a total increase of ~ 40 K for both transitions at 0.9 GPa. A high pressure anomaly in the form of a kink was noted for both transitions at 0.6 GPa. This pressure dependence makes TiPO_4 a very interesting compound for further studies. From the thermal expansion measurements, lattice expansion is observed along the **a** and **b** axes whereas contraction occurred along the **c**-axis with decreasing temperature. These results clearly indicated that T_{c1} and T_{c2} are first and second order phase transitions respectively consistent with the literature. In an applied magnetic field, the transition T_{c1} shifts by ~ 90 mK at 9 Tesla. The quadratic magnetic field shift of T_{c1} is consistent with standard spin-Peierls theory but the magnitude of the shift is about 50% smaller than expected according to theory. The reduced magnitude of the T_{c1} transition shift in the applied magnetic fields and the pressure dependence of the two phase transitions highlight the intriguing features of this non-conventional spin-Peierls compound.

Chromium Oxychloride

5.1 Introduction

As described in detail in the preceding chapter, TiPO_4 shares many similarities with the TiOX ($X = \text{Cl}, \text{Br}$) compounds. In contrast to TiPO_4 , which contains well defined quasi one-dimensional magnetic chains, the TiOX compounds are rather two-dimensional system with significant interchain spin exchange coupling.[21, 122, 123, 140, 141, 158] TiOCl and TiOBr have been investigated intensively, particularly their spin-Peierls properties. The interest in TiOX compounds refocused attention also on the magnetic properties of the analogous compounds with different $3d$ transition metals (i.e V, Cr and Fe). For example, VOCl and CrOCl are isostructural to TiOCl whereas FeOCl crystallizes with a slightly modified structure. From the crystal appearance (thin platelets) and their mechanical properties (the thin platelets cleave which readily in the **ab**-plane), the MOCl compounds are identified as compounds with a pronounced two-dimensional character. To what extent this behaviour is also reflected on the magnetic properties remained widely unclear, so far.

In this Chapter, I will describe the magnetic and the magnetostructural properties of CrOCl . From various characterization methods (magnetic susceptibility, heat capacity, dielectric spectroscopy, electron paramagnetic resonance, thermal expansion and Raman scattering measurements), detailed (H, T) magnetic phase diagrams are constructed which reveal the complex nature of the spin exchange interactions in CrOCl . The complexity of the (H, T) magnetic phase diagram has lately been alluded to in a collaboration of the Chemieservice group (Max Planck Institute for Solid State Research) with the crystallography

group of Prof. van Smaalen (University of Bayreuth).[159, 160]

5.2 The structural and the magnetic properties of CrOCl observed in previous studies

Studies of the magnetic and the structural properties of CrOCl have been performed as early as 1961. Schäfer *et al.* performed the first crystal structure determination in 1961 by x-ray diffraction on a single crystal grown using chemical vapour transport techniques. Schäfer *et al.* also proposed that CrOCl is isostructural to TiOCl and VOCl.[161] Subsequently, in 1962 Forsberg determined the space group of the crystal structure of CrOCl on the crystal used by Schäfer *et al.* before.[162] Later in 1974, Christensen *et al.* confirmed these earlier observations.[25] At room temperature, the MOCl compounds crystallize in the FeOCl structure-type with space group no. 59 ($Pm\bar{m}n$). The lattice parameters of MOCl (M = Ti, V and Cr) compounds are listed in Table 5.1.

Compound	a (Å)	b (Å)	c (Å)	Reference
CrOCl	3.863(4)	3.182(2)	7.694(7)	[25]
VOCl	3.780(5)	3.300(5)	7.91(1)	[163]
TiOCl	3.779(6)	3.341(5)	8.017(16)	[140]

Table 5.1: The lattice parameters of the isostructural MOCl (M = Ti, V and Cr) compounds

The crystal structure of the MOCl compounds (see Figure 5.1a) consist of MO double layers sandwiched between the halogen atom layers stacked along the c -axis. Linear metal atom chains connected by oxygen atoms run along the b -axis. The two metal oxygen atom strands stack along the a direction with a variation of the z -coordinates, $\pm z \approx 0.11$, of the Cr atoms. The Cr atoms are hexagonal arranged when projected on the ab -plane (see Figure 5.1b). The metal atoms in the double layers are connected by the oxygen anions and by the halogen atoms forming a two-dimensional stack. The stacks are connected via halogen-halogen van der Waals contacts to the neighbouring stacks along the c -axis.

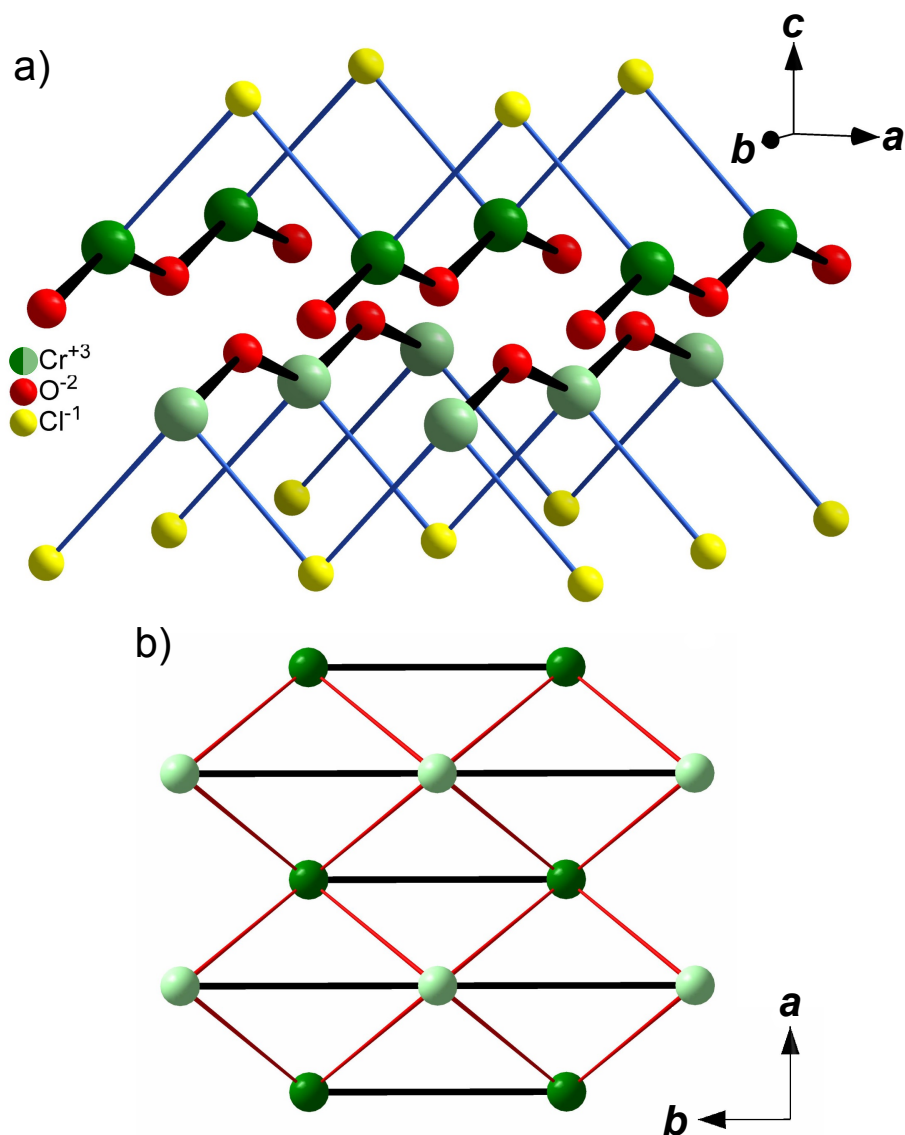


Figure 5.1: The orthorhombic crystal structure of CrOCl at room temperature with the lattice parameters of $a = 3.8638(2) \text{ \AA}$, $b = 3.1793(1) \text{ \AA}$ and $c = 7.7157(3) \text{ \AA}$. [159] (a) The Cr atom chains running along the *b*-axis (b) The top view of the Cr atoms at $-z$ (light green) and $+z$ (dark green) showing the Cr atom zig-zag chains and the linear chains in red and black lines respectively.

Temperature dependent magnetization measurements on CrOCl between 90 K and room temperature were first performed by Schäfer *et al.* [161] in 1961. They observed Curie-Weiss paramagnetism down to ~ 90 K with an effective moment of $3.9(1) \mu_B$ in good agreement with a spin-only moment of $S = \frac{3}{2}$ and a g-factor close to the free electron value.[161] Subsequently, Christensen *et al.* [25] measured the magnetic susceptibility down to 4.2 K (see Figure 5.2) and observed a similar effective moment and a positive Curie-Weiss temperature $\theta \approx 18$ K indicating predominant ferromagnetic spin exchange interactions.[25]

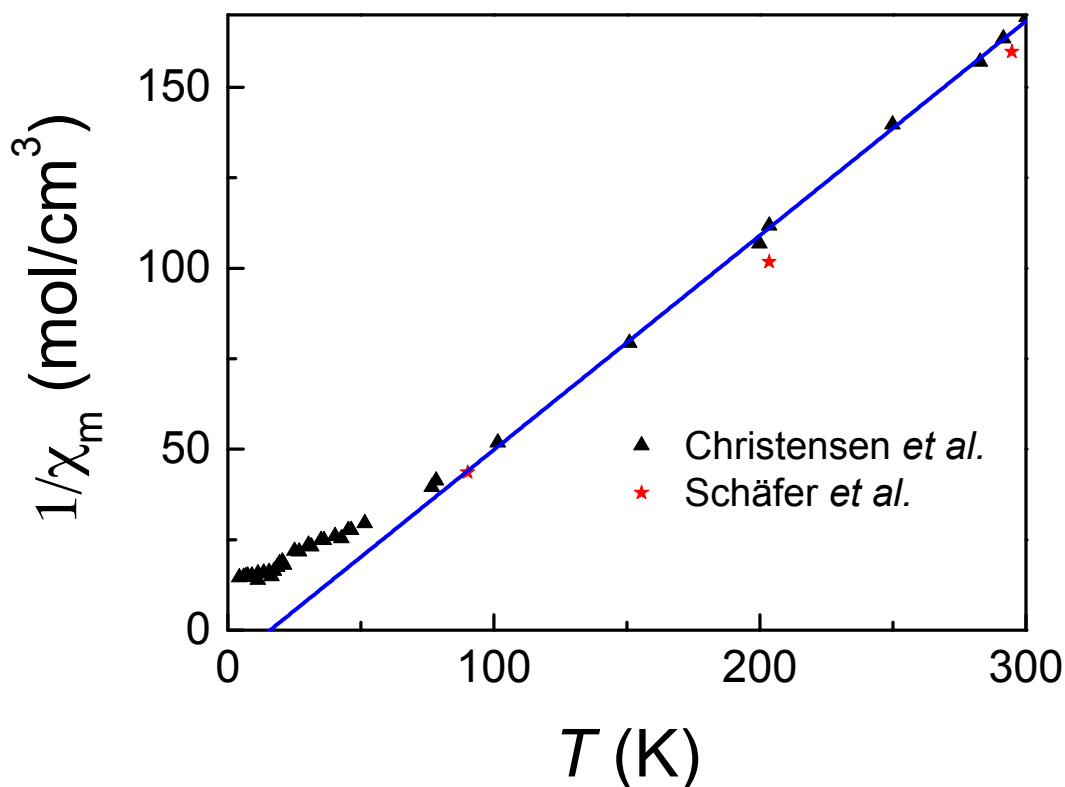


Figure 5.2: The temperature dependent inverse molar magnetic susceptibility of CrOCl showing the results from Schäfer *et al.* [161] and Christensen *et al.* [25]. The fit of the Curie-Weiss law to the data is indicated by the solid blue line intersecting the temperature axis at ~ 18 K. The results in these Figure were obtained from aforementioned references.

Christensen *et al.* also studied the low temperature magnetism using neutron powder diffraction. The neutron powder diffraction results indicated antiferromagnetic order at 4.2 K. They discovered that the magnetic supercell structure (see Figure 5.3) at 4.2 K was four-fold (**a**, **4b**, **c**) with a Cr magnetic moment $\mu = 3.36 \mu_B$. The Cr magnetic moments are collinear to the *c*-axis.[25]

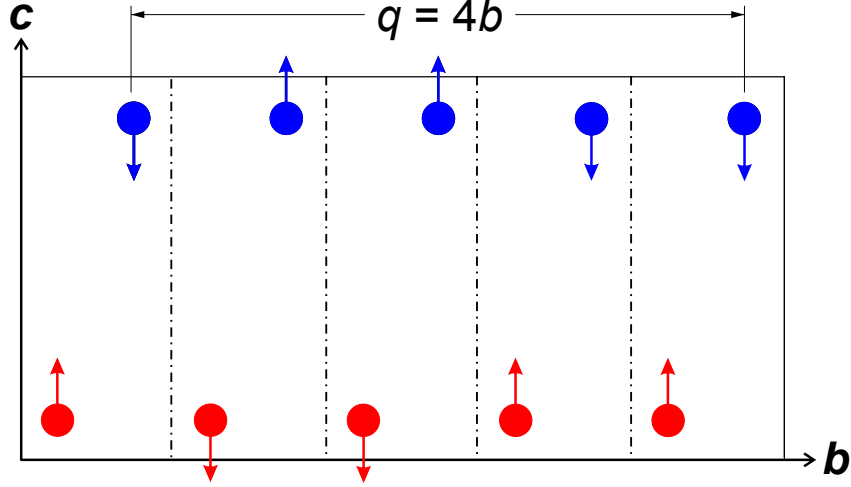


Figure 5.3: The low temperature magnetic structure of CrOCl projected along a -axis from Christensen *et al.* showing the chromium atoms aligned along c -axis. The Cr atoms at $a = \frac{1}{4}$ and $\frac{3}{4}$ are represented by red and blue circles respectively. This Figure was reproduced from Ref. [25].

In 2009, the magnetic and the structural properties of CrOCl were reinvestigated by a collaboration of our group with Prof. van Smaalen's group at the University of Bayreuth using magnetic susceptibility, synchrotron and heat capacity measurements.[159] Figure 5.4 displays the magnetic susceptibility for the magnetic field aligned parallel and perpendicular to the c -axis, i.e. perpendicular and parallel to the crystal platelets. Magnetic susceptibility measurements (see Figure 5.4) were performed down to 2 K for the two crystal orientations ($H \parallel c \rightarrow \chi_{\parallel}$ and $H \perp c \rightarrow \chi_{\perp}$).[159] The inverse magnetic susceptibility above 175 K follows the Curie-Weiss law with an effective magnetic moment $\mu_{\text{eff}} = 3.82(1) \mu_{\text{B}}$ and a positive Curie-Weiss temperature $\theta = 19.2(5)$ K. The effective magnetic moment μ_{eff} was consistent with the $3d^3$ electronic configuration of Cr^{+3} in the spin-only $S = \frac{3}{2}$ state and a g-factor¹ of $g \approx 1.97$. The g-factor was in good agreement with previous studies. The magnetic susceptibilities for both orientations begin to deviate from each other below 80 K and pass through broad maxima near ~ 30 K. An anomaly was observed for both orientations near 27.2 K but the origins remained unclear. Below 27 K, the magnetic susceptibilities for both orientations decreases below

¹The effective magnetic moment is given by $\mu_{\text{eff}} = g\sqrt{S(S+1)}$ for spin only where S is the spin quantum number.[57]

~ 14 K with χ_{\parallel} rapidly dropping to a value near zero² and χ_{\perp} leveling off at 3.88×10^{-2} cm³/mol. This low temperature magnetic behaviour suggested that long-range antiferromagnetic ordering occurred below ~ 14 K consistent with the previous results from Christensen *et al.* [25]. From the low temperature magnetic susceptibilities, it was concluded that CrOCl is an uniaxial antiferromagnet with the easy axis parallel or near to the *c*-axis of the crystal.

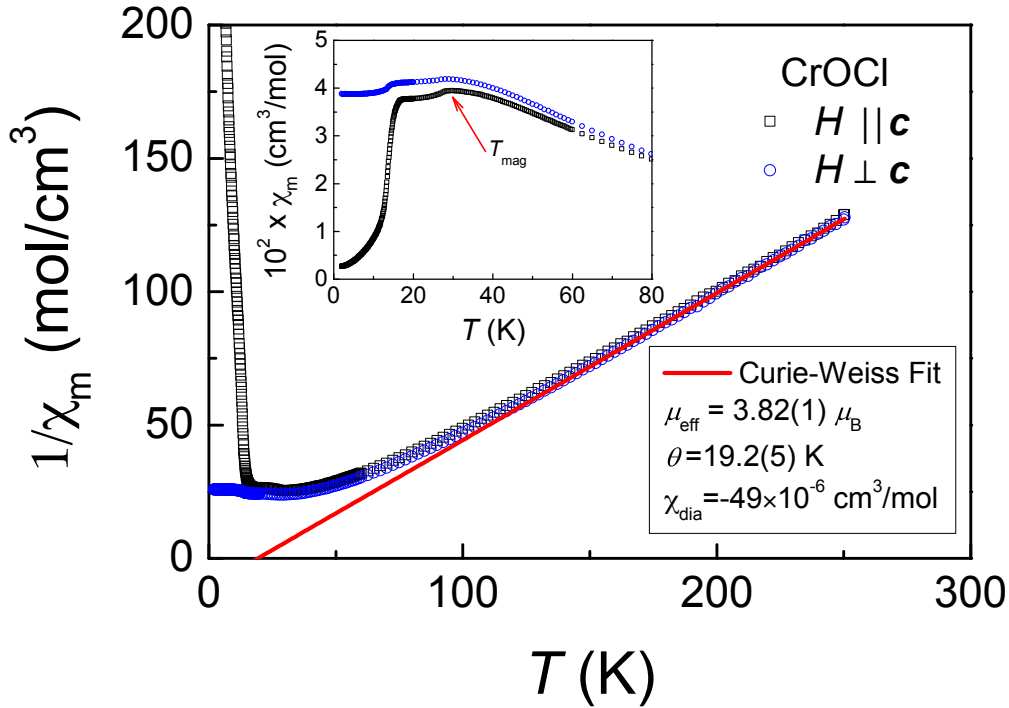


Figure 5.4: Main: The temperature dependent inverse molar magnetic susceptibility of CrOCl measured parallel and perpendicular to the *c*-axis with an applied magnetic field of 0.1 Tesla. The Curie-Weiss law fit of the inverse magnetic susceptibility above 175 K is illustrated by the solid blue line intersecting the temperature axis at ~ 20 K. Inset: A weak anomaly occurs in the temperature dependent molar magnetic susceptibilities around 27 K. This Figure was produced results from Ref. [159].

²The non-zero χ_{\parallel} was attributed to a small misalignment of the crystal.[159]

Long-range antiferromagnetic ordering at 13.9 K was also indicated by an anomaly in the heat capacity data (see Figure 5.5). Interestingly, two close anomalies ($\Delta T \approx 1$ K) were observed at 26.7 K and 27.8 K. The former (T_{mag}) was attributed to a magnetic origin due to its similarity to the anomaly in the susceptibility whereas the origin of the latter (T^*) remained unclear in the magnetic susceptibility results. It was proposed that the T_{mag} anomaly may arise from incommensurate magnetic order.[159]

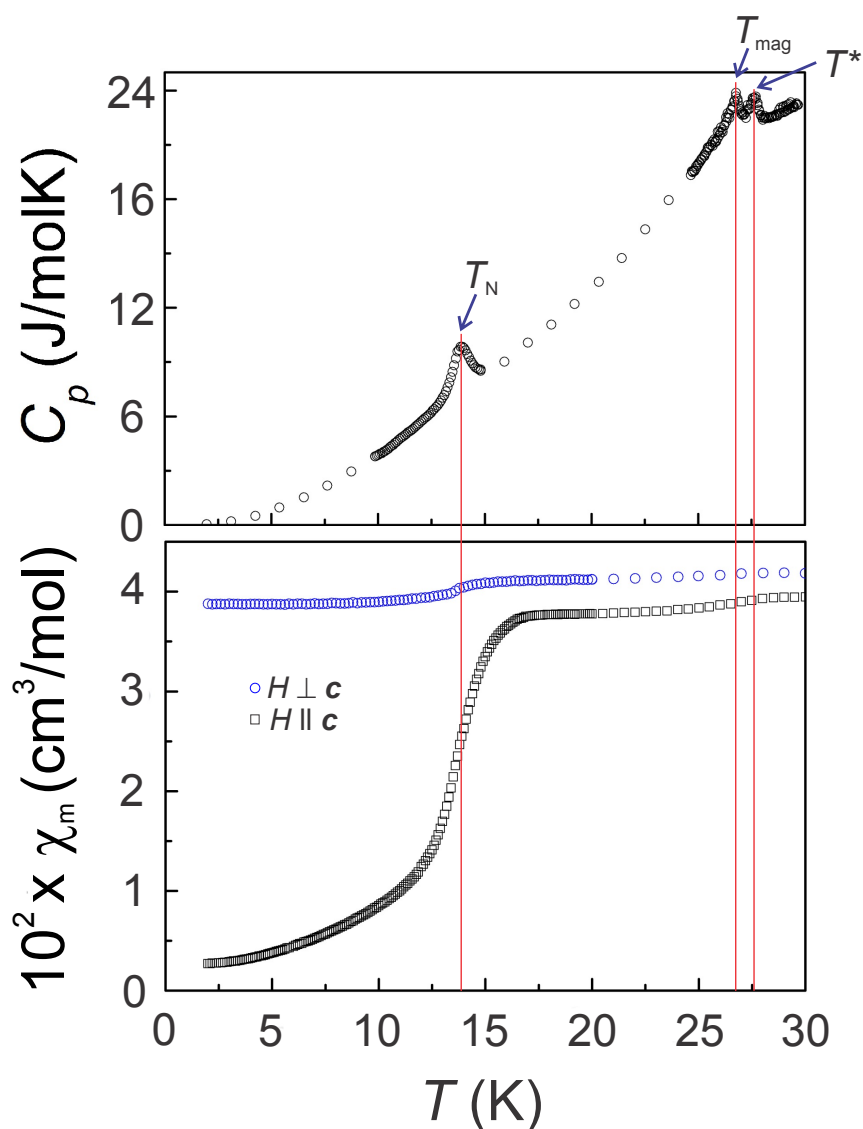


Figure 5.5: The low temperature heat capacity C_p and the molar magnetic susceptibilities (χ_{\parallel} and χ_{\perp}) of CrOCl. The positions of the three transition (T_N , T_{mag} and T^*) are denoted with the solid red lines. This Figure was generated from results in Ref. [159].

Magnetic field dependent ($H \parallel c$) heat capacity and magnetization measurements were performed up to 9 Tesla and used to construct a tentative phase diagram (see Figure 5.6).

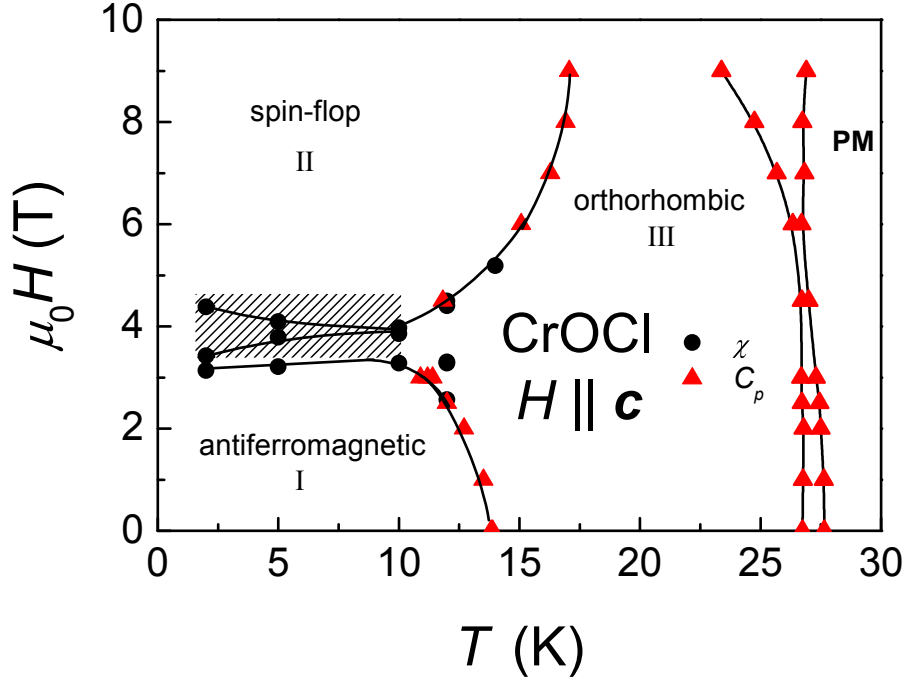


Figure 5.6: The preliminary (H, T) magnetic phase diagram of CrOCl for $H \parallel c$ with the spin-flop phase denoted as SF. **P** indicates the paramagnetic state of CrOCl. This Figure was obtained from Ref. [159].

Above 4 Tesla, a new phase was detected which was attributed to the spin-flopped phase. A complex dependence of the boundary regime separating the parallel aligned phase and spin-flopped phase was observed. A very steep magnetic field dependence was measured for the two phase boundaries separating the paramagnetic and the magnetically order phases. Whereas the T_{mag} bends slightly towards to lower temperatures with increasing magnetic field, T^* remains largely unchanged by the applied magnetic field. This finding suggests that T^* is a structural phase transition.

Angelkort *et al.* [159] reinvestigated the low temperature crystal structure of the CrOCl using x-ray synchrotron diffraction measurements. The orthorhombic (room temperature) crystal structure distorts into a monoclinic structure at the Néel temperature of $T_N \approx 13.5$ K similar to the situation in VOCl.^[26, 159] Additional Bragg reflections occur which can be indexed assuming a two-fold nuclear supercell along the b -axis. These supercell reflections below 13 K were

attributed to the magnetically induced charge scattering³ based on a propagation vector of $q_{nuclear} = \frac{1}{2}b^*$. The magnetic induced scattering demonstrates the magnetoelastic nature of the antiferromagnetic state. The synchrotron measurements of the structural Bragg reflection $\rightarrow (0 \bar{2} 5)$ and the nuclear supercell reflection $\rightarrow (2 \bar{1.5} 1)$ near the Néel transition are presented in Figure 5.7.

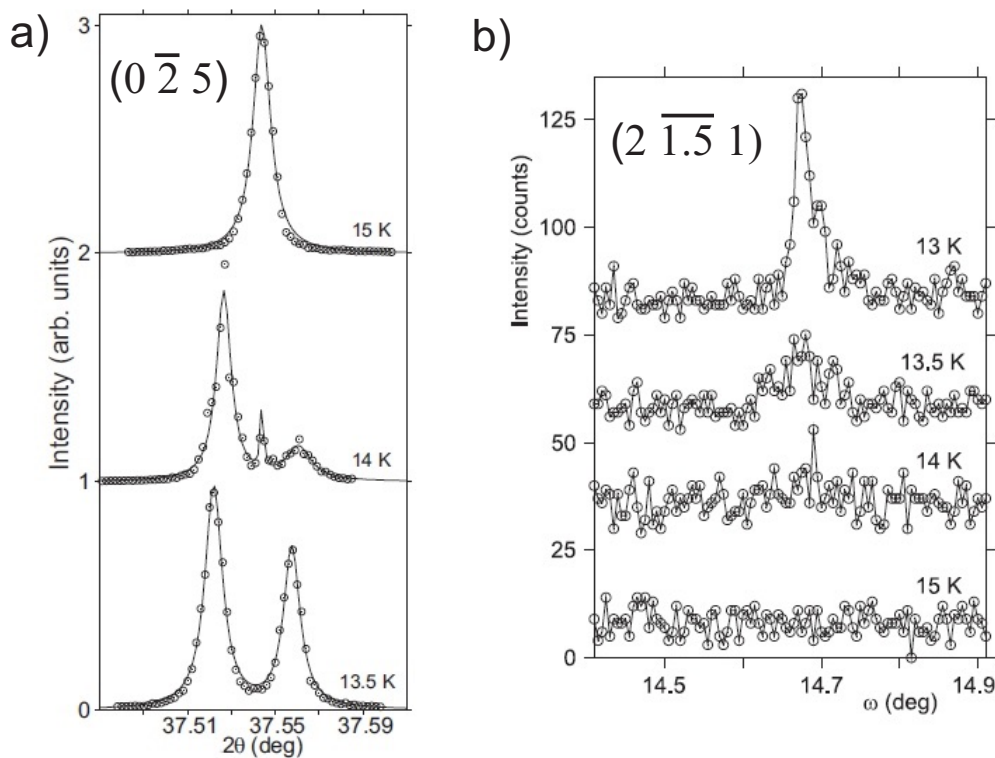


Figure 5.7: The temperature dependence of two strong reflections of CrOCl near the Néel transition ($T_N \approx 13.5$ K) : a) The structural reflection $\rightarrow (0 \bar{2} 5)$ b) The supercell reflection $\rightarrow (2 \bar{1.5} 1)$. This Figure was produced from results in Ref. [159].

In summary, these early results indicated a very complex interplay between the magnetic and the lattice degrees of freedom. These observations are reminiscent of the behaviour seen in magnetically frustrated materials where similar magnetostructural coupling has been observed.[165–167]

³Magnetically induced charge scattering occurs when magnetic ordering causes magnetoelastic distortions in the crystal lattice which results in a lattice modulation.[164]

5.3 Sample preparation and experimental methods

The CrOCl crystals used in this thesis were grown by Prof. van Smaalen's group at the University of Bayreuth using the chemical vapor transport method. Details of the method employed for growing the crystals have been published by Schäfer *et al.* [161], Christensen *et al.* [25] and Nocker *et al.* [168]. For the purpose of the experiments, the crystals were grown using the following method [160]:

1. Cr₂O₃ and CrCl₃ were mixed in stoichiometric amounts with a tiny amount of the transport agent HgCl₂ and placed in the quartz glass tube.
2. The quartz glass tube was then evacuated and sealed to produce a quartz glass ampoule with a length of ~ 10 cm.
3. The ampoule was placed in a furnace with a temperature gradient from 1223 K to 1123 K for five days. The crystals grew on the cold side of ampoule.

The greenish CrOCl crystals (see Figure 5.8) were irregularly shaped with lateral dimensions varying from 0.5 mm - 1.5 mm. The crystallographic *c*-axis is oriented perpendicular to the platelets. The thickness of the platelets was on average 0.02 mm or less. All measurements were performed on crystals grown in the same batch.

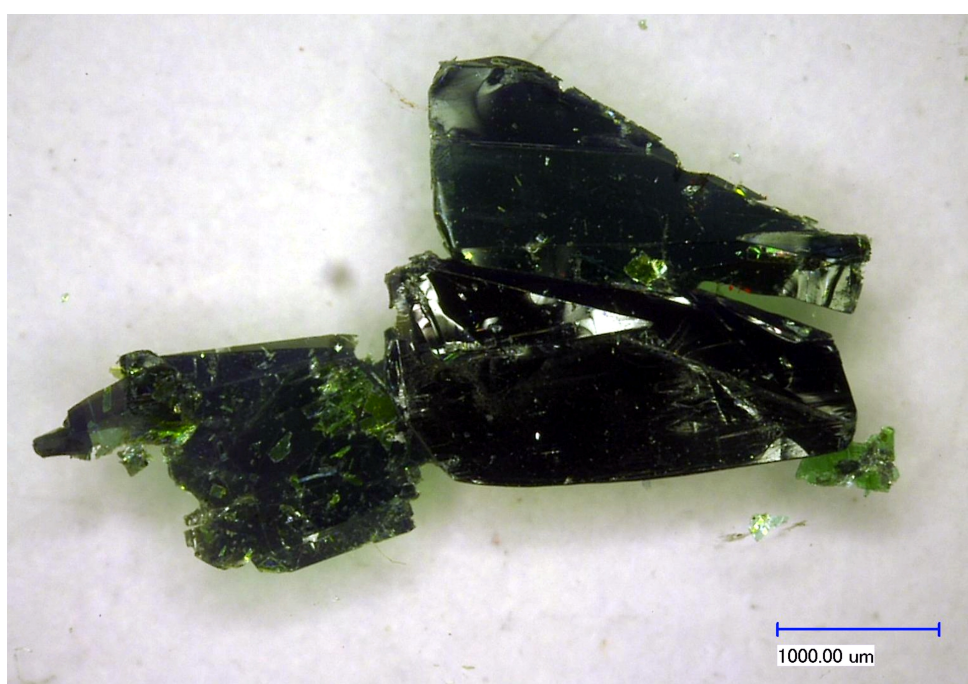


Figure 5.8: Multiple CrOCl crystals with a greenish appearance.

5.3.1 Magnetic measurements

The magnetic measurements were performed on three CrOCl samples using a Magnetic Property Measurement System (Quantum Design, MPMS-XL7) and a pulsed field magnetometer (see Ref. [169]) at the Dresden High Magnetic Field Laboratory. I would like to thank Dr. J. M. Law for performing the high magnetic field measurements. Sample #1 consisted of many randomly orientated CrOCl with a total mass of ~ 25 mg. Sample #2 contained several crystals mounted in a vertical orientation with a total mass of 7.50 mg and glued in place using Clou® Zapon-Lack. Sample #1 and #2 were placed in Suprasil© quartz glass tubes. Sample #3 was composed of one large crystal with a mass of 2.50 mg and folded upon itself in order to fit into magnetometer. The sample was then mounted on a 2 mm holder and loaded in the small chamber of the pulsed field magnetometer (approx. 3 mm inner diameter).

The temperature dependent magnetic susceptibility of sample #1 was measured between 2 K and 800 K in a magnetic field of 1 Tesla (see Figure 5.9). Below 300 K, the results are very similar to the findings of the previous magnetic studies.[25, 159, 161] The low temperature behaviour implies that the majority of the randomly orientated crystals have a preferred orientation with $H \perp c$. In the low temperature regime, the T_N and T_{mag} transitions occur at temperatures consistent with literature.[159] The results of Curie-Weiss fitting in the high temperature regime (200 K - 800 K) are similar to the previous results and except the Curie-Weiss temperature is $\sim 35\%$ larger in the new results. The g-factor from Curie-Weiss fitting ($g = 1.966(5)$) is consistent with the electron paramagnetic resonance measurements as well as the previous studies.[159, 161]

Sample #2 was used to investigate the spin-flop (SF) region for $H \perp c$. The magnetic field dependent magnetization at fixed temperatures were measured between 2 K and 18 K with magnetic fields swept up to 7 Tesla. The results are displayed in Figure 5.10. In Figure 5.10, the area enclosed in the magnetization loops decreases with increasing temperature and the magnetization loops disappear between 16 K and 18 K. The 2 K magnetization loop was compared with the results obtained by Angelkort *et al.* [159]. It is observed that the magnetic moment per chromium atom is six times smaller for the $H \perp c$ orientation than the $H \parallel c$ orientation at 7 Tesla. These results are consistent with the magnetic moments of the chromium atoms aligning along the c -axis as discussed in the

introduction. Above 16 K, the magnetization loops flatten exhibiting a linear magnetization dependence on the magnetic field. Peaks are observed in the derivatives of the magnetization loops with respect to the magnetic field H for temperatures less than 16 K. The peak positions from the derivatives are used to construct part of the extended (H, T) magnetic phase diagram discussed in Section 5.4.1.

The high field magnetization was investigated using sample #3 with $H \perp \mathbf{c}$ and $H \parallel \mathbf{c}$. The measurements were performed at constant temperatures ranging from 4.2 K to 20 K with magnetic fields up to 35 Tesla. The results are presented in Figures 5.11 to 5.13. The magnetization results clearly indicate that saturation occurs at high magnetic fields above ~ 25 Tesla in both orientations. The saturated magnetization decreases by $\sim 15\%$ from 4.2 K to 20 K for both orientations. In addition, the spin-flop transitions can be seen in $H \parallel \mathbf{c}$ orientation consistent with previous results.[159] At 4.2 K, the magnetization results were calibrated using a SQUID magnetometer (see upper part of Figure 5.12). For $H \parallel \mathbf{c}$, the plateau is observed for magnetic fields between ~ 4.5 Tesla and ~ 10 Tesla with a magnetization of $\sim 0.6 \mu_B$ consistent with Angelkort *et al.* results. But no plateau can be seen for $H \perp \mathbf{c}$ near 7 Tesla due to the small magnetization of the crystal in this orientation. At low temperatures, the saturated magnetic moment of CrOCl with $S = \frac{3}{2}$ can be calculated using following equation [170]:

$$M_{sat} = g\mu_B S \rightarrow M_{sat} \approx 3 \mu_B \quad (5.1)$$

Above the saturation field (~ 30 Tesla at 4.2 K), all the spins are parallel when $H \parallel \mathbf{c}$ whereas only $\approx \frac{1}{5}$ of spins are parallel when $H \perp \mathbf{c}$. As the temperature increases, the saturation field decreases to ~ 25 Tesla at 20 K independent of the magnetic field orientation. The anomalies are observed in the derivatives of the magnetization for both orientations. The anomalies are used to construct part of the extended (H, T) magnetic phase diagram discussed in Section 5.4.1.

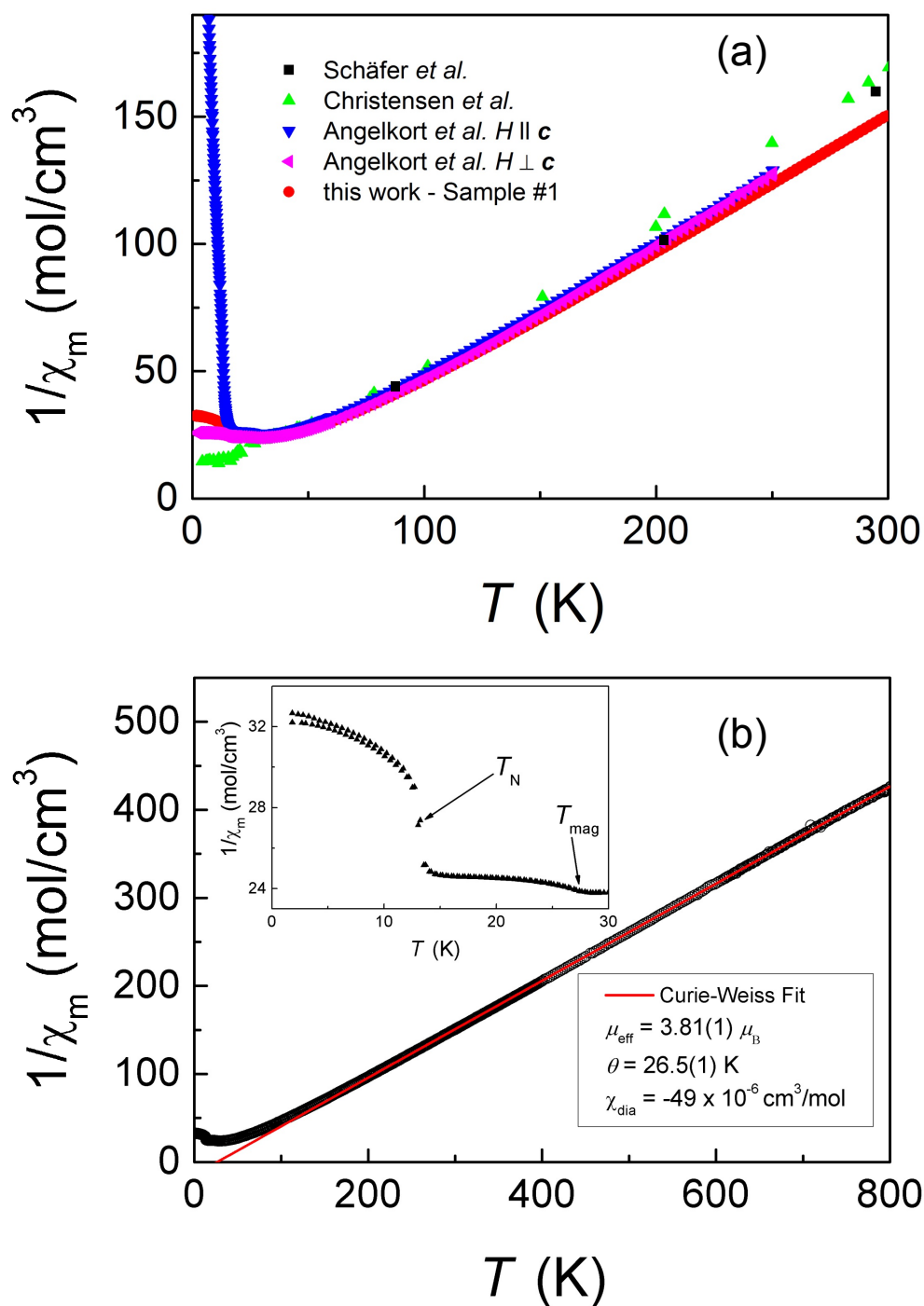


Figure 5.9: a) The temperature dependent inverse molar magnetic susceptibility of CrOCl measured up to 300 K in a magnetic field of 1 Tesla including the reference data from literature.[25, 159, 161] b) The temperature dependent inverse molar magnetic susceptibility of CrOCl up to 800 K. The solid red line is the fit of the experimental data to the Curie-Weiss law with the parameters given in the lower inset. The upper inset enlarges the low temperature regime.

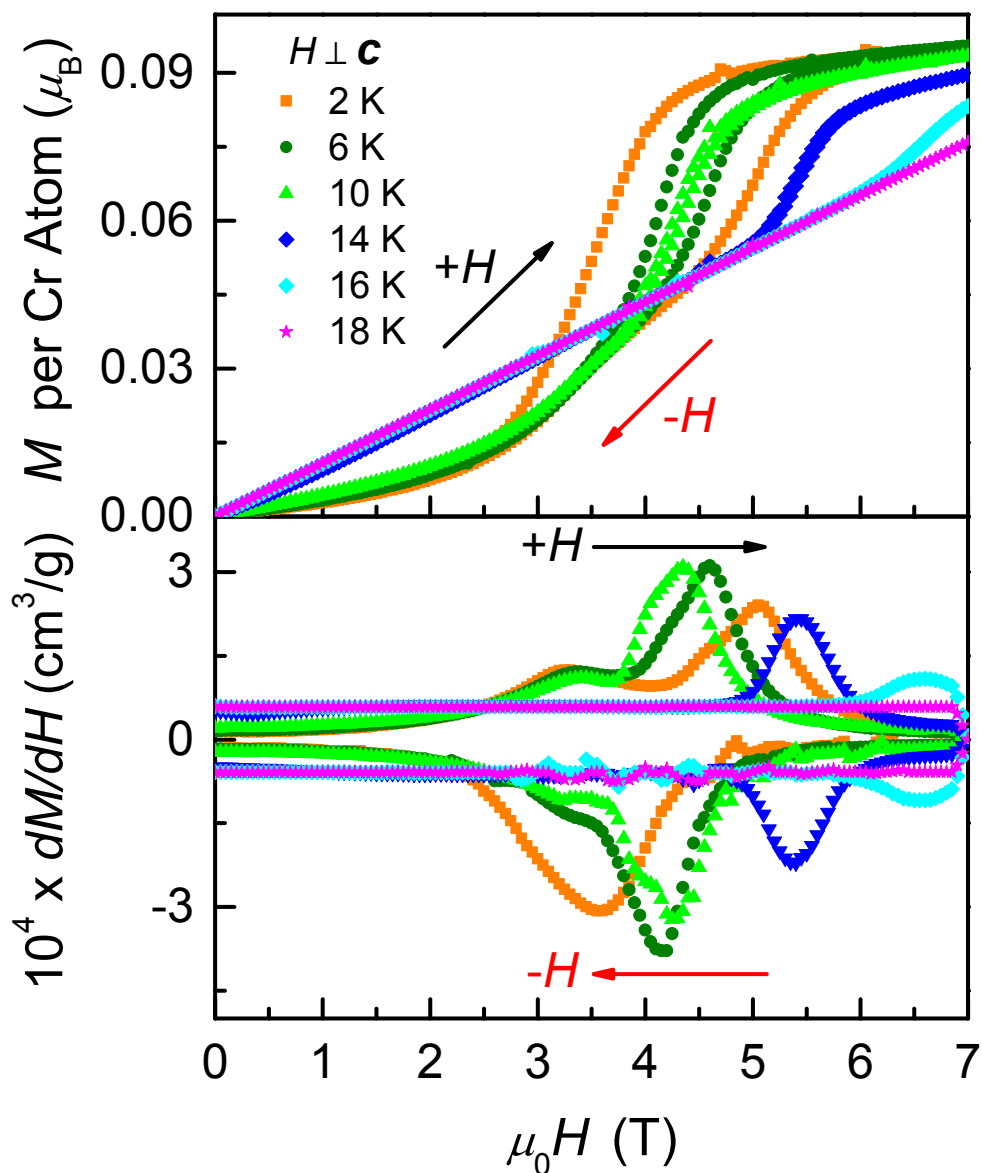


Figure 5.10: The magnetization loops of CrOCl and their derivatives with respect to the magnetic field with $H \perp c$ for temperatures between 2 K and 18 K. The left $+H$ (black) and right $-H$ (red) arrows indicates the magnetization measured with increasing and decreasing magnetic fields respectively. The colour code indicating the temperatures are the same in both frames.

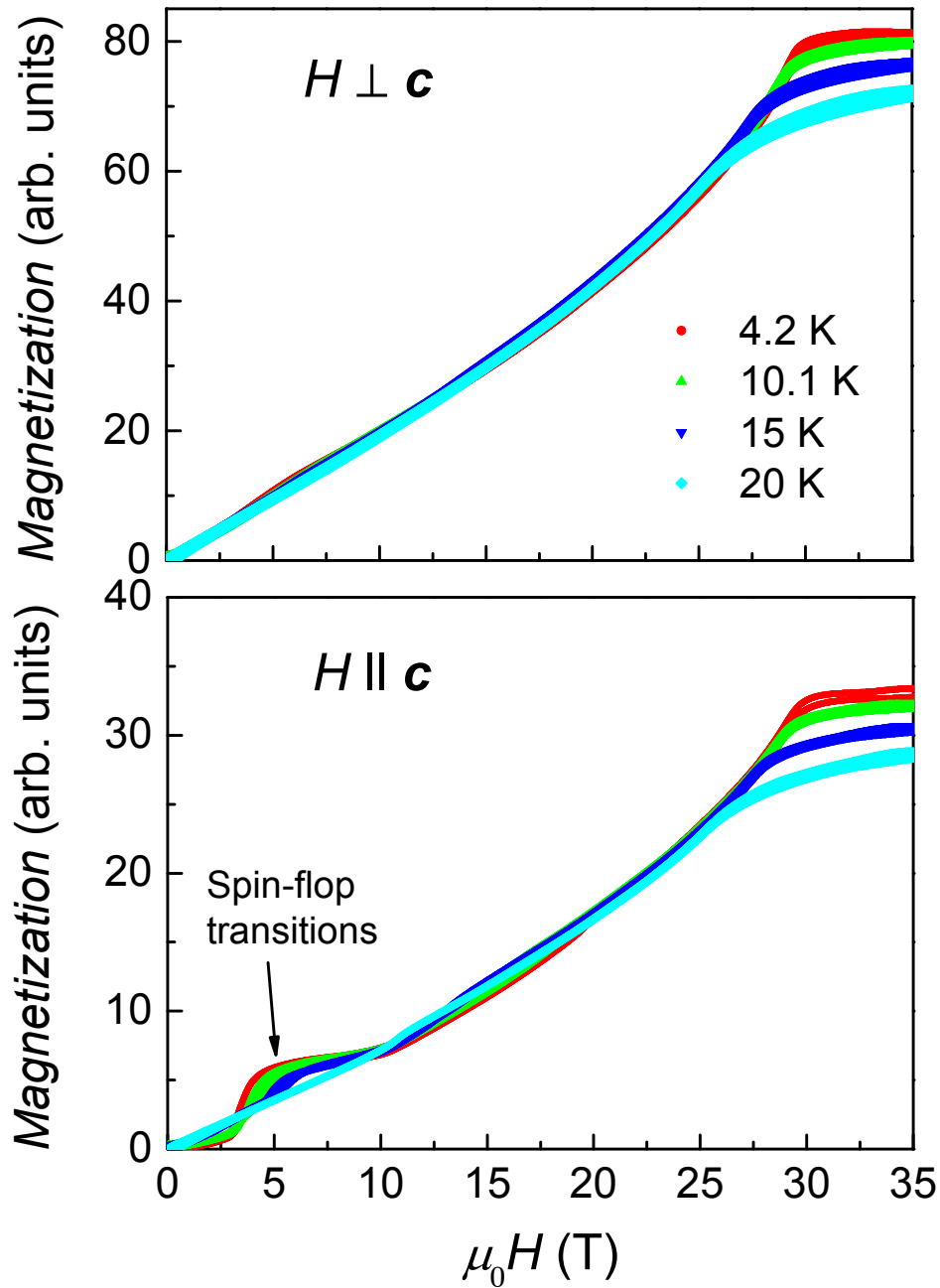


Figure 5.11: The magnetization of a CrOCl crystal with $H \perp c$ and $H \parallel c$ at 4.2 K, 10.1 K, 15 K and 20 K as measured in a pulsed magnetic field.

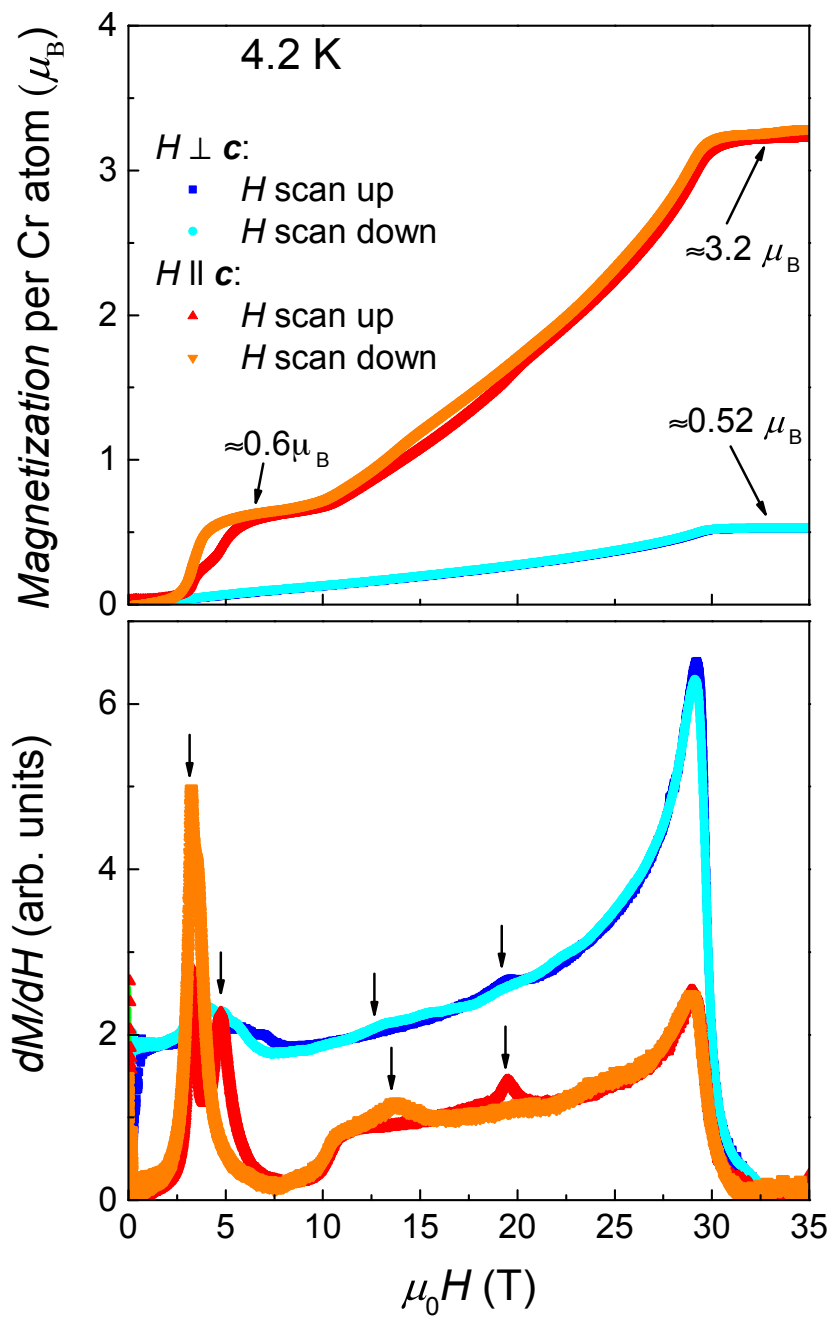


Figure 5.12: The magnetization per Cr atom of a CrOCl crystals and the derivative of the magnetization with respect to the magnetic field at 4.2 K with $H \perp c$ and $H \parallel c$.

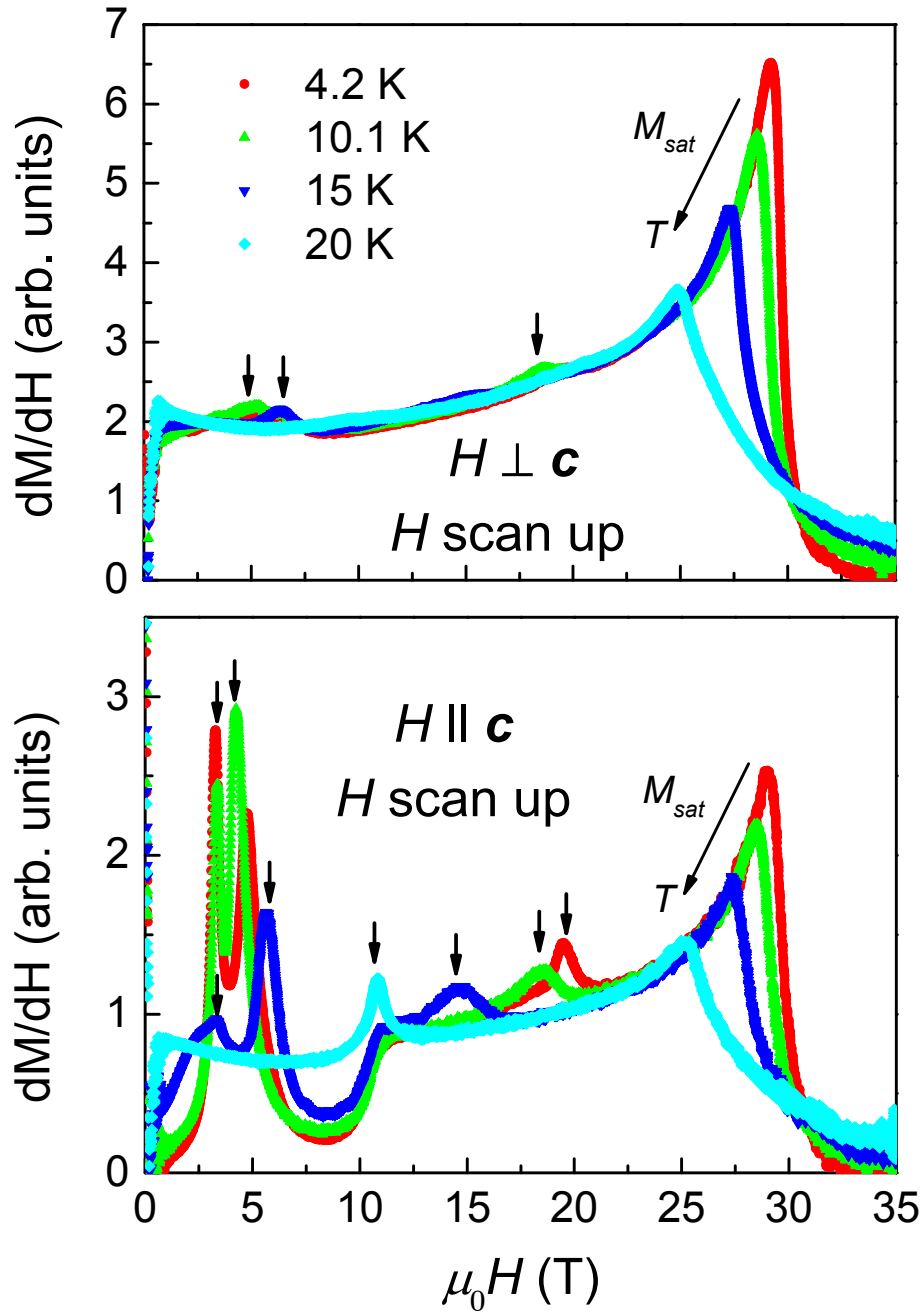


Figure 5.13: The derivative with respect to magnetic field of the magnetization of a CrOCl crystal with $H \perp c$ and $H \parallel c$ at 4.2 K, 10.1 K, 15 K and 20 K.

5.3.2 Heat capacity measurements

Heat capacity measurements were performed on a crystal with a mass of ~ 2 mg. A triangular shaped sapphire wedge⁴ (see Figure 5.14) was used to align the crystal platelet in the magnetic field. The heat capacities were measured using the thermal relaxation method as implemented in the Physical Property Measurement System (Quantum Design, PPMS)⁵.

Initially, the heat capacity measurements were performed in a zero magnetic field from 2 K to 30 K. These results are presented in Figure 5.14.

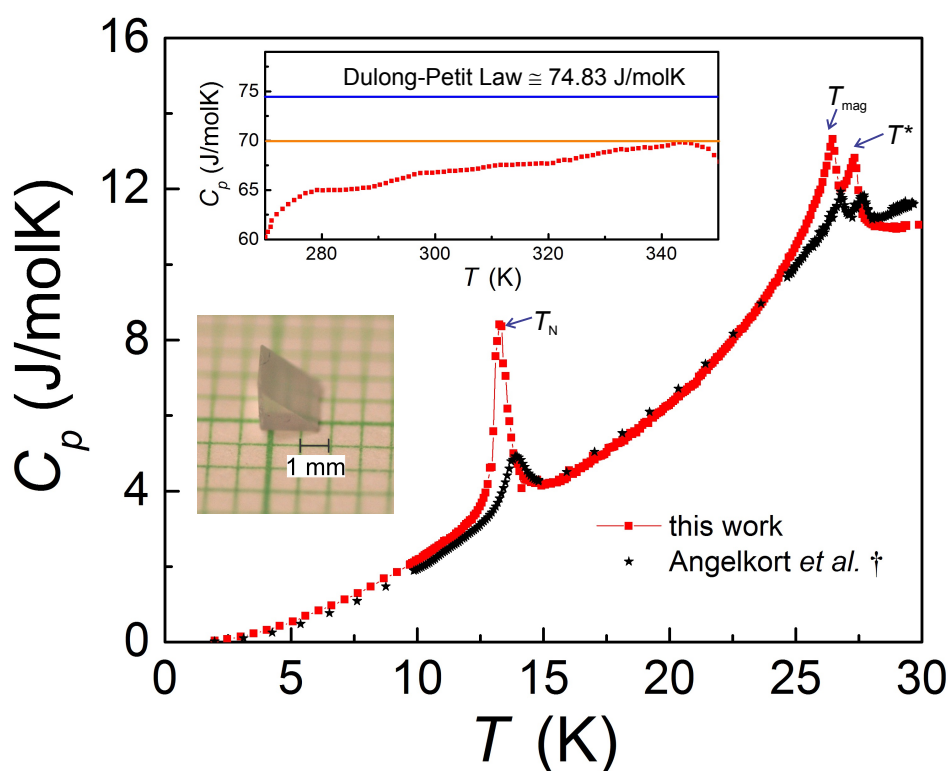


Figure 5.14: Main: The zero magnetic field temperature dependent heat capacity of a CrOCl crystal at low temperatures (2 K to 30 K) and high temperatures (270 K to 350 K). (†) Angelkort *et al.* [159] results were divided by two and graphed for a comparison with the new data. The lines on the red curve in the main graph are a guide to the eyes. Inset: The triangular shaped sapphire wedge used in the heat capacity measurements with a mass of 10 mg is also shown. The dimensions of the wedge's base were 1.95 mm x 1.72 mm with a height of 1.43 mm.

⁴A high purity sapphire cubic crystal was cut diagonal to produce the triangular shaped wedge. The wedge adds a small magnetic field independent contribution to the total heat capacity at low temperatures which is accounted for in the addenda measurement.

⁵The thermal relaxation method is discussed in detail in Section 3.3 on p. 28.

There is a significant discrepancy in the magnitude of C_p between the new results and the preceding results from Angelkort *et al.* [159] (see Figure 5.5 on p. 117). In the preceding results, the measured crystal had a mass of 0.45 mg whereas the new results used a crystal with four times the aforementioned mass. When the preceding results are divided by two, both results have a very similar magnitude. The discrepancy in the magnitude of C_p most likely resulted from an error in the mass determination of the small crystal used in the preceding results. The anomalies in C_p at the three transitions are particularly sharper in the new results. The sharper anomalies may be a result of the thermal hysteresis effects. The new results are measured in a heating cycle whereas the preceding results were measured in a cooling cycle. As will be seen in the thermal expansion results, heating cycle measurements produce better well-defined anomalies. The small mass of the crystal used in the previous experiments may also contribute to the weaker anomalies in C_p through poor thermal coupling of the crystal to the platform. When the temperature of the three transitions are compared in the preceding and the new data, the transitions occur at approximately the same temperatures with a difference of ± 0.40 K. To verify the magnitude of new C_p data, additional C_p measurements were performed between 275 K and 350 K. The results are displayed as an inset in Figure 5.14. At 350 K, the heat capacity is equal to ~ 70 J/molK which is similar to the predicted heat capacity at high temperature from the Dulong-Petit law for three atoms (~ 75 J/molK).

The magnetic field dependence of the heat capacity was further investigated through additional measurements between 2 K and 30 K in magnetic fields up to 9 Tesla (see Figure 5.15). The transitions T_N , T_{mag} and T^* are indicated by their labels. Below 5 Tesla, T_N and T^* are independent of the magnetic fields occurring at 13.28(5) K and 27.34(4) K respectively. In contrast, T_{mag} decreases by 0.61 K at a magnetic field of 4 Tesla compared to the zero magnetic field transition temperature. Above 5 Tesla, all three transitions are affected by the magnetic fields. T_N increased by 2 K up to 9 Tesla from the zero field transition temperature. T_{mag} and T^* decrease by 5.3 K and 0.150 K at 9 Tesla respectively compared to the zero magnetic field transition temperatures. Both anomalies at T_N and T_{mag} broaden with increasing magnetic field whereas the T^* transition does not exhibit broadening in magnetic fields up to 9 Tesla. The peak positions of the three transitions in Figure 5.15 are used to construct part of the extended (H, T) magnetic phase diagram in Section 5.4.1.

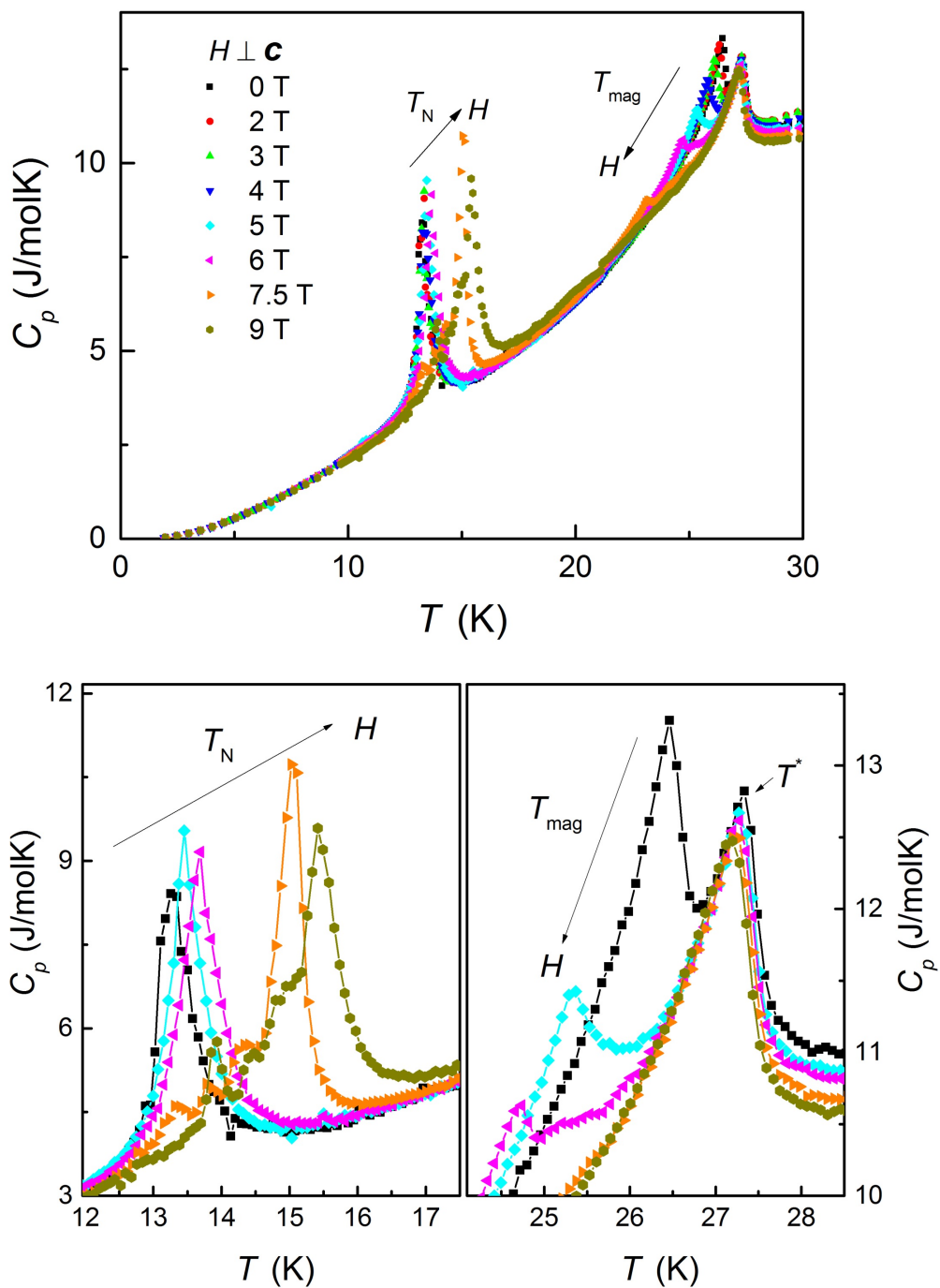


Figure 5.15: The temperature dependent heat capacity of a CrOCl crystal at various magnetic field with $H \perp c$.

Magnetic field scans of C_p up to 9 Tesla were also performed at various constant temperatures below 30 K with $H \perp c$ and $H \parallel c$. The results for two temperatures (3.5 K and 11 K) are shown in Figure 5.16. Three anomalies are noted in the $H \parallel c$ field scans whereas only one anomaly is observed for $H \perp c$ field scans. The anomalies are used to construct part of the extended (H, T) magnetic phase diagram discussed in Section 5.4.1.

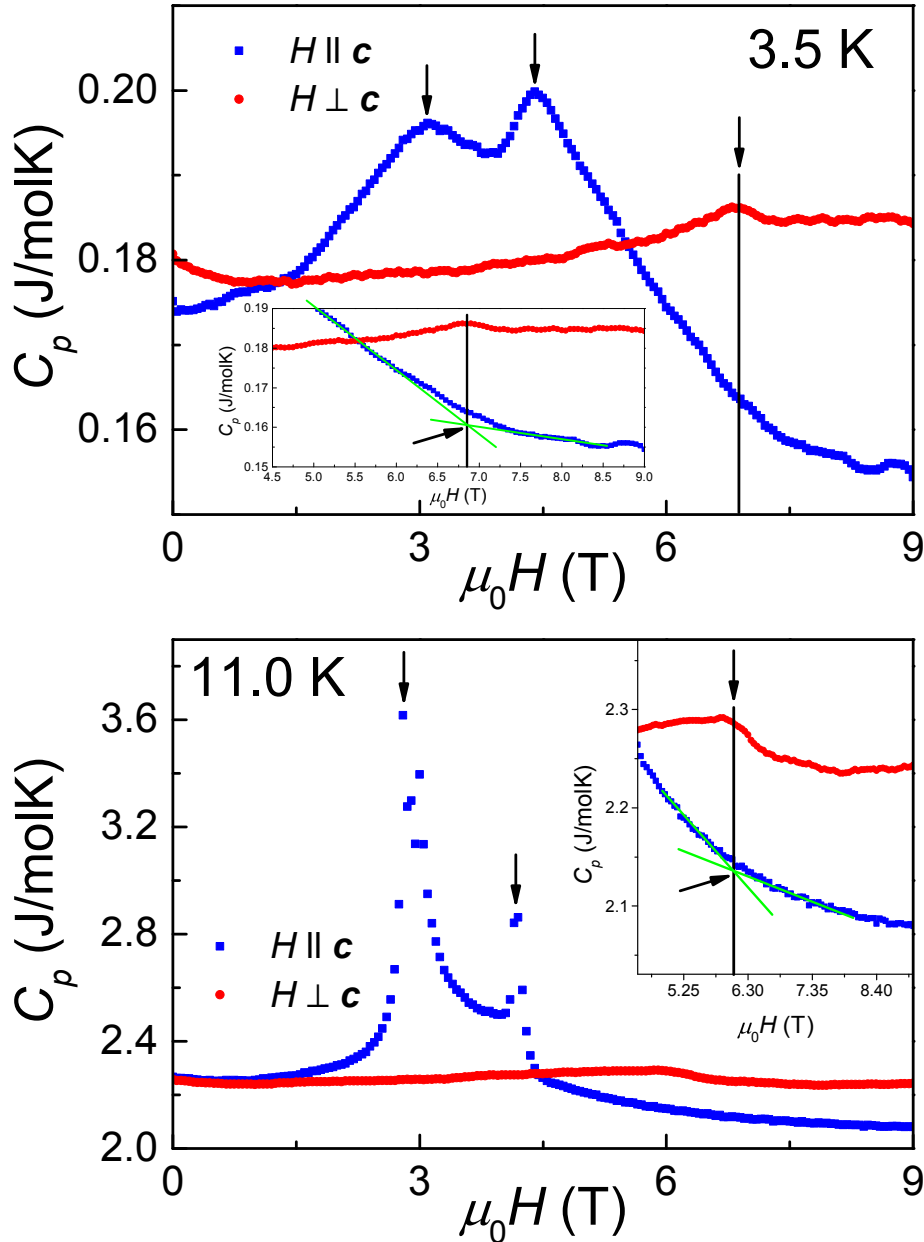


Figure 5.16: The magnetic field dependent heat capacity of a CrOCl crystal at constant temperatures of 3.5 K and 11.0 K with $H \perp c$ and $H \parallel c$.

5.3.3 Thermal expansion measurements

The thermal expansion measurements were carried out on a polycrystalline pellet and a crystal stack. A polycrystalline pellet was produced by pressing many small crystals in ~ 3 mm stainless steel mold using a maximum applied pressure of 150 N/m. The pressed pellet had a final thickness of 0.594 mm. For the crystal stack, thirteen irregularly shaped crystals were arranged together resulting in a final thickness of 0.10 mm. Ethanol was used to temporarily adhere the crystals together during the stacking process and later evaporated using a high vacuum system.

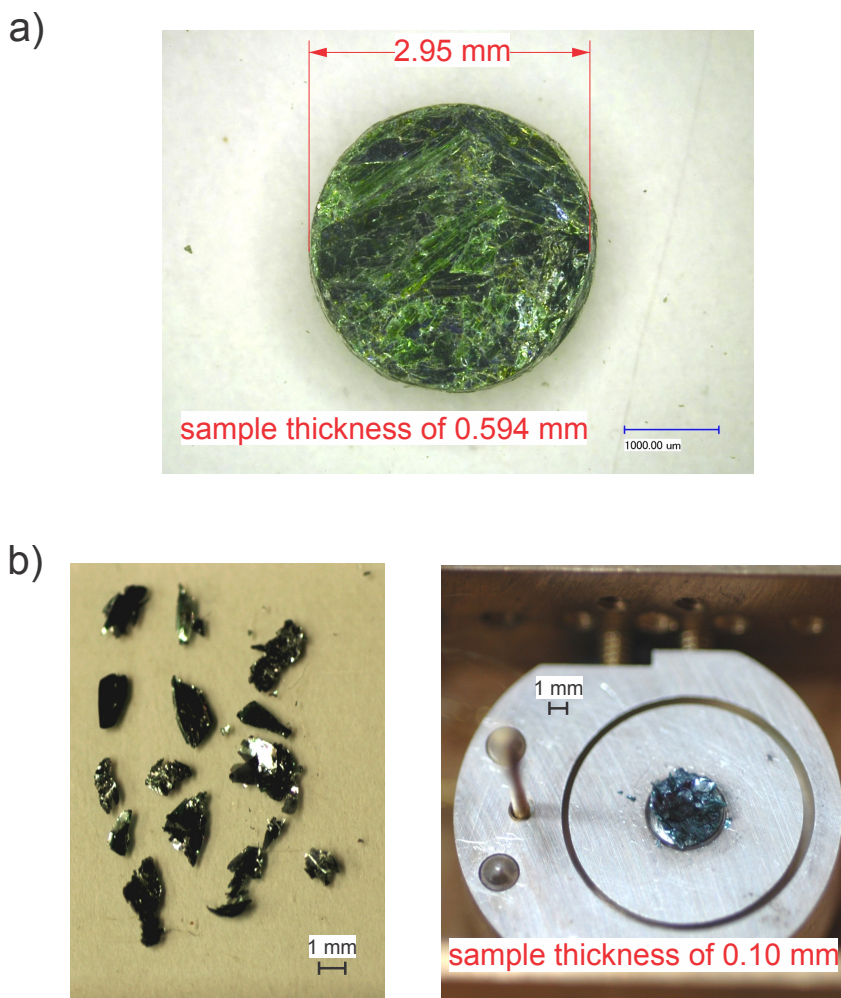


Figure 5.17: The CrOCl samples used for the thermal expansion measurements. a) The pressed pellet with a diameter of 2.95 mm and a thickness of 0.594 mm. b) The crystal stack constructed on the sapphire disk by stacking thirteen crystals together with a total thickness of 0.10 mm.

Zero magnetic field thermal expansion measurements were performed on the crystal stack and the pressed pellet. For the crystal stack, only the c -axis thermal expansion was measured since the a and b axes could not be accessed due to the morphology of the platelets. The cylindrically shaped pellet comprises crystals with random orientations but most likely with a largely preferred orientation of the platelets perpendicular to the cylinder axis. The zero magnetic field measurements were performed between 5 K and 300 K in sweep mode at a rate of 0.45 K/min. The length change curves for each sample are presented in Figure 5.18.

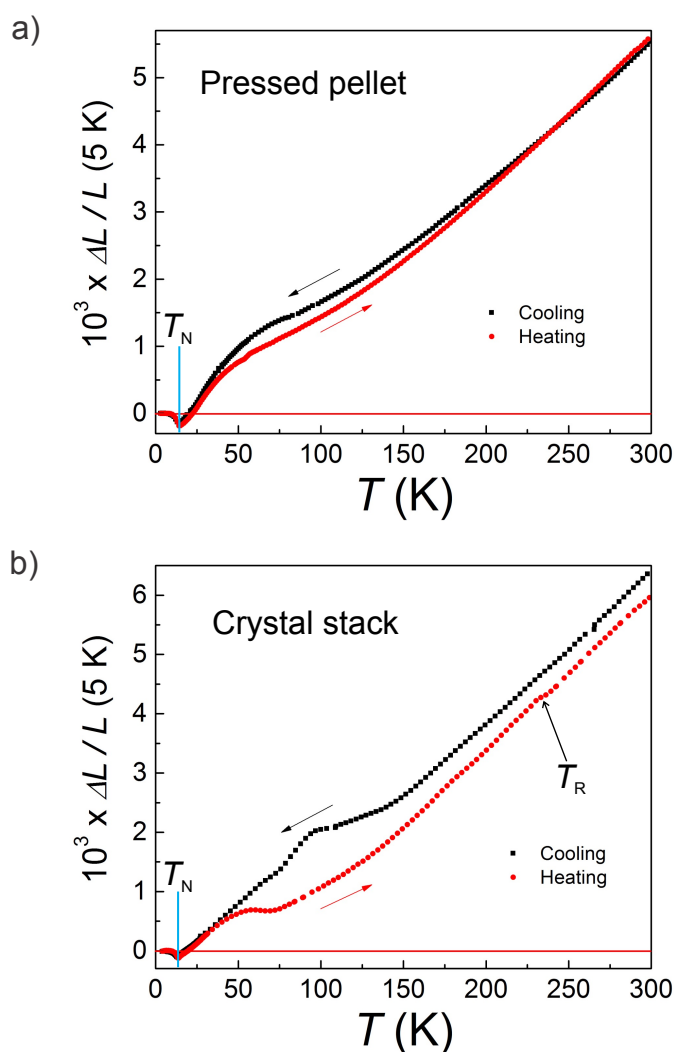


Figure 5.18: The temperature dependent length change relative to 5 K of two CrOCl samples (the pressed pellet and the crystal stack) for the heating and the cooling cycles at $H = 0$ Tesla. The T_R transition is discussed in Section 5.4.3 on p. 160.

The low temperature thermal expansion of each sample for temperatures less than 35 K can be seen in Figure 5.19.

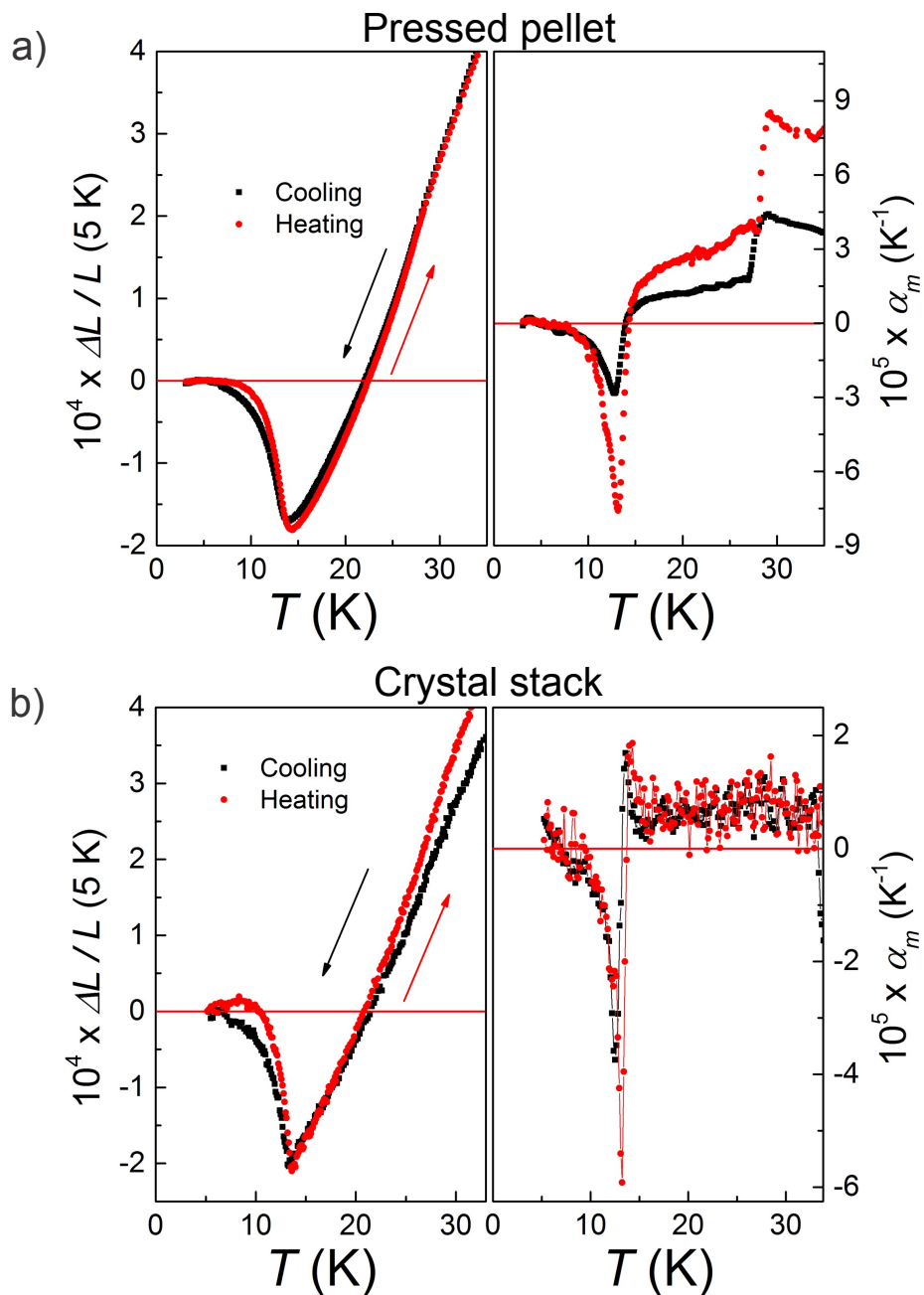


Figure 5.19: The temperature dependent length change relative to 5 K and the average linear coefficient of thermal expansion $\alpha_m(T)$ for the cooling and the heating cycles of two CrOCl samples at $H = 0$ Tesla: a) The pressed pellet b) The crystal stack. The precise Néel transition temperatures are obtained by fitting a Gaussian to the anomalies in the $\alpha_m(T)$ curves. The lines in the lower right graph are a guide to the eyes.

Initially exploratory measurements were performed with lower temperature resolution. Upon cooling, the crystal stack and the pressed pellet exhibit thermal contraction of the same order of magnitude. Anomalies due to the magnetic ordering at temperatures denoted as T_N are observed for both samples. Below ~ 15 K, expansion occurs with decreasing temperature indicating the sizable magnetoelastic coupling associated with the magnetic ordering. The anomalies are very sharp in the temperature region for the crystal stack but somewhat smeared out for the pressed pellet. The data collected on the pressed pellet are less noisy when compared to the crystal stack due to the increased thickness of the pressed pellet. The transition temperatures are magnetic field dependent and have subsequently been investigated in detail with fine temperature steps as described below. Splittings in the heating and the cooling cycles collected by raising and lowering the temperature are observed for both samples with different magnitudes. These splittings which are more pronounced for the crystal stack are not affected by the magnetic field. At the present time, they are attributed to a systematic error due to the thermally induced movements of the platelets in the crystal stack and the pressed pellet.

Highly temperature resolved zero magnetic field measurements below 35 K are displayed in Figure 5.19. The anomalies at T_N occur at similar temperatures with a comparable magnitude and shape for both samples. Below T_N , expansion occurs as the temperature decreases with a magnitude of $\sim 2 \times 10^{-4}$ which levels off below 7 K. Similar expansion behaviour occurs below ~ 13 K along the c -axis in the first temperature dependent neutron powder diffraction data. In contrast, the neutron powder diffraction data also indicated that the a and b axes exhibit contraction at low temperature.[171] T_N can be clearly observed in the average linear coefficient of thermal expansion $\alpha_m(T)$. The transition temperatures are similar to the heat capacity, the magnetic susceptibility and the literature results. The T_N transition exhibits thermal hysteresis for the cooling and the heating cycles consistent with a first order phase transition. The thermal hysteresis of the transition at T_N in the case of the crystal stack is nearly three times larger than that of the pressed pellet. The larger thermal hysteresis of the T_N transition for the crystal stack is attributed to the slight thermally induced movements of the crystals composing the crystal stack.

An additional anomaly in the $\alpha_m(T)$ is noted for the pressed pellet near 28 K which is attributed to the T^* transition (see Figure 5.6 on p. 118). This anomaly is absent in the thermal expansion data along the c -axis for the crystal stack. This observation implies that the anomaly seen in the randomly oriented pressed pellet is most likely due to thermal contraction upon cooling within the \mathbf{ab} plane. The transition temperatures of T^* in $\alpha_m(T)$ are comparable with the literature and the heat capacity results. A splitting of this anomaly has been observed in the heat capacity data however this behaviour is not detected in $\alpha_m(T)$. For all measurements, the transitions are sharper for the heating cycle $\alpha_m(T)$ curves. Hence, only the heating cycle curves are discussed in the following sections.

The thermal expansion of the crystal stack was measured with $H \perp c$ and $H \parallel c$. The temperature dependent length change at various magnetic field can be seen in Figure 5.20. With the magnetic field aligned parallel ($H \parallel c$) and perpendicular ($H \perp c$) to the stack, the low temperature region ($T < 22$ K in Figure 5.20) of the length change curves shift upwards with increasing magnetic fields. The shift of T_N with $H \parallel c$ is large and non-monotonic whereas T_N with $H \perp c$ is almost independent of the magnetic field up to 5 Tesla. With increasing parallel magnetic fields ($H \parallel c$), T_N decreases to a minimum of ~ 10 K at 3.25 Tesla and subsequently increases again to ~ 17 K at 9 Tesla. The magnitude of the anomalies at T_N also change significantly with the orientation of the magnetic field. For $H \perp c$, the negative thermal expansion disappears for magnetic fields above 7.5 Tesla whereas tiny dips still survive when $H \parallel c$. The effect of magnetic fields on the length change curves can be further analyzed through the average linear coefficient of thermal expansion $\alpha_m(T)$ (see Figure 5.21). $\alpha_m(T)$ is obtained by taking the derivative of a length change curve with respect to temperature. These results reveal negative peaks below 6 Tesla which flip to positive anomalies for magnetic fields higher than 6 Tesla (see Figure 5.21). The temperatures of the maxima and minima in $\alpha_m(T)$ are used to construct part of the extended (H, T) magnetic phase diagrams in Section 5.4.1.

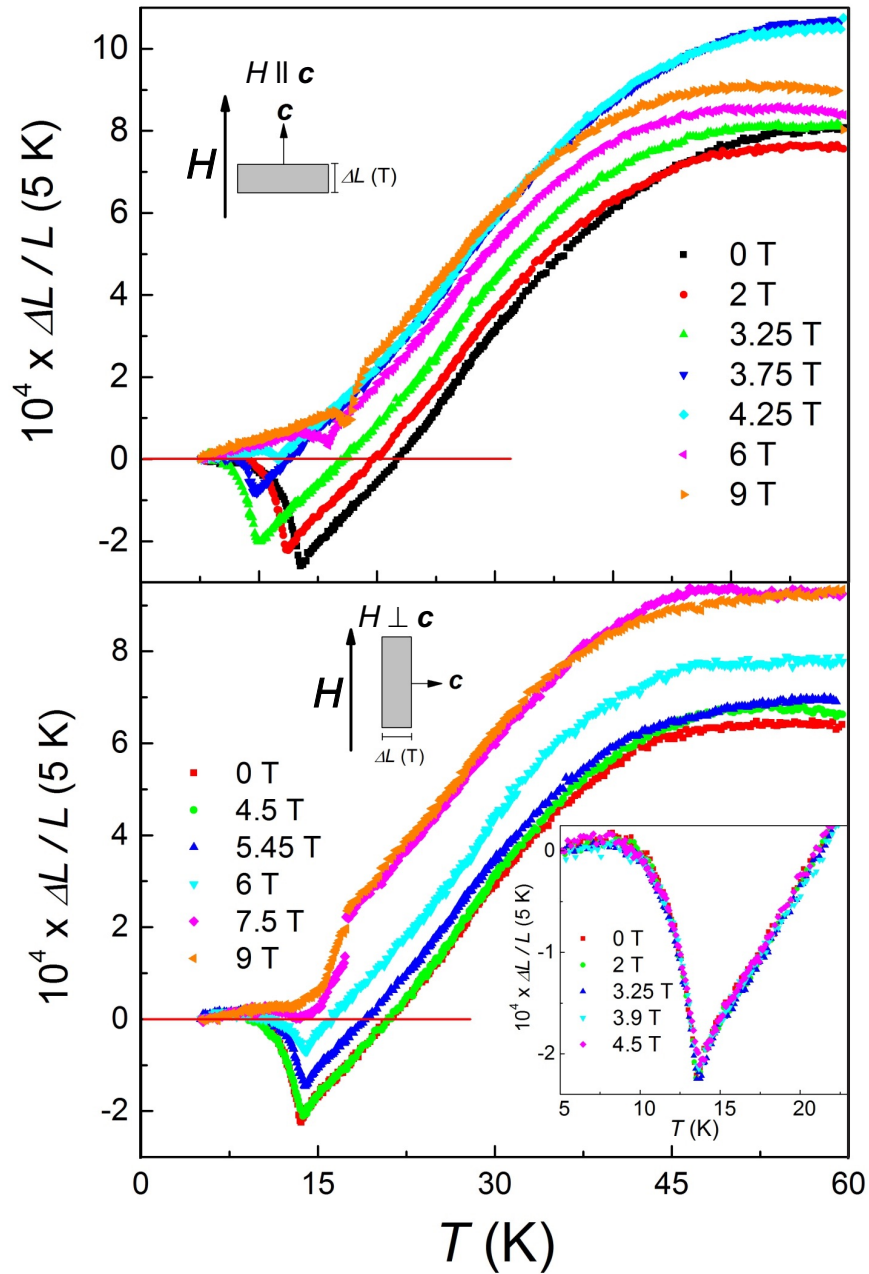


Figure 5.20: The temperature dependent length change of the CrOCl crystal stack at various magnetic fields ($H \parallel c$ and $H \perp c$). The magnetic fields are indicated in the inset legends.

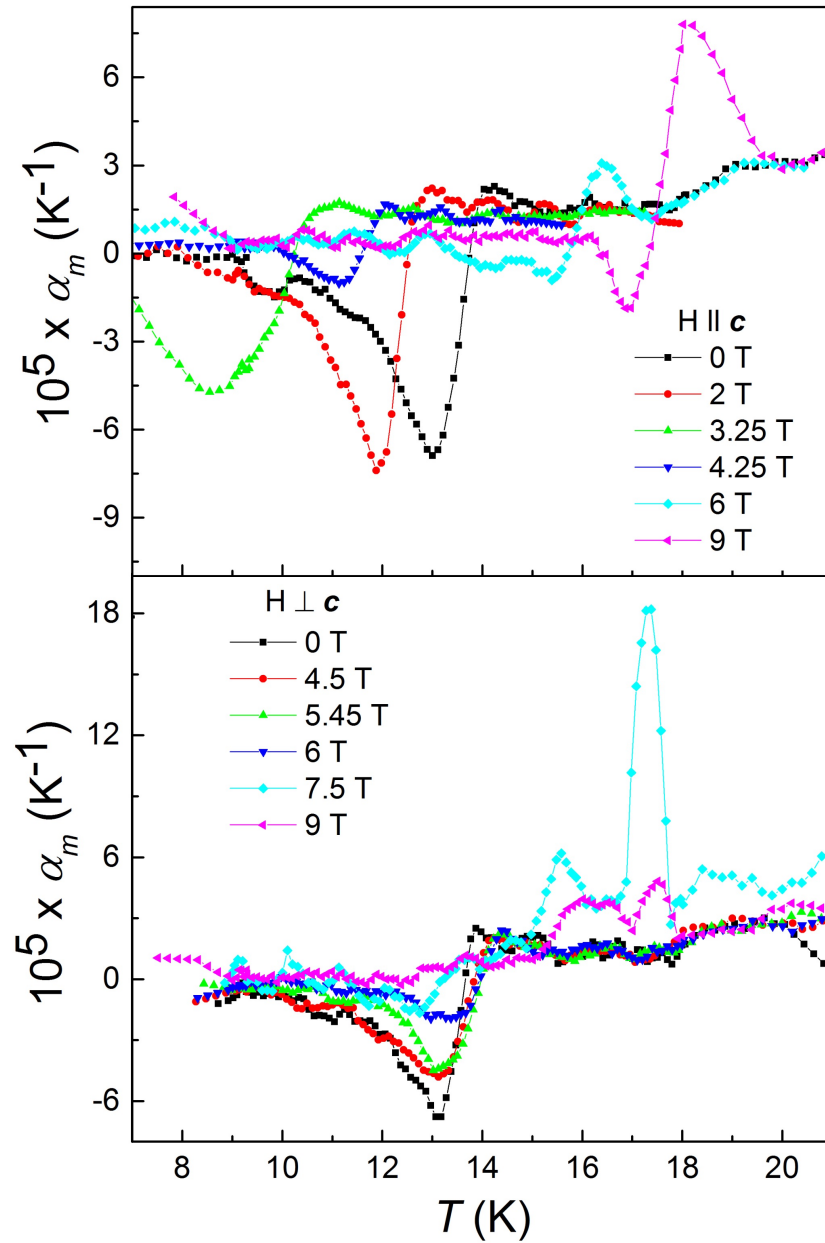


Figure 5.21: The temperature dependent average linear coefficient of thermal expansion $\alpha_m(T)$ of the CrOCl crystal stack at various magnetic fields ($H \parallel c$ and $H \perp c$). The magnetic fields are indicated in the inset legends.

In order to complete the extended (H, T) magnetic phase diagrams, the magnetostriction⁶ with $H \perp \mathbf{c}$ and $H \parallel \mathbf{c}$ was also measured. The data are compiled in Figures 5.22 and 5.23. For $H \perp \mathbf{c}$, the magnetic field scans reveal only one transition occurring between 6 and 7 Tesla which becomes weaker with increasing temperature. For $H \parallel \mathbf{c}$, up to three transitions can be seen depending on the temperature. The width of the transition region in the curves initially decreases with increasing temperature up to ~ 8.0 K. Above 8.0 K, the transition region widens with increasing temperature and eventually disappears near ~ 17 K. The magnetic fields at which the transitions occur are used to construct part of the extended (H, T) magnetic phase diagrams in Section 5.4.1.

⁶In the magnetostriction measurements, magnetic field scans of the thermal expansion at constant temperatures were performed.

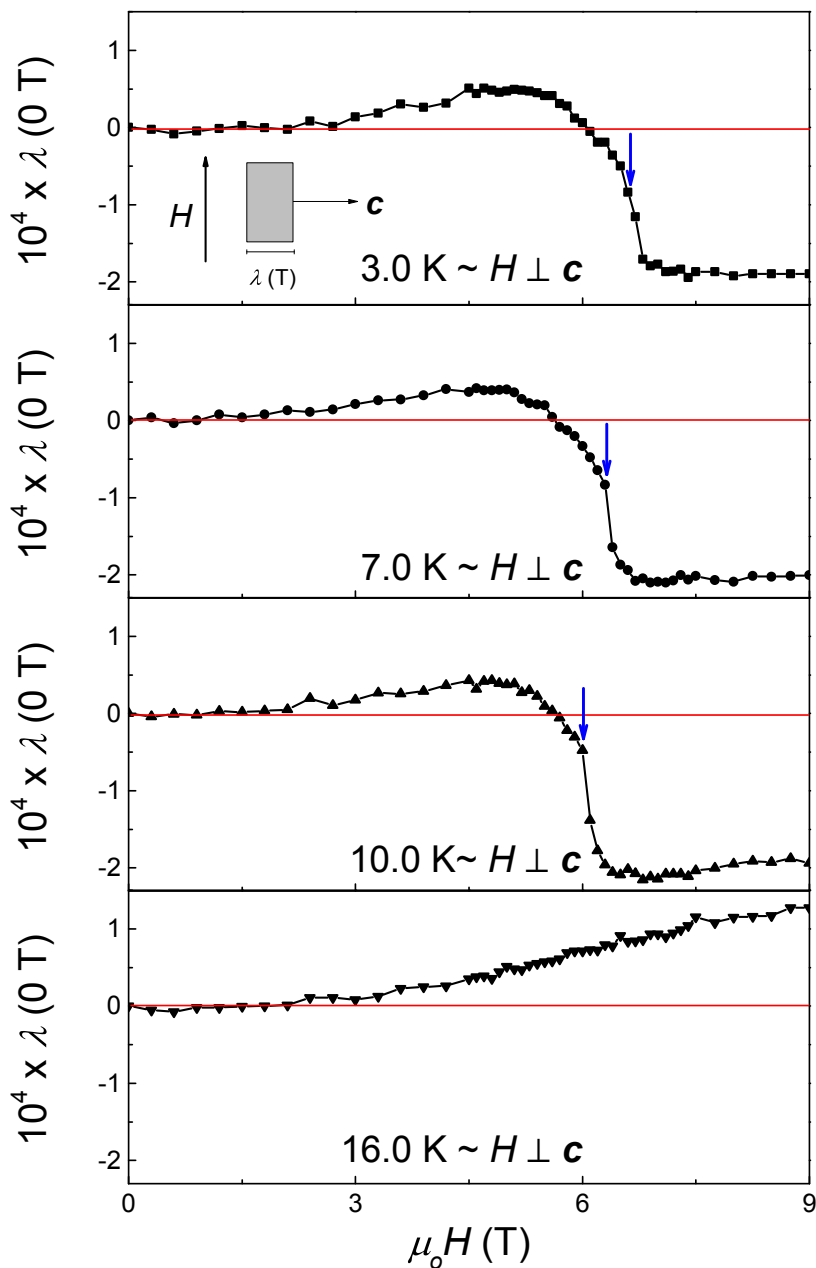


Figure 5.22: The magnetostriction at constant temperatures of the CrOCl crystal stack for $H \perp c$ showing the 3.0 K, 7.0 K, 10.0 K and 16.0 K curves. $\lambda(0 \text{ T})$ is the longitudinal magnetostriction equal to $\frac{\Delta L}{L}(0 \text{ T})$. Longitudinal magnetostriction is discussed in Section 2.1.2 on p. 14.

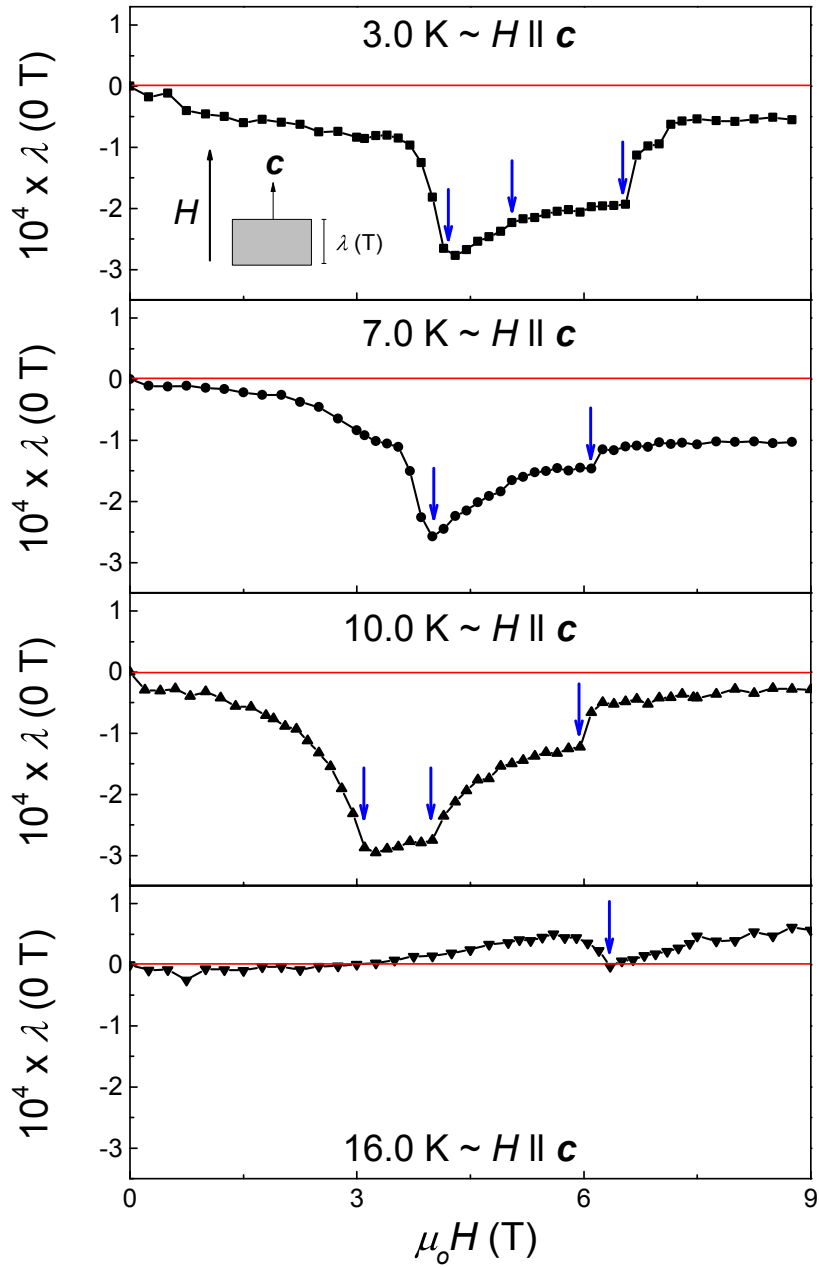


Figure 5.23: The magnetostriction at constant temperatures of the CrOCl crystal stack for $H \parallel c$ showing the 3.0 K, 7.0 K, 10.0 K and 16.0 K curves. $\lambda(0 \text{ T})$ is the longitudinal magnetostriction equal to $\frac{\Delta L}{L}(0 \text{ T})$. Longitudinal magnetostriction is discussed in Section 2.1.2 on p. 14.

5.3.4 Dielectric measurements

The dielectric measurements were performed using an Agilent Technologies E4980A Precision LCR meter. In Figure 5.24, electrode plate/contacts were created on the top/bottom of the crystal using SPI-Paint high purity silver paint diluted with SPI-Paint silver paint thinner (SPI Supplies, P.O. Box 656, West Chester PA, 19381 U.S.A). The CrOCl crystals chosen for the dielectric measurements (see Figure 5.24) had a typical thickness of ~ 0.02 mm. A twenty micron gold wire was inserted into the wet silver paint on both sides of the crystals. After the silver paint was dry, the crystals were placed on the sample holder and secured with double sided Tesa tape. Special care was taken to use a very thin silver paint layer in order to prevent cleaving of the crystals due to mechanical stress induced by the temperature cycles. Cleaving can be easily identified by ‘jumps’ in the capacitance curves.

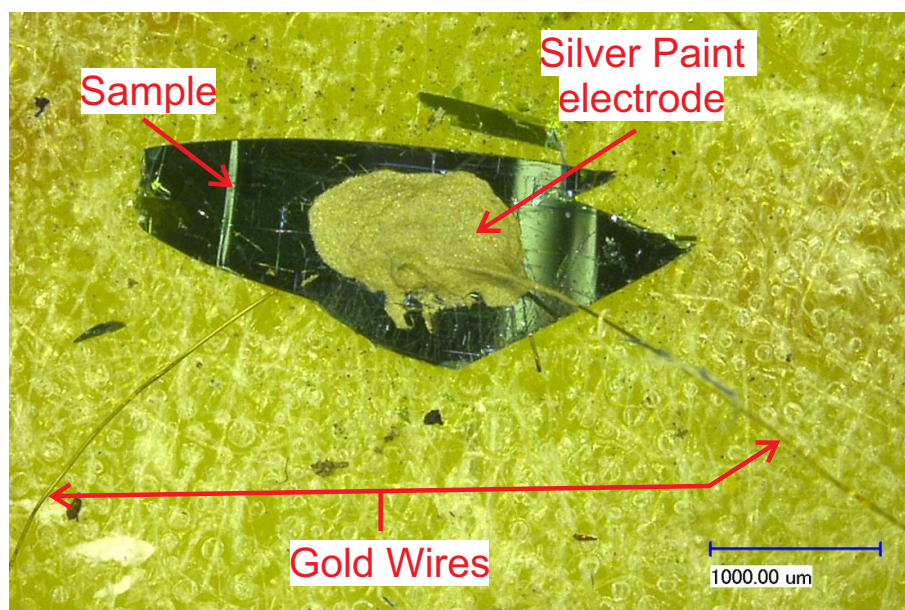


Figure 5.24: Mounting of a CrOCl crystal for the dielectric measurements showing a closeup view of the crystal and the top electrode plate.

Dielectric measurements were performed between 300 K and 1.3 K with magnetic fields up to 12 Tesla. A constant applied electric field and frequency of ~ 1000 V/m and 5 kHz respectively were used during the measurements. Below 6 Tesla, a sealed sample environment filled with ~ 300 mbar of ^4He exchange gas at room temperature was used. Above 6 Tesla, a variable temperature insert with flowing Helium gas (an open sample environment) surrounding

the crystal was utilized with the ^4He gas pressure stabilized to ~ 150 mbar. The measurements were performed using a temperature sweep rate of 1.0 K/min. Generally, the curves obtained by heating are less noisy and hence these results are discussed here. Figure 5.25 displays an overview of the relative dielectric constant ϵ_r of a CrOCl crystal measured with the electric field applied parallel to the c -axis at $H = 0$ Tesla.

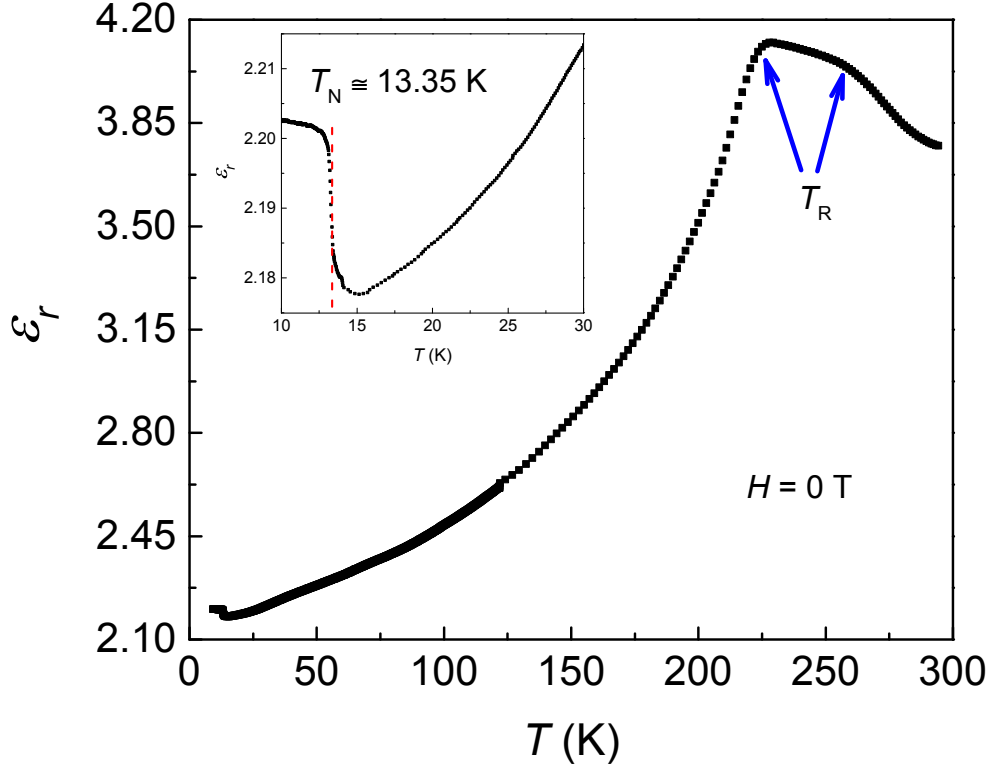


Figure 5.25: Main: The temperature dependence of the relative dielectric constant ϵ_r of a CrOCl crystal in a zero magnetic field for the heating cycle measured in a sealed sample environment. The blue arrows point to the temperature region where the T_R transition occurs. Inset: The low temperature region of the curve plotted in the main part of the Figure showing the anomaly near ~ 13 K resulting from the Néel transition. The electric field was applied parallel to the c -axis.

At room temperature (RT), ϵ_r has a value of ~ 3.78 . A broad peak occurs in ϵ_r as the temperature decreases with a maximum ϵ_r value of ~ 4.12 (+9% increase from the RT value) between ~ 200 and ~ 250 K. Indications for this anomaly had previously been observed in the dielectric measurements by Williamson in her placement thesis for other batches of CrOCl crystals.[172] This anomaly will be discussed in more detail later in this Chapter (see Section 5.4.3 on

p. 160). Below the anomaly (the T_R transition), ϵ_r decreases monotonically passing through a minimum at ~ 15 K with a minimum value of ~ 2.18 . The T_{mag} and the T^* transitions near 27 K known from the magnetic susceptibility and the heat capacity results are not observed in the ϵ_r data. Below 15 K, ϵ_r rapidly increases to ~ 2.20 (+1.1% from the 15 K value of ϵ_r) and saturates at very low temperature with value ~ 2.205 . The rapid increase in ϵ_r can be attributed to the magnetoelastic nature of the antiferromagnetic transition as seen in the thermal expansion results. From the steepest slope, the exact transition temperature is identified as $\sim 13.35 \pm 0.05$ K consistent with the literature and the previous measurements.

Similar to the thermal expansion measurements, the magnetic field dependence of the relative dielectric constant ϵ_r was also measured. Magnetic fields up to 12 Tesla in two orientations ($H \perp c$ and $H \parallel c$) were utilized. First, the temperature dependence of ϵ_r was measured at various constant magnetic fields (see Figure 5.26 and 5.27). The effect of the magnetic field on T_N is similar for both orientations but the shift in T_N is slightly higher (~ 1 K) for $H \parallel c$. In general, T_N shifts downward with increasing magnetic fields below 4 Tesla. The minimum value of T_N occurs at ~ 10 K near ~ 3.3 Tesla. Above 4 Tesla, the ϵ_r curves flip over and T_N shifts upward with increasing magnetic fields. At 12 Tesla, T_N increases by ~ 2.2 K and ~ 1.3 K respectively for the $H \parallel c$ and $H \perp c$ orientations relative to 0 Tesla. Magnetic field scans of ϵ_r at constant temperatures ('magnetocapacitance') from 0 Tesla \rightarrow 6 Tesla and 6 Tesla \rightarrow 0 Tesla were also performed. The results of the magnetocapacitance measurements are presented in Figures 5.28 to 5.29. Again, the results for both orientations are similar but the width of the anomalies in the ϵ_r curves are slightly larger for $H \perp c$ particularly below 5 K. In general, a single broad anomaly is observed at the lowest temperatures and the width of the anomaly decreases with increasing magnetic field (see the ~ 7 K curves in Figures 5.28 and 5.29). The anomaly in the ϵ_r curves remains narrow up to approximately ~ 9.0 K. Above 9 K, two anomalies are observed in ϵ_r and the anomalies move apart with increasing magnetic fields. No anomalies are observed above 16.0 K. For both orientations, the magnetic field dependence of T_N and the anomalies in the magnetocapacitance results are used to construct part of the extended (H, T) magnetic phase diagrams in Section 5.4.1.

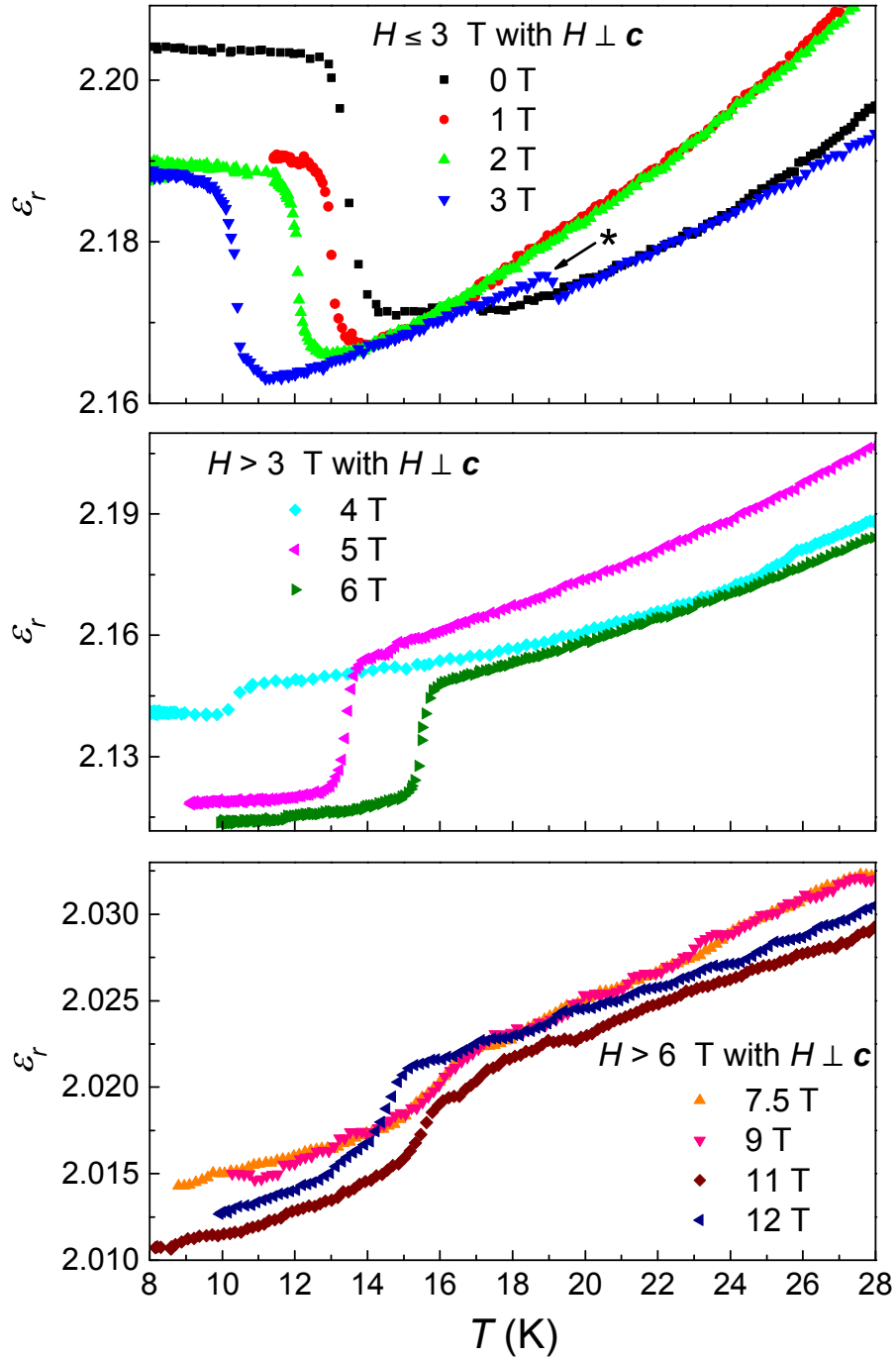


Figure 5.26: The temperature dependence of the relative dielectric constant ϵ_r of a CrOCl crystal at various magnetic fields ($H \perp c$) obtained from the heating cycle measurements. The anomaly denoted by the asterisk (*) (see upper panel) is only observed once and is tentatively attributed to gas contamination on the electrode surfaces. The magnetic fields are indicated in the inset legends.

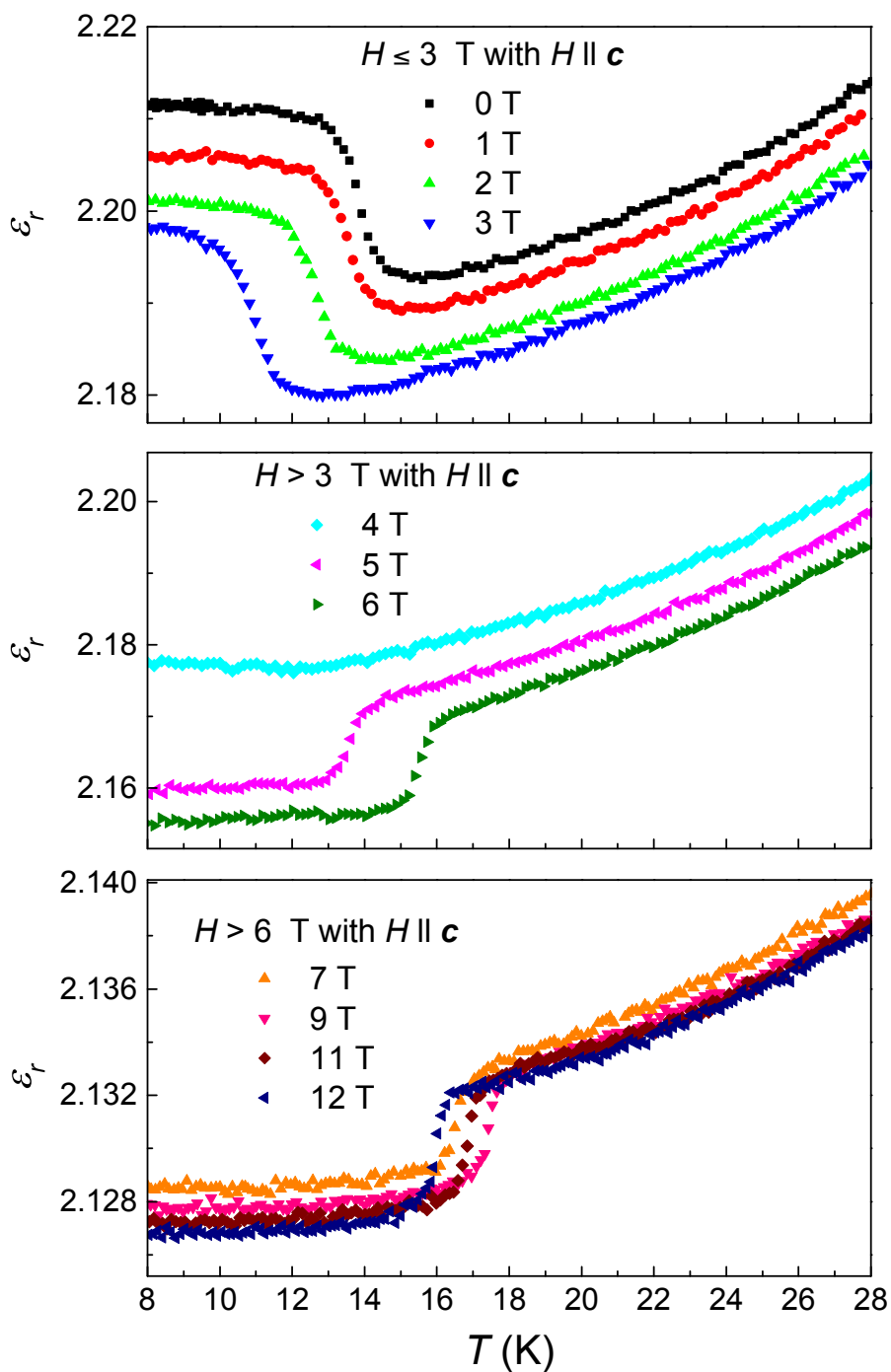


Figure 5.27: The temperature dependence of the relative dielectric constant ϵ_r of a CrOCl crystal at various magnetic fields ($H \parallel c$) obtained from the heating cycle measurements. The magnetic fields are indicated in the inset legends.

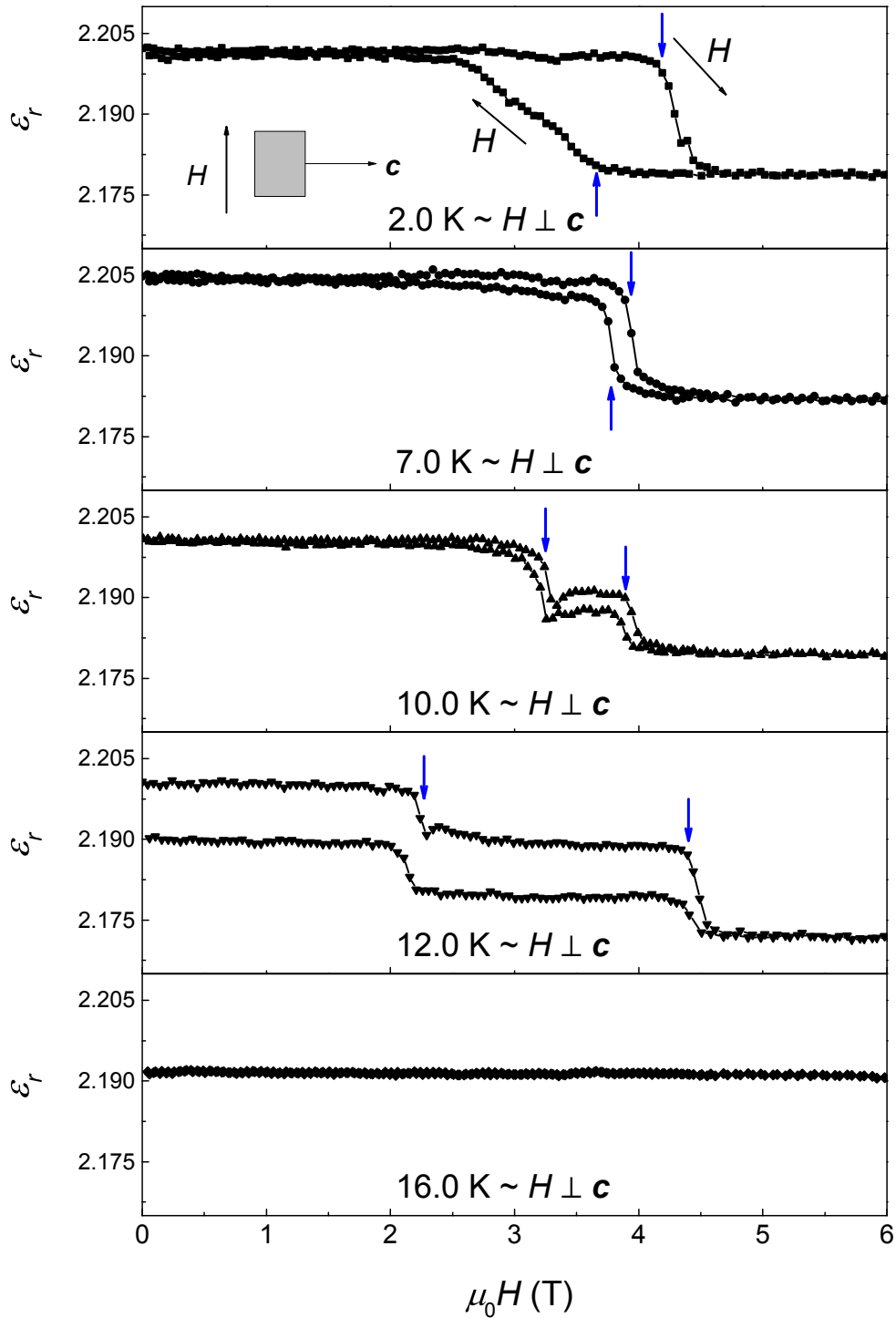


Figure 5.28: The magnetocapacitance of a CrOCl crystal at constant temperatures with $H \perp c$ showing the results for 2.0 K, 7.0 K, 10.0 K, 12.0 K and 16.0 K.

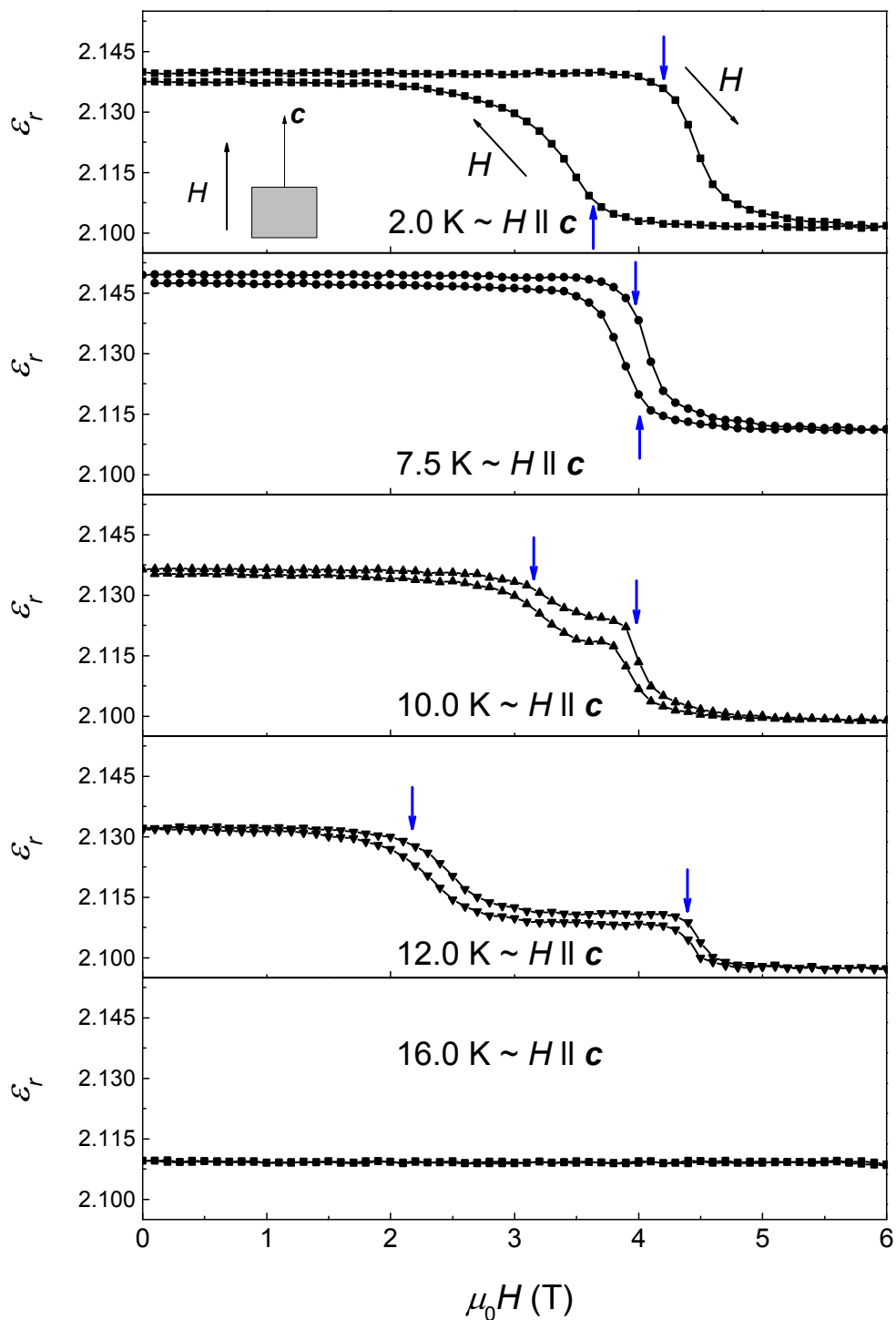


Figure 5.29: The magnetocapacitance of a CrOCl crystal at constant temperatures with $H \parallel c$ showing the results for 2.0 K, 7.5 K, 10.0 K, 12.0 K and 16.0 K.

5.4 Results

5.4.1 Magnetic phase diagrams

The anomalies and the magnetic field dependence of the three transitions (T_N , T_{mag} and T^*) from the various measurements were used to construct the extended (H, T) magnetic phase diagrams for $H \parallel \mathbf{c}$ and $H \perp \mathbf{c}$ (see Figure 5.30). Dielectric measurements were particularly useful for resolving the region around the spin-flop (SF) phase. As compared to the previously published preliminary (H, T) magnetic phase diagram which only consider the $H \parallel \mathbf{c}$ orientation, the new extended (H, T) magnetic phase diagrams clarifies the following points:

1. The spin-flop phase (phase II) is significantly smaller than previously concluded.
2. In both orientations ($H \parallel \mathbf{c}$ and $H \perp \mathbf{c}$), magnetostriction and magnetic field dependent heat capacity measurements reveal an additional phase above the spin-flop phase denoted as phase IV. The detailed nature of this phase is not known yet.
3. In both orientations, the bifurcation of the spin-flop phase line enclosing a triangular shaped region at low temperatures and magnetic fields below ~ 5 Tesla has been clarified. This area of the previous phase diagram was dubious and is now denoted as phase VI.
4. With the magnetic field perpendicular to \mathbf{c} , two additional phases (phase V and VII) becomes apparent enclosed by I, II and III. The boundaries of these phases have been established by the heat capacity and the thermal expansion measurements.
5. The low field magnetization and the dielectric data are the only measurements which are similar for both magnetic field orientations. These anomalies established the boundaries between phases I, II, III and VI.

6. The pulsed field magnetization data indicate that the upper critical field for both orientations is approximately 19 Tesla. An additional weaker anomaly is also observed in the pulsed field results when the magnetic field is ramped down. Another high field phase is formed by the boundaries obtained from the results of these high magnetic field measurements denoted as phase VIII.
7. The phases IV, V, VI, VII and VIII have not been observed previously.
8. The T_{mag} and T^* phase boundaries near ~ 27 K, so far, can only be detected by heat capacity experiments. They are not observed in the thermal expansion and the dielectric capacitance measurements.
9. T^* is largely independent of the applied magnetic field in both orientations which strongly suggests that it is a structural phase transition.

In conclusion, these investigations find that the extended (H, T) magnetic phase diagrams are even more complex than originally proposed. Especially the thermal expansion, the heat capacity and the pulsed field magnetization measurements revealed new phases which had not been seen before. These newly established intricate magnetic phase diagrams also demonstrate the complex relation between the spin exchange coupling constants. This complex relationship is examined in detail by spin polarized electronic structure calculations later in this Chapter (see Section 5.4.4 on p. 166).

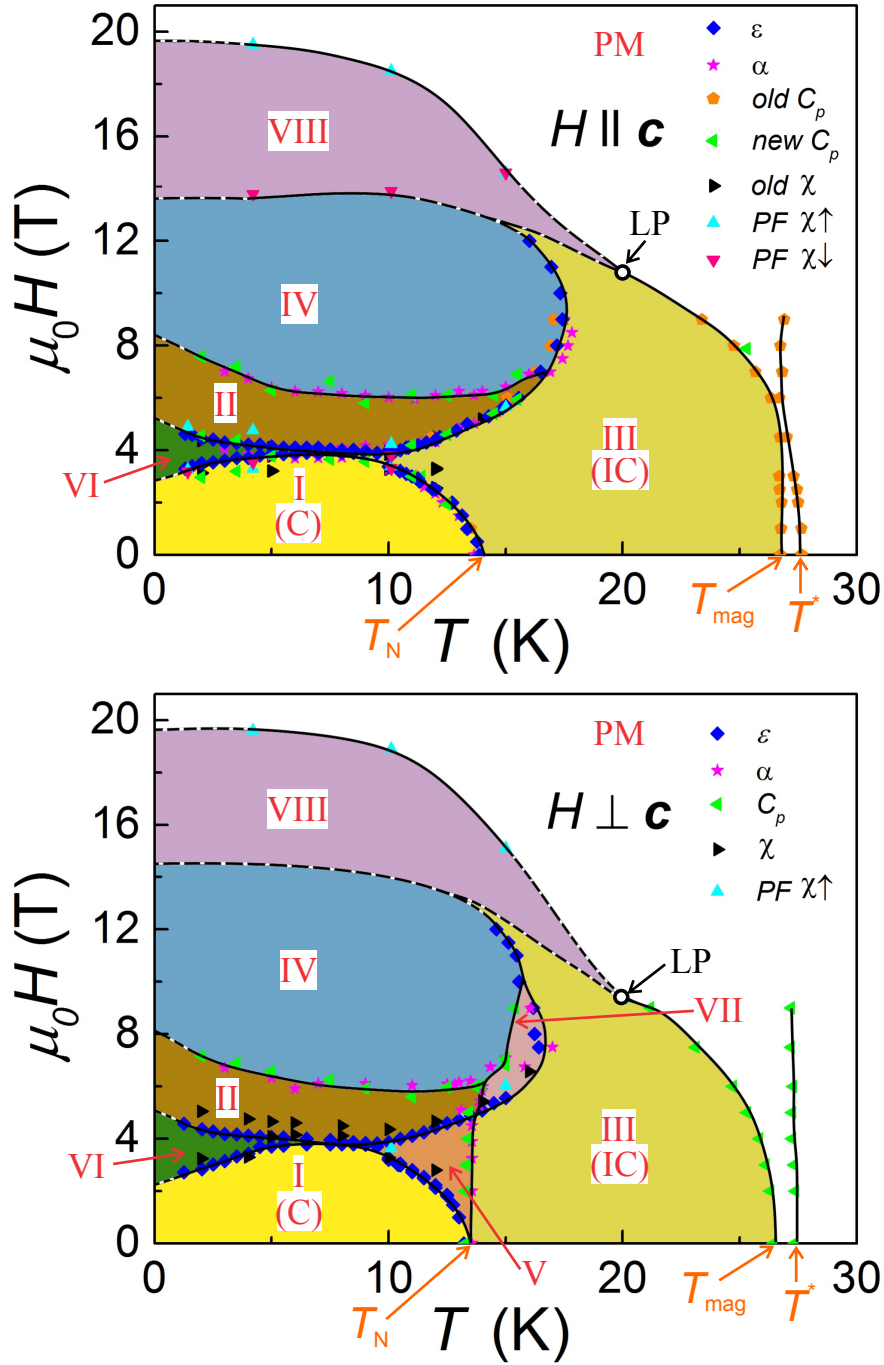


Figure 5.30: The extended (H, T) magnetic phase diagrams of CrOCl for $H \parallel c$ and $H \perp c$ where the solid lines denotes a verified phase boundary and the dashed lines indicate an extrapolated phase boundary. $PF \chi \uparrow$ and $PF \chi \downarrow$ indicate the data obtained from measurements in the pulsed fields by raising and lowering the magnetic field respectively. IC and C refer to the incommensurate and commensurate magnetic phases respectively. LP identifies the multicritical ‘Lifshitz’ point. The previously published results referred to as ‘Old C_p ’ in the top diagram were obtained from Angelkort *et. al.* [159].

5.4.2 Neutron diffraction measurements

In a collaboration with Prof. van Smaalen's group at the University of Bayreuth, the magnetic structures associated with the phases I and III in the (H, T) magnetic phase diagrams were investigated using neutron powder diffraction measurements at zero magnetic field. Patterns were collected using a wavelength of 1.54 Å at stabilized temperatures covering the magnetic ordering temperature ranges. In addition to the nuclear Bragg peaks, magnetic superstructure Bragg peaks are detected below T_{mag} and below T_{N} . Weak magnetic Bragg reflections are observed between 18° and 24° in the powder patterns below the T_{mag} transition. As the temperature is further decreased, the intensity of the magnetic reflections increased continuously. Below T_{N} , the magnetic Bragg peaks are found to be commensurate with the distorted monoclinic structure established by the single crystal synchrotron diffraction measurements.[159] Between T_{N} and T_{mag} , the magnetic structure is incommensurate with the orthorhombic (room temperature) structure.

The superspace approach [142] is used to analyze the nuclear and the magnetic contributions to the neutron powder diffraction patterns. As discussed previously, three phase transitions (T_{N} , T_{mag} and T^*) occur below 30 K. The room temperature orthorhombic crystal structure remains down to T_{N} . The \mathbf{a} and \mathbf{b} axes expand and the \mathbf{c} -axis contracts with decreasing temperatures (see Table 5.2). Below T_{N} , a distorted monoclinic crystal structure is observed with a tiny increase of the monoclinic angle α from the orthorhombic 90° to 90.07°. Additionally, the \mathbf{c} -axis increases slightly (see Table 5.2) in the monoclinic crystal structure. Nevertheless, the \mathbf{c} -axis in the orthorhombic and the monoclinic crystal structures can be considered to be essentially parallel. These findings are consistent with the thermal expansion data and the previous single crystal synchrotron x-ray diffraction results.[159] There is no indication of the T^* transition in the patterns. But T_{mag} can be detected when the magnetic contributions to the patterns are analyzed. The magnetic contributions to the patterns will be discussed in the next paragraph.

	$T = 3 \text{ K}$	$T = 17 \text{ K}$	$T = 50 \text{ K}$
Structure	monoclinic $P2_1/m$	orthorhombic $Pmmn$	orthorhombic $Pmmn$
a (Å)	3.86319(3)	3.86379(4)	3.86218(4)
b (Å)	3.17751(2)	3.17818(3)	3.17717(4)
c (Å)	7.67552(9)	7.67198(10)	7.68011(15)
α (°)	90.0739(13)	90	90
V (Å ³)	94.2195(13)	94.2105(15)	94.2410(21)

Table 5.2: The lattice parameters and the structural details from the low temperature neutron powder diffraction measurements on CrOCl

The sudden appearance of the strongest magnetic Bragg reflection at $\sim 7^\circ$ in 2θ below T_N indicates that the T_N transition is of first order and represents a lock-in transition into a commensurate phase from the existing incommensurate phase between T_N and T_{mag} . In the superspace approach, the additional magnetic Bragg reflections below T_{mag} are indexed based on a propagation vector $q_{\text{magnetic}} = \sigma_2 \mathbf{b}^*$. The incommensurate (orthorhombic) and the commensurate (monoclinic) phase can be clearly differentiated through the temperature dependence of σ_2 . In the commensurate phase below T_N , σ_2 is found to be temperature independent with a value $\sigma_2 = \frac{1}{4}$ indicating a quadrupling of the magnetic unit cell⁷ along \mathbf{b} . The nuclear propagation vector of the low temperature monoclinic structure is $q_{\text{nuclear}} = \frac{1}{2} \mathbf{b}^*$ which amounts to two times the magnetic propagation vector $q_{\text{magnetic}} = \sigma_2 \mathbf{b}^*$. The magnetic induced charge scattering theory predicts that $q_{\text{nuclear}} = 2 \times q_{\text{magnetic}}$ which is confirmed by the aforementioned results. The doubling of the magnetic propagation vector is caused by the sensitivity of the atomic displacements to the magnetic modulation in the antiferromagnetic state.[164] In the incommensurate phase between T_N and T_{mag} , σ_2 is found to be temperature dependent with values given by the following equation: $\sigma_2(T) \approx 0.2403(2) - 0.000048(8) \cdot T$ for $T_N < T \leq T_{\text{mag}}$. A jump in σ_2 occurs at T_N from $\frac{1}{4}$ to 0.2393(3) with discontinuities in the lattice parameters and the unit cell volume being indicative of a first-order lock-in transition.

⁷The \mathbf{b} -axis in the low temperature monoclinic cell is identical to the \mathbf{b} -axis of the orthorhombic high temperature cell.

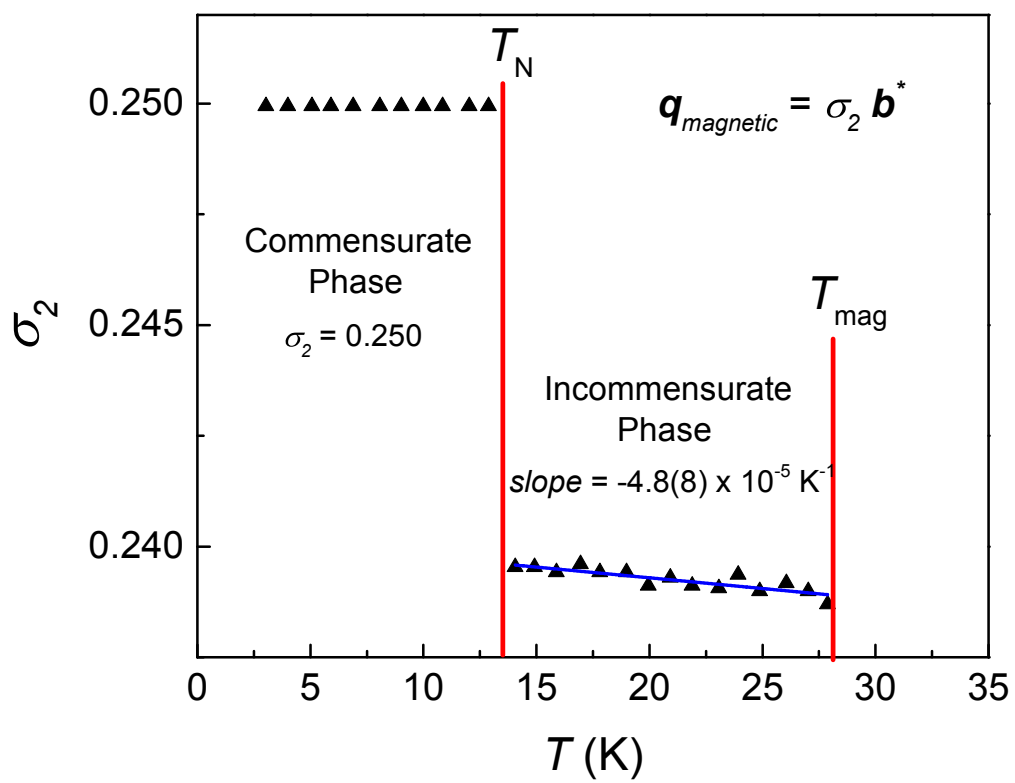


Figure 5.31: The temperature dependence of the propagation vector component σ_2 below 27 K for CrOCl.

The transition temperature of T_{mag} is estimated by integrating the intensities of three magnetic Bragg peaks between T_N and T_{mag} . The integrated intensities I_i follow the typical temperature dependence of a continuous (second order) phase transition (see Figure 5.32).

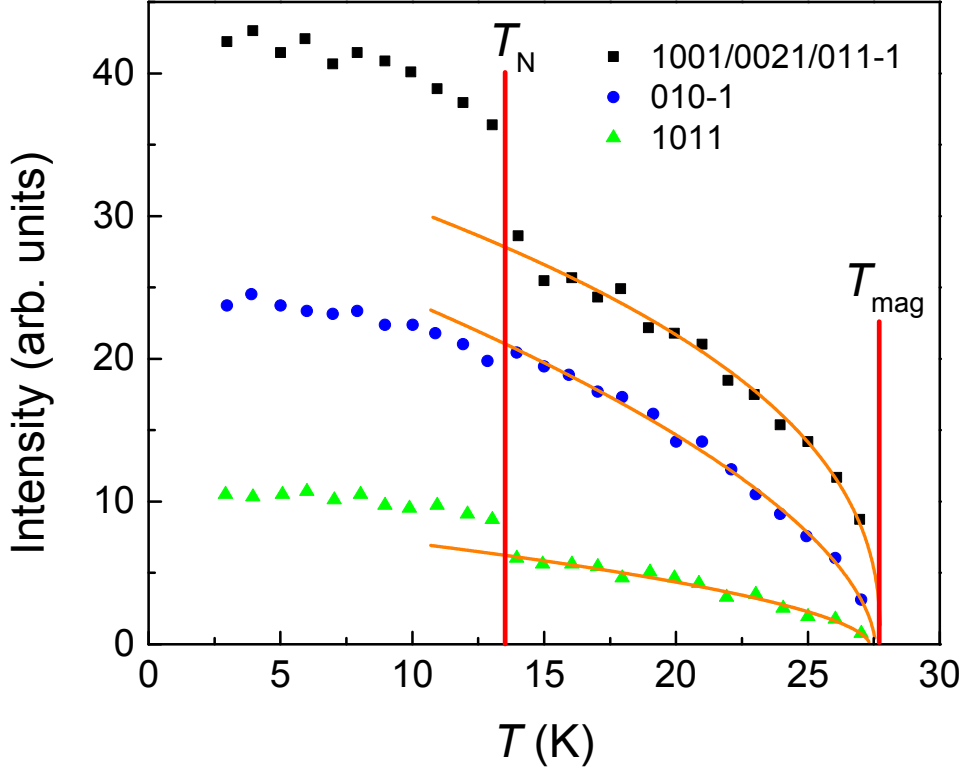


Figure 5.32: The temperature dependent intensities of three magnetic Bragg reflections for CrOCl showing the critical power law fits (the solid orange lines).

The intensities were fitted to the following critical power law:

$$I_i c(T) = I_{i0} (1 - T/T_{i,\text{mag}})^{2\beta} \quad (5.2)$$

where β is the critical exponent ($\beta \approx 0.30$) and $T_{i,\text{mag}}$ ($i = 1, 2$ and 3) are the critical temperatures derived from the fits of the intensities of the three magnetic Bragg reflections. When the three $T_{i,\text{mag}}$ temperatures are averaged, a critical temperature for T_{avermag} of $27.7(1)$ K is obtained. T_{avermag} is higher than the other measurement methods such as the heat capacity and the magnetic susceptibility. This may be due to slight differences in the calibration of the temperature sensors employed in the various instruments.

The refinement of the magnetic structures of CrOCl in the incommensurate and the commensurate lock-in phase was performed using the low temperature neutron diffraction patterns in the respective temperature ranges. In the commensurate monoclinic phase, the magnetic structure is refined at 3 K and 8 K based on a four-fold supercell with two different chromium sites in the magnetic supercell. The refinements converged to two slightly different chromium magnetic moments, ($\mathbf{S}_1 = 2.6(5) \mu_B$ and $\mathbf{S}_2 = 3.2(3) \mu_B$), with all moments aligned along the c -axis. Within experimental error, the refined spin moments are equal at 3 K and 8 K. Figure 5.33 displays a schematic outline of the magnetic structure of CrOCl. Fishnet patterned ferromagnetic stripes are formed along the a -axis with strands of four Cr moments - two at atomic position $+z$ and two at $-z$. The moment direction within the stripes themselves are aligned either parallel or antiparallel to the c -axis. Along the b -axis, the variation in the spin moments can be described by a spin density wave which is commensurate below T_N and incommensurate between T_N and T_{mag} . The amplitudes of the spin density wave decreases with increasing temperature as illustrated in Figure 5.34. Apart from the differentiation of the Cr moments, the magnetic structure (see Figure 5.3) is consistent with that proposed by Christensen *et al.* [25] previously.

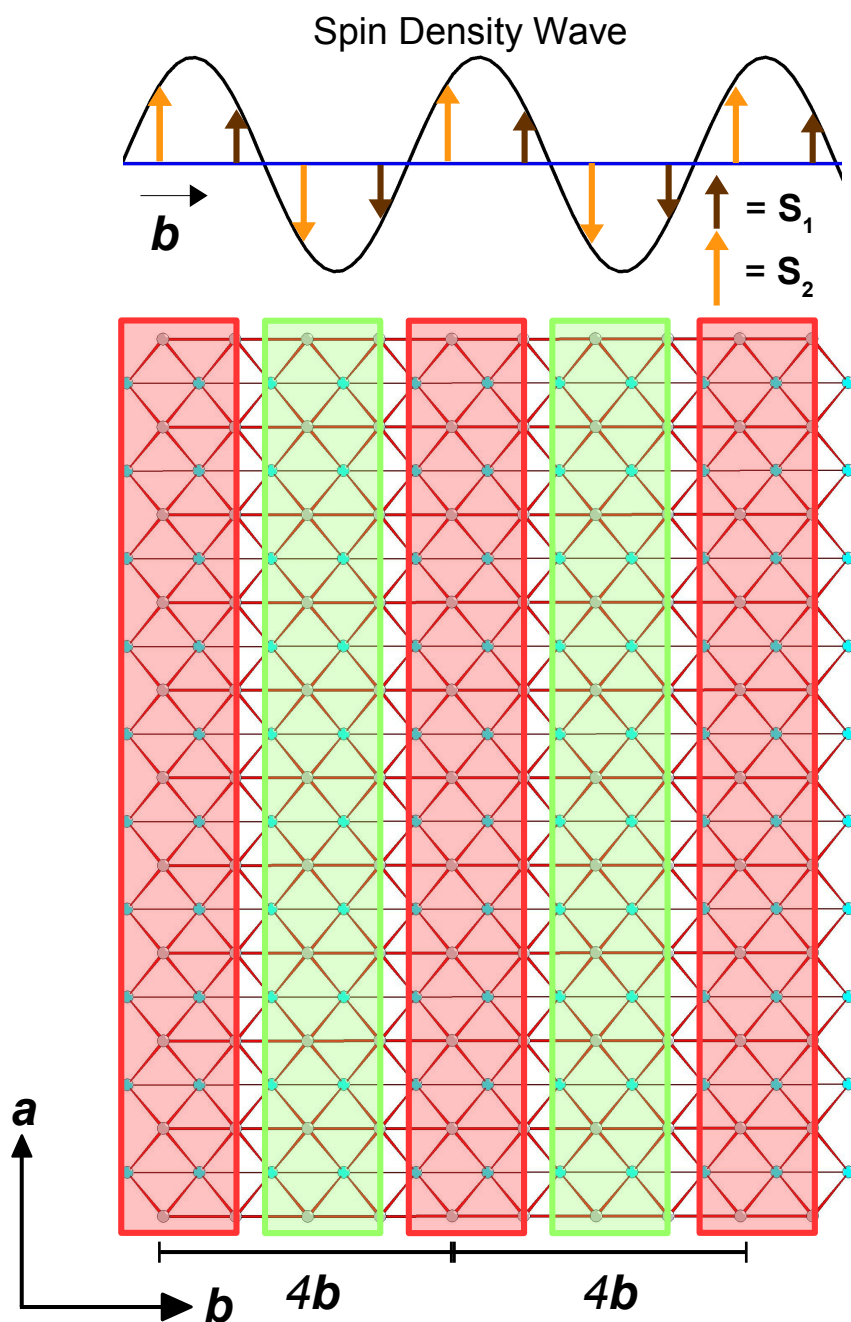


Figure 5.33: The low temperature magnetic structure of CrOCl in the commensurate and the incommensurate phases. The upper frame displays the spin density wave formed by the variation of the two Cr moments propagating along the b -axis. The stripe ordered magnetic structure is shown in the lower frame. The red and the green regions correspond to the Cr moment pointing up or down respectively along the c -axis.

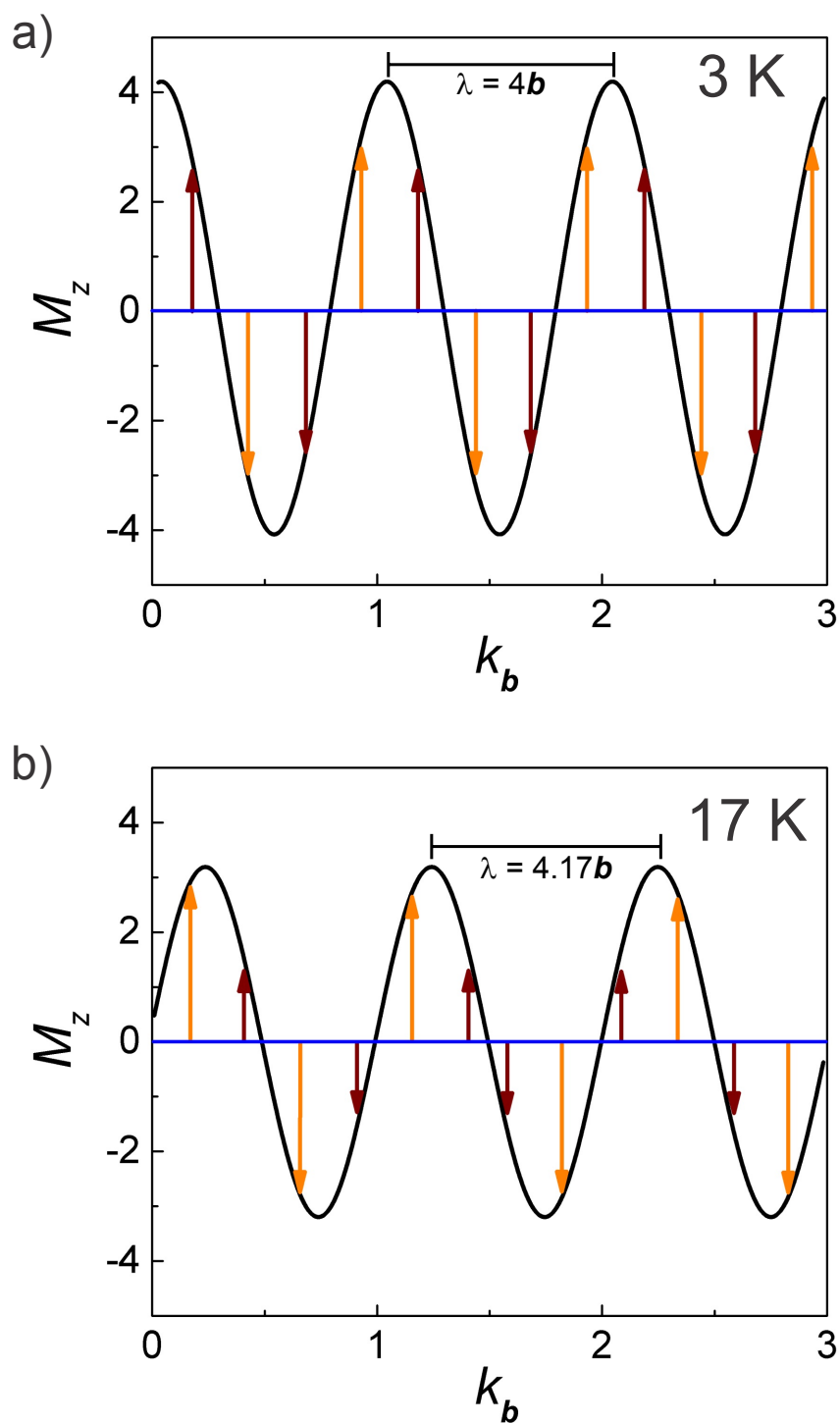


Figure 5.34: The magnetic spin density waves of CrOCl along the b -axis for the commensurate and the incommensurate phases. a) The four-fold magnetic superstructure in the commensurate phase with $q_{magnetic} = 0.25b^*$ or $\lambda = 4b$ b) The incommensurate intermediate phase with $q_{magnetic} \approx 0.2393b^*$ or $\lambda = 4.17b$. This Figure was produced from results in Ref. [173].

5.4.3 High temperature anomalies

The broad high temperature anomaly centred near ~ 240 K which was first observed in the dielectric capacitance measurements will now be discussed. Single crystal x-ray and neutron diffraction measurements gave no indication of a structural change at ~ 240 K whereas anomalies can be seen in the dielectric and the thermal expansion data (see Figure 5.35).

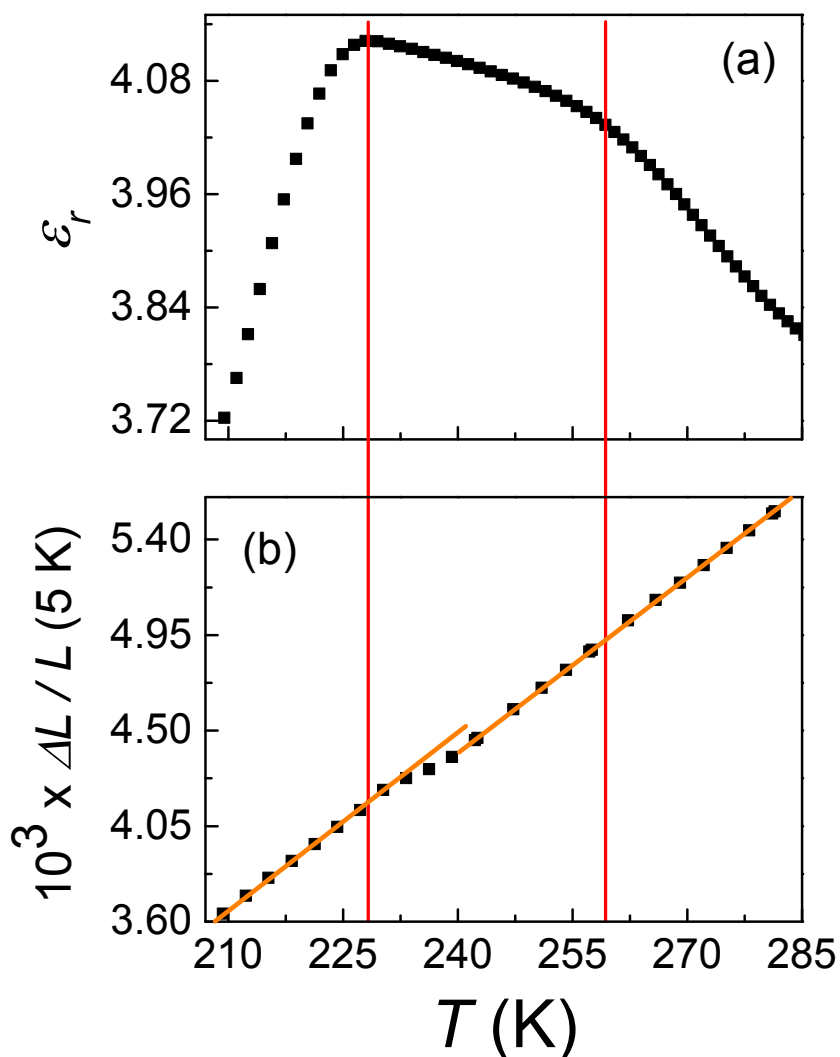


Figure 5.35: a) The temperature dependence of the relative dielectric constant ϵ_r for CrOCl b) The temperature dependence of the length change relative to 5 K for the CrOCl crystal stack.

In order to shed light on the anomalies near ~ 240 K, electron paramagnetic resonance and Raman scattering measurements were performed. The Raman scattering measurements are sensitive to structural changes whereas the electron paramagnetic resonance measurements detect changes in the spin sector. Electron Paramagnetic Resonance (EPR) spectra were measured on a thin platelet crystal ($\sim 2\text{mm} \times \sim 1\text{mm} \times \sim 0.2\text{mm}$) using a X-Band EPR spectrometer (see Section 3.2 on p. 24). Spectra with $H \parallel c$ were measured for temperatures between 200 K and 285 K with small temperature steps of 5 K. The spectrum measured at 245 K is presented in Figure 5.36.

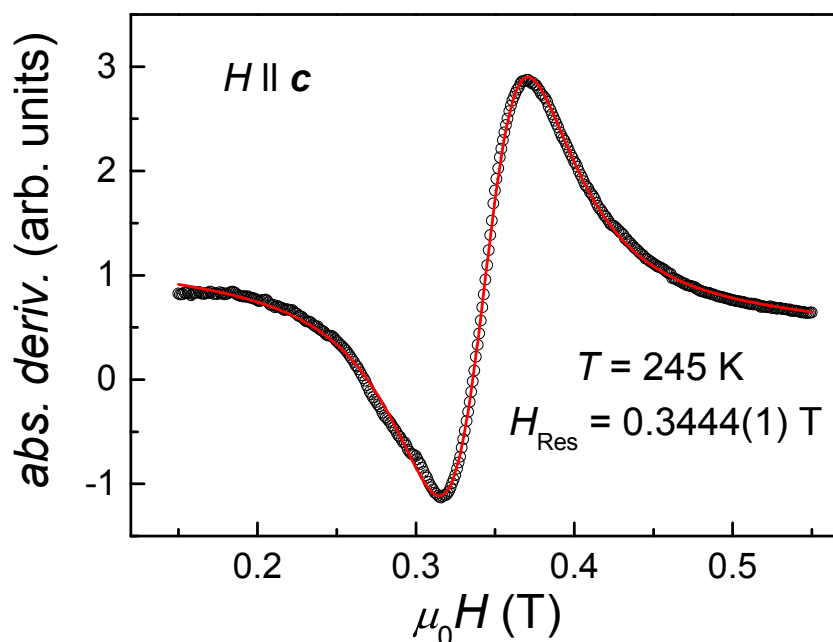


Figure 5.36: The electron paramagnetic resonance spectrum of a tiny CrOCl crystal with $H \parallel c$ measured at 245 K. N.B. *abs. deriv.* is the first derivative of the microwave absorption (see pg. 24-25 for more details).

Each spectrum was fitted using Equation 3.5 (see p. 25) in order to obtain the line width, the intensity and the resonance field at the fixed temperature. The results of these fits are plotted in Figure 5.37. An anomaly can clearly be seen in the intensity, the resonance field and the g-factor near 250 K. The thermal expansion and the dielectric measurements exhibit anomalies in the same temperature regime. These findings, especially the change of the resonance field, suggest the anomaly near 250 K has most likely a magnetic origin.

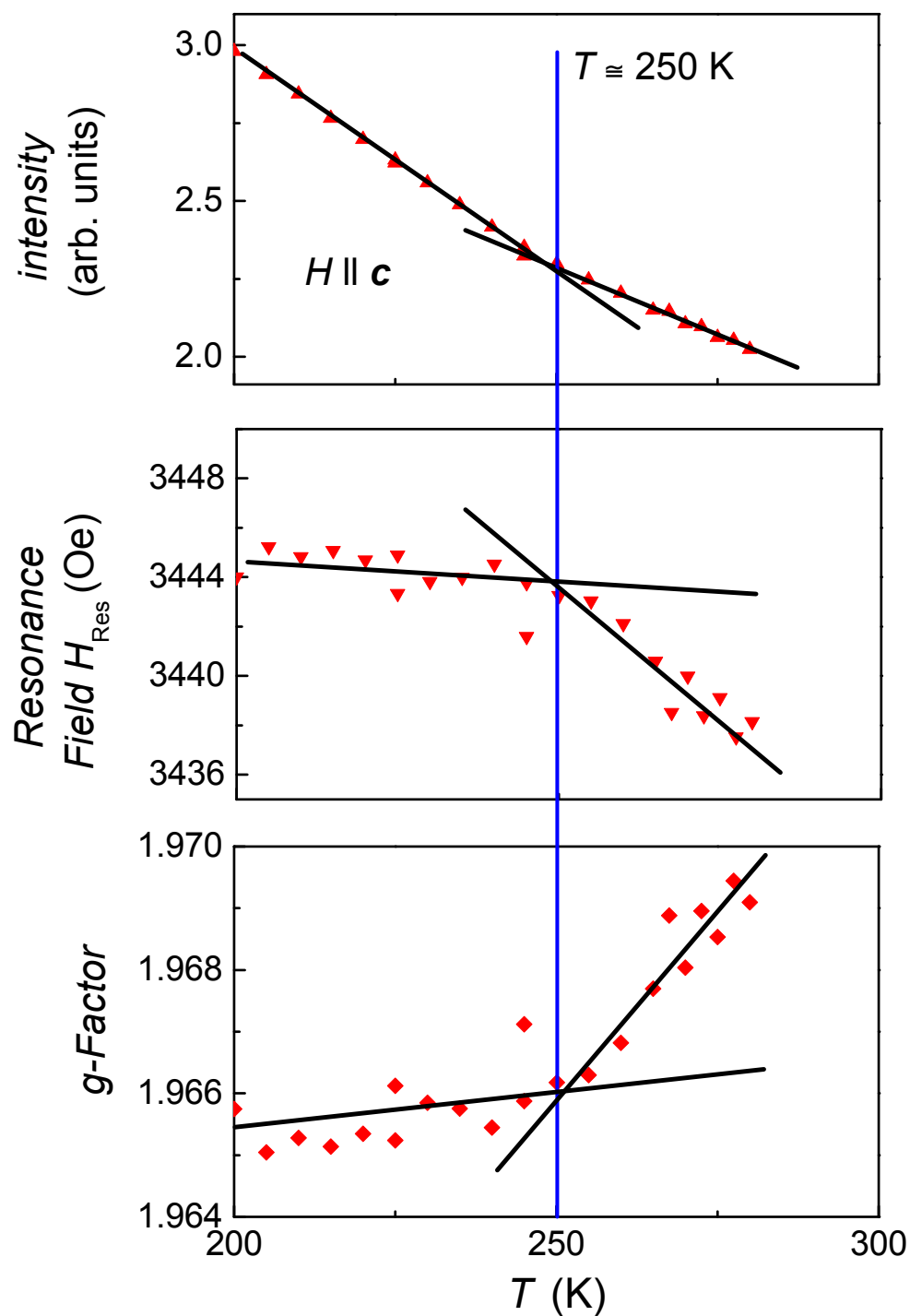


Figure 5.37: The temperature dependence of the intensity, the resonance field and the g -factor ($H \parallel c$) for a CrOCl crystal obtained by fitting the EPR spectra to a Lorentzian.

High temperatures anomalies were also seen in the temperature dependence of the Raman spectra. The Raman measurements⁸ were performed using linearly polarized He/Ne gas laser light with a wavelength of 632.817 nm and a power of less than 1 mW. The laser light was focused on a 10 μm spot using a 50x microscope. The Raman spectra were measured on a tiny trapezoidally shaped homogenous crystal platelet around $\sim 40 \mu\text{m} \times \sim 130 \mu\text{m}$ (see Figure 5.38).

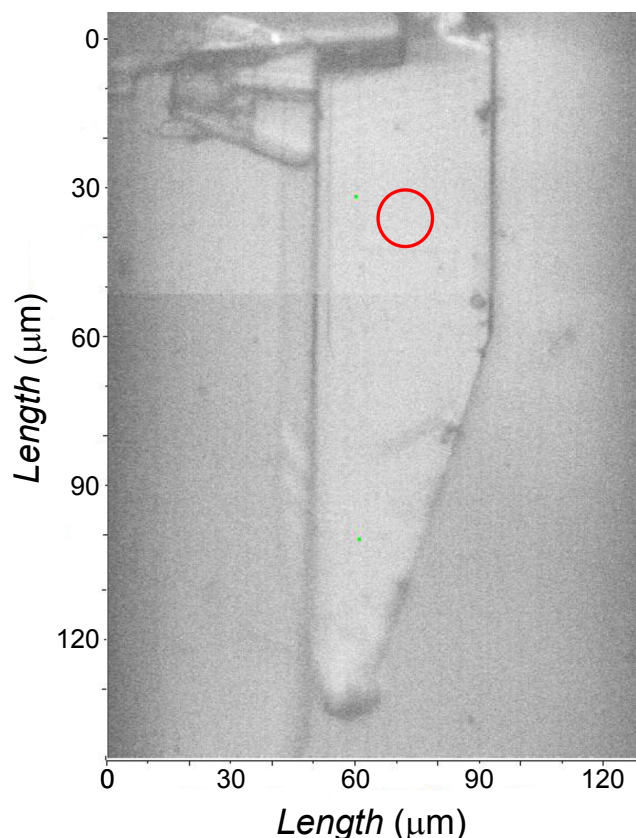


Figure 5.38: A microscope image of a tiny CrOCl crystal ($\sim 40 \mu\text{m} \times \sim 130 \mu\text{m}$) showing the position, denoted by the red circle, at which the Raman spectra were measured.

Raman spectra were measured for temperatures down to 5 K with a special focus on the temperature range between 150 K and 290 K. The crystal was placed on a copper cold finger located in the centre of the Cryovac Mikocryo continuous flow cryostat. The measurements were performed in a high vacuum environment.

⁸I would like to thank Hr. Schultz at the Max Planck Institute for Solid State Physics for performing the Raman scattering measurements.

The Raman spectra at different temperatures is presented in Figure 5.39.

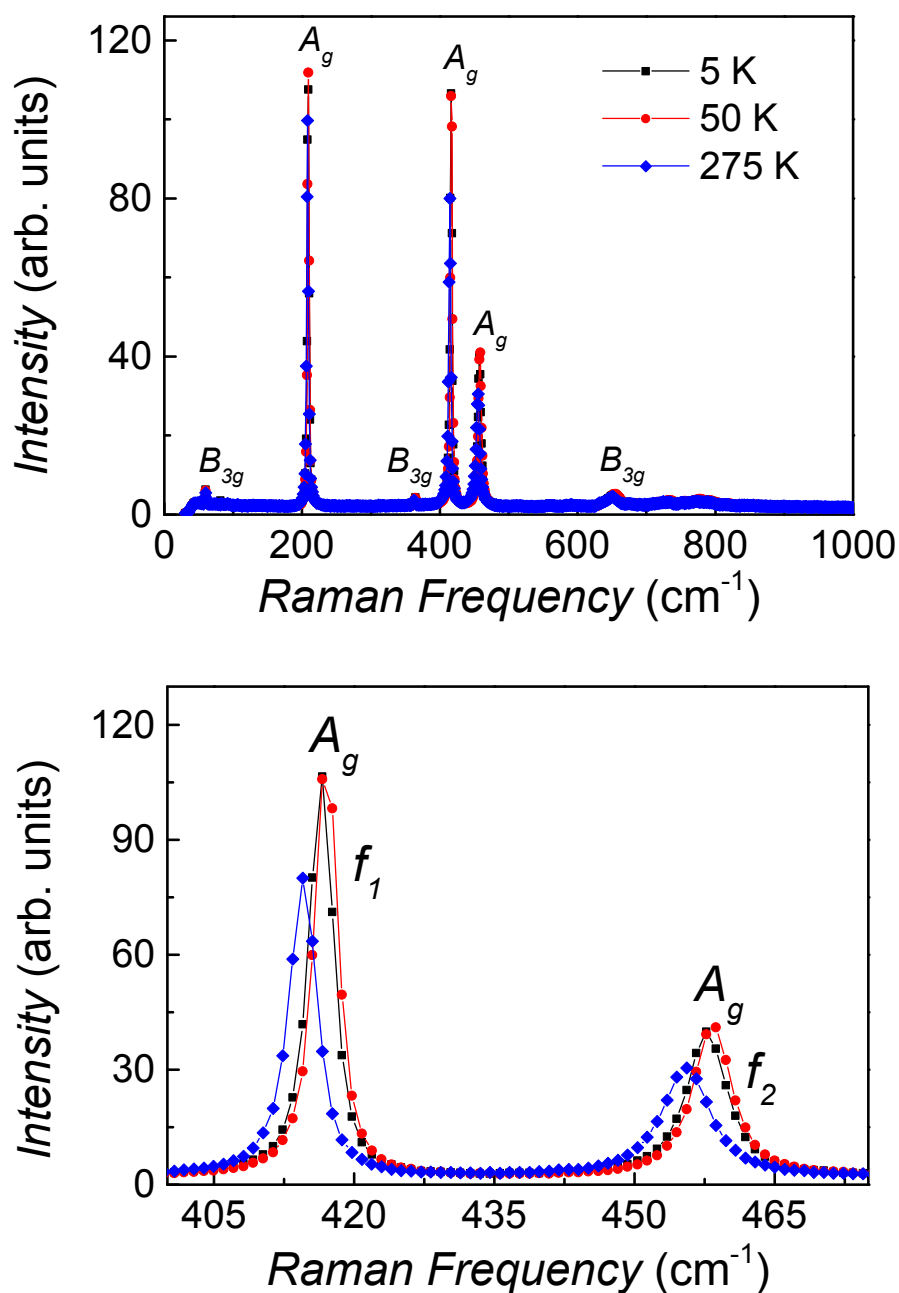


Figure 5.39: The Raman spectra of a tiny CrOCl crystal at 5 K, 50 K and 275 K. The lines used in both graphs are a guide to the eyes.

The peaks in the Raman spectra can be assigned to the three strong A_g and the three weak B_{3g} vibrational modes according to Ref. [139]. No splitting in the Raman peaks occurs between 5 K and 275 K even in the monoclinic low temperature crystal structure below T_N . A similar behaviour can also be seen in

the isostructural antiferromagnetic VOCl compound.[139] These results imply that the structure does not significantly change over the large temperature range consistent with the previous studies by Angelkort *et. al.* [159].

The temperature dependence of the two A_g modes (f_1 and f_2) are obtained by fitting Gaussian functions to the peaks in the Raman spectra (see Figure 5.40).

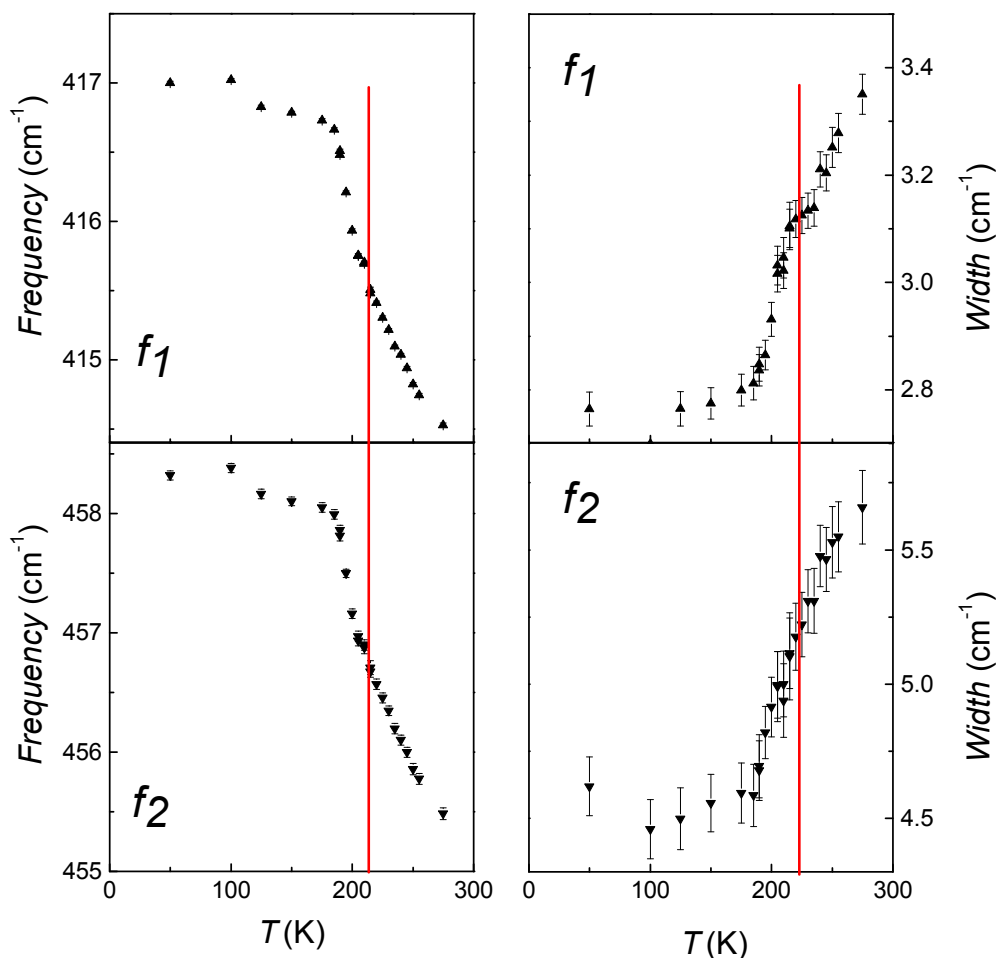


Figure 5.40: The temperature dependence of the two A_g modes (f_1 and f_2) in CrOCl for $50 \text{ K} < T < 290 \text{ K}$.

Upon further inspection, the temperature dependence of the Raman frequency and the width of two strong Raman lines near 420 cm^{-1} and 460 cm^{-1} change near $\sim 225 \text{ K}$. When the data from the various measurements are compared, the data suggests that two phase transitions are present at $\sim 223 \text{ K}$ and $\sim 250 \text{ K}$. The origin and the nature of these transitions currently remain unclear.

5.4.4 Density functional calculations of the spin exchange interactions

In order to clarify the antiferromagnetic order and the complex phase diagrams of CrOCl, the spin exchange interactions were determined by performing a mapping analysis.[174, 175] The absolute energies of eight spin configurations were determined by spin-polarized first principles density functional theory (DFT) calculations⁹. The relevant spin exchange parameters are derived by mapping these energies onto a corresponding Heisenberg Hamiltonian,

$$\mathcal{H} = - \sum J_{ij} \vec{S}_i \vec{S}_j, \quad (5.3)$$

where the exchange coupling between the spin sites i and j are denoted by the exchange parameter J_{ij} . This mapping analyses method has been extensively tested for a number of insulating low-dimensional spin systems [176–178] and found to reproduce the sign and the ratios between the spin exchange constants reliably. However, the magnitude of the spin exchange constants is typically overestimated by a factor of three to five.[179, 180]

For CrOCl, the electronic energies of the ordered spin configurations were calculated using the projected augmented-wave (PAW) method [181, 182] and implemented using the Vienna *ab initio* simulation package (VASP) [183]. The exchange and correlation functional were estimated using the generalized gradient approximation (GGA).[184] The DFT calculations were performed using a plane-wave cutoff energy of 450 eV and a set of 64 \mathbf{k} -points for the irreducible Brillouin zone. The electron correlation of the Cr $3d^3$ state was accounted for using an additional on-site repulsion (GGA+ U , $U=0, 1, 2, 3$ and 4 eV) in the calculations.

The DFT calculations were performed based on the distorted low temperature structure. The low temperature nuclear structure exhibits a doubling along the \mathbf{b} -axis¹⁰ and a distorted monoclinic symmetry. In order to identify the relevant spin exchange pathways, a closer inspection of the room temperature (orthorhombic) crystal structure revealed three possible spin exchange pathways between the Cr atoms in the \mathbf{ab} -plane. Additionally, the next-nearest

⁹I would like to thank Prof. M. H. Whangbo at the North Carolina State University for performing these DFT calculations.

¹⁰The doubling along the \mathbf{b} -axis results from magnetic induced charge scattering. Please see p. 154 for more information about this effect.

neighbour pathways between the Cr atoms along a and b axes were also considered. Overall, only the spin exchange pathways within the two-dimensional planes were considered. The coupling of the Cr atoms along the c -axis were assumed to be very small and negligible. In the low temperature structure, the monoclinic distortion required an additional differentiation of the spin exchange parameters along the b -axis and diagonally across the ab -plane. Figure 5.41 displays the identified spin exchange pathways in CrOCl for the spin exchange paths.

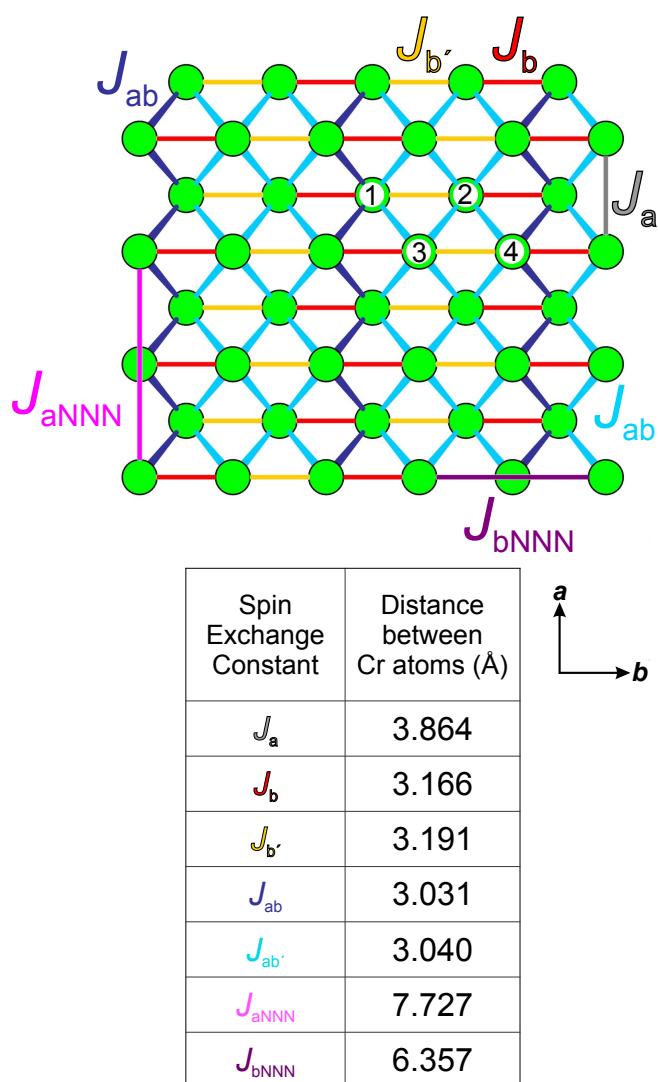


Figure 5.41: The relevant spin exchange pathways in the low temperature monoclinic structure of CrOCl showing the distances between the Cr atoms for each pathway and the four Cr sites (labelled 1 to 4) later on used in the *mcpas* [185] simulations.

The DFT calculations were performed for the eight colinearly ordered spin configurations displayed in Figures 5.42 and 5.43. Six ordered spin configurations (AF1 and AF3 - AF7) consist of ferromagnetic stripes with alternating spin directions producing antiferromagnetic striped arrangements. AF2 is composed of ferromagnetic layers of Cr atoms chains running along the b -axis with alternating spin directions. The ferromagnetic spin configuration with all spins in the same direction is denoted as FM.

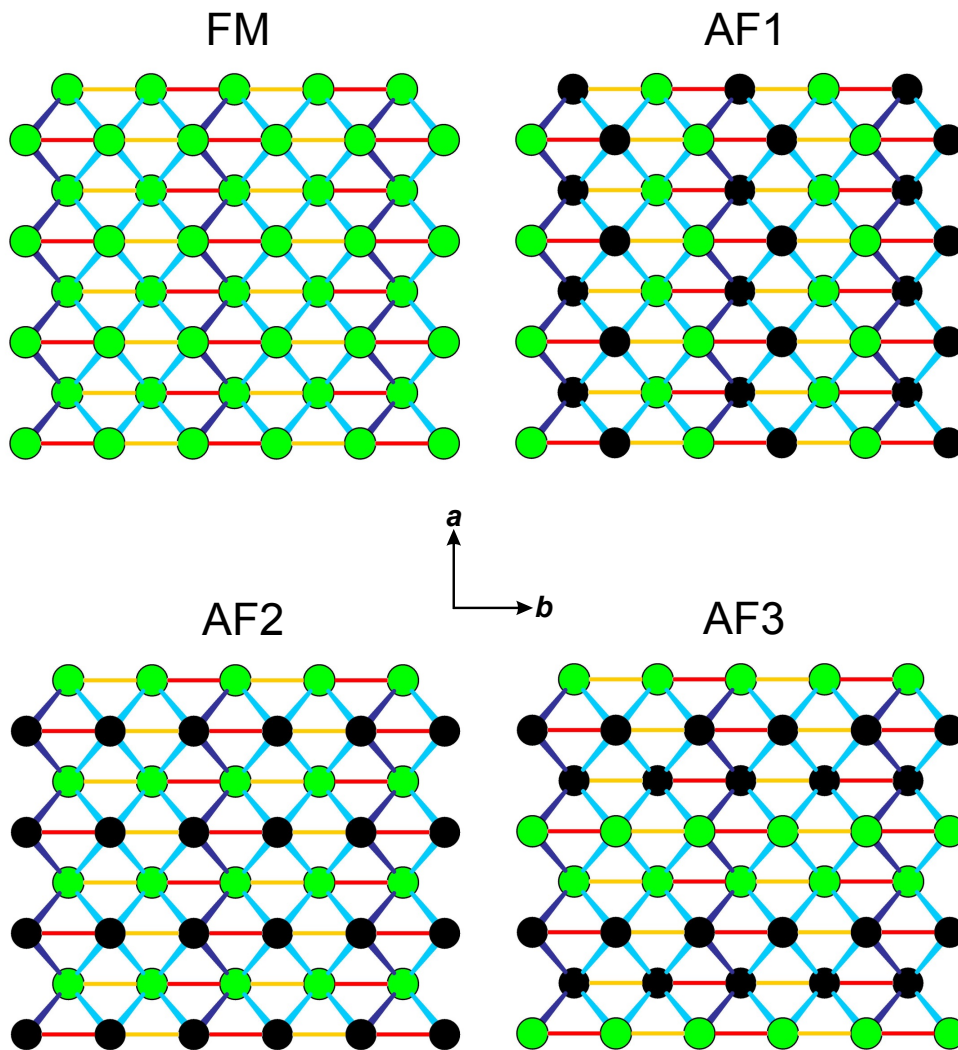


Figure 5.42: The spin configurations for the GGA+ U calculations – Part 1 of 2. The green and the black spheres denote the atoms with opposite spin directions.

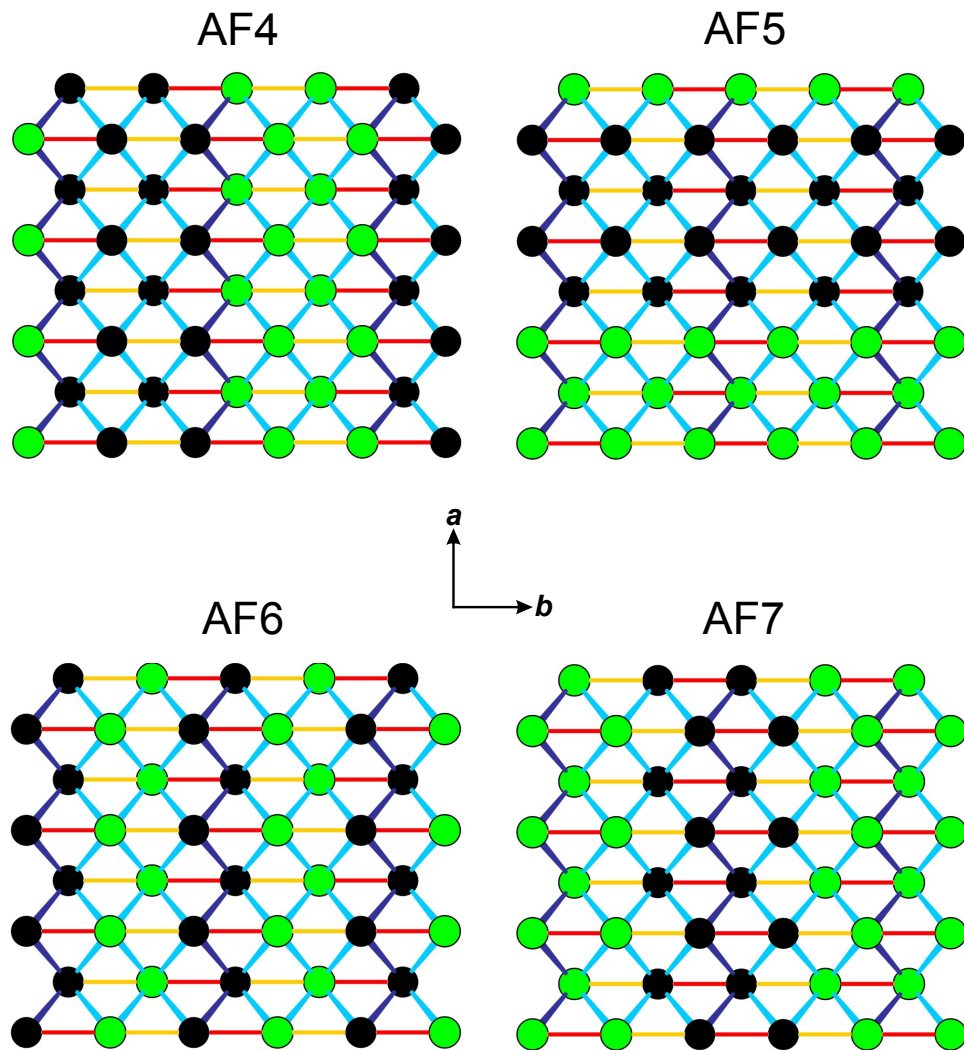


Figure 5.43: The spin configurations for the GGA+ U calculations – Part 2 of 2. The green and the black spheres denote the atoms with opposite spin directions.

Table 5.3 lists the relative energies (in meV) per formula unit for $U = 0$ eV and 2 eV of the eight ordered spin configurations in the low temperature monoclinic structure.

Arrangements	Relative energies in meV per formula unit	
	$U = 0$ eV	$U = 2$ eV
FM	0.00	0.00
AF1	-2.62	+6.72
AF2	+15.06	+16.43
AF3	+45.24	+37.77
AF4	-4.39	+1.33
AF5	+20.95	+18.87
AF6	-1.45	+7.41
AF7	-0.72	+3.61

Table 5.3: The relative energies (in meV) of the eight ordered spin configurations with on-site repulsion $U = 0$ eV and 2 eV obtained from $GGA + U$ calculations.

The spin exchange coupling constants for each on-site repulsion U were then determined by mapping the relative energies of the eight ordered spin configurations (see Table 5.3).

Pathway	Spin exchange coupling constants in Kelvin				
	$U = 0$ eV	$U = 1$ eV	$U = 2$ eV	$U = 3$ eV	$U = 4$ eV
J_a	+97.24	+85.93	+76.21	+67.97	+60.77
J_b	-25.91	-10.67	-1.54	+4.27	+8.04
$J_{b'}$	-23.45	-11.53	-4.38	+0.16	+3.12
J_{ab}	+14.90	+17.42	+18.52	+18.92	+18.89
$J_{ab'}$	+20.93	+21.38	+22.07	+21.74	+21.15
J_{aNNN}	-4.30	-1.42	-0.02	+0.68	+1.02
J_{bNNN}	-5.83	-5.37	-5.06	-4.85	-4.71

Table 5.4: The spin exchange coupling constants from the DFT calculations for on-site repulsion $U = 0, 1, 2, 3$ and 4 eV.

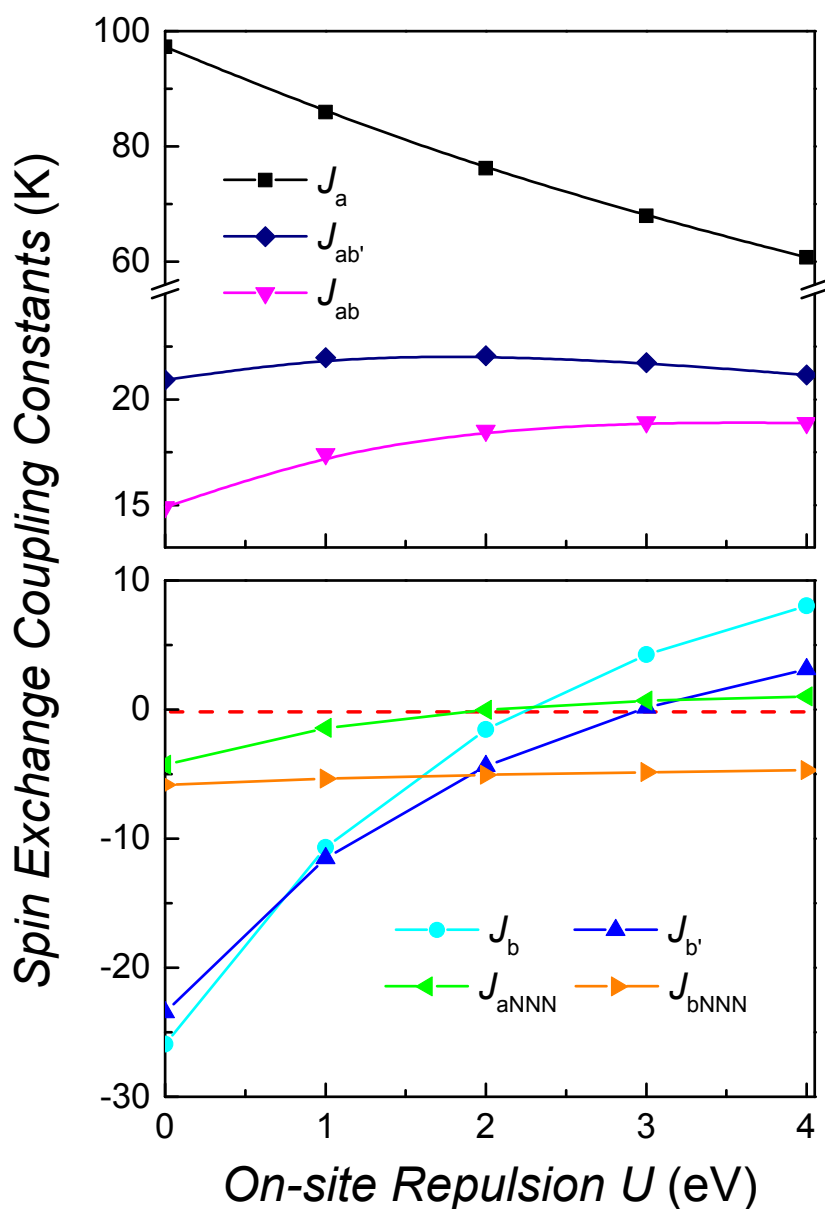


Figure 5.44: The spin exchange coupling constants as a function of the on-site repulsion U .

The dependence of the spin exchange coupling constants as a function of the on-site repulsion U is presented in Figure 5.44. $J_{b'}$, J_b and J_{aNNN} shift from antiferromagnetic to ferromagnetic coupling with increasing U crossing over near ~ 3 eV. J_a decreases by $\sim 37\%$ at $U = 4$ eV whereas J_{ab} , $J_{ab'}$ and J_{bNNN} remain largely unchanged with U .

In the mean-field approximation, the Curie-Weiss temperature θ is related to the spin exchange coupling constants by the following equation[170]:

$$\theta_{\text{MF}} = \frac{1}{3} \sum_i z_i J_i S(S+1) \quad (5.4)$$

wherein the summation runs over the nearest and the next-nearest neighbours. The number of nearest neighbours and next-nearest neighbours is given by z_i . J_i are the spin exchange coupling constants and S is the spin quantum number of the spin site (i.e. $S = \frac{3}{2}$ for CrOCl). For the low temperature distorted structure, the two slightly different diagonal spin exchange coupling constants $J_{ab'}$ and J_{ab} result in two different θ_{MF} values. The θ_{MF} values for the two unique atomic sites (1 and 2) in the spin configurations for 0 eV are calculated as follows:

$$\begin{aligned} \theta_{\text{MF}}(1) &= \frac{1}{3} \frac{15}{4} (2J_a + J_b + J_{b'} + 2J_{ab} + 2J_{ab'} + 2J_{a\text{NNN}} + 2J_{b\text{NNN}}) \approx 246 \text{ K} \\ \theta_{\text{MF}}(2) &= \frac{1}{3} \frac{15}{4} (2J_a + J_b + J_{b'} + 4J_{ab'} + 2J_{a\text{NNN}} + 2J_{b\text{NNN}}) \approx 261 \text{ K} \end{aligned}$$

The average Curie-Weiss temperature is given by:

$$\theta_{\text{MF}}(\text{avg}) = \frac{1}{2} [\theta_{\text{MF}}(1) + \theta_{\text{MF}}(2)] \approx 254 \text{ K}$$

The Curie-Weiss temperatures for the various U values are tabulated in Table 5.5.

On-site Repulsion	$\theta_{\text{MF}}(1)$	$\theta_{\text{MF}}(2)$	$\theta_{\text{MF}}(\text{avg})$
$U = 0 \text{ eV}$	246 K	261 K	254 K
$U = 1 \text{ eV}$	267 K	277 K	272 K
$U = 2 \text{ eV}$	272 K	281 K	277 K
$U = 3 \text{ eV}$	267 K	274 K	270 K
$U = 4 \text{ eV}$	257 K	262 K	260 K
Average	262 K	271 K	266 K

Table 5.5: The Curie-Weiss temperatures θ_{MF} (1 and 2) at the two unique atomic sites in the low temperature monoclinic structure and the average value as a function of the on-site repulsion $U = 0, 1, 2, 3$ and 4 eV.

For all U values, the θ_{MF} (average) value is approximately ten times larger than the experimental Curie-Weiss temperature of 26.1(1) K. Thus, the scaled spin exchange coupling constants are obtained by dividing all of the J values by ten.

The scaled spin exchange coupling constants and their on-site repulsion U dependence were further analyzed using the McPhase package [186]. The low temperature magnetic structure for each U value was found using the *mcp*has program [185, 187] implemented in the McPhase package. The *mcp*has program uses the combination of a classical mean-field and Monte Carlo simulations to find the lowest energy magnetic structure¹¹. A four atom basis (see Figure 5.41) was used for CrOCl *mcp*has simulations due to the two different diagonal (J_{ab} and $J_{\text{ab}'}$) and \mathbf{b} -axis (J_{b} and $J_{\text{b}'}$) spin exchange coupling constants. The results of the simulations are discussed in detail in the next section.

¹¹For more information, please visit the following *mcp*has help page located at Ref. [185].

5.5 Discussion

The complex magnetic ordering behaviour of the two-dimensional antiferromagnet CrOCl has been investigated in detail by various experimental and theoretical techniques. The crystal structure of CrOCl is characterized by slabs of quadratic Cr single layers as displayed in Figure 5.45.

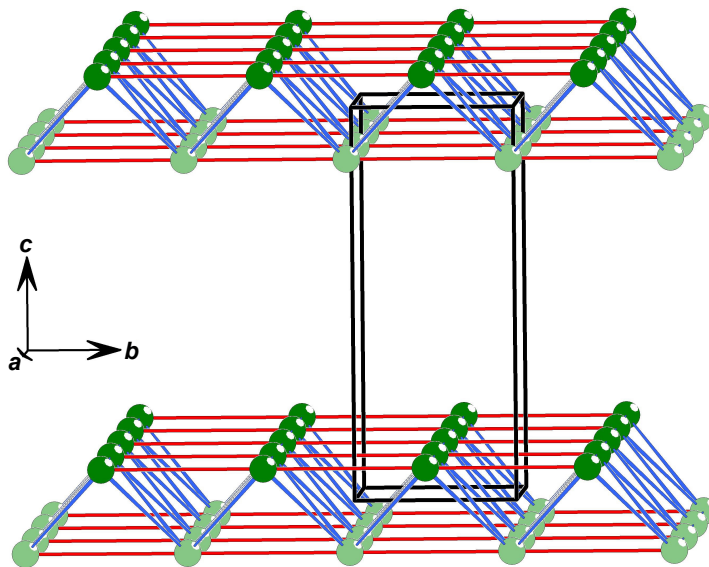


Figure 5.45: The slabs of the quadratic Cr single layers showing the unit cell (the black rectangular prism) N.B. only the Cr atoms are shown. The slabs are connected through van der Waals interactions via the Cl-Cl contacts.

The magnetic phase diagram turns out to be rather intricate and contains a number of new phases previously not detected. This complexity appears to arise from spin exchange interactions to further distant neighbours within the same Cr layer but also between interlayer neighbours within the same slab. This is indicated by detailed density functional calculations of the spin exchange constants. Some of the spin exchange constants depend noticeably on the Coulomb repulsion parameter U . This dependence makes quantitative interpretations even more difficult. Additionally, magnetic ordering and magnetoelastic coupling induces a slight structural distortion (the monoclinic angle changes by $\Delta\alpha = \alpha - \frac{\pi}{2} \approx 0.07^\circ$) to monoclinic symmetry below $T_N \approx 13.5$ K. No significant enlargement of the unit cell occurs in the low temperature structure. The symmetry reduction is also reflected in the density functional calculations and leads to an alternation ($< 30\%$) of the spin exchange constants along the b -axis.

According to the DFT calculations, the nearest neighbour spin exchange between the Cr moments along the \mathbf{a} direction in a single layer is ferromagnetic and constitutes the dominant exchange interaction pathway. The next-nearest neighbour spin exchange interactions along \mathbf{a} are about two orders of magnitude smaller and negligible. Within the same layer along the crystallographic \mathbf{b} direction, the nearest neighbour spin exchange interaction is antiferromagnetic. It competes with the next-nearest neighbour antiferromagnetic spin exchange interactions. Especially interesting is the fact that the nearest neighbour spin exchange constants along \mathbf{b} direction (J_b and $J_{b'}$) depend strongly on correlations (U). Initially J_b and $J_{b'}$ are antiferromagnetic but they cross zero and finally become even ferromagnetic between $U = 2$ eV and 3 eV (see Figure 5.44 on p. 171). For U values typically applicable for Cr^{3+} ($3d^3$, $1\text{eV} \leq U \leq 2$ eV), the nearest and the next-nearest neighbour spin exchange along \mathbf{b} within the same layer are of the same order of magnitude. The diagonal interlayer spin exchange interactions (J_{ab} and $J_{ab'}$), between the Cr moments in the neighbouring single layers, are especially pertinent to understand the low temperature magnetic structure. This interlayer spin exchange appears to be rather insensitive to correlations and accordingly is independent of the Coulomb repulsion parameter U in the DFT calculations.

Another peculiarity of the magnetic behaviour of CrOCl is the discrepancy between the positive Curie-Weiss temperature and the low temperature antiferromagnetic ordering. In order to determine the Curie-Weiss temperature more reliably, the magnetic susceptibility of CrOCl has been measured up to 800 K for the first time in this thesis. The extrapolation of the Curie-Weiss law is in agreement with the positive Curie-Weiss temperature detected in previous studies[25, 159, 161] indicating predominant ferromagnetic spin exchange interactions consistent with the DFT results. The extension of the experimental temperature range enables a more precise determination of the Curie-Weiss temperature which according to the analysis is +26.1(1) K and thus about $\sim 35\%$ larger than found previously.[25, 159, 161] The comparison of the Curie-Weiss temperatures calculated from the DFT results reveals a significant mismatch in the magnitude of the experimental data and the theoretical values. Typically, DFT calculations overestimate the spin exchange constants by a factor of three to five.[188] However, the DFT spin exchange constants are an order of magnitude too large in the case of CrOCl . Agreement of the experimental Curie-Weiss temperature with the DFT results is obtained if all

the spin exchange constants are scaled by 1/10. Previous DFT calculations of the spin exchange constants for several systems have demonstrated that despite the need for an overall scaling, the relative ratios of the DFT spin exchange constants are very reliable.[176–178] Below it is demonstrated that the low temperature magnetic structure and its propagation vector can be understood based on the scaled DFT results keeping the relative ratios unchanged.

The positive Curie-Weiss temperature of CrOCl result from predominant ferromagnetic spin exchange interactions. Similarly, positive Curie-Weiss temperatures have also been observed in other compounds which order antiferromagnetically at low temperatures.[189–191] This observation signals that competing spin exchange interactions and a complex magnetic order are present.[189] For CrOCl, deviations from the Curie-Weiss fit due to antiferromagnetic correlations become apparent below about 200 K. This behaviour can clearly be seen in a $\chi_M \times T$ vs. T representation as displayed in Figure 5.46. Below ~ 200 K, the experimental data are significantly lower than the Curie-Weiss susceptibilities extrapolated with the parameters gained from the high temperature Curie-Weiss law indicating the build-up of antiferromagnetic correlations.

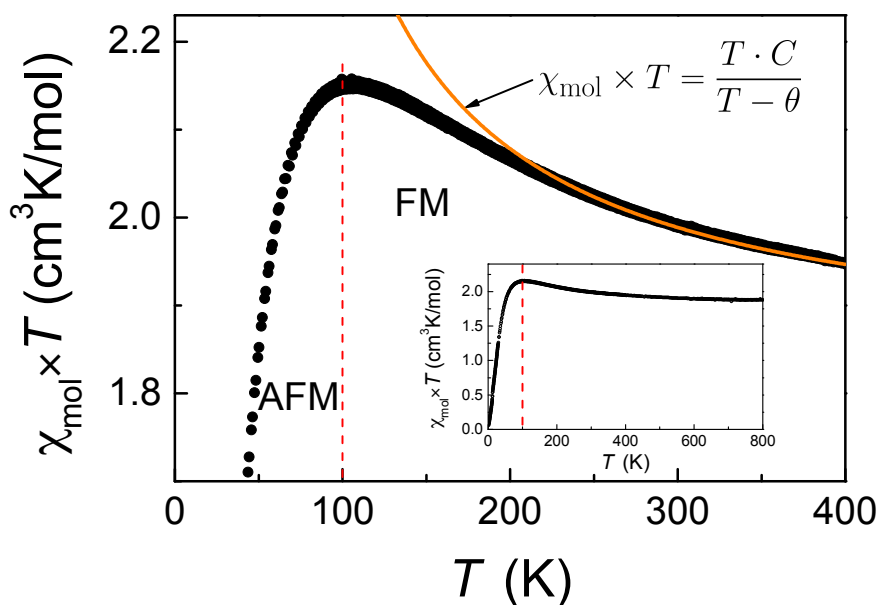


Figure 5.46: The temperature dependence of $\chi_M \times T$ for CrOCl. Below ~ 100 K (denoted by the dashed red line), antiferromagnetic correlations become pertinent.

The zero field magnetic structure of CrOCl consists of two-dimensional magnetically identical slabs comprising two quadratic Cr single layers. The slabs stack along the crystallographic c direction. The dominant ferromagnetic spin exchange interactions between the Cr moments result in collinear ferromagnetic chains running along the crystallographic a direction. Two of these chains form collinear ferromagnetic stripes with the neighbouring stripes being antiferromagnetically aligned along the b direction. This arrangement leads to a commensurate phase below a first order phase transition at ~ 13.5 K. The commensurate phase is characterized by a quadrupling of the magnetic structure along the crystallographic b direction. According to the magnetization measurements, the moments are aligned perpendicular to the Cr layers. The commensurate magnetic ordering is preceded by a magnetically incommensurate phase with a wavevector close to $\frac{1}{4}$. The incommensurate phase starts to develop below ~ 27 K. In the incommensurate phase, a spin density wave is formed which anticipates the essential features of the low temperature commensurate magnetic structure.

In order to verify the low temperature magnetic structure, classical mean-field Monte Carlo simulations at $H = 0$ Tesla were performed using the scaled spin exchange constants obtained from the DFT calculations. These calculations were implemented by considering all of the scaled spin exchange constants within the two quadratic layers of a single Cr slab. The Monte Carlo calculations were carried out using the *mcphas* program [185] contained in the McPhase package [186]¹². An additional term $\sim Ds_z^2$ with $D < 0$ was introduced in order to account for uniaxial anisotropies forcing the Cr moments to align along c as found by the magnetization measurements. Figure 5.47 displays the $T = 0$ K magnetic phases obtained from an energy minimization using a classical Monte Carlo mean-field algorithm. The Monte Carlo simulations correctly predict the commensurate magnetic structure ($H = 0$ Tesla) with the quadrupling along b for $U = 0$ and 1 eV. For $2 \leq U \leq 4$ eV, ferromagnetic spin configurations have a lower energy than the commensurate magnetic structure. The incommensurate magnetic structure preceding the commensurate phase could not be reproduced by the Monte Carlo simulations.

¹²As a basic feature of the McPhase package, the *mcphas* program performs Monte Carlo simulations using a classical mean-field approach. A set of spin exchange constants and also anisotropies for the specific system can be defined as parameters.

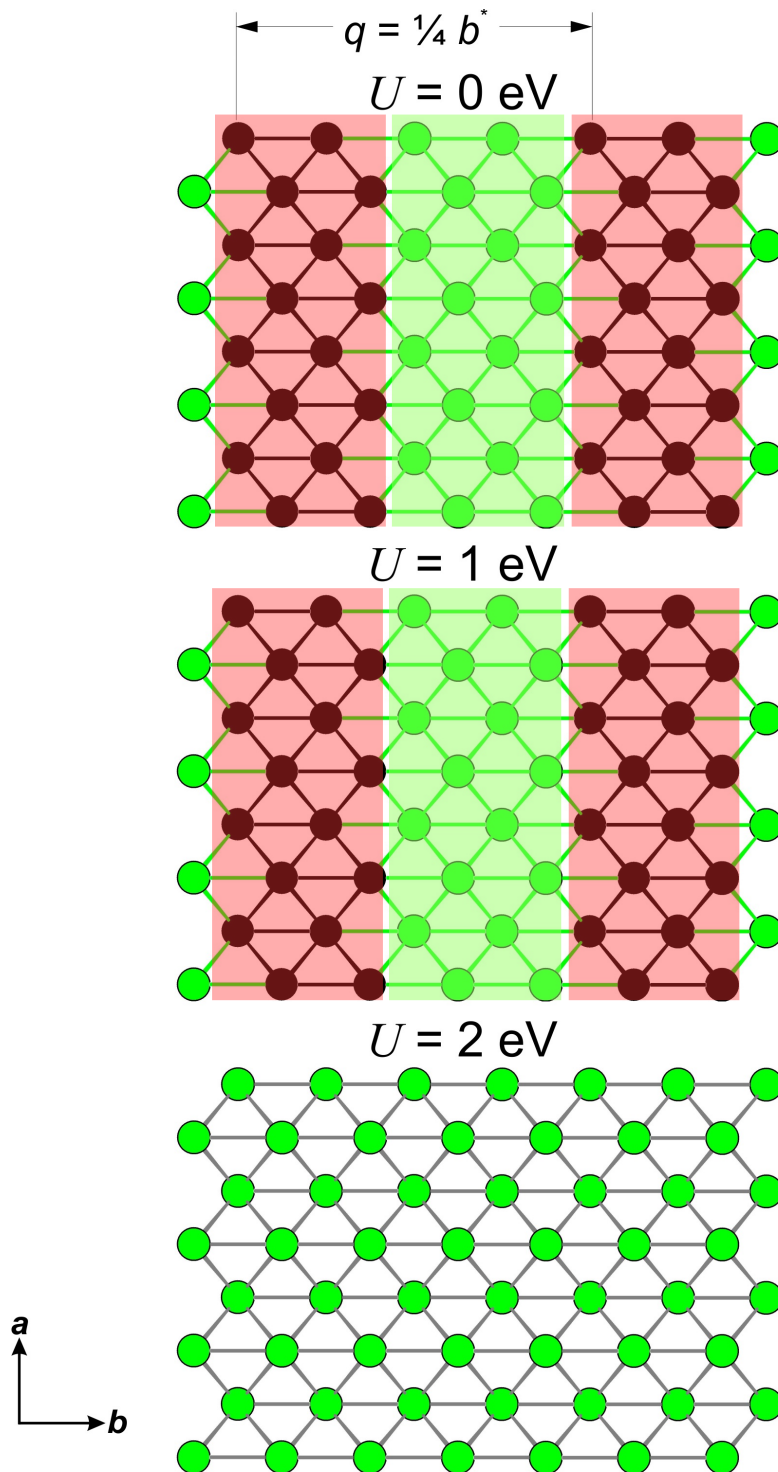


Figure 5.47: The low temperature magnetic structures calculated in the *mcpas* simulations [192] using the scaled spin exchange constants derived from the DFT calculations (for more details please see Section 5.4.4 on p. 166). The striped phase is observed for $U = 0 \text{ eV}$ and 1 eV with $q_{\text{magnetic}} = \frac{1}{4}b^*$. For $U > 2 \text{ eV}$, a ferromagnetic spin configuration is seen.

Incommensurate spatially modulated magnetic structures are a consequence of competing spin exchange interactions. The occurrence of the incommensurate phase can be understood in terms of the axial next-nearest neighbour Ising model¹³. A three-dimensional version of this model was developed by Elliott to describe the incommensurate chiral magnetic ordering of heavy rare-earth metals.[193] Fisher and Selke investigated this model (later on called the ANNNI model¹⁴) with a particular focus on the multicritical points in the phase diagram.[195, 196] These multicritical points (also called ‘Lifshitz’ points) separate a completely disordered (paramagnetic) phase, a uniformly ordered (antiferro/ferromagnetic) phase and a sinusoidally ordered (incommensurate) phase. The ANNNI model phase diagram (see the lower part of Figure 5.48) predicts that the transition from the paramagnetic to the antiferromagnetic phase may pass through an incommensurate phase depending on the ratio of the competing spin exchange interactions. The uniformly ordered phase can be modeled by using a $--+-+--$ phase which is commonly denoted as the (2,2) antiphase state or the $\langle 2 \rangle$ structure in the ANNNI literature.[195] The spin arrangement seen for a single Cr layer in CrOCl is consistent with the (2,2) antiphase state. It is favoured by an antiferromagnetic next-nearest neighbour spin exchange. Figure 5.48 displays the phase diagram of the three-dimensional tetragonal ANNNI model. A single Cr layer of CrOCl can be identified as a (011) plane of a tetragonal lattice if J_0 , J_1 and J_2 are identified with J_a , $J_{b,b'}$ and J_{bNNN} respectively. According to Fisher and Selke [195], the phase diagram (see the lower part of Figure 5.48) predicts a sinusoidal phase preceding the antiferromagnetic phase for $-0.5 < -J_2/J_1 < -0.24$. This compares well with the spin exchange ratios observed for CrOCl with U values $0 \text{ eV} \leq U \leq 1 \text{ eV}$.

¹³Magnetization measurements indicate an easy axis Ising anisotropy exists along the \mathbf{c} -axis.

¹⁴A review of the one-dimensional, the two-dimensional and three-dimensional ANNNI models (state of the art in 1986) is discussed by R. Liebmann in Ref. [194].

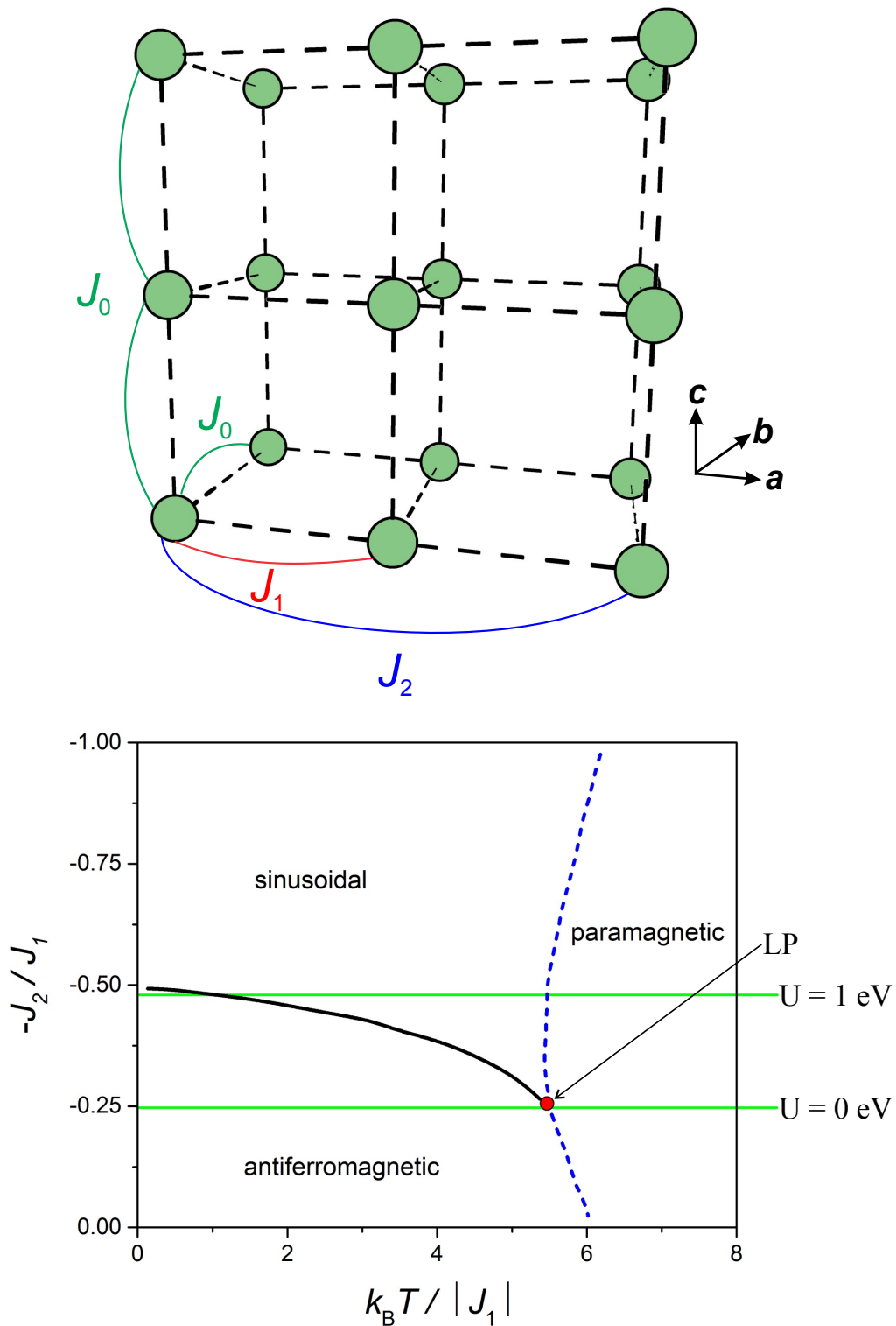


Figure 5.48: The three-dimensional axial next-nearest neighbour Ising (ANNNI) model showing the spin exchange interactions in a cubic lattice and the phase diagram plotted according to Ref. [195]. The Lifshitz point (LP) is denoted by the solid red dot.

From the extended (H, T) magnetic phase diagrams of CrOCl (see Figure 5.30 on p. 152), the incommensurate phase (phase III) must be crossed in order to reach the lower temperature phases analogous to the scenario observed in the ANNNI model. Elliott [193], Fisher and Selke [195] derived a mean-field equation to relate the mean-field critical temperature to the spin exchange constants J_1 ($\equiv J_{b,b'}$) and J_2 ($\equiv J_{b,NNN}$) [195]:

$$k_B T_N^{MF} = 4|J_1| + 2J_1 \cos(q) + 2J_2 \cos(2q) \quad (5.5)$$

with a propagation vector of q equal to $2\pi \cdot \frac{1}{4}$. The mean-field transition temperatures T_N^{MF} for CrOCl are calculated using the spin exchange constants presented in Table 5.4 and tabulated in Table 5.6.

U (eV)	0	1	2	Experimental
T_N^{MF} (K)	11	6	2	13.5

Table 5.6: The mean-field Néel transition temperature T_N^{MF} as a function of the on-site repulsion $0 \leq U \leq 2$ eV.

The calculated transition temperatures compare reasonably well with the experimental observations. However, the additional inter-slab diagonal spin exchange pathways (J_{ab} and $J_{ab'}$) add additional frustration to the system which could be the origin of the intricate magnet phase diagram of CrOCl. In the future, the (H, T) magnetic phase diagrams need to be explored further using neutron scattering measurements in high magnetic fields. The occurrence of Lifshitz points in the phase diagrams are particularly interesting. The Lifshitz points occur at $T \approx 20$ K and $H \approx 10 - 12$ Tesla depending on the magnetic field orientation.

In addition to the complex low temperature magnetic behaviour found for CrOCl, two high temperature transitions are also detected by various experimental methods. The two transitions occur just below room temperature at ~ 223 K and ~ 250 K. In the dielectric measurements, both transitions can clearly be seen as a pronounced maximum with two kinks (see Figure 5.35 on p. 160). Initially, the dielectric constant ϵ_r increases steeply with decreasing temperature down to ~ 257 K. Below ~ 257 K, the slope of ϵ_r decreases resulting in the first kink. As the temperature is further decreased, ϵ_r increases to its maximum value of ~ 4.1 near ~ 225 K. Subsequently, ϵ_r decreases with decreasing temperature below 225 K resulting in the second kink. A single transition is noted in the thermal expansion data (see p. 160) near ~ 227 K in the form of a small plateau. Electron paramagnetic resonance (see p. 162) and Raman (see p. 165) measurements clearly reveal a single phase transition at ~ 250 K and ~ 223 K respectively. The coincidence of the first transition near ~ 223 K detected by the Raman spectroscopy, the thermal expansion and dielectric measurements suggest that this transition is probably structural. The second transition near ~ 250 K noted in the dielectric data and the Electron paramagnetic resonance results indicate a slight change in the temperature dependence of the g-factor (viz. the magnetic susceptibility). This behaviour may tentatively be ascribed to a transition which modifies the crystal electric field and the electronic structure due to a slight rearrangement of the anion environment of the Cr³⁺ cations. In the dielectric measurements, the behaviour of ϵ_r is reminiscent of the dipolar/orientation polarization mechanism in polar dielectrics.[76] But no permanent dipoles are present in CrOCl which implies that this effect may result from induced dipoles in a dynamic regime. Below 225 K, the sharp decrease in ϵ_r is most likely due to the loss or the freezing of the induced dipole. The transitions near ~ 223 K and ~ 250 K deserve further clarification e.g. by high resolution x-ray diffraction experiments.

5.6 Summary

In Chapter Five, the magnetic and the structural properties of the two-dimensional antiferromagnetic chromium oxychloride CrOCl were discussed. In order to understand the magnetic behaviour of CrOCl, a combination of experimental and theoretical techniques were utilized. The magnetoelastic nature of the low temperature antiferromagnetic state was observed below $T_N \approx 13.5$ K with pronounced features in the dielectric and the thermal expansion measurements. Using the anomalies in the magnetic field scans and the magnetic field dependence of the three low temperature phase transitions (T_N , T_{mag} and T^*), the extended (H, T) magnetic phase diagrams for $H \parallel \mathbf{c}$ and $H \perp \mathbf{c}$ were constructed. Five new phases were discovered in the course of these measurements which reveal the intricate nature of the (H, T) magnetic phase diagrams of CrOCl. The occurrence of Lifshitz points near ~ 20 K at magnetic fields between 10 to 12 Tesla depending on the magnetic field orientation is especially interesting. The complex (H, T) magnetic phase diagrams established in this Chapter result from the frustration of the competing spin exchange interactions. The spin exchange interactions were studied using spin polarized DFT calculations. The DFT results reproduced the principle features of the zero field magnetic structure. The low temperature magnetic structure was then analyzed further by simulations using the spin exchange coupling constants in a classical mean-field/Monte Carlo algorithm. The simulations clearly indicated that quadrupling occurs along the \mathbf{b} -axis consistent with the neutron diffraction measurements. The presence of high temperature anomalies near ~ 240 K were first noted in the dielectric measurements. Using various experimental methods, it was concluded that two new phase transitions occur at ~ 223 K and ~ 250 K. The first and the second phase transitions most likely have a structural and an electronic origin respectively.

Conclusions

This thesis focuses on the experimental investigation into the magnetic and the structural properties of the two new low-dimensional quantum anti-ferromagnets. The first system studied was the non-conventional spin-Peierls compound TiPO_4 which consists of quasi one-dimensional Ti^{3+} spin $S = \frac{1}{2}$ chains with strong antiferromagnetic intrachain spin exchange coupling ($J_{\text{intra}} = -965$ K, $J_{\text{inter}} = -20$ K). The second system was the two-dimensional antiferromagnetic compound CrOCl (Cr^{3+} electronic configuration with $S = \frac{3}{2}$) which features strong ferromagnetic chains and an intricate interchain spin exchange scenario. CrOCl is isostructural to TiOX ($X = \text{Cl}$ and Br) which exhibits spin-Peierls behaviour similar to TiPO_4 . TiPO_4 and CrOCl are subject to substantial magnetoelastic coupling associated with their magnetic ordering. In order to investigate this coupling, a miniaturized thermal expansion dilatometer cell was commissioned and utilized extensively. Software for the data acquisition and the processing of the thermal expansion results was developed and tested. In addition, other experimental techniques i.e. magnetic susceptibility under pressure, heat capacity, dielectric, Raman scattering and electron paramagnetic resonance measurements were also performed. The experimental results were compared and analyzed using spin-Peierls theory, electronic structural calculations and classical mean-field Monte Carlo simulations.

The non-conventional spin-Peierls compound TiPO_4 is characterized by a two-stage spin-Peierls transition which comprises two phase transitions at $T_{c1} \approx 74$ K and $T_{c2} \approx 110$ K. Between T_{c2} and T_{c1} , the partial dimerization of the chains and an incommensurate intermediate phase are present. Below the lock-in transition T_{c1} , a commensurate phase is observed with a singlet non-magnetic ground state and fully dimerized chains. The thermal expansion measurements

clearly indicated that T_{c1} and T_{c2} were first and second order phase transitions respectively. A noticeable magnetostriction occurred in the incommensurate intermediate phase. Previously published DFT results indicated that three low temperature crystal structures with almost degenerate energies coexist in the incommensurate intermediate phase. The incommensurate phase was attributed to thermally induced fluctuations between these energetically almost degenerate dimerized phases. The significant magnetostriction observed in the incommensurate phase between 74 K and 110 K is ascribed to the magnetic field affecting these fluctuations. The nature of the incommensurate intermediate phases, especially the intermediate magnetic structure of the incommensurate phase, should be investigated in the future using neutron and synchrotron diffractions methods in high magnetic fields. Marked anisotropies of the thermal expansion with negative thermal expansion perpendicular to the Ti Chains were observed.

The magnetic field dependence of T_{c1} and T_{c2} was investigated using thermal expansion measurements. In the spin-Peierls compounds, the shift of the transition temperature exhibits a distinct quadratic magnetic field dependence ($\Delta T_{sp} \propto H^2$). The T_{c1} transition shifted with magnetic field resulting in a downshift of ~ 90 mK at 9 Tesla. The quadratic magnetic field shift of T_{c1} was consistent with standard spin-Peierls theory but the magnitude of the reduction was about 50% smaller than expected according to theory.

Previous studies have demonstrated that spin-Peierls transitions are particularly sensitive to pressure. The intrachain spin exchange and the magnetoelastic coupling can increase under pressure resulting in a positive enhancement of the spin-Peierls transition temperature in almost all cases investigated so far¹. The pressure dependence of T_{c1} and T_{c2} in TiPO_4 were extensively studied using magnetic susceptibility measurements. In TiPO_4 , the transitions T_{c1} and T_{c2} exhibited a sizable non-linear pressure dependence with a total increase of ~ 40 K for both transitions at 0.9 GPa. A high pressure anomaly in the form of a kink was noted for both transitions at 0.6 GPa. To follow the effect of pressure, the crystal structure should be studied e.g. by using high pressure Raman scattering and/or high precision x-ray diffraction measurements. In addition, theoretical calculations should also be performed in order to determine the effect of the pressure on the intrachain and interchain coupling constants.

¹An exception is the case of the spin-Peierls transition temperature in TTF-CuBDT which decreases under pressure (see Table 4.4 on p. 102).[113]

The two-dimensional antiferromagnetic compound CrOCl is characterized by three phase transitions: $T_N \approx 13.5$ K, $T_{\text{mag}} \approx 27$ K and $T^* \approx 28$ K. Similar to TiPO_4 , incommensurate and commensurate magnetic phases are observed below T_{mag} and T_N , respectively. Below T_N , a monoclinic distortion of the crystal structure occurs with the onset of the commensurate antiferromagnetic ordering. Various measurement techniques were used to study CrOCl in temperatures between 1.3 K and 800 K with magnetic fields up to 35 Tesla. The high temperature magnetization data up to 800 K indicated that ferromagnetic spin exchange interactions were dominant in contrast to the low temperature long-range antiferromagnetic ordering. Anomalies were noted in the dielectric measurements near ~ 250 K. Upon further investigation, it was concluded that two phase transitions occur at ~ 223 K and ~ 250 K. The first and the second phase transitions most likely have a structural and an electronic origin respectively. High resolution x-ray diffraction measurements should be performed in this temperature range to relate these anomalies with possible changes in the crystal structure.

The majority of the experiments on CrOCl were focused on the construction of the extended (H, T) magnetic phase diagrams for $H \parallel c$ and $H \perp c$. The complexity of the (H, T) magnetic phase diagrams has been anticipated in a previously published preliminary (H, T) magnetic phase diagram for $H \parallel c$. However, the intricate phase boundaries between the antiferromagnetic and the spin-flop phases were not resolved in the preliminary (H, T) magnetic phase diagram. Dielectric, thermal expansion, heat capacity and magnetic susceptibility measurements were carried out in order to clarify the phase boundaries and extend the temperature/magnetic field ranges. Using the anomalies in the magnetic field scans and the magnetic field dependence of the three low temperature phase transitions (T_N , T_{mag} and T^*), the extended (H, T) magnetic phase diagrams for $H \parallel c$ and $H \perp c$ were finalized. In addition to the three previously known phases, five new phases were discovered in the extended (H, T) magnetic phase diagrams. These new phases should be explored further using neutron scattering measurements in high magnetic fields. The multicritical Lifshitz points were detected near ~ 20 K at magnetic fields between 10 to 12 Tesla depending on the magnetic field orientation. In the future, more measurements (i.e heat capacity and pulsed magnetic field measurements) should be performed above 9 Tesla in order to determine the extrapolated phase boundaries and to study the Lifshitz points in more detail.

The complex (H, T) magnetic phase diagrams of CrOCl results from the frustration of the competing spin exchange interactions. The spin exchange interactions were investigated using spin polarized DFT calculations in the low temperature monoclinic crystal structure. The intricate interchain and intrachain spin exchange scenario in CrOCl were explored by identifying seven relevant spin exchange pathways. The DFT results indicated that dominate ferromagnetic spin exchange interactions occur along the \mathbf{a} -axis whereas the antiferromagnetic spin exchange interactions were present along the \mathbf{b} -axis. Rescaling of the spin exchange constants was required in order for the DFT and the experimental results to agree with each other. The scaled DFT results reproduced the principle features of the zero field magnetic structure. The low temperature magnetic structure was then analyzed further by simulations using the scaled spin exchange coupling constants in a classical mean-field/Monte Carlo algorithm. The simulations clearly indicated that quadrupling occurs along the \mathbf{b} -axis consistent with the neutron diffraction measurements. The low temperature magnetic structure consists of antiferromagnetic coupled collinear ferromagnetic stripes. The dominant ferromagnetic spin exchange interactions between the Cr moments results in collinear ferromagnetic chains running along the \mathbf{a} -axis. Two of these chains form collinear ferromagnetic stripes with the neighbouring stripes being antiferromagnetically aligned along the \mathbf{b} -axis. The scaled DFT spin exchange constants were further discussed in terms of the axial next-nearest neighbour Ising (ANNNI) model. The ANNNI model in a tetragonal lattice correctly predicted essential features, especially the incommensurate precursor phase, of the (H, T) magnetic phase diagrams. The spin exchange pathways between the Cr layers in the Cr slabs lead to additional magnetic frustration.

Zusammenfassung

Meine Dissertation befasst sich mit der experimentellen Untersuchung der magnetischen und strukturellen Eigenschaften zweier niedrigdimensionaler antiferromagnetischer Systeme. Bei dem zunächst untersuchten System handelt es sich um die nicht-konventionelle Spin-Peierls Verbindung TiPO_4 . Strukturell enthält TiPO_4 quasi-eindimensionale TiO_2 Bänder, die durch die Verknüpfung über gegenüberliegenden Kanten von schwach entlang der vierzähligen Achse gestauchter TiO_6 Okteder entstehen. Diese Oktaederketten sind untereinander über PO_4^{3-} Tetraedergruppen verknüpft.

In TiPO_4 weisen die Ti Atome die Oxydationstufe +3 auf und haben somit die elektronische Konfiguration $3d^1$ mit einem Spin von $S = \frac{1}{2}$. Die magnetischen Momente der Ti Ionen in TiPO_4 sind über sehr starken antiferromagnetischen Superaustausch ($J_{\text{intra}} = -965$ K) zu eindimensionalen magnetischen Ketten verknüpft. Die Zwischenkettenwechselwirkung beträgt nur etwa 2% des Austauschs innerhalb der Ketten. Magnetisch zeigt TiPO_4 eine interessante Abfolge von zwei Phasenübergängen von der paramagnetischen über eine strukturell inkommensurable Phase zu einem unmagnetischen Spin-Peierls Grundzustand.

Bei dem zweiten in meiner Dissertation untersuchten System handelt es sich um den zwei-dimensionalen Heisenberg Antiferromagneten CrOCl . Strukturell ist CrOCl isotyp zu dem Spin-Peierls System TiOCl , das sich magnetisch sehr ähnlich zu TiPO_4 verhält und ebenfalls eine Abfolge zweier Phasenübergänge und einen unmagnetischen Spin-Peierls Grundzustand aufweist. CrOCl enthält Ketten von Cr^{3+} Ionen (elektronische Konfiguration $3d^3$, $S = \frac{3}{2}$) mit starker ferromagnetischer Wechselwirkung entlang der Ketten. Konkurrierende Austauschwechselwirkung zu Cr Momenten in nächsten und übernächsten

Nachbarketten führt zu komplexem magnetischem Verhalten und einem überaus reichhaltigen Phasendigramm, was sich nach ersten Voruntersuchungen in unserer Gruppe in groben Zügen abzeichnete. Ähnlich zu TiPO_4 findet der Übergang in die langreichweitig geordnete antiferromagnetische Phase über eine strukturell und magnetisch inkommensurable Vorstufe statt.

Beiden Systemen eigen ist die ausgeprägte magnetoelastische Kopplung, die in dieser Dissertaion mittels Messungen der Längenausdehnung als Funktion der Temperatur und des Magnetfeldes verfolgt wurde. Dazu wurde ein miniaturisiertes Dilatometer in Betrieb genommen, in bestehende Kryostatensysteme implementiert und Datenaquisitions- und Auswertesoftware erstellt und getestet. Parallel dazu wurden Messungen der Wärmekapazität und der Magnetisierung als Funktion der Temperatur und des Magnetfeldes, Messungen der Dielektrizitätskonstanten, Elektronenspinresonanz - und Raman Spektroskopiemessungen durchgeführt. Die Messungen werden mit Dichtefunktionalrechnungen der Austauschkonstanten verglichen und durch erste Mean-Field Monte-Carlo Rechnungen des Phasendigramms (für CrOCl) ergänzt. Für TiPO_4 wurde erstmals die Druckabhängigkeit der Phasenübergänge mit Hilfe von Suszeptibilitätsmessungen unter quasihydrostatischem Druck in einem SQUID Magnetometer ermittelt.

Das neue unkonventionelle Spin-Peierls System TiPO_4 wurde als ein System mit zwei sukzessiven Phasenübergängen bei $T_{c1} \approx 74$ K und $T_{c2} \approx 110$ K charakterisiert. Zwischen beiden Temperaturen liegt eine inkommensurable Phase vor, die bisher nur durch Kernresonanzmessungen an ^{31}P belegt war. Mit Hilfe von Einkristall-Strukturuntersuchungen wurde bei 74 K ein struktureller Phasenübergang identifiziert. Die Streudaten können allerdings nicht eindeutig einem Strukturmodell zugeordnet werden. Vielmehr bietet die Symmetrieanalyse drei alternative Strukturmodelle zur Auswahl. Alle drei Modelle belegen aber eine Dimerisierung der Ti-Ti Abstände entlang der Ti-Ketten, allerdings mit leicht unterschiedlichen Dimerisierungsmustern. Dichtefunktionalrechnungen der absoluten Energie dieser drei Strukturalternativen erlauben die Identifikation einer Strukturvariante mit minimaler Energie. Überraschenderweise sind die drei alternativen Kristallstrukturen energetisch sehr nahe beieinander. Die Gesamtenergien der beiden angeregten Strukturvarianten liegen nach den Dichtefunktionalrechnungen nur um weniger als 10 meV oberhalb der Energie der Grundzustandsstruktur. Im Licht dieses Resultats wurde die zwischen 110 K und 74 K auftretende inkommensurable Zwischenphase einer thermisch

induzierten Fluktuation zwischen den Strukturalternativen zugeordnet.

Die Messungen der Temperaturabhängigkeit der anisotropen Längenausdehnung an TiPO_4 Einkristallen¹ belegen klar die beiden Phasenübergänge bei 74 und 110 K. Die Form der jeweils bei den Phasenübergängen auftretenden Anomalien sowie die thermische Hysterese des Lock-in Übergangs aus der inkommensurablen in die kommensurable dimerisierte Phase bei 74 K identifizieren die beiden Phasenübergänge als von zweiter bzw. erster Ordnung. Dieser Befund ist im Einklang mit den Wärmekapazitäts- und Suszeptibilitätsmessungen sowie der Röntgenstrukturuntersuchungen bei tiefen Temperaturen.

Die Längenänderung mit der Temperatur ist erkennbar anisotrop. Während man entlang der Ti Ketten eine Kontraktion mit abnehmender Temperatur feststellt, beobachtet man senkrecht zu den Ketten eine Verlängerung der Kristallabmessungen, d.h. negative thermische Ausdehnung des Gitters, die aber betragsmäßig erheblich geringer ist als die Kontraktion entlang der Ketten. Dieser Befund muss sterischen Effekten der chemisch relativ fest gebundenen PO_4^{3-} Gruppen zugewiesen werden, welche die Ti-Oktaederketten untereinander verknüpfen.

Die Standardtheorien der Magnetfeldabhängigkeit der kritischen Temperatur des Spin-Peierls Übergangs machen detaillierte Voraussagen der Magnetfeldabhängigkeit der kritischen Temperatur, die mit dem Quadrat des Magnetfeldes absinken sollte. Es war aber zu erwarten, dass die relativ hohen kritischen Temperaturen in TiPO_4 und die zur Verfügung stehenden Labormagnetfelder nur zu kleinen Absenkungen der kritischen Temperaturen führen werden. Mittels der sehr empfindlichen Messungen der Längenausdehnung an TiPO_4 konnte die Magnetfeldabhängigkeit der kritischen Temperaturen T_{c1} und T_{c2} gut verfolgt werden. Im Falle des Lock-in Übergangs bei 74 K zeigen die Experimente eine Absenkung der kritischen Temperatur von 90 mK bei einem Magnetfeld von 9 Tesla. Im Rahmen der Messgenauigkeit erfolgt die Reduktion der kritischen Temperatur quadratisch mit dem Feld, im Einklang mit der Theorie. Allerdings ist der Absolutbetrag der Temperaturabsenkung nur etwa halb so groß, wie nach der gängigen Theorie erwartet wird. Für den Übergang aus der paramagnetischen in die inkommensurable Phase bei 110 K ist im Rahmen der Messgenauigkeit keine Magnetfeldabhängigkeit nachweisbar. Die Analyse der magnetfeldinduzierten Längenänderung zwischen 110 K und 74 K zeigt

¹Die Einkristalle zu dieser Untersuchung wurde am Institut für Anorganische Chemie der Universität Bonn in der Gruppe von Prof. R. Glaum synthetisiert.

te aber als überraschendes Ergebnis eine beträchtliche Magnetostriktion der inkommensurablen Zwischenphase, welche auf einen beträchtlichen Einfluss des Magnetfeldes auf die Magnetstrukturfluktuationen im inkommensurablen Zwischenbereich hinweist.

Unter Druck kann die Austauschkopplung entlang der Spinkette erhöht werden. Zusätzlich erlaubt die Anwendung äußerer Drucks eine Beeinflussung der magnetoelastischen Kopplung und damit auch des Spin-Peierls Übergangs. In der Mehrzahl der bekannten Spin-Peierls Systeme sind in der Tat teilweise erhebliche druckinduzierte Anstiege der kritischen Temperatur auch beobachtet worden. Mittels einer Miniaturdruckzelle, die Suszeptibilitätsmessungen bis zu etwa 1 GPa in einem SQUID Magnetometer erlaubt, wurden Messungen der kritischen Temperaturen unter quasihydrostatischem Druck an TiPO_4 durchgeführt. Obwohl die Übergänge unter hohem Druck durch zunehmende nicht-hydrostatische Komponenten des Druckmediums (Fluorinert FC-77) erheblich verschmieren, zeigt die Analyse der Ergebnisse Druckerhöhungen der kritischen Temperaturen bis zu 40 K bei etwa 1 GPa. Dabei beobachtet man bis zu etwa 0.6 GPa einen linearen Anstieg von +27 K/GPa. Nach einem Knick wachsen die kritischen Temperaturen wieder linear an, bis kritische Temperaturen von +39(3) K und +42(5) K bei 0.9 GPa beobachtet werden.

Die vorgelegten Ergebnisse, insbesondere die Messungen der Magnetostriktion der inkommensurablen Zwischenphase sowie der Druckabhängigkeit der Phasenübergänge indizieren weitere Messungen unter erhöhten Magnetfeldern und Drücken, um insbesondere die Änderungen der Kristallstrukturen z.B. mittels Ramanmessungen oder Röntgenstrukturanalyse eingehender zu untersuchen.

Im zweiten Teil der Dissertation beschreibe ich die Ergebnisse meiner Untersuchungen der magnetischen Eigenschaften des zwei-dimensionalen Heisenberg Antiferromagneten CrOCl . Strukturell weist CrOCl Doppelschichten von Cr^{3+} Ionen auf (parallel zur **ab** Ebene), die sowohl über Sauerstoff- als auch über Chloranionen verknüpft sind. Solche Schichtpakete sind über van der Waals Kontakte entlang der kristallographischen *c*-Achse gestapelt. Wie schon eingangs erwähnt, ist CrOCl strukturell isotyp zu dem Spin-Peierls System TiOCl , das viele Analogien zu TiPO_4 aufweist. Der Ursprung der Spin-Peierls Übergänge in TiOCl und insbesondere die aufgrund der zweidimensionalen Kristallstruktur zu erwartenden komplexeren Austauschkopplungspfade sind für TiOCl noch weitgehend ungeklärt. Dies gab Anlass zur Untersuchung der magnetischen Eigenschaften des isotypen Systems CrOCl .

Die Proben zu diesen Untersuchungen wurden uns im Rahmen einer Zusammenarbeit mit der Gruppe um Prof. van Smaalen an der Universität Bayreuth zur Verfügung gestellt. Dort werden auch Untersuchungen der Tieftemperaturkristallstruktur sowie der magnetischen Struktur mittels Neutronenbeugung durchgeführt. Nach vorausgehenden Untersuchungen wurden in CrOCl drei magnetische Phasenübergänge beobachtet, die bei $T_N \approx 13.5$ K, bei $T_{\text{mag}} \approx 27$ K sowie bei $T^* \approx 28$ K auftreten. Während der Phasenübergang bei 13.5 K als Phasenübergang erster Ordnung in eine langreichweitig (kollinear) geordnete antiferromagnetische Phase identifiziert werden konnte, blieb insbesondere der Charakter der Phasenübergänge bei 27 K und 28 K nach den ersten Untersuchungen mysteriös. Erste Röntgenuntersuchungen bei tiefen Temperaturen an Einkristallen zeigten, dass der Phasenübergang bei 13.5 K in die langreichweitig geordnete kollinear antiferromagnetische Phase mit einer sehr kleinen strukturellen Verzerrung der Kristallstruktur von orthorhombischer in monokline Symmetrie einhergeht. Wie schon bei TiPO_4 beobachtet, deutete dieser Befund auf die Bedeutung magnetoelastischer Kopplung hin. Ebenfalls bemerkenswert war, dass erste Messungen der magnetischen Suszeptibilität bei hohen Temperaturen vorherrschend ferromagnetische Austauschkopplung belegen. Dieser Befund steht im Kontrast zu der bei tiefen Temperaturen gefundenen antiferromagnetischen Ordnung und weist auf das Vorliegen konkurrierender Austauschkopplungen und magnetischer Frustration hin.

Der Schwerpunkt der Untersuchungen in meiner Dissertation lag auf der Aufklärung der teilweise sehr komplexen magnetischen Phasendiagramme mittels verschiedener experimenteller Techniken. Dazu wurden temperatur- und magnetfeldinduzierte Anomalien mit Hilfe der temperatur- und magnetfeldabhängigen Dilatometrie verfolgt. Messungen dielektrischer Anomalien entlang der Phasengrenzen, Messungen der spezifischen Wärmekapazität, Magnetisierungsmessungen an orientierten Kristallen mittels Labortechniken (SQUID Magnetometrie bis 7 Tesla) sowie an Pulverproben in gepulsten Magnetfeldern bis zu 60 Tesla erlaubten die Vervollständigung der Phasendiagramme. Insbesondere die Thermodilatometrie sowie Anomalien in der Dielektrizitätskonstanten enthüllten weitere magnetostrukturelle Phasenübergänge knapp unterhalb Zimmertemperatur bei etwa 250 K. Diese wurden mittels sehr empfindlicher Messungen der Ramanspektren in diesem Temperaturbereich sowie der Auswertung der Temperaturabhängigkeit der bei 9 GHz gemessenen Elektronenspinresonanzspektren eingehend verfolgt. Zunächst wurden die Suszepti-

bilitätsmessungen an CrOCl zu sehr hohen Temperaturen (800 K) ausgedehnt. Die Ergebnisse dieser Experimente erlaubten eine sehr genaue Festlegung der Curie-Weiss Temperatur zu $+26.1(1)$ K. Dieser Wert ist etwa zu 30% erhöht gegenüber dem bisher aus Messungen bis Zimmertemperatur bestimmten Wert. Die präzise Festlegung der Curie-Weiss Temperatur ermöglichte die Skalierung der Austauschkonstanten, die aus Dichtefunktionalrechnungen bestimmt wurden (siehe unten).

Die Mehrzahl der Experimente diente der detaillierten Aufklärung der magnetischen Phasendiagramme. Die Morphologie der sehr dünnen Kristallplättchen erlaubte dazu zunächst Messungen mit Magnetfeldorientierung sowohl senkrecht als auch parallel zu den Chrom-Sauerstoff-Chlor Schichten, d.h. parallel (\mathbf{c}) und senkrecht zur leichten Richtung der Spinorientierung. Zusätzlich zu den drei bekannten magnetischen Phasen im bisher bestimmten Phasendiagramm (bisher wurde nur das Diagramm für $H \parallel \mathbf{c}$ untersucht) konnten insgesamt fünf neue Phasenbereiche in den Phasendiagrammen ($H \parallel \mathbf{c}$ und $H \perp \mathbf{c}$ in der \mathbf{ab} Ebene) identifiziert werden. Vergleiche mit der aus Neutronenpulveruntersuchungen bestimmten magnetischen Struktur zeigen, dass die Phasengrenze bei ≈ 27 K den Übergang aus der paramagnetischen Phase in eine inkommensurabel antiferromagnetisch geordnete Phase markiert. Der Phasenübergang erster Ordnung bei ≈ 13 K markiert den Übergang aus der inkommensurablen Phase in die kollinear langreichweitig geordnete kommensurable antiferromagnetische Phase, in der entlang der \mathbf{a} Richtung kollinear ferromagnetisch angeordnete Cr Ketten ausgebildet werden. Senkrecht zur \mathbf{a} -Achse bildet sich eine antiferromagnetische Streifenstruktur aus. Sie ist gekennzeichnet durch eine Alternierung von jeweils zwei ferromagnetischen Ketten in den Chrom Schichten, so dass insgesamt eine Vervierfachung der nuklearen Elementarzelle innerhalb der Chrom-Doppelschichten resultiert. Die zwischen 27 K und 13.5 K ausgebildete inkommensurable magnetische Struktur nimmt unter Ausbildung einer Spindichtewelle die wesentlichen Züge der vervierfachten kommensurablen Überstruktur vorweg. Magnetisierungsmessungen in gepulsten Magnetfeldern am Hochfeldmagnetlabor in Dresden-Rossendorf durchgeführt, legen die obere Phasengrenze bei etwa 20 Tesla fest. Mit zunehmender Temperatur wird die Phasengrenze abgesenkt und mündet bei einem Lifshitz Punkt bei etwa 20 K und 10 - 12 Tesla (abhängig von der Orientierung des Magnetfeldes) in die Phasengrenze ein, die die paramagnetische von der inkommensurablen Phase trennt.

Spin-polarisierte Dichtefunktionalrechnungen der absoluten Energie einer Reihe magnetisch geordneter Konfigurationen erlauben einen ersten Zugang zu den überaus komplexen Phasendiagrammen von CrOCl. Bildet man die berechneten Energien der ferro- und antiferromagnetisch geordneten Strukturen auf einen Heisenberg-Austauschoperator ab, so erhält man folgendes Bild der Austauschkopplungen: Entlang der Cr Ketten parallel zur \mathbf{a} Richtung findet man sehr starke ferromagnetische Austauschkopplung zu den nächsten Cr Nachbarn innerhalb der Ketten. Die Austauschkopplung zu übernächsten Nachbarn ist sehr schwach und kann in erster Näherung vernachlässigt werden. Senkrecht zu \mathbf{a} , parallel \mathbf{b} findet man ein weitaus komplexeres Szenario: Zwischenkettenkopplung zu nächsten Nachbarn in derselben Chromatom Schicht ist antiferromagnetisch. Darüber hinaus findet man aber auch eine beträchtliche ferromagnetische Kopplung zu übernächsten Nachbarn, die mit der antiferromagnetischen Kopplung zu den nächsten Nachbarn in Konkurrenz tritt. Zusätzlich findet man auch ferromagnetische Austauschkopplung zu nächsten Nachbarn innerhalb der Chrom Doppelschichten. Die Befunde der spinpolarierten Dichtefunktionalrechnungen belegen ein überaus komplexes Szenario der Austauschkopplungen, wobei der Austauschkopplung zwischen den Chrom Ebenen in einer Doppelschicht offenbar besondere Bedeutung zukommt. Darüber hinaus hängen einige der Austauschkopplungen noch erheblich von elektronischen Korrelationen ab und wechseln mit anwachsenden Korrelationsparameter U sogar ihr Vorzeichen.

Erste Mean-Field Monte Carlo Simulationen der magnetischen Struktur mithilfe der McPhase Software erlauben ein Verständnis der Vierfach-Überstruktur, nicht aber der inkommensurablen Phase. Die Existenz der inkommensurablen Phase ist offenbar Folge der konkurrierenden Wechselwirkungen entlang \mathbf{b} und der damit einhergehenden magnetischen Frustration senkrecht zu den ferromagnetischen Ketten. Solche magnetische Systeme mit konkurrierenden Wechselwirkungen zu nächsten und übernächsten Nachbarn zwischen ferromagnetisch geordneten Ketten oder Schichten sind im Rahmen des ANNNI (axial next-nearest neighbour Ising)-Modells untersucht worden. Für einen Austauschparametersatz, J_{nn} and J_{nnn} , $-J_{nnn}/J_{nn} \leq 0.5$ werden im Rahmen des ANNNI-Modells in der Tat inkommensurable Vorphasen beobachtet, bevor die geordnete (sogenannte) $\langle 2,2 \rangle$ Antiphasenstruktur einsetzt, wie sie auch für CrOCl beobachtet wird.

Software for the collection and the analysis of the thermal expansion data

To collect and process the thermal expansion (TE) data, two software applications were developed. The TE data were measured, collected and stored in data files by an independent measuring program. The data file is processed by a separate program called ‘The TE Dilatometer data processor’. This program uses calibration files and mathematical algorithms to obtain the length change $\frac{\Delta L}{L}(H, T)$ of a sample.

A.1 Data collection

On a Physical Property Measuring System (Quantum Design, PPMS), small scripts or macros were written using the SAX Basic language within the PPMS MultiVi program to obtain capacitance data, e.g. from Andeen-Hagerling capacitance bridge. Macros were written for all possible measurement scenarios. These scenarios included sweep/stable temperature scans, magnetic field scans at constant temperatures and combinations of the both magnetic and temperature scans. By using one of these macros, all internal functions of the PPMS MultiVi program as well as external devices connected by GPIB IEEE-488 can be controlled. The data collection can be fully automated similar to a commercial PPMS sequence. Upon execution of the macro, a window will be displayed allowing the user to enter the required information and the parameters for the measurement. The user input window can be seen in Figure A.1. Once the user inputs the required information and clicks the ‘OK’ button, the macro will execute and perform requested measurements.

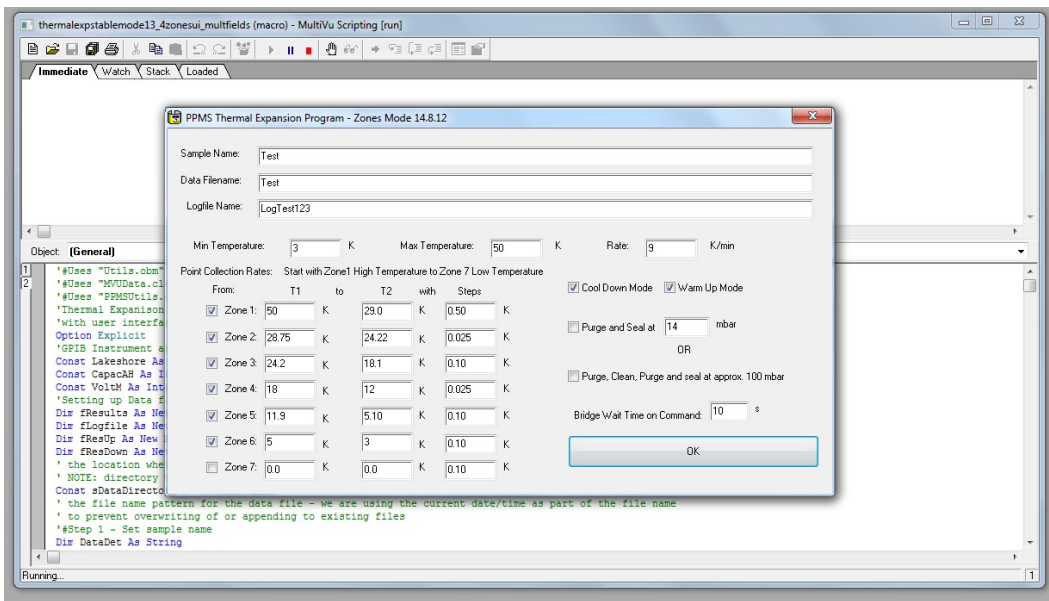


Figure A.1: The PPMS MultiVi user input window for the thermal expansion macro allowing the user to specify the name of the sample, the datafile name, the logfile name and the desired measurement temperature range.

A.2 Data processing

The collected TE data must be processed in order to convert the measured capacitance values into TE data. The program which I wrote to perform the processing and the analysis of the data is based on the TU Wien PAT program. The original PAT program was produced by the designers of our miniaturized thermal expansion dilatometer cell at TU Wien.[197] To develop this data processing program¹, the original python code was translated into delphi code and a graphically user interface with additional functionalities was added. The results from each step in the original python algorithms were systematically checked against the new delphi code to verify the validity of the translated algorithms. The graphical user interface of the my TE data processing program can be seen in Figure A.2.

¹The full source code, the binary executable and the example files are available upon request.

APPENDIX A: SOFTWARE FOR THE COLLECTION AND THE ANALYSIS OF THE THERMAL EXPANSION DATA

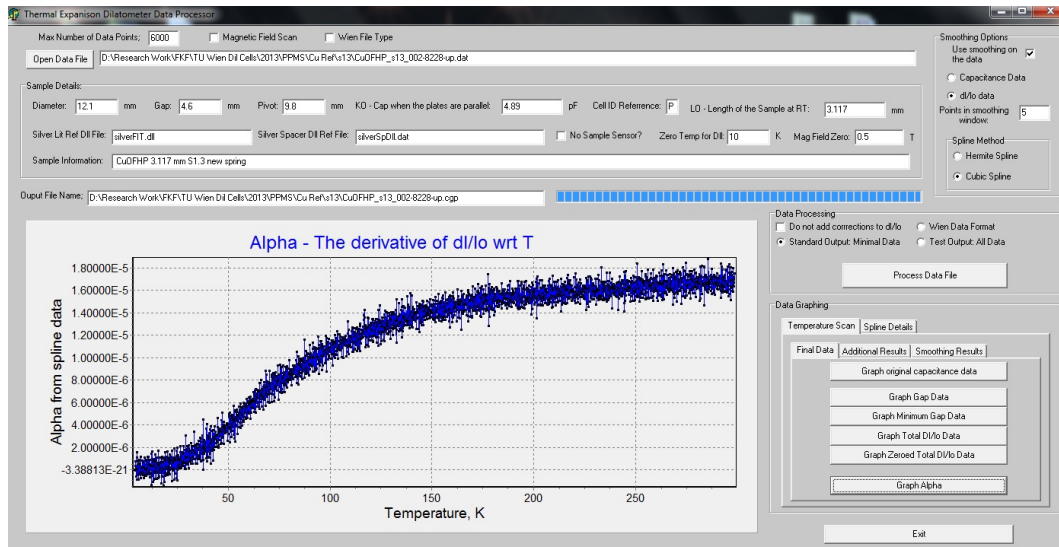


Figure A.2: The graphical user interface (GUI) for the thermal expansion data processing program showing the processed data for a copper reference standard.

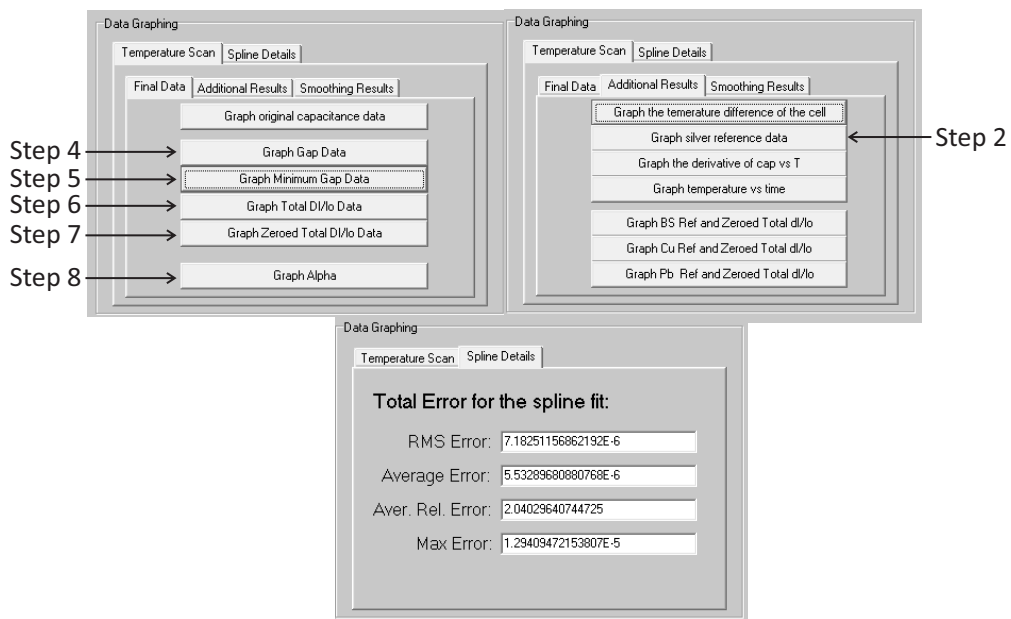


Figure A.3: The graphical user interface (GUI) and the information available for temperature scans in the data graphing tab of the TE data processing program. The step labels pointing to the buttons correspond to the eight-step algorithm discussed on p. 202.

In Figure A.2, the average linear coefficient of thermal expansion $\alpha_m(T)$ vs temperature can be seen for a small cylinder of oxygen free high thermal conductivity (OFHC) copper. The software allows the user to graphically examine each step of the data processing algorithms. The input or the output data can be smoothed out using spline fittings² (i.e. cubic and hermite) [198]. The spline fittings are calculated by iteratively fitting a spline curve to the user specified number of data points in the smoothening window. Once the user clicks the ‘Process Data File’ button (see Figure A.2), the program will generate the final data and allow the user to graph all pertinent information. By navigating the many tabs and buttons on the lower right corner of program (see Figure A.3), the user can graphically examine the conditions of the measurement and the steps in the eight-step processing algorithm (see p. 203).

The TE data processing described in the previous paragraph uses the tilted plate capacitance (TPC) equation (see Refs. [79] and [199]) to process the raw capacitance data. The tilted plate capacitance formula is required since the raw capacitance data only reflects the relative length change of sample.[79] In the TPC formula (see Equation A.1), the variation of the raw capacitance $C(H, T)$ is determined by the following parameters: the length of the sample and the silver sample plate holders on top of the sample, the capacitor plates inner and outer radii as well as the body of dilatometer. The raw capacitance data $C(H, T)$ is described by the following equation³ [79, 197, 199] :

$$C(H, T) = \frac{2\epsilon_0}{d(H, T)} \left[\hat{A}_0(T) \frac{(1 - \sqrt{1 - \gamma_0^2})}{\gamma_0^2} - \hat{A}_i(T) \frac{(1 - \sqrt{1 - \gamma_i^2})}{\gamma_i^2} \right] \quad (\text{A.1})$$

where

$$\gamma_0 = \frac{r_0}{b} \left[\frac{k(T)}{d(H, T)} - 1 \right] \quad (\text{A.2})$$

$$\gamma_i = \frac{r_i}{b} \left[\frac{k(T)}{d(H, T)} - 1 \right] \quad (\text{A.3})$$

$$\hat{A}_0(T) = \pi r_0^2 \left[1 + \frac{\Delta L_{Ag-Lit}(T)}{L} \right] \quad (\text{A.4})$$

²The implemented cubic and hermite spline fitting algorithms were obtained from the Delphi ALGLib library. For further details, please consult the ALGLib website at www.alglib.net.

³The full derivation of these equations is discussed in detail in Ref. [199].

$$\hat{A}_i(T) = \pi r_i^2 \left[1 + \frac{\Delta L_{Ag-Lit}}{L}(T) \right] \quad (\text{A.5})$$

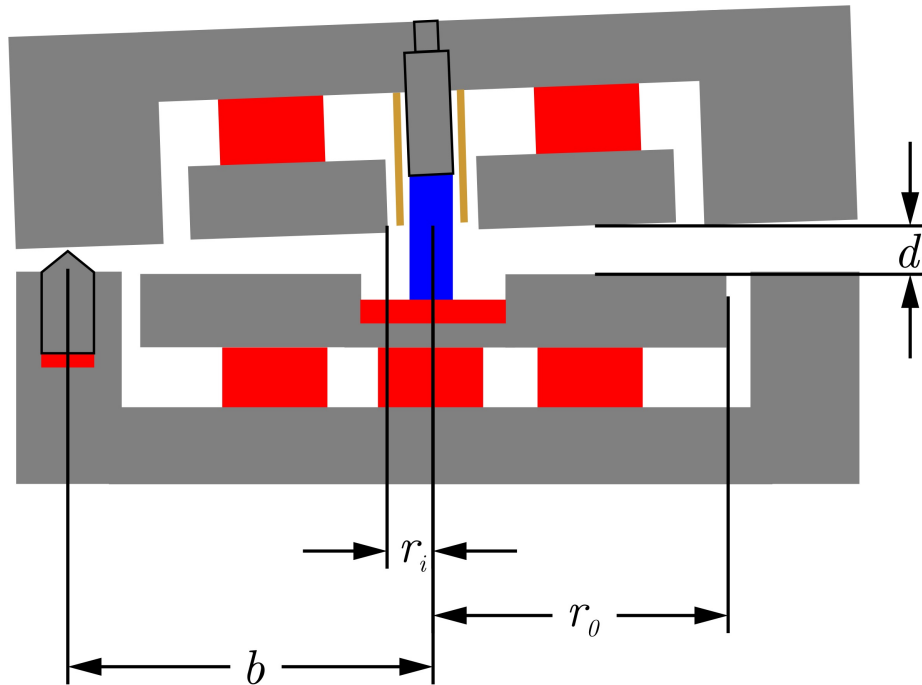
$$k(T) = k(T_0) \left[1 + \frac{\Delta L_{Ag-Lit}}{L}(T) \right] \quad \text{from} \quad (\text{A.6})$$

$$k(T_0) = \frac{\epsilon_0}{K_0} [r_0^2 \pi - r_i^2 \pi] \quad (\text{A.7})$$

The pertinent variables present in Equation A.1 – A.7 are described in Table A.1 and shown in Figure A.4.

Table A.1: The description of all parameters in the titled plate capacitance formula for the miniaturized thermal expansion dilatometer cell. For further details about the parameters, please consult M. Rotter *et al.* [79].

Variable	Description
$d(H, T)$	The gap $d(H, T)$ of the dilatometer cell is calculated from Equation A.1 using Newton's method.
r_i and r_0	The inner radius r_i and outer radius r_0 can be estimated by measuring the specified length in Figure A.4 as well as applying a correction for edge effects.[200, 201] The correct values of r_i and r_0 are obtained by fitting the zero $\frac{\Delta l_{sample}}{l}(T)$ of a reference sample. By adjusting r_i and r_0 , the measured curve can be fitted onto the reference curve from literature.
b	The pivot distance b is obtained by measuring the length specified in Figure A.4.
$\frac{\Delta l_{Ag-Lit}}{l}(T)$	The literature values for the percentage thermal expansion of silver ($\frac{\Delta l_{Ag-Lit}}{l}(T)$) are stored in a data file and read into memory. The $\frac{\Delta l_{Ag-Lit}}{l}(T)$ values were originally published by White <i>et al.</i> [202].
K_0	The capacitance of the dilatometer cell when the plates are parallel is denoted as K_0 .
L_{RT}	The original length of the sample L_{RT} is obtained by measuring the sample along the measurement axis using a caliper or a micrometer.



Materials:

- Sapphire
- Silver
- Sample
- Brass

Figure A.4: The schematic diagram of the miniaturized thermal expansion dilatometer cell indicating the essential distance parameters summarized in Table A.1. This Figure was reproduced figures in Refs. [45] and [79]. N.B. The gap between the top and the bottom of the dilatometer is exaggerated. The components are not to scale.

For TE data processing, the TPC equation is implemented using an eight-step algorithm [197]:

1. The reference files for the silver spacer and the body of the dilatometer cell are loaded into memory. The diameter, the gap, the pivot and the K_0 values specified in the TE data processing program window are equated to the following variables:

$$\begin{aligned} r_i &= \frac{1}{2} \cdot \text{Gap} \cdot 10^{-3} \text{ m} \\ r_0 &= \frac{1}{2} \cdot \text{Diameter} \cdot 10^{-3} \text{ m} \\ b &= \text{Pivot} \cdot 10^{-3} \text{ m} \\ kr &= K_0 \cdot 10^{-12} \text{ F} \end{aligned}$$

where K_0 is the capacitance of dilatometer cell when the top and the bottom plates are parallel ($K_0 = 4.89 \text{ pF}$).

2. The silver reference values for each measurement temperature are linearly interpolated from the reference files loaded in the previous step and stored in memory.
3. The characteristic parameters of the dilatometer cell described in Table A.1 and the zero $\frac{\Delta L}{L}$ temperature/magnetic field point are read into memory.
4. Using Newton's method, the gap of the dilatometer cell ($d(H, T)$ in Equation A.1) is calculated for each measurement in the data set. If smoothening of the capacitance data using a cubic/hermite spline is selected, the capacitance data will be smoothened before the gap $d(H, T)$ is calculated.
5. The minimum gap of the dilatometer cell $MinGap$ is found by searching the complete data set for the smallest calculated gap $d(H, T)$. The minimum gap is then subtracted from all points in the data set using the following equation for the sample length change $\frac{\Delta d_{sample}}{L_{RT}}$ [197]:

$$\frac{\Delta d_{sample}}{L_{RT}}(H, T) = \frac{d(H, T) - MinGap}{L_{RT}} \quad (\text{A.8})$$

6. The total $\frac{\Delta L}{L}$ is subsequently evaluated by adding all the reference values, calculated in step 2, to all the measurements in the data set. The following equation is used to calculate $\frac{\Delta L_{total}}{L}$ from Refs. [79] and [199]⁴:

$$\frac{\Delta L_{total}}{L}(H, T) = \frac{\Delta d_{sample}}{L_{RT}}(H, T) - \frac{\Delta d_{Ag-Spacer}}{L_{Ag-Spacer \text{ at } RT}}(T) + \frac{\Delta L_{Ag-Lit}}{L_{Ag \text{ at } RT}}(T) \quad (\text{A.9})$$

7. The zeroed $\frac{\Delta L_{total}}{L}(H, T)$ is then obtained by first identifying the $\frac{\Delta L_{total}}{L}(H, T)$ closest to the user provided zero temperature T_1 or magnetic field H_1 point. The zeroed $\frac{\Delta L_{total}}{L}(H, T)$ is then calculated by subtracting all calculated values of $\frac{\Delta L_{total}}{L}(H, T)$ by the $\frac{\Delta L_{total}}{L}(H_1 \text{ or } T_1)$ value at the desired temperature T_1 or magnetic field H_1 . If smoothening of the zeroed $\frac{\Delta L_{total}}{L}(H, T)$ data using a cubic/hermite spline is selected, the zeroed $\frac{\Delta L_{total}}{L}(H, T)$ data will be smoothened before step 8.
8. For temperature scans, the average linear coefficient of thermal expansion $\alpha_m(H, T)$ (the derivative of zero $\frac{\Delta L_{total}}{L}(H, T)$ with respect to temperature) is calculated by iteratively computing the slope between pairs of data points. If smoothening using a cubic/hermite spline is selected, $\alpha_m(H, T)$ will also be calculated from the smoothened zero $\frac{\Delta L_{total}}{L}(H, T)$ data.

The two most important quantities from the eight-step algorithm described above are $\frac{\Delta L_{total}}{L}(H, T)$ which is also simply called $\frac{\Delta L}{L}(H, T)$ along with the average linear coefficient of thermal expansion $\alpha_m(H, T)$. These quantities can be examined in the data processing program. The final data is stored in an ASCII data file which can be easily imported into a graphing program for further examination and presentation.

⁴The full derivation of this equation is discussed in detail in Ref. [199].

A.3 Selected excerpts of the data processing code

A.3.1 Calculation of the gap and $\Delta L/L$

The Delphi code reproduced below was translated from the TU Wien's PAT software.[197] An additional code was added to allow the user to smoothen the input or the output data in the processing algorithm.

```

-----
{This procedure calculates the pivot distance k(T0) at room
temperature and stores the value in the variable V. V is then
used in the CompDistanceFunction. V is the distance between
the parallel plates with a typically value around 0.2 mm.
EPS0 = permittivity of free space}
procedure TiltPlate();
begin
    V:=EPS0/kr*(ro*ro*pi - ri*ri*pi); //Equation A.7
    //showmessage(floattoStr(V));
end;
-----

{This function computes the difference between the left and
the right side of the Equation A.1}
function CompDistanceFunction(d:extended;w:integer):extended;
var
    dllAg,Q,go,gi,a,ai,AExp,Cap,t,ti:extended;
begin
    dllAg:=TrefAg[w];           //correction for the silver spacer
    Cap:=Tc[w]*1.0E-12;        //capacitance of the TE cell

    Q:=V*(1+dllAg); //Equation A.6
    go:=ro/b*(Q/d-1); //Equation A.3
    gi:=ri/b*(Q/d-1); //Equation A.2

    AExp:=(1+dllAg);
    Ai:=ri*ri*pi*AExp; //Equation A.5
    A:=ro*ro*pi*AExp; //Equation A.4

    t:=A*(1.-sqrt(1.-go*go))/go/go; //Equation A.1
    ti:=Ai*(1.-sqrt(1.-gi*gi))/gi/gi; //Equation A.1

    Result:=Cap - (2.*EPS0/d *(t-ti));
end;

```

```

-----
{This function calculates the distance or the gap of the plates
using Newton's method. This method will only work if the
capacitance of the dilatometer cell is less than or equal
to 9.7 pF. From testing, a capacitance value of 11.2 pF produces
the f0*f1>0 error condition resulting in the inability of this
method to calculate the gap. The upper limit of the capacitance
value is between 9.7 pF and 11.2 pF. The lower limit of the
capacitance for this method is not known at this time. }
function NewtonMeth(x0:extended;x1:extended;i:integer):extended;
var
  f0,f1,xm,xmm1,falt,fm,fmm1,xmp1,fneu,ddx,fmp1:extended;
  n:integer;
begin
  f0:=CompDistanceFunction(x0,i);
  f1:=CompDistanceFunction(x1,i);
  if f0*f1>0 then
  begin
    showmessage('f(x0)=f(%f)=%g and f(x1)=
      f(%f)=%g must have a different sign');
    result:=0;
    exit;
  end;
  if abs(f0) < Delta then
  begin
    result:=x0;
    exit;
  end;
  if abs(f1) < Delta then
  begin
    result:=x1;
    exit;
  end;

  xm:=x1;
  xmm1:=x0;
  falt:=0;
  n:=0;

  while True do
  begin
    n:=n+1;
    fm:=CompDistanceFunction(xm,i);

```

```

fmm1:=CompDistanceFunction(xmm1,i);
xmp1:=xm - fm /((fm-fmm1)/(xm-xmm1));
fneu:=CompDistanceFunction(xmp1,i);
ddx:=abs((xm-xmp1)/xm);

if ddx < abs(dx)then break;
if abs(fneu-falt) <= Epsilon then break;
if abs(fneu)<Delta then break;

falt:=fneu;
fmp1:=CompDistanceFunction(xmp1,i);

if fmp1*fm<0 then
begin
xmm1:=xmp1;
Continue;
end;

if fmp1*fmm1<0 then
begin
xm:=xmp1;
Continue;
end;
end;
result:=xmp1;
end;
-----
{This procedure feeds the input data into Newton's method
and fills the gap array with the calculated values}
procedure CalcGap();
var
i:integer;
x0,x1:extended;
begin
for i:=0 to (NumPoints-1) do
begin
//read in the data points
ST:=Tb[i];
{SmoothTF,CapSmoTF}
if SmoothTF then
begin
SC:=Tcapsmooth[i]
end
else SC:=Tc[i];

```

```

//Calculate the starting values for Newton's method
if SC > 2*kr then x0:=0.4*V
else x0:=0.5*V;
if SC < 0.6*kr then x1:=2.5*V
else x1:=2*V;
//Calculate the gap using Newton's method
Tg[i]:=NewtonMeth(x0,x1,i);
end;
end;
-----
{This function finds the smallest gap in the gap array and
returns the value}
function FindMinGap():extended;
var
  i:integer;
  MinVal:extended;
begin
  MinVal:=Tg[0];

  for i:=0 to (NumPoints-1) do
    begin
      if Tg[i] < MinVal then MinVal:=Tg[i];
    end;

  result:=MinVal;
end;
-----
{This procedure calculates the dl/l0 using the gap array and the
FindMinGap function}
procedure DllCalc();
var
  i:integer;
  MinGap:extended;
begin
  MinGap:=FindMinGap();
  //showmessage('MinGap is ' + floattostr(MinGap));
  for i:=0 to (NumPoints-1) do
    begin
      Tdll[i]:=(Tg[i]-MinGap)/L0e; //Equation A.8
    end;
end;
-----
{This procedure calculates the final dll value using the
measured dll array (Tdll), the spacer ref dll value (Tspref)

```

```

and the ref Ag value (TrefAg) at each temperature.}
procedure FinalDllData();
var
  i:integer;
begin
  for i:=0 to (NumPoints-1) do
    begin
      if CorrectCheck = false then
        Tfdll[i]:=Tdll[i]-Tspref[i]+TrefAg[i] //Equation A.9
      else Tfdll[i]:=Tdll[i];
    end;
  end;
end;

```

A.3.2 Spline smoothening algorithm

The smoothening procedure uses the ALGLib spline library to fit a cubic or hermite spline to a set number of data points.[198]

```

procedure SmoothFinalDllData();
var
  i,j,counter,startingpoint,endingpoint:integer;
  info:integer;
begin
  {Tderiv1 = Derivative of the final DLL data
  Tderiv2 = Derivative of the cap data
  X = 1D array of the temperatures
  Y = 1D array of the data to be smoothened
  D = 1D array of the original data
  TFdllSmooth = Smoothened Final Dll Data
  PointWindow = Number of points to average}

  startingpoint:=0;
  endingpoint:=0;
  TotalRMSError:=0;
  TotalAvgError:=0;
  MaxError:=0;
  AvgRelError:=0;

  SetLength(X,PointWindow);
  SetLength(Y,PointWindow);
  SetLength(D,PointWindow);

```

```

while startingpoint < Numpoints do
  begin
    counter:=0;

    startingpoint:=endingpoint;

    while ((counter < PointWindow) and
           ((counter+startingpoint)<Numpoints)) do
      begin
        {-----}
        if MagFieldBool then
          X[counter]:=TMag[counter+startingpoint]
        else X[counter]:=Tb[counter+startingpoint];
        {-----}
        Y[counter]:=Tzd11[counter+startingpoint];
        D[counter]:=Tderiv1[counter+startingpoint];
        counter:=counter+1;
      end;

      endingpoint:=startingpoint+counter;

      //showmessage(inttostr(counter));

      {herminSplineTF,cubicSplineTF}

      if counter > 2 then
        begin
          if herminSplineTF then
            begin
              Spline1DBuildHermite(X,Y,D,counter,S);
              Spline1DFitHermite(X,Y,counter,6,info,S,rep);
            end;
          if cubicSplineTF then
            Spline1DFitCubic(X,Y,counter,6,info,S,Rep);
          For i:=startingpoint to endingpoint do
            TFd11Smooth[i]:=Spline1DCalc(S,Tb[i]);
          end;

          {TotalRMSError,TotalAvgError,MaxError,AvgRelError}
          TotalRMSError:=TotalRMSError+Rep.RMSError;
          TotalAvgError:=TotalAvgError+rep.AvgError;
          MaxError:=MaxError+Rep.MaxError;
          AvgRelError:= AvgRelError+Rep.AvgRelError;
        end;
      end;
    end;
  end;
end;

```

Bibliography

- [1] E. Ising, *Zeitschrift für Physik A Hadrons and Nuclei* **31**, 253 (1925).
- [2] L. Onsager, *Physical Review* **65**, 117 (1944).
- [3] J. C. Bonner and M. E. Fisher, *Physical Review* **135**, A640 (1964).
- [4] X. Wang and T. Xiang, *Physical Review B* **56**, 5061 (1997).
- [5] T. Xiang, *Physical Review B* **58**, 9142 (1998).
- [6] T. Xiang and X. Wang, *Lecture Notes in Physics: Density-matrix renormalization*, vol. 528 (Springer, 1999).
- [7] J. M. Law, H. Benner, and R. K. Kremer, *Journal of Physics: Condensed Matter* **25**, 065601 (2013).
- [8] D. C. Johnston, R. K. Kremer, M. Troyer, X. Wang, A. Klümper, S. L. Bud'ko, A. F. Panchula, and P. C. Canfield, *Physical Review B* **61**, 9558 (2000).
- [9] N. D. Mermin and H. Wagner, *Physical Review Letters* **17**, 1133 (1966).
- [10] V. L. Berezinskii, *Soviet Physics - Journal of Experimental and Theoretical Physics* **32**, 493 (1971).
- [11] J. Des Cloizeaux and J. J. Pearson, *Physical Review* **128**, 2131 (1962).
- [12] L. J. de Jongh and A. R. Miedema, *Advances in Physics* **23**, 1 (1974).

- [13] M. Steiner, J. Villain, and C. G. Windsor, *Advances in Physics* **25**, 87 (1976).
- [14] L. J. de Jongh, ed., *Magnetic Properties of Layered Transition Metal Compounds* (Kluwer Academic Publishers, 1990).
- [15] R. Dingle, M. E. Lines, and S. L. Holt, *Physical Review* **187**, 643 (1969).
- [16] H. J. Mikeska, *Journal of Magnetism and Magnetic Materials* **13**, 35 (1979).
- [17] J. W. Bray, H. R. Hart, L. V. Interrante, I. S. Jacobs, J. S. Kasper, G. D. Watkins, S. H. Wee, and J. C. Bonner, *Physical Review Letters* **35**, 744 (1975).
- [18] A. J. Berlinsky, *Contemporary Physics* **17**, 331 (1976).
- [19] M. Hase, Ph.D. thesis, The University of Tokyo (1993).
- [20] M. Hase, I. Terasaki, and K. Uchinokura, *Physical Review Letters* **70**, 3651 (1993).
- [21] A. Seidel, C. A. Marianetti, F. C. Chou, G. Ceder, and P. A. Lee, *Physical Review B* **67**, 020405 (2003).
- [22] L. Palatinus, A. Schönleber, and S. van Smaalen, *Acta Crystallographica Section C: Crystal Structure Communications* **61**, i47 (2005).
- [23] J. M. Law, Ph.D. thesis, Loughborough University (2011).
- [24] J. M. Law, C. Hoch, R. Glaum, I. Heinmaa, R. Stern, J. Kang, C. Lee, M. H. Whangbo, and R. K. Kremer, *Physical Review B* **83**, 180414 (2011).
- [25] A. N. Christensen, T. Johansson, and S. Quézel, *Acta Chemica Scandinavica A* **28**, 1171 (1975).
- [26] A. Schönleber, J. Angelkort, S. van Smaalen, L. Palatinus, A. Senyshyn, and W. Morgenroth, *Physical Review B* **80**, 064426 (2009).
- [27] Y. Touloukian, *Thermal Expansion: Metallic Elements and Alloys*, vol. 12 of *Thermophysical Properties of Matter* (IFI/Plenum, 1977).

- [28] R. S. Krishnan, R. Srinivasan, and S. Devanarayanan, *Thermal Expansion of Crystals* (Pergamon Press, 1979).
- [29] B. Yates, *Thermal Expansion* (Plenum Press, 1972).
- [30] The 1920 Nobel Prize in Physics, URL http://www.nobelprize.org/nobel_prizes/physics/laureates/1920/.
- [31] C. Ho, R. Taylor, and R. Taylor, *Thermal Expansion of Solids*, Cindas Data Series on Material Properties (ASM International, 1998).
- [32] K. F. Slotte, Öfersigt af Finska Vetenskaps-Societeten Förhanlingar **25**, 16 (1893).
- [33] K. F. Slotte, Acta Societatis Scientiarum Fennicae **26** (1900).
- [34] K. F. Slotte, Öfersigt af Finska Vetenskaps-Societeten Förhanlingar **48** (1906).
- [35] G. Mie, Annals of Physics **316**, 657 (1903).
- [36] F. H. Koenemann, *Relation between compressibility, thermal expansion, atom volume and atomic heat of the metals* (2007), URL <http://www.elastic-plastic.de/Grueneisen1908.pdf>.
- [37] E. Grüneisen, Annals of Physics **26**, 393 (1908).
- [38] E. Grüneisen, Annals of Physics **39**, 257 (1912).
- [39] T. H. K. Barron and G. White, *Heat Capacity and Thermal Expansion at Low Temperatures* (Kluwer Academic/Plenum Publishers, 1999).
- [40] O. P. Pahuja, *Solid State Physics* (University Science Press, 2011).
- [41] A. Moral, *Handbook of Magnetostriction and Magnetostrictive Materials*, vol. 1 of *Handbook of Magnetostriction and Magnetostrictive Materials* (Del Moral Publisher, 2008).
- [42] A. Moral, *Handbook of Magnetostriction and Magnetostrictive Materials*, vol. 2 of *Handbook of Magnetostriction and Magnetostrictive Materials* (Del Moral Publisher, 2008).

- [43] É. du Tremolet de Lacheisserie, *Magnetostriction: Theory and Applications of Magnetoelasticity* (CRC Press, 1993).
- [44] B. Cullity and C. Graham, *Introduction to Magnetic Materials* (Wiley, 2011).
- [45] C. Dietl, Master thesis, University of Heidelberg (2012).
- [46] B. A. Green and B. S. Chandrasekhar, *Phys. Rev. Lett.* **11**, 331 (1963).
- [47] F. Reif, *Fundamentals of Statistical and Thermal Physics* (McGraw-Hill Inc., 1965).
- [48] E. S. R. Gopal, *Specific Heats at Low Temperatures*, International Cryogenics monograph series (Plenum Press, 1966).
- [49] S. J. Joshua, *Australian Journal of Physics* **37**, 305 (1984).
- [50] F. Han, *A Modern Course in the Quantum Theory of Solids* (World Scientific, 2013).
- [51] J. M. Coey, *Magnetism and Magnetic Materials* (Cambridge University Press, 2010).
- [52] M. G. Banks, Ph.D. thesis, Loughborough University (2007).
- [53] M. Evangelisti, Ph.D. thesis, University of Leiden (2001).
- [54] F. Pobell, *Matter and Methods at Low Temperatures* (Springer, 2007).
- [55] S. Blundell, *Magnetism in Condensed Matter - Oxford Master Series in Condensed Matter Physics* (Oxford University Press USA, 2001).
- [56] H. Gould and J. Tobochnik, *Statistical and Thermal Physics: With Computer Applications* (Princeton University Press, 2010).
- [57] N. Spaldin, *Magnetic Materials: Fundamentals and Applications* (Cambridge University Press, 2010).
- [58] M. McElfresh, *Fundamentals of Magnetism and Magnetic Measurements* (1994).
- [59] M. Tinkham, *Introduction to Superconductivity* (McGraw-Hill Inc., 1996).

- [60] J. Clark and A. I. Braginski, *The SQUID Handbook, Vol 2: Applications of SQUIDs and SQUID systems* (Wiley-VCH, New York, 2006).
- [61] *Quantum Design MPMS Application Note 1014-203: Outline of Regression Routines* (2000).
- [62] D. Tunstall and D. Barford, *High Temperature Superconductivity*, Scottish Graduate Series (Taylor & Francis, 1992).
- [63] D. Bruce and D. O'Hare, *Inorganic Materials* (Wiley, 1997).
- [64] R. Hein, T. Francavilla, and D. Liebenberg, *Magnetic Susceptibility of Superconductors and Other Spin Systems* (Springer, 1991).
- [65] J. Weil, J. Bolton, and J. Wertz, *Electron Paramagnetic Resonance: Elementary Theory and Practical Applications*, Wiley-Interscience publication (Wiley, 1994).
- [66] EPR products offered by Bruker, URL <http://www.bruker.com/products/mr/epr.html>.
- [67] Experimental Techniques available at the Dresden High Magnetic Field Laboratory using Pulsed Magnetic Fields, URL <http://www.hzdr.de/db/Cms?pNid=2687>.
- [68] S. A. Zvyagin, E. Čížmár, M. Ozerov, J. Wosnitza, R. Feyerherm, S. R. Manmana, and F. Mila, *Physical Review B* **83**, 060409 (2011).
- [69] P. Rieger, *Electron Spin Resonance*, URL http://fen.nsu.ru/posob/organic/phymethods/lit/NMR/add/Rieger_Electron%20spin%20resonance.pdf.
- [70] B. M. Weckhuysen, R. Heidler, and R. A. Schoonheydt, in *Characterization I* (Springer, 2004), pp. 295–335.
- [71] A. Lund, S. Shimada, and M. Shiotani, *Principles and Applications of ESR Spectroscopy* (Springer, 2011).
- [72] E. Gmelin, *Thermochimica Acta* **110**, 183 (1987).
- [73] *Quantum Design Physical Property Measurement System: Heat Capacity Option User's Manual 1085-150* (2004).

- [74] J. C. Lashley, M. F. Hundley, A. Migliori, J. L. Sarrao, P. G. Pagliuso, T. W. Darling, M. Jaime, J. C. Cooley, W. L. Hults, and L. Morales, *Cryogenics* **43**, 369 (2003).
- [75] J. S. Hwang, K. J. Lin, and C. Tien, *Review of Scientific Instruments* **68**, 94 (1997).
- [76] M. S. Vijaya and G. Rangarajan, *Materials Science* (Tata McGraw Hill Education Private Limited, 2003).
- [77] A. M. Thompson, *IRE Transactions on I-7* **3** (1958).
- [78] Andeen-Hagerling, *AH2700A 50 Hz - 20 kHz Ultra Precision Capacitance Bridge: Operation and Maintenance Manual* (2003).
- [79] M. Rotter, H. Muller, E. Gratz, M. Doerr, and M. Loewenhaupt, *Review of Scientific Instruments* **69**, 2742 (1998).
- [80] Lake Shore Cryotronics temperature sensor catalog, URL http://www.lakeshore.com/Documents/LakeShoreTC_h.pdf.
- [81] B. L. Brandt, D. W. Liu, and L. G. Rubin, *Review of Scientific Instruments* **70**, 104 (1999).
- [82] H. Müller and M. Rotter, *Capacitance Dilatometer DIL20-11 User Manual*, Institute of Solid State Physics, Vienna University of Technology, Austria (2011).
- [83] S. Pilla, J. A. Hamida, K. A. Muttalib, and N. S. Sullivan, *Physical Review B* **77** (2008).
- [84] Webpage for the Leybold CERAVAC CTR 1000 manometer, URL https://leyboldproducts.oerlikon.com/products/produktkatalog_04.aspx?cid=2568.
- [85] F. R. Kroeger and C. A. Swenson, *Journal of Applied Physics* **38**, 853 (1977).
- [86] N. Kinomura, F. Muto, and M. Koizumi, *Journal of Solid State Chemistry* **45**, 252 (1982).

- [87] R. Glaum and R. Gruehn, *Zeitschrift für Anorganische und Allgemeine Chemie* **580**, 78 (1990).
- [88] R. Glaum and R. Gruehn, *Zeitschrift für Kristallographie* **198**, 41 (1992).
- [89] R. Glaum, M. Reehuis, N. Stüsser, U. Kaiser, and F. Reinauer, *Journal of Solid State Chemistry* **126**, 15 (1996).
- [90] M. Bykov, J. Zhang, A. Schönleber, A. Wölfel, S. I. Ali, S. van Smaalen, R. Glaum, H. J. Koo, M. H. Whangbo, P. G. Reuvekamp, et al., *Physical Review B* **88**, 184420 (2013).
- [91] N. Majlis, *The Quantum Theory of Magnetism* (World Scientific, 2007).
- [92] M. Enderle, Habilitation thesis, Universität des Saarlandes (1999).
- [93] V. Korepin, N. Bogoliubov, and A. Izergin, *Quantum Inverse Scattering Method and Correlation Functions*, Cambridge Monographs on Mathematical Physics (Cambridge University Press, 1997).
- [94] B. Lake, D. A. Tennant, C. D. Frost, and S. E. Nagler, *Nature Materials* **4**, 329 (2005).
- [95] B. Lake, A. M. Tsvelik, S. Notbohm, D. A. Tennant, T. G. Perring, M. Reehuis, C. Sekar, G. Krabbes, and B. Büchner, *Nature Physics* **6**, 50 (2009).
- [96] B. Lake, D. A. Tennant, J. S. Caux, T. Barthel, U. Schollwöck, S. E. Nagler, and C. D. Frost, *Physical Review Letters* **111**, 137205 (2013).
- [97] D. A. Tennant, T. G. Perring, R. A. Cowley, and S. E. Nagler, *Physical Review Letters* **70**, 4003 (1993).
- [98] S. E. Nagler, D. A. Tennant, R. A. Cowley, T. G. Perring, and S. K. Satija, *Physical Review B* **44**, 12361 (1991).
- [99] M. Arai, M. Fujita, M. Motokawa, J. Akimitsu, and S. Bennington, *Physical Review Letters* **77**, 3649 (1996).
- [100] M. Fujita, C. D. Frost, S. M. Bennington, R. Kajimoto, M. Nakamura, Y. Inamura, F. Mizuno, K. Ikeuchi, and M. Arai, *Journal of the Physical Society of Japan* **82**, 084708 (2013).

- [101] S. Eggert, I. Affleck, and M. Takahashi, *Physical Review Letters* **73**, 332 (1994).
- [102] A. Klümper and D. C. Johnston, *Physical Review Letters* **84**, 4701 (2000).
- [103] A. Klümper, *The European Physical Journal B - Condensed Matter and Complex Systems* **5**, 677 (1998).
- [104] R. Peierls, *More Surprises in Theoretical Physics*, Princeton Series in Physics (Princeton University Press, 1991).
- [105] R. Peierls and R. Dalitz, *Selected Scientific Papers of Sir Rudolf Peierls: With Commentary*, Series in 20th Century Physics (World Scientific Publishing Company Incorporated, 1997).
- [106] S. Roth and D. Carroll, *One-Dimensional Metals* (Wiley-VCH, 2004).
- [107] Peierls Instability and Charge Density Waves, URL http://www.pi1.physik.uni-stuttgart.de/glossar/Peierls_e.php.
- [108] G. A. Toombs, *Physics Reports* **40**, 181 (1978).
- [109] A. J. Berlinsky, *Reports on Progress in Physics* **42**, 1243 (1979).
- [110] J. T. Tiedje, Master thesis, University of British Columbia (1975).
- [111] T. Sambongi, K. Tsutsumi, Y. Shiozaki, M. Yamamoto, K. Yamaya, and Y. Abe, *Solid State Communications* **22**, 729 (1977).
- [112] A. I. Buzdin and L. N. Bulaevskii, *Soviet Physics Uspekhi* **23**, 409 (1980).
- [113] J. W. Bray, L. V. Interrante, I. S. Jacobs, and J. C. Bonner, *Chapter Seven - "The Spin-Peierls Transition" in Extended Linear Chains Compounds Editor: J. S. Miller*, vol. 3 (Plenum Press, 1983).
- [114] I. S. Jacobs, J. W. Bray, H. R. Hart, L. V. Interrante, J. S. Kasper, G. D. Watkins, D. E. Prober, and J. C. Bonner, *Phys. Rev. B* **14**, 3036 (1976).
- [115] J. Miller and M. Drillon, *Magnetism: Molecules to Materials*, vol. 1 of *Magnetism: Molecules to Materials* (Wiley-VCH, 2001).
- [116] Y. Nakazawa, A. Sato, M. Seki, K. Saito, K. Hiraki, T. Takahashi, K. Kanoda, and M. Sorai, *Physical Review B* **68**, 085112 (2003).

- [117] P. Foury-Leylekian, P. Auban-Senzier, C. Coulon, O. Jeannin, M. Fourmigué, C. Pasquier, and J. Pouget, *Physical Review B* **84**, 195134 (2011).
- [118] M. Isobe and Y. Udea, *Journal of the Physical Society of Japan* **65**, 1178 (1996).
- [119] A. Bernert, P. Thalmeier, and P. Fulde, *Physical Review B* **66**, 165108 (2002).
- [120] L. N. Bulaevskii, *Soviet Physics - Journal of Experimental and Theoretical Physics* **11**, 921 (1969).
- [121] K. Uchinokura, *Journal of Physics: Condensed Matter* **14**, R195 (2002).
- [122] R. Rückamp, J. Baier, M. Kriener, M. W. Haverkort, T. Lorenz, G. S. Uhrig, L. Jongen, A. Möller, G. Meyer, and M. Grüninger, *Physical Review Letters* **95**, 097203 (2005).
- [123] M. Shaz, S. van Smaalen, L. Palatinus, M. Hoinkis, M. Klemm, S. Horn, and R. Claessen, *Physical Review B* **71**, 100405 (2005).
- [124] M. Hofmann, Ph.D. thesis, Universität zu Köln (2002).
- [125] Y. K. Kuo, D. K. Powell, and J. W. Brill, *Solid State Communications* **98**, 1027 (1996).
- [126] J. W. Bray, *Solid State Communications* **26**, 771 (1978).
- [127] V. Kiryukhin and B. Keimer, *Physical Review B* **52**, 704 (1995).
- [128] V. Kiryukhin, B. Keimer, and D. E. Moncton, *Physical Review Letters* **74**, 1669 (1995).
- [129] V. Kiryukhin, B. Keimer, J. Hill, and A. Vigliante, *Physical Review Letters* **76**, 4608 (1996).
- [130] H. M. Rønnow, M. Enderle, D. F. McMorrow, L. P. Regnault, G. Dhalenne, A. Revcolevschi, A. Hoser, K. Prokes, P. Vorderwisch, and H. Schneider, *Physical Review Letters* **84**, 4469 (2000).
- [131] L. N. Bulaevskii, A. I. Buzdin, and D. I. Khomskii, *Solid State Communications* **27**, 5 (1978).

- [132] M. C. Cross, *Physical Review B* **20**, 4606 (1979).
- [133] J. W. Bray, L. V. Interrante, I. S. Jacobs, D. Bloch, D. E. Moncton, G. Shirane, and J. C. Bonner, *Physical Review B* **20**, 2067 (1979).
- [134] D. Bloch, J. Voiron, C. Vettier, J. W. Bray, and S. Oostra, *Physica B+C* **119**, 43 (1983).
- [135] J. W. Bray, *Solid State Communications* **35**, 853 (1980).
- [136] Y. Lépine, *Solid State Communications* **57**, 189 (1986).
- [137] H. Takahashi, N. Mori, O. Fujita, J. Akimitsu, and T. Matsumoto, *Solid State Communications* **95**, 817 (1995).
- [138] S. Blanco-Canosa, F. Rivadulla, A. Pineiro, V. Pardo, D. Baldomir, D. I. Khomskii, M. M. Abd-Elmeguid, M. A. López-Quintela, and J. Rivas, *Physical Review Letters* **102**, 056406 (2009).
- [139] D. Fausti, T. Lummen, C. Angelescu, R. Macovez, J. Luzon, R. Broer, P. Rudolf, P. van Loosdrecht, N. Tristan, and B. Büchner, *Physical Review B* **75**, 245114 (2007).
- [140] A. Schönleber, S. van Smaalen, and L. Palatinus, *Physical Review B* **73**, 214410 (2006).
- [141] A. Schönleber, G. Shcheka, and S. van Smaalen, *Physical Review B* **77**, 094117 (2008).
- [142] S. van Smaalen, *Incommensurate Crystallography* (Oxford University Press, 2007).
- [143] A. Eiling and J. S. Schilling, *Journal of Physics F: Metal Physics* **11**, 623 (1981).
- [144] S. Klotz, *Techniques in High Pressure Neutron Scattering* (Taylor & Francis, 2012).
- [145] S. Kakaç, H. Yüncü, K. Hijikata, and H. Hijikata, *Cooling of Electronic Systems*, 258 (Springer, 1994).
- [146] T. Varga, A. P. Wilkinson, and R. J. Angel, *Review of Scientific Instruments* **74**, 4564 (2003).

- [147] C. Gribble and A. Hall, *Optical Mineralogy: Principles And Practice* (Taylor & Francis, 2003).
- [148] The website for the OrientExpress Instrument, URL <http://www.i11.eu/?id=13537>.
- [149] P. Selwood, *Magnetochemistry* (Interscience, 1956).
- [150] Error propagation rules, URL <http://www.physics.brocku.ca/Courses/1P91/lab-manual/errorrules.pdf>.
- [151] W. Schnelle, Y. Grin, and R. K. Kremer, *Physical Review B* **59**, 73 (1999).
- [152] S. G. Bompadre, A. F. Hebard, V. N. Kotov, D. Hall, G. Maris, J. Baas, and T. Palstra, *Physical Review B* **61**, R13321 (2000).
- [153] T. Caldwell, P. L. Kuhns, W. Moulton, A. P. Reyes, P. N. Rogers, and R. N. Shelton, *International Journal of Modern Physics B* **16**, 3298 (2002).
- [154] L. Weckhuysen, S. V. Demishev, A. V. Semeno, J. Vanacken, L. Trappeniens, A. A. Pronin, and V. V. Moshchalkov, *Europhysics Letters* **53**, 667 (2001).
- [155] W. Qing-Bo, X. Xiang-Fan, T. Qian, W. Hong-Tao, and X. Zhu-An, *Chinese Physics B* **17**, 3490 (2008).
- [156] J. Northby, F. Greidanus, W. Huiskamp, L. de Jongh, I. Jacobs, and L. Interrante, *Journal of Applied Physics* **53**, 8032 (1982).
- [157] M. Bykov, J. Zhang, A. Schönleber, A. Wölfel, S. I. Ali, S. van Smaalen, R. Glaum, H. J. Koo, M. H. Whangbo, P. G. Reuvekamp, et al., *Supplemental material: Spin-Peierls distortions in TiPO₄* (2013).
- [158] A. Schönleber, G. Shcheka, and S. van Smaalen, *Physical Review B* **77**, 094117 (2008).
- [159] J. Angelkort, A. Wölfel, A. Schönleber, S. van Smaalen, and R. K. Kremer, *Physical Review B* **80**, 144416 (2009).
- [160] J. Angelkort, Ph.D. thesis, Universität Bayreuth (2009).
- [161] H. Schäfer and F. Wartenpfehl, *Zeitschrift für Anorganische und Allgemeine Chemie* **308**, 292 (1961).

- [162] H. Forsberg, *Acta Chemica Scandinavica* **16**, 777 (1962).
- [163] A. Haase and G. Brauer, *Acta Crystallographica Section B: Structural Crystallography and Crystal Chemistry* **31**, 2521 (1975).
- [164] S. Lovesey and S. Collins, *X-ray Scattering and Absorption by Magnetic Materials*, Oxford Science Publications (Clarendon Press, 1996).
- [165] C. Kant, J. Deisenhofer, V. Tsurkan, and A. Loidl, in *Journal of Physics: Conference Series* (IOP Publishing, 2010), vol. 200, p. 032032.
- [166] S. Bhattacharjee, S. Zherlitsyn, O. Chiatti, A. Sytcheva, J. Wosnitza, R. Moessner, M. Zhitomirsky, P. Lemmens, V. Tsurkan, and A. Loidl, *Physical Review B* **83**, 184421 (2011).
- [167] V. Tsurkan, S. Zherlitsyn, S. Yasin, V. Felea, Y. Skourski, J. Deisenhofer, H.-A. K. von Nidda, J. Wosnitza, and A. Loidl, *Physical Review Letters* **110**, 115502 (2013).
- [168] K. Nocker and R. Gruehn, *Zeitschrift für Anorganische und Allgemeine Chemie* **619**, 699 (1993).
- [169] Y. Skourski, M. D. Kuz'min, K. P. Skokov, A. V. Andreev, and J. Wosnitza, *Physical Review B* **83**, 214420 (2011).
- [170] R. L. Carlin, *Magnetochemistry* (Springer Berlin, 1986).
- [171] A. Schönleber, S. van Smaalen, R. K. Kremer, and A. Senyshyn, unpublished 16.7.12 - Supplemental Material.
- [172] H. L. Williamson, Placement thesis @ Max Planck Institute for Solid State Research (2011).
- [173] A. Schönleber, S. van Smaalen, R. K. Kremer, and A. Senyshyn, unpublished 16.7.12 - Article.
- [174] M. H. Whangbo, H. J. Koo, and D. Dai, *Journal of Solid State Chemistry* **176**, 417 (2003).
- [175] H. Xiang, C. Lee, H. J. Koo, X. Gong, and M. H. Whangbo, *Dalton Transactions* **42**, 823 (2013).

- [176] M. G. Banks, R. K. Kremer, C. Hoch, A. Simon, B. Ouladdiaf, J. M. Broto, H. Rakoto, C. Lee, and M. H. Whangbo, *Physical Review B* **80**, 024404 (2009).
- [177] C. Lee, J. Liu, M. H. Whangbo, H. J. Koo, R. K. Kremer, and A. Simon, *Physical Review B* **86**, 060407 (2012).
- [178] K. Caslin, R. K. Kremer, F. S. Razavi, A. Schulz, A. Muñoz, F. Pertlik, J. Liu, M. H. Whangbo, and J. M. Law, *Physical Review B* **89**, 014412 (2014).
- [179] H. J. Koo and M. H. Whangbo, *Inorganic Chemistry* **47**, 128 (2008).
- [180] H. J. Koo and M. H. Whangbo, *Inorganic Chemistry* **47**, 4779 (2008).
- [181] P. E. Blöchl, *Physical Review B* **50**, 17953 (1994).
- [182] G. Kresse and D. Joubert, *Physical Review B* **59**, 1758 (1999).
- [183] G. Kresse and J. Furthmüller, *Physical Review B* **54**, 11169 (1996).
- [184] J. P. Perdew, A. Ruzsinszky, G. I. Csonka, O. A. Vydrov, G. E. Scuseria, L. A. Constantin, X. Zhou, and K. Burke, *Physical Review Letters* **100**, 136406 (2008).
- [185] M. Rotter et al., *Website of the mcphas program*, URL http://www2.cpfs.mpg.de/~rotter/homepage_mcphase/manual/node22.html.
- [186] M. Rotter et al., *Website of the McPhase package*, URL <http://mcphase.de/>.
- [187] M. Rotter and A. T. Boothroyd, *Physical Review B* **79**, 140405 (2009).
- [188] Private communication with Prof. M. H. Whangbo (2014).
- [189] Y. Savina, O. Bludov, V. Pashchenko, S. Gnatchenko, P. Lemmens, and H. Berger, *Physical Review B* **84**, 104447 (2011).
- [190] Y. V. Goryunov, A. V. Levchenko, and A. N. Nateprov, in *Journal of Physics: Conference Series* (IOP Publishing, 2012), vol. 400, p. 032013.
- [191] J. Hemberger, H. A. K. von Nidda, V. Tsurkan, and A. Loidl, *Physical Review Letters* **98**, 147203 (2007).

- [192] M. Rotter, *Journal of Magnetism and Magnetic Materials* **272**, E481 (2004).
- [193] R. J. Elliott, *Physical Review* **124**, 346 (1961).
- [194] R. Liebmann, *Statistical Mechanics of Periodic Frustrated Ising Systems*, vol. 251 of *Lecture Notes in Physics* (Springer-Verlag, 1986).
- [195] W. Selke and M. E. Fisher, *Physical Review B* **20**, 257 (1979).
- [196] W. Selke, *Physics Reports* **170**, 213 (1988).
- [197] H. Müller and M. Rotter, *Pat general purpose data analysis software*, URL <http://www.ifp.tuwien.ac.at/homepages/Personen/herbert.mueller/pat/.the/>.
- [198] S. Bochkhanov and V. Bystritsky, *Website of the ALGLIB package*, URL www.alglib.net.
- [199] N. Mehboob, Master thesis, Technische Universität Wien (2009).
- [200] Private communication with M. Rotter (2012).
- [201] M. A. Brown and C. E. Bulleid, *Journal of Physics E: Scientific Instruments* **11**, 429 (1978).
- [202] G. K. White and J. G. Collins, *Journal of Low Temperature Physics* **7**, 43 (1972).

CURRICULUM VITAE

PATRICK REUVEKAMP

1 PERSONAL DETAILS

Place of birth: St. Catharines, Ontario, Canada



2 EDUCATION

- 09/2003–05/2007 Undergraduate Studies in Physics and Mathematics at Brock University in St. Catharines, Ontario, Canada
Completed B.Sc. degree with first class standing
Thesis: *Single Crystals and Epitaxial Thin Films of Sodium Cobalt Oxide*
Thesis Supervisor: Prof. F. S. Razavi, Ph.D.
- 09/2007–08/2009 M.Sc. in Condensed Matter and Material Science at Brock University in St. Catharines, Ontario, Canada
Thesis: *The Magnetic and Transport Properties of $Ba_{1-x}K_xFe_2As_2$*
Thesis Supervisor: Prof. F. S. Razavi, Ph.D.
- 09/2009–08/2014 Ph.D. studies in Physics at the International Max Planck Research School for Condensed Matter Science at the Max Planck Institute for Solid State Physics (Chemieservice Group) in collaboration with the University of Stuttgart
Thesis: *Investigation into the magnetic and the structural properties of two low-dimensional antiferromagnets $TiPO_4$ and $CrOCl$*
Thesis Supervisor: Prof. Dr. B. Keimer
Scientific Advisor: Dr. R. K. Kremer

Stuttgart, Deutschland – November 10, 2014

Acknowledgements

Firstly, I would like to thank Prof. Dr. B. Keimer for enabling me to carry out my doctoral work at the Max Planck Institute for Solid State Research. This work would not have been possible without the financial support of the International Max Planck Research School for Condensed Matter Research (IMPRS-CMS) and the Max Planck Society. I would especially like to thank the Coordinator of IMPRS-CMS Dr. H. G. Libuda for his assistance in the many administrative matters. I am grateful to Prof. Dr. M. Dressel and Prof. Dr. H. P. Büchler for participating in my thesis committee. Ms. E Reinéry, OCT, M.A. assistance in proofreading this thesis was greatly appreciated.

Above all, I was privileged to have Dr. R. K. Kremer as my scientific advisor. His experimental expertise, especially his vast knowledge of cryogenics, which he imparted to me was a critical factor in the completion of this thesis. The experimental and the technical assistance from the technicians in his group Fr. E. Brücker, Fr. G. Siegle and Hr. S. Höhn was instrumental in solving many of challenges presented in this work. I truly appreciate the many interesting scientific collaborations which I had with Prof. Dr. A. Bussmann-Holder, Prof. R. S. Gonnelli, Prof. F. S. Razavi, Dr. J. M. Law, K. Caslin, Dr. J. Chun, Prof. M. Johnsson and Dr. M. Stingaciu over the years. I have gained of a multitude of experiences and insights from these fruitful collaborations. In particular, I will distinctly remember the many noteworthy conversations which I had with the late Prof. Dr. M. Cardona since I first met him in 2008.

The intriguing results discovered in this thesis would not have been possible without the high quality crystalline samples prepared by Prof. R. Glaum's group at the University of Bonn and Prof. van Smaalen's group at University of Bayreuth. In addition, the crystallography results from the collaborations with Prof. van Smaalen's group were essential in the comprehending the low temperature magnetic behaviour of both compounds. The density functional theory calculations from Prof. M. H. Whangbo and the pulsed magnetic field measurements performed with Dr. J. M. Law were crucial in understanding the complex magnetic behaviour of CrOCl. The assistance of the Dr. J. Nuss and Dr. B. Ouladdiaf in the alignment of the TiPO_4 crystals was vital for the thermal expansion measurements. The high-precision Raman scattering measurements from Hr. Schultz were key in recognizing the one of the high temperature phase transitions in CrOCl. The high quality images of the samples were captured by Fr. V. Duppel in the Nanochemistry group.

Lastly, I would like to thank my parents and late maternal grandparents for their support and constant encouragements along my long educational journey.